In-vitro In-silico Modeling of Glioblastoma Tumor Growth and Invasion

by

Meitham Amerehbozchalouee
B.Sc., Tehran Polytechnic, 2014
M.Sc., The University of British Columbia, 2018

A Dissertation Submitted in Partial Fulfillment of the
Requirements for the Degree of

DOCTOR OF PHILOSOPHY

in the Department of Mechanical Engineering

In-vitro In-silico Modeling of Glioblastoma Tumor Growth and Invasion

by

Meitham Amerehbozchalouee
B.Sc., Tehran Polytechnic, 2014
M.Sc., The University of British Columbia, 2018

Supervisory Committee

Prof. Mohsen Akbari, Co-Supervisor
(Department of Mechanical Engineering)

Prof. Ben Nadler, Co-Supervisor
(Department of Mechanical Engineering)

Prof. Patrick Walter, Outside Member
(Department of Biology)

Prof. Roderick Edwards, Outside Member
(Department of Mathematics and Statistics)

ABSTRACT

In this thesis, we investigate various aspects of tumor progression through formation, growth, and invasion, by a multidisciplinary approach involving mathematical modeling and experimental validation. We begin this study by modeling the transient formation of tumors by a system of reaction-diffusion partial differential equations (PDEs) that considers adhesion forces, cell proliferation, and pressure-induced growth. The process of tumor formation includes a preliminary contraction phase where adhesion forces densify cell aggregation. This phase proceeds until the cell concentration reaches a threshold, the so-called "relaxed concentration" at equilibrium. Afterwards, cell proliferation raises concentration and produces pressure which breaks the equilibrium. Providing analytical and numerical solutions, the model's reliability is confirmed through experiments with tumor-cultured human glioblastoma (hGB) cancer cell lines. We expand the model to analyze the instability of radially symmetric growth in response to asymmetric perturbations. By improving the model to incorporate additional variables such as nutrient concentration, consumption rates, and surface tension, we focus on the asymmetric modes of growth, which grow in time and change the spherical configuration of the tumor. We show that a high nutrient source concentration allows for a large tumor size, which increases the number of unstable excited asymmetric modes. However, high rates of nutrient consumption and surface tension can lead to a smaller size of the tumor and a smaller number of growing asymmetric modes. This analysis, indicating the natural instability of the spherical configuration of tumor was confirmed by a comparison between the shapes of in-vitro hGB tumors and the configuration of the first few asymmetric modes predicted by the model.

To further understand the effect of tumor microenvironment (TME) on tumor configuration, we study biomechanical stimulus-induced remodeling of tumors in response to gradients of external biochemical stimuli, considering the tumor as an evolving material. We develop an evolution law for the remodeling-associated deformation which correlates the remodeling to a characteristic tensor of external biochemical stimuli. The asymmetric remodeling and the induced mechanical stresses are analyzed for different types of biochemical distributions. Using a tumor-on-a-chip platform, the degree of remodeling is estimated for the ellipsoidal tumors over time. Additionally, we explore invasion as one of the key hallmarks of tumors by introducing a continuum model that integrates various factors to predict a distinctive shell-type invasion

pattern in which cells at the outer layer of the tumor collectively move away from the core and form a shell-type shape. We adopt a non-convex free energy that allows for phase separation to model the motion of the invasive shell.

To develop a more realistic model, we extend our mathematical framework to include heterogeneities within a tumor as they play a crucial role in cancer diagnosis, treatment, and prognosis. We present a hybrid discrete-continuum (HDC) model incorporating experimental measurements and in-vitro tumor-on-a-chip platforms to study tumor growth, invasion, and their dependency on matrix stiffness. The model integrates the continuum field of variables with a discrete approach and incorporates the random walk method for individual cell migration. Moreover, we study the influence of matrix stiffness on tumor growth and invasion using a PEGDA-printed tumor-on-a-chip platform. The presented framework is capable of distinguishing the growth and invasion of non-resistant versus chemo-resistant tumors, as well as the inhibitory effect of a chemotherapeutic drug. We also show that U251 non-resistant tumors grow faster compared to the temozolomide (TMZ)-resistant tumors, whereas the TMZ-resistant tumors have the longest invasion length. We utilize a stochastic approach that is consistent with observed biological behavior and provides a more realistic representation of the invasion process. This hybrid model, validated against an in-vitro co-culturing of non-resistant and TMZ-resistant hGB tumors with healthy neurons all embedded within a hydrogel matrix, shows promise in quantitative predictions on volumetric growth, invasion length, and invasion patterns of tumors.

Our study concludes by highlighting the comprehensive understanding achieved through analytical modeling, experimental validation, and hybrid modeling techniques. The findings lay the groundwork for future investigations into therapeutic interventions, considering the intricate interplay between biological and mechanical factors in the TME.

Contents

List of Tables

List of Figures

ACKNOWLEDGEMENTS

I would like to express my sincere gratitude to:

My supervisors, Prof. Mohsen Akbari and Prof. Ben Nadler, for their invaluable guidance, wonderful support, and scholarly insights throughout my research journey. Their expertise and encouragement have been instrumental in shaping this work, and I am truly grateful for the opportunity to learn under their mentorship.

My mentors, Prof. Patrick Walter and Prof. Roderick Edwards, who taught me not to be afraid of exploring new topics, learning and growing.

My fellow labmates, at Laboratory for Innovation in Microengineering (LiME), for their help and friendship.

My wife, for her love and support, which has been my anchor throughout this journey. Her encouragement means the world to me.

This research was financially supported by the Natural Sciences and Engineering Research Council of Canada (NSERC).

Freedom of thought is best promoted by the gradual illumination of men's minds which follows from the advance of science.

Charles Darwin

ACRONYMS

DNA Deoxyribonucleic Acid

ODE Ordinary Differential Equation

PDE Partial Differential Equation

CA Cellular Automata

HDC Hybrid Discrete Continuum

ECM Extracellular Matrix

TME Tumor Microenvironment

GBM Glioblastoma Multiforme

hGB Human Glioblastoma

pdGBM patient-derived Glioblastoma Mutiform

3D Three-Dimensional

ENS Enteric Nervous System

CN Crank–Nicolson

DMEM Dulbecco's Modification of Eagle's Medium

FBS Fetal Bovine Serum

PBS Phosphate-Buffered Saline

SFMA Self-Filling Micro-Well Array

EMT-TF Epithelial to Mesenchymal Transit-inducing Transcription Factor

AML Acute Myeloid Leukemia Transformation

HA Hyaluronic Acid

IHC Immunohistochemistry

CH Composite Hydrogel

DAPI 4', 6-diamidino-2-phenylindole

MMPs Matrix Metalloproteases

ASCs Adipose Stromal Cells

EGFR Epidermal Growth Factor Receptor

TMZ Temozolomide

HIF Hypoxia-Induced Factor

ATP Adenosine Triphosphate

ROS Reactive Oxygen Species

MDE Matrix Degradative Enzymes

PHC Proliferative-to-Hypoxic Conversion

GOD Glucose Oxidase

POD Peroxidase

UV Ultra-Violate

DLP Digital Light Processing

PEGDA Poly-(Ethylene Glycol) Diacrylate

LAP Lithium phenyl-2,4,6-trimethylbenzoylphosphinate

DEDICATION

To my beloved wife, Zahra

Chapter 1

Introduction

1.1 Background and Literature Review

Understanding the complexities of tumor biology remains a difficult challenge in the fields of cancer biology and medicine. Tumors exhibit intricate molecular dynamics, involving genetic instabilities, therapeutic resistance, and inter- and intra-tumor heterogeneity [3]. Despite substantial efforts to develop therapeutic strategies, there is an ongoing need for deeper insights into these complex aspects of tumor behavior.

Mathematical modeling stands out as a powerful approach to predict various aspects of tumor progression [4]. By offering quantitative predictions of biological processes, mathematical models aid in interpreting the intricate physiological interactions within the tumor microenvironment [5]. Collaborative efforts between mathematical modelers and experimentalists can yield mechanistic solutions with practical implications, particularly in the field of cancer treatment. The cross-disciplinary integration of mathematical and biological models, holds significant promise for enhancing cancer treatment strategies.

Various mathematical approaches, including continuum, discrete, and hybrid models, have been employed to study tumor formation and growth [6–11]. Continuum models describe a tumor as a continuous mass and quantify cell concentration. Single cell models consider cells the only component in the system. They are able to model tumors made of only one type of cells, typically small spheroids. On the other hand, multiphase models are capable of tracking multiple cell species and the ECM components. Subcellular phenomena and stochastic effects are usually neglected in these models. Therefore, they are well-suited to investigate the growth of large tumors in

the range of few millimetres. In the continuum approach, variables are considered continuous, described by partial differential equations (PDEs) capturing growth, kinetic interactions, and diffusion for transport phenomena [12–14]. This approach allows for analysis of oxygen and chemical distributions to determine tumor radius and growth inhibition [15, 16]. Researchers have utilized the continuum modeling framework to consider a tumor as an incompressible fluid responding to local nutrient concentration, and have incorporated cell-cell adhesion to predict modes of instability [17]. pH and oxygen levels were later identified as key parameters influencing tumor growth rate [18, 19]. Moreover, the role of mechanical stress was explored via the continuum framework by considering tumors as hyperelastic materials [20–24]. These studies used multiplicative decomposition of the deformation gradient to investigate spatial distribution of stresses. More continuum-based studies reviewed solid tumor growth [25–28].

Discrete approaches are another framework of modeling tumors that capture cellular responses, signaling pathways, and microenvironment effects, and contribute to a comprehensive understanding of solid tumor growth [11]. In discrete cell modeling, each cell in a tumor is assigned to a set of parameter values and behavioural rules and their collection makes the body of the tumor. This approach has been used to study tumor invasion and formation of clonal structures. For instance, the effect of microenvironment, e.g. extracellular matrix density and oxygen concentration, on the growth of tumor and phenotypic diversity was studied in [11, 29]. It is shown that a low level of oxygen can change the phenotype of tumor cells to aggressive phenotypes. Lattice Monte Carlo is another type of discrete model which could predict spheroid growth under varying nutrient supply conditions [30]. Another example of discrete models is cellular automata (CA), which predict the collective behavior of self-organizing systems, such as tumors, by focusing on the interactions between the components [31]. It is notable that although discrete cell modeling enables capturing the effect of cellular response and signaling pathways, the increased complexity and level of detail raise the cost of calculations required for clinical size tumors [32].

Hybrid discrete continuum (HDC) models, combining both continuum and discrete approaches, offer insights into macroscopic variables and discrete biological interactions, and therefore overcome the weaknesses of both approaches [26, 33–37]. This approach not only provides macroscopic observation on the behaviors of the biological structure but captures a realistic description of microscopic phenomena [38]. In the case of solid tumor growth, the clinical-size morphology of tumors can be stud-

ied in hybrid models while the cellular pathways and subcellular interactions are also involved [37]. For instance, Stokes and Lauffenburger combined RD model of TAF with the probabilistic equation of endothelial cell movement [39]. They showed that a significant level of random motility was necessary for growing a vasculature network. Hybrid models rely on information transfer between cellular and subcellular scales [40, 41]. Therefore, these models relate the cell-level interactions to macroscopic morphology of tumors. For more details about discrete and hybrid approaches, the reader is encouraged to refer to the following papers [26, 33–36].

Mathematical modeling has significant potential for understanding of biological models of cancer and to accelerate the progress in cross-disciplinary approaches of cancer treatment. The simplest, yet predominantly used in-vitro model of tumors, are spheroids. The size of spheroids and their cell number are easy to track, making them a simple in-vitro model to investigate tumor behavior, quantitatively [42–46]. The growth of tumor spheroids is comprised of three main stages: transient formation, monotonic growth and a plateau phase. Similar to tumor spheroids, primary malignant tumors originate from small numbers of cells which become highly proliferative through mutations occurring in oncogenes, tumor suppressors or DNA repair genes [47]. Although the genetic mutations eventually lead to formation of large and complex vascular tumors, they all go through an avascular (devoid of blood vessels) mode at their early stage of growth [48]. Having insight into this stage of growth is valuable in understanding the behavior of tumors at subsequent phases. Tumor formation is a crucial phase in tumor development, providing valuable insights into subsequent phases of growth. Mathematical models focusing on avascular tumors have been instrumental in in-vitro models, allowing quantitative investigation of factors such as tumor size, cell numbers, and the fractions of hypoxic, quiescent, and proliferative cells [42–46, 49–51].

Spanning theoretical studies to clinical trial design, mathematical oncology has become pivotal in personalized medicine [52]. Applications of continuum-based in-silico models in simulating vascularized solid tumor growth have been reviewed in [53]. It has been shown that extracellular cues, including nutrients, growth factors, oxygen, and stresses, profoundly influence tumor pathophysiology [54]. Remodeling mechanisms, such as breaking and making adherent junctions, contribute to tumor response to nutrient supply [55]. The stability of radially symmetric growth to asymmetric perturbation has been explored within the same mathematical framework [56], but existing studies lack a comprehensive description of mechanical stress distribu-

tion, anisotropic growth, and mechanical interaction with the extracellular matrix (ECM) [57, 58]. While continuum mechanics studies delve into anisotropic growth and stress distribution, they often overlook remodeling [57, 58]. Tumor progression, a multi-aspect process involving growth and remodeling requires collaborative efforts to bridge theoretical models and experimental reality.

After the initial formation and growth, tumor invasion is the subsequent stage, where cancer cells penetrate surrounding tissues and may spread to other parts of the body. Cancer cell migration which is integral to tumor invasion and metastasis is another complex hallmark of tumors [59]. Understanding invasion patterns is critical for prognosis and treatment planning [60]. Cell migration starts when cells attain a malignant morphology enabling them to detach the tumor body and move along the ECM [61]. Cancer cell migration in three-dimensional (3D) tissue involves different cellular mechanisms; hence, various invasion patterns have been observed [62, 63]. In general, cancer cells show two main migration patterns in histological sections: single and collective. In single-cell migration, e.g., in breast cancer, cells break intercellular contacts and acquire mobility via either mesenchymal or amoeboid morphology. Details of this invasion mode, the corresponding cell morphology characteristics, and the cellular mechanisms were reviewed in [64]. Collective and single-cell migration patterns are influenced by factors such as ECM composition [65–68]. Collective migration is evidenced by human cancer pathology as the primary pattern of invasion in most epithelial cancers [69]. The tumor microenvironment (TME) plays a crucial role in determining invasion patterns, with studies highlighting the impact of ECM components on migration [67, 68, 70]. The diversity of mechanisms involved in tumor invasion requires different areas of knowledge to contribute to the development of treatment strategies [71, 72].

Glioblastoma multiforme (GBM), one of the most aggressive brain cancers, presents unique challenges in invasion modeling [73, 74]. The invasion of glioblastoma involves intricate routes, including the leptomeningeal space, brain parenchyma, white matter tracts, and perivascular space [75]. Models focusing on glioblastoma invasion patterns emphasize the role of ECM stiffness in directing invasion [76]. The mechanical properties of the ECM, governed by factors like collagen composition and organization, significantly influence tumor invasion dynamics [77]. Thus, mathematical models considering the impact of ECM stiffness on invasion patterns are crucial for understanding and targeting aggressive cancers like glioblastoma. GBM heterogeneity, arising from genetic mutations, epigenetic modifications, and environmental

factors, is a major challenge in brain tumor diagnosis and treatment [78, 79]. In the mathematical context, evolutionary game theory and metabolic modeling have been employed to gain insights into tumor heterogeneity [80–82]. These models provide a framework for understanding the dynamics of heterogeneous cancer cell populations, shedding light on the evolutionary processes driving tumor development [80]. Additionally, personalized and precision medicine approaches, guided by mathematical modeling, aim to tailor treatments based on individual tumors' unique features [83].The integration of mathematical models with advanced experimental platforms is crucial for enhancing the accuracy and relevance of predictions. HGB 3D-tumor cultures and tumor-on-a-chip systems provide more realistic model parameters and monitoring techniques compared to traditional 2D culture systems and animal models [84, 85]. These platforms allow researchers to capture transient aspects, such as time-dependent metabolite concentrations and spatial heterogeneity in cancer cell populations [82]. The combination of in-silico models with advanced experimental setups, including the GBM-neuron interaction, holds promise for developing realistic models of tumor progression [86, 87].

In summary, the synergy between mathematical modeling and experimental platforms is crucial for a comprehensive understanding of tumor dynamics, from avascular growth to invasion mechanisms. This cross-disciplinary approach not only enhances our theoretical understanding of tumor behavior but also holds the potential to revolutionize cancer treatment strategies by predicting optimal and personalized therapeutic interventions. As we delve deeper into the complex world of tumors, the integration of mathematical models with advanced experimental technologies becomes increasingly essential for translating theoretical insights into impactful clinical applications. The ongoing collaboration between mathematicians and experimental biologists is vital for overcoming the challenges posed by cancer and developing effective therapeutic strategies.

1.2 Motivation and Problem Statement

In the current landscape of tumor dynamics research, while significant strides have been made in developing models of tumors, there are critical gaps in understanding the role of tumor formation, growth stability, and remodeling, complex biomechanical processes involving cell–cell/ECM adhesion and tumor microenvironmental cues. Existing mathematical models often oversimplify these processes, hindering a compre-

hensive exploration of the dynamics of interactions within tumors. Moreover, despite the importance of investigating various invasion patterns exhibited by tumors, existing models frequently overlook several distinct modes and the exciting interplay between cell–cell and cell–matrix adhesion. Understanding the factors influencing this invasion pattern is crucial for comprehension of tumor behavior.

Additionally, current models lack realism in metabolic rate schemes, especially in hypoxic conditions. The absence of consideration for the interaction between cancer cells and neurons in glioblastomas further limits the accuracy of predictions. A more comprehensive approach that quantitatively assesses metabolic rates, accounting for the intricate interplay of glucose and oxygen uptake, is necessary for advancing our understanding of glioblastoma progression.

Furthermore, exploring the influence of matrix stiffness and presence of neurons, as functional units of the nervous system surrounding brain tumors, on the invasive behavior of glioblastoma tumoroids is a critical aspect that demands attention. Integrating experimental and computational approaches can provide a more comprehensive understanding of how these key factors influence invasion behavior.

In this work, we provide solutions to bridge the aforementioned gaps in current tumor dynamics research, which help in advancing our knowledge and enhancing our ability to predict tumor progression. Addressing these challenges will pave the way for a more comprehensive understanding of the multi-faceted dynamics underlying tumor behaviour.

1.3 Thesis overview

In this chapter, a brief summary of the thesis is provided.

In **Chapter 1**, a background on mathematical modeling of tumor growth and invasion, followed by motivation and problem statement are provided.

In **Chapter 2**, modeling of initial transient formation of tumor spheroids is formulated. The analytical and numerical solutions are validated with in-vitro formation and growth of glioblastoma spheroids.

In **Chapter 3**, analysis of configurational instability to asymmetric perturbations in radially symmetric growth of tumor spheroids is presented.

In **Chapter 4**, a mathematical framework based on the principles of continuum mechanics to study the role of biochemical stimuli in tumor remodeling is presented.

In **Chapter 5**, we study the spherical shell-type pattern of invasion where tumoroids exhibit a collective motion of cells moving away from the core and forming a shell-type shape.

In **Chapter 6**, we report on a hybrid discrete-continuum (HDC) mathematical framework focusing on the role of metabolic rate variation in driving tumor heterogeneity and controlling growth and invasion.

In **Chapter 7**, we investigate the effect of matrix stiffness on the invasion pattern of human glioblastoma tumoroids using an open surface tumor-on-a-chip platform and HDC model.

In **Chapter 8** conclusions and future works are discussed.

Chapter 2

In-Silico Modeling of Tumor Spheroid Formation and Growth

Contributions:

Meitham Amereh: Conceptualization, methodology, formal analysis, experiments, writing—original draft preparation, writing—review and editing

Roderick Edwards: Methodology, formal analysis, writing—original draft preparation, writing—review and editing, supervision

Mohsen Akbari: Methodology, resources, writing—original draft preparation, writing—review and editing, supervision

Ben Nadler: Conceptualization, methodology, writing—review and editing, supervision

Meitham Amereh[1], Roderick Edwards [2], Mohsen Akbari[1,*] and Ben Nadler[3]

[1] Laboratory for Innovations in MicroEngineering (LiME), Department of Mechanical Engineering, University of Victoria, Victoria, BC, V8P 5C2, Canada; makbari@uvic.ca

[2] Department of Mathematics and Statistics, University of Victoria, Victoria, BC, Canada; edwards@uvic.ca

[3] Department of Mechanical Engineering, University of Victoria, Victoria, BC, V8W 2Y2 Canada; bnadler@uvic.ca

*Correspondence: makbari@uvic.ca; Tel.: (+1) 250-721-6038

Micromachines 2021, 12, 749. https://doi.org/10.3390/mi12070749 https://www.mdpi.com/journal/micromachines

Abstract

Mathematical modeling has significant potential for understanding of biological models of cancer and to accelerate the progress in cross-disciplinary approaches of cancer treatment. In mathematical biology, solid tumor spheroids are often studied as preliminary *in vitro* models of avascular tumors. The size of spheroids and their cell number are easy to track, making them a simple *in vitro* model to investigate tumor behavior, quantitatively. The growth of solid tumors is comprised of three main stages: transient formation, monotonic growth and a plateau phase. The last two stages are extensively studied. However, the initial transient formation phase is typically missing from the literature. This stage is important in the early dynamics of growth, formation of clonal sub-populations, *etc.* In the current work, this transient formation is modeled by a reaction-diffusion partial differential equation (PDE) for cell concentration, coupled with an ordinary differential equation (ODE) for the spheroid radius. Analytical and numerical solutions of the coupled equations were obtained for the change in the radius of tumor spheroids over time. Human glioblastoma (hGB) cancer cells (U251 and U87) were spheroid cultured to validate the model prediction. Results of this study provide insight into the mechanism of development of solid tumors at their early stage of formation.

Keywords: tumor formation; reaction–diffusion equation; human glioblastoma cancer cells

2.1 Introduction

Understanding tumors has been recognized as one the most challenging problems in biology and medicine. Their behavior involves complicated molecular biology and correspondingly complicated dynamics. Although tremendous effort has been devoted to developing therapeutic approaches for tumor suppression, there is still a significant need for new insights into complex aspects of tumors such as genetic instabilities, therapeutic resistance, inter- and intra-tumor heterogeneity, *etc.* Mathematical modeling is one of the most powerful approaches in predicting different aspects of tumor progression. It can provide quantitative prediction of biological processes and help

interpret complicated physiological interactions in the tumor microenvironment. Provided collaboration with experimentalists, mathematical modeling can generate practical mechanistic solutions. Mathematical oncology, for example, promises to allow quantitative determination of effective individual therapies [3]. Therefore, the cross-disciplinary approach of combining mathematical and biological models of cancer has great potential to enhance cancer treatment.

Primary malignant tumors originate from small numbers of cells which become highly proliferative through mutations occurring in oncogenes, tumor suppressors or DNA repair genes [47]. Although the genetic mutations eventually lead to formation of large and complex vascular tumors, they all go through an avascular (devoid of blood vessels) mode at their early stage of growth [48]. Having insight into this stage of growth is valuable in understanding the behavior of tumors at subsequent phases. Tumor spheroids are predominantly used in *in vitro* models of avascular tumor growth [42–46]. They are spherical aggregations of cancer cells which are supplemented with a controlled amount of nutrient concentration. Spheroid size, cell numbers, and fractions of hypoxic, quiescent and proliferative cells are easy to track, which enables researchers to quantitatively investigate the effect of various parameters on the tumors' behavior [49–51].

Over the past decades, avascular tumor spheroids have been extensively studied in the field of mathematical biology [6–10]. In particular, the growth of tumor spheroids is mathematically modeled from different perspectives, *e.g.*, continuum, discrete and hybrid (continuum-discrete)[11].

In the continuum approach, the variables are assumed to be continuous, and described by means of PDEs that incorporate growth and kinetic interaction between components, and diffusion for transport phenomena [12–14]. For instance, Burton developed one of the early mathematical models to determine the radius of tumor spheroids by analysis of oxygen distribution inside the tumor [15]. The model could generate a growth curve, which was fitted well by a Gompertzian function. As an another example of studies that examined the oxygen dynamics of spheroids, Grimes *et al.* demonstrated that the growth of spheroids can be obtained using two key parameters: rates of oxygen consumption and proliferation [88]. Greenspan established a model focusing on the growth-inhibiting effect of chemicals produced by disintegrated dead cells at the core of the tumor [16]. He concluded that the growth pattern strongly depends on a balance between the inhibitory effect of chemical components and the proliferation of living cells. Byrne and Chaplain introduced a model that

provides the growth of tumor spheroids in response to local nutrient concentration [17]. They assumed that the tumor is an incompressible fluid in which the inside motion is induced by local proliferation of cells. They also incorporated cell-cell adhesion by the Gibbs-Thomson relation, which maintains the tumor's compactness. They further studied asymmetric perturbations to predict the modes of instability of radially symmetric growth. Further studies considered the effects of pH and the level of oxygen and nutrient as key parameters for the tumor growth rate [18, 19]. Anisotropic growth of avascular tumor spheroids was also modeled in the context of continuum mechanics in references [20–24]. These studies modeled the tumor as a hyperelastic material and used multiplicative decomposition of the deformation gradient to investigate spatial distribution of stresses. They highlight the role of mechanical stress on the growth of tumors. Additional continuum-based studies of solid tumor growth are reviewed in references [25–28].

On the other hand, discrete approaches are capable of capturing the effects of cellular response, signaling pathways, inter- and intra-cellular interactions and tumor microenvironment on the growth of solid tumors [11]. For example, the dynamics of avascular tumor growth is presented using a lattice Monte Carlo model in [30]. The model predicts the growth of spheroids under various nutrient supply conditions. Hybrid models are another approach to modeling the growth of tumors that combine both continuum and discrete approaches to allow descriptions of macroscopic environmental variables (such as nutrient concentration) as well as discrete biological interactions. In the case of solid tumor growth, the clinical-size morphology of tumors can be studied in hybrid models while the cellular pathways and subcellular interactions are also involved [37]. For more details about discrete and hybrid approaches, the reader is encouraged to refer to the following papers [26, 33–36].

Development of biological patterns, such as animal coat markings and evolution of the enteric nervous system (ENS), is another type of process that often involves cellular proliferation and reaction/diffusion of materials [89–91]. In order to describe such processes, the evolution of a domain boundary is incorporated into the mathematical modeling [92–95]. This boundary evolution of patterns is very similar to that of tumors, *i.e.*, growth, from a mathematical point of view. In ENS, for instance, the motion of neural precursor cells is studied by solving a PDE describing migrating cells [96–98]. Another example is the study done by Simpson to derive an exact solution for a linear reaction-diffusion PDE on a uniformly growing domain [99]. The method was verified by comparing the solution with a numerical approximation. Although

they successfully obtained the exact solution for the density function in a growing domain, their solution is restricted to one dimensional linear and exponential domain growth in Cartesian coordinates, whereas in tumor growth the evolution of a tumor's boundary is not prescribed and is obtained as the solution in spherical coordinates.

Despite the rich literature on mathematical modeling of solid tumor growth, the initial stage of tumor formation is either neglected or not comprehensively modeled. At this stage, the interplay between adhesive force, due to cell-cell interactions, and repulsive force, due to local pressure gradient, defines the dynamic formation of tumor spheroids, which further affects the subsequent growth phases. To better understand the involved mechanisms, there is still a need to conduct more collaborative research involving biological and mathematical modeling approaches.

Here, we focus on the early phase of tumor spheroid formation, which is mostly missing from previous studies. In this initial phase of spheroid formation, the cell-cell adhesion forces are dominant and drag cells toward each other to make a compact aggregation. This causes the spheroid to shrink. Once cells start to proliferate, the raised concentration of cells within the spheroid produces a pressure which compensates the adhesion forces. At this point, the balance between forces stops spheroids from shrinking and leads to monotonic growth. This phase carries on until necrosis occurs where the competition between mitosis and necrosis defines the growth pattern. This early transient behavior of cells in tumor spheroid formation is modeled by a reaction-diffusion equation coupled with an ODE. The effect of adhesion forces between cells are incorporated into the system by prescribing a constant boundary condition. This fixed concentration, the so-called relaxed concentration, implicitly models an equilibrium condition at which adhesion forces and intrinsic pressure are in balance.

Both analytical and numerical solutions were obtained for the change in the radius of a tumor spheroid at the early stage of formation. The theoretical model was validated against the formation and growth of tumor spheroids generated from glioblastoma cell lines.

2.2 Model Formulation

A tumor spheroid is considered as a system of particles (cells) with continuous change in their properties such as concentration, velocity, *etc.* To start modeling this system, the material time derivative of the tumor spheroid's mass is written as a balance

equation for the continuum concentration of cells within the system:

$$\frac{\partial m}{\partial t} = \frac{\partial}{\partial t}\int_V C\left(\mathbf{x},t\right) dV = \int_V \Pi\, dV\,, \tag{2.1}$$

where m is the mass of the tumor, $C\left(\mathbf{x},t\right)$ is local concentration of cells, $\mathbf{x}$ is the position vector, Π is a volumetric source of mass, dV is a volume element and $\frac{\partial}{\partial t}\int_V C(\mathbf{x},t)dV$ is a material time derivative when particle locations are held fixed. Using the Reynolds transport theorem, one can write

$$\frac{\partial}{\partial t}\int_V C\left(\mathbf{x},t\right) dV = \int_V \left(\frac{\partial C\left(\mathbf{x},t\right)}{\partial t} + \nabla\cdot\left(C\left(\mathbf{x},t\right)\mathbf{v}\left(\mathbf{x},t\right)\right)\right) dV\,, \tag{2.2}$$

where $\mathbf{v}\left(\mathbf{x},t\right)$ is the velocity of particles. Followed by localization, equation (2.1) gives:

$$\frac{\partial C\left(\mathbf{x},t\right)}{\partial t} + \nabla\cdot\left(C\left(\mathbf{x},t\right)\mathbf{v}\left(\mathbf{x},t\right)\right) = \Pi\,. \tag{2.3}$$

A constitutive statement analogous to Darcy's law can be proposed for the flux of cells as $q = C\left(\mathbf{x},t\right)\mathbf{v}\left(\mathbf{x},t\right) = -k\nabla p\left(\mathbf{x},t\right)$, where $p\left(\mathbf{x},t\right)$ is the pressure inside the tumor and k is the proportionality of cell flux to the gradient of pressure, noting that cells move from higher pressure to lower pressure regions. Here we propose that this pressure is linearly proportional to the concentration of cells. Hence, equation (2.3) yields:

$$\frac{\partial C\left(\mathbf{x},t\right)}{\partial t} = K\,\nabla^2 C\left(\mathbf{x},t\right) + \Pi\,, \tag{2.4}$$

where K denotes ability of cells to respond to the gradient of concentration. This property depends on cell diffusivity (D) in response to the gradient of the concentration and adhesion forces between cells (f), *i.e.*, $K = \hat{K}(D,f)$. Cell adhesion reduces the ability of cells to move in response to the gradient of concentration. Therefore, to simplify the model we propose a linear relation, $K = \epsilon D$, where $0 < \epsilon < 1$. The volumetric growth depends on the type of cells, concentrations of nutrients, growth factors and also environmental cues. Here we propose a simple linear relation for volumetric growth, $\Pi = \eta\, C\left(\mathbf{x},t\right)$, where η is the rate of cell proliferation. This assumption is correct for early growth of tumor spheroids since they are usually small, such that all cells can receive enough oxygen and nutrient and no hypoxia occurs in

the tumor. Under this assumption, equation (2.4) can be rewritten as:

$$\frac{\partial C\left(\mathbf{x},t\right)}{\partial t} = K\,\nabla^2 C\left(\mathbf{x},t\right) + \eta\, C\left(\mathbf{x},t\right)\,. \tag{2.5}$$

Spherical coordinates, which are well suited to represent the spherical shape of tumor spheroids, can be used to advantage. Since the early stage of growth is radially symmetric, our analysis focuses on radially-symmetric solutions. Equation (2.5) in spherical coordinates become:

$$\frac{\partial C\left(r,t\right)}{\partial t} = \frac{K}{r^2}\frac{\partial}{\partial r}\left(r^2\frac{\partial C\left(r,t\right)}{\partial r}\right) + \eta\, C\left(r,t\right)\,, \tag{2.6}$$

subject to the following boundary and initial conditions:

$$\left.\frac{\partial C\left(r,t\right)}{\partial r}\right|_{r=0} = 0\,, \tag{2.7a}$$

$$\left.C\left(r,t\right)\right|_{r=R(t)} = C_0\,, \tag{2.7b}$$

$$C\left(r,t=0\right) = C_i\,, \quad \text{for } 0 < r < R(0)\,, \tag{2.7c}$$

where $R(t)$ is tumor radius, C_0 is the imposed boundary condition on concentration of cells, and C_i is the initial cell concentration, assumed spatially constant. Denoting the free surface boundary by $\Omega\left(t\right) = \{\mathbf{x} \in \mathbb{R}^3 | \, r - R(t) = 0\}$, the change in radius can be derived by integrating cell motion on the entire volume of the tumor as (see Appendix 2.5.1)

$$\frac{dR\left(t\right)}{dt} = -K\left.\frac{\partial C\left(r,t\right)}{\partial r}\right|_{r=R(t)}\,; \;\; R(0) = R_0\,, \tag{2.8}$$

in which R_0 is the initial radius. The proliferation inside the tumor increases local concentration of cells and generates a pressure gradient, and consequently a concentration gradient. Equation (2.5) indicates that cells move from higher concentration regions to lower concentration regions to create a uniform concentration (relaxed concentration) everywhere so that cells do not feel any extra pressure. In order for this pressure increment to be stabilized by the adhesion forces between cells, the volume of the tumor has to increase to reach the relaxed concentration. To model this equilibrium, we introduce boundary condition (2.7b) which imposes a constant relaxed concentration on the boundary of the tumor spheroid. Solutions to equations (2.6) and (2.8) with corresponding initial and boundary conditions in (2.7) give the

distribution of cells and change in radius of the tumor spheroids over time.

2.2.1 Analytical Solution

Equation (2.6) is a linear concentration-dependent reaction-diffusion equation with mixed boundary conditions. The reaction-diffusion form with constant source term is:

$$\frac{\partial C\left(r,t\right)}{\partial t} = K\,\nabla^2 C\left(r,t\right) + \eta C_i\,. \tag{2.9}$$

Proposition 1. *If* $C_1\left(r,t\right)$ *is a solution of* (2.9)*, the following is a solution of* (2.6) (see Appendix 2.5.2):

$$C\left(r,t\right) = -\eta \int_0^t C_1\left(r,\tau\right) e^{\eta\tau} d\tau + C_1\left(r,t\right) e^{\eta t}\,. \tag{2.10}$$

If a solution to (2.9) satisfies the initial and boundary conditions (2.7), then so does (2.10). Therefore, the first step is to solve Equation (2.9) subject to initial and boundary conditions (2.7). Using the variable change $C_1\left(r,t\right) = U\left(r,t\right) + C_0$, Equation (2.9) becomes a standard homogeneous PDE with zero boundary conditions and constant initial condition, as follows:

$$\frac{\partial U\left(r,t\right)}{\partial t} = K\,\nabla^2 U\left(r,t\right) + \eta C_i\,, \tag{2.11a}$$

$$\frac{\partial U\left(r,t\right)}{\partial r}\Big|_{r=0} = 0\,, \tag{2.11b}$$

$$U\left(R_1\left(r\right),t\right) = 0\,, \tag{2.11c}$$

$$U\left(r,t=0\right) = C_i - C_0\,, \quad \text{for } 0 < r < R(0)\,, \tag{2.11d}$$

where $R_1(t)$ is the radius of tumor spheroids without proliferation. The following solution is obtained for $R_1(t)$ (see Appendix A.3):

$$R_1(t) = \frac{C_i - C_0}{\sqrt{\eta C_i}}\,\mathrm{erfi}\sqrt{\eta C_i K t} + R(0)\,. \tag{2.12}$$

The solution to the full reaction-diffusion equation (2.5), is obtained as (see Ap-

pendix 2.5.4):

$$\frac{dR(t)}{dt} = -Kf_i\left(-\eta\sum_{n=1}^{\infty}\frac{(-1)^n}{n}\int_0^t R(0)e^{(\eta-\lambda_n^2K+\eta C_iK)\tau}F(R(t),n)d\tau \right. \\ \left. +R(0)\sum_{n=1}^{\infty}\frac{(-1)^n}{n}e^{(\eta-\lambda_n^2K+\eta C_iK)\tau}F(R(t),n)\right). \tag{2.13}$$

2.2.2 Model simplification

By introducing a new variable, $\bar{R} = n\pi\dfrac{R(t)}{R_1(t)}$, $\quad F(R(t),n)$ can be written as

$$F(R(t),n) = \frac{\bar{R}(t)\cos(\bar{R}(t)) - \sin(\bar{R}(t))}{R(t)^2}\,. \tag{2.14}$$

The timescale of proliferation is small enough compared to that of cell motility such that at each instant the radius of the diffusion-only model, $R_1(t)$, is close to the concentration-dependent reaction-diffusion one, $R(t)$. In the limit of separation of time scales this approximation becomes exact. Therefore, it can be assumed that $\bar{R}(t) \approx n\pi$. Substitution of equation (2.14) into equation (2.13) simplifies the rate of change of radius to

$$\frac{dR(t)}{dt} = -\pi Kf_i\left(-\eta\int_0^t \frac{R(0)}{R^2(\tau)}\sum_{n=1}^{\infty}e^{(\eta-\lambda_n^2K+\eta C_iK)\tau}d\tau + \frac{R(0)}{R^2(t)}\sum_{n=1}^{\infty}e^{(\eta-\lambda_n^2K+\eta C_iK)t}\right), \tag{2.15}$$

which simplifies to (see Appendix 2.2.2)

$$R(t) = \alpha\left(\frac{\sqrt{\pi}\ (2\eta t-1)}{2\sqrt{\eta}}\,\mathrm{erfi}(\sqrt{\eta t}) - \sqrt{t}\,e^{\eta t}\right). \tag{2.16}$$

2.2.3 Numerical Solution

In this section, numerical solutions of the model expressed in equations (2.6) and (2.8) are presented. Equation (2.6) is a reaction-diffusion equation with mixed boundary conditions coupled with the ODE in equation (2.8). To solve this system of equations, temporal and spatial discretizations are required. The boundary of the tumor spheroid is moving in time, which requires a new spatial discretization at each time-step. To keep the number of nodes constant, the position of each node must be able to move

in time. To this end, a mapping is introduced by non-dimensional variables $\bar{t} = \dfrac{t}{\tau}$ and $\bar{r}\,(\bar{t}\,) = \dfrac{r}{R\,(\bar{t}\,)}$, where $\tau = t_{max}$ and $R(\bar{t})$ is the moving boundary of the tumor. Using this change of variables, the moving domain of the solution is mapped to a new domain which always stays between zero and one. Equations (2.6) and (2.8) can be rewritten in the new variables as

$$\frac{\partial C\,(r,\bar{t}\,)}{\partial \bar{t}} = \lambda\left(\frac{2}{\bar{r}}\frac{\partial C\,(\bar{r},\bar{t}\,)}{\partial \bar{r}} + \frac{\partial^2 C\,(\bar{r},\bar{t}\,)}{\partial \bar{r}^2}\right) + \eta\,\tau\,C\,(\bar{r},\bar{t}\,) \tag{2.17a}$$

$$\frac{dR\,(\bar{t})}{d\bar{t}} = -\lambda R(\bar{t})\frac{\partial C\,(\bar{r},\bar{t}\,)}{\partial \bar{r}}\bigg|_{\bar{r}=1}, \tag{2.17b}$$

where $\lambda = \dfrac{\tau K}{R\,(\bar{t}\,)^2}$, subject to the following boundary and initial conditions:

$$\frac{\partial C\,(\bar{r},\bar{t})}{\partial \bar{r}}\bigg|_{\bar{r}=0} = 0\,, \tag{2.18a}$$

$$C\,(\bar{r},\bar{t})\,\bigg|_{\bar{r}=1} = C_0\,, \tag{2.18b}$$

$$C\,(\bar{r},\bar{t})\,\bigg|_{\bar{t}=0} = C_i\,, \quad \text{for } 0 < \bar{r} < 1\,, \tag{2.18c}$$

$$R(0) = R_0\,. \tag{2.18d}$$

Here In order to solve this system of equations, the Crank–Nicolson (CN) finite difference scheme was employed [100] (see Appendix 2.5.6).

2.3 Results and Discussion

2.3.1 Model Analysis

The term α in equation (2.16) contains the influence of both cell motility in response to the gradient of concentration, K, and the relaxed concentration of cells, C_0. The higher the absolute difference, $C_0 - C_i$, the more shrinkage is expected. This qualitative effect holds for K as well, *i.e.*, the higher the motility, the faster cells respond to the gradient of concentration. To show this effect quantitatively, the value of the normalized radius, $R^*(t) = \dfrac{R(t) - R_0}{R_0}$, versus normalized time, $t^* = \dfrac{t}{t_{max}}$, is plotted in Figure (2.1a) for $C_i \leqslant C_0$ and different values of $K^* = \dfrac{K}{K_0}$ holding other parame-

ters fixed. Note that we selected $t_{max} = 210$h to be consistent with the experimental results in the next section. Also, we take K_0 to be 10^{-10} cm^2.s^{-1} [101]. As can be seen, the shrinkage of the tumor is faster for cells with higher motility (K). The tumor spheroid decays further until the concentration of cells reaches the relaxed concentration where the diffusivity of cells and adhesion forces are in balance (minimum tumor radius). At this point, the proliferation continues to elevate cell concentration and breaks the balance. To reach a new balance, the tumor spheroid increases its radius to reduce the local concentration which finally leads to monotonic growth. Rate of proliferation for highly proliferative cancer cells is normally in the order of $\eta_0 = 10^{-2}\, h^{-1}$. This value was used as a reference number to non-dimensionalize the proliferation rates in our analysis. The effect of cell motility on formation of spheroids is illustrated in Figure (2.1a) in which parameters are set as $\eta = 1.8 \times \eta_0$, $\frac{C_0}{C_i} = 1.5$ and $R_0 = 0.01$ cm. The higher K in the figure corresponds to lower minimum radius and faster shrinkage. This result also shows that tumor spheroids with higher K grow faster since cells are able to rapidly respond to local proliferation and reach balance by moving the boundary of the tumor. Unlike many types of mammalian cells which have an intrinsic cell program that restricts their proliferation, most cancer cells are highly proliferative [47]. When cells proliferate, the local concentration increases and the generated pressure moves cells away. The formation of a tumor spheroid is faster if cells have a high proliferation rate. To illustrate this effect, the formation of a tumor spheroid is depicted in Figure (2.1b) for different values of $\eta^* = \frac{\eta}{\eta_0}$, holding other parameters fixed, *i.e.*, $K^* = 1$, $\frac{C_0}{C_i} = 1.5$ and $R_0 = 0.01$ cm. As can be seen, a tumor spheroid with a higher proliferation rate assembles faster.

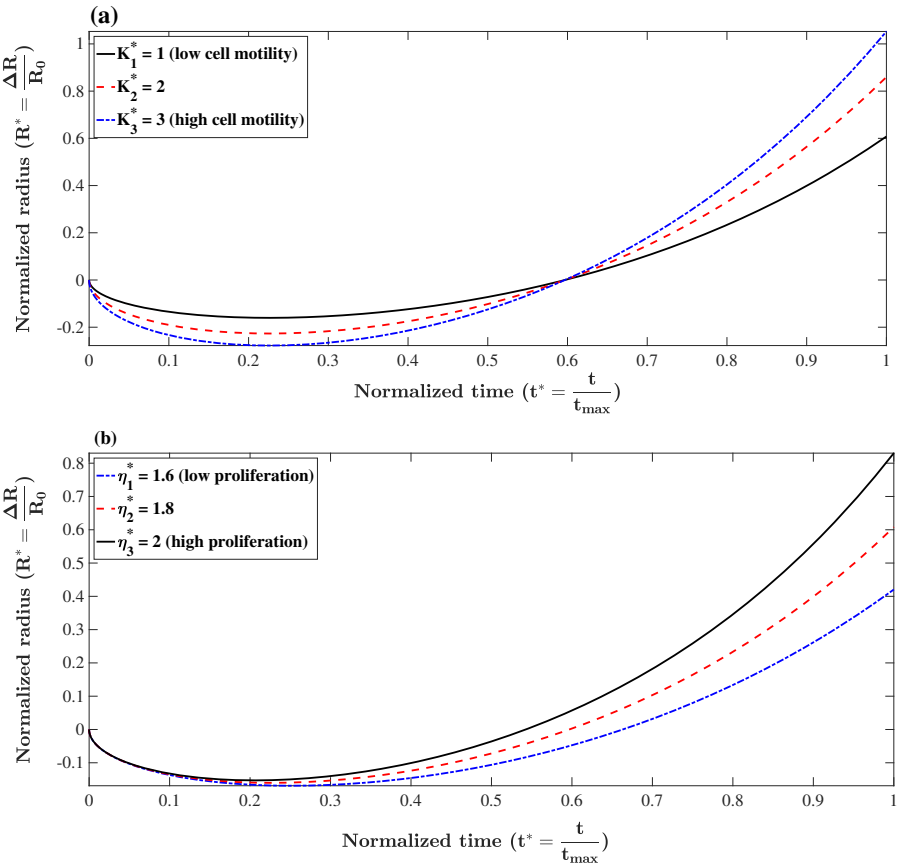

Figure 2.1: Formation of tumor spheroids with different values of (a) cell motility, $K_1^* = 1$, $K_2^* = 2$ and $K_3^* = 3$ (with $\eta^* = 1.8$, $\frac{C_0}{C_i} = 1.5$ and $R_0 = 0.01$ cm), (b) proliferation rate, $\eta_1^* = 1.6$, $\eta_2^* = 1.8$ and $\eta_3^* = 2$ (with $K^* = 1$, $\frac{C_0}{C_i} = 1.5$ and $R_0 = 0.01$ cm). A tumor spheroid with higher cell motility grows faster since cells are able to rapidly respond to local proliferation and reach balance by moving the boundary of the tumor. Also, a tumor spheroid with a higher proliferation rate assembles faster.

To compare the analytical and numerical solutions, the formation of the tumor spheroids was obtained for two sets of parameters, *i*) $\eta^* = 1.6$, $\dfrac{C_0}{C_i} = 1.5$, $K^* = 1$, $R_0 = 0.01$ cm, and *ii*) $\eta^* = 2$, $\dfrac{C_0}{C_i} = 2$, $K^* = 1$, $R_0 = 0.02$ cm, using the Crank-Nicolson scheme outlined in Appendix 2.5.6. Results are compared with the analytical solution in Figure (2.2).

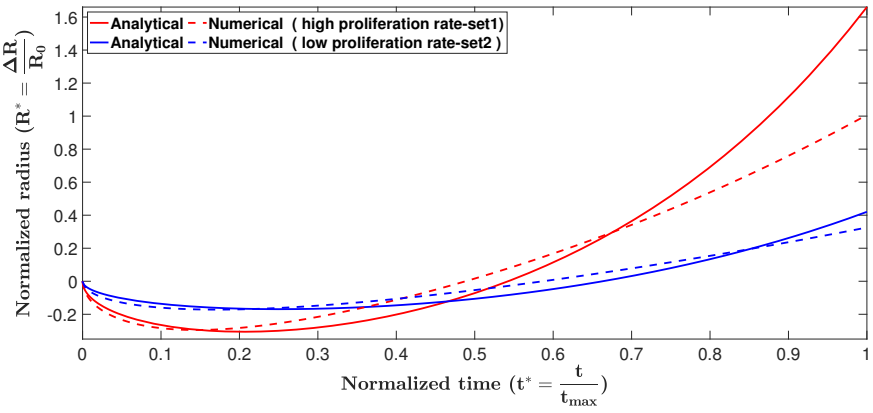

Figure 2.2: Formation of tumor spheroid obtained by analytical solution and numerical prediction, using two sets of parameters; set 1: $\eta^* = 1.6$, $\frac{C_0}{C_i} = 1.5$, $K^* = 1$, $R_0 = 0.01$ cm, and set 2: $\eta^* = 2$, $\frac{C_0}{C_i} = 2$, $K^* = 1$, $R_0 = 0.02$ cm. In the contraction phase the analytical and numerical solutions reasonably match. The analytical solution loses accuracy once growth becomes dominant. This is a result of the simplification we made in equation (2.14).

As can be seen in the figure, analytical and numerical solutions match very well in the contraction phase. The analytical solution loses accuracy once growth becomes dominant. This is a result of the simplification we made in equation (2.14). Both solutions predict that the tumor spheroid in parameter set 2, which has higher proliferation rate, experiences faster contraction and faster growth.

2.3.2 Model Validation

In this section, the theoretical model is validated against the formation of *in vitro* solid tumor spheroids generated from glioma cell lines (U251 and U87 hGB cells), as the most lethal type of intracranial tumors. Reproducibility, ease of assembly and ability to provide high-throughput screening make them a promising candidate for *in vitro* three-dimensional tumor models. Figure (2.3) shows the rates of proliferation of the two cell lines, $\eta_{U251} = 0.037 \pm 0.004\, h^{-1}$ and $\eta_{U87} = 0.026 \pm 0.003\, h^{-1}$, which are in the range of data reported in [102], *i.e.* $\eta_{U251} = 0.038\, h^{-1}$ and $\eta_{U87} = 0.033\, h^{-1}$. Results of U251 spheroid formation over 210h are shown in Figure (2.4). During the formation phase, intercellular interactions generate adhesion forces which pull cells together and increase the concentration of cells within the spheroid. The size of the spheroid reduces since the proliferation is not yet dominant. The tumor spheroid

shrinks until the concentration reaches the relaxed concentration (C_0). At this minimum radius, the driving forces are in balance, *i.e.*, adhesion forces and forces due to high concentration of cells within the spheroid. This balance breaks once the proliferation of cells becomes dominant, elevating the local concentration above the relaxed concentration. To remove the produced force, the boundary of the tumor spheroid moves to increase the volume. This volume increment reduces the concentration of cells and equilibrates the forces inside the tumor spheroid.

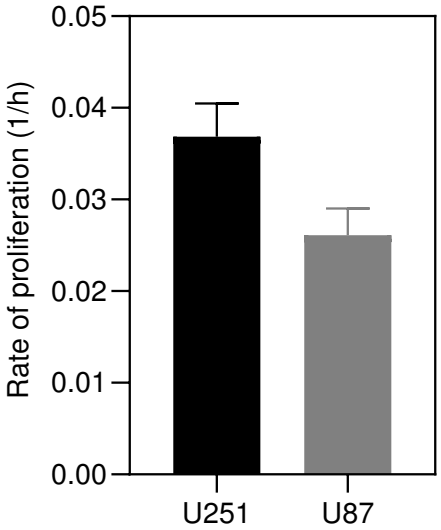

Figure 2.3: Proliferation rates of U251 and U87 cells cultured in DMEM supplemented with 10% (v/v) Fetal Bovine Serum (FBS) and 1% (v/v) Penicillin/Streptomycin, and incubated at 37°C in 5% CO_2. Rates were calculated by counting cells using Trypan blue assay over 24h.

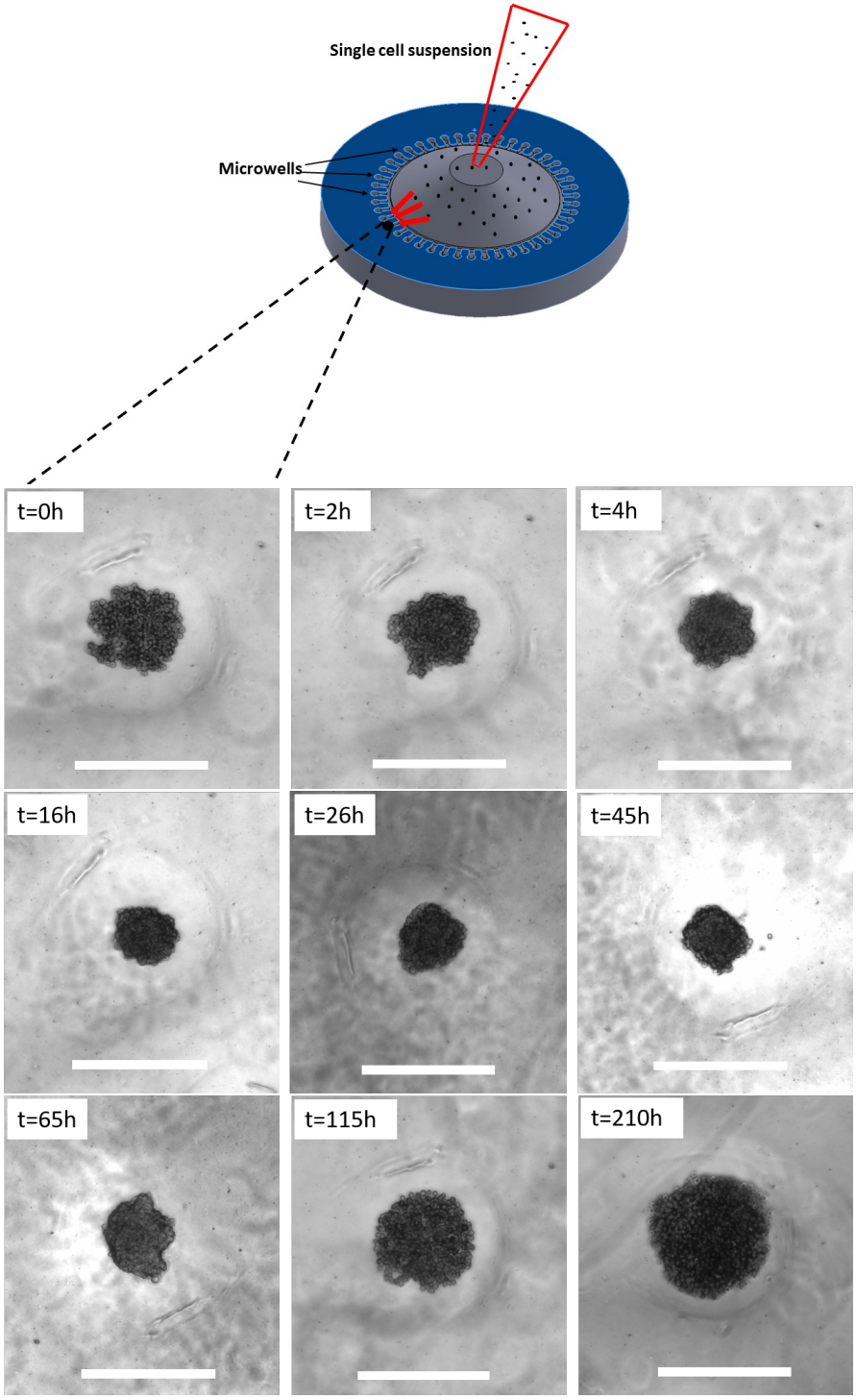

Figure 2.4: *In vitro* formation of U251- spheroids over 210 hours. Spheroids undergo an initial shrinkage and subsequent growth due to the competition between adhesion forces and proliferation pressure. Scale bars show $500\mu m$.

For spheroids which did not have a full spherical shape, the average of the largest

and smallest diameters was considered as the spheroid diameter. Figure (2.5) shows the size of the tumor spheroids over time compared with analytical and numerical solutions. As shown in the figure, the mathematical model provides a reasonable prediction of the formation of tumor spheroids and the minimum diameter. The model predictions were able to follow the trend of formation and growth until approximately 160∼180 hours, after which the tumor spheroids lost their homogeneity in terms of cell viability level. It is evident that in big spheroids, cells close to the core become hypoxic and change their metabolism. This can reduce the accuracy of the model.

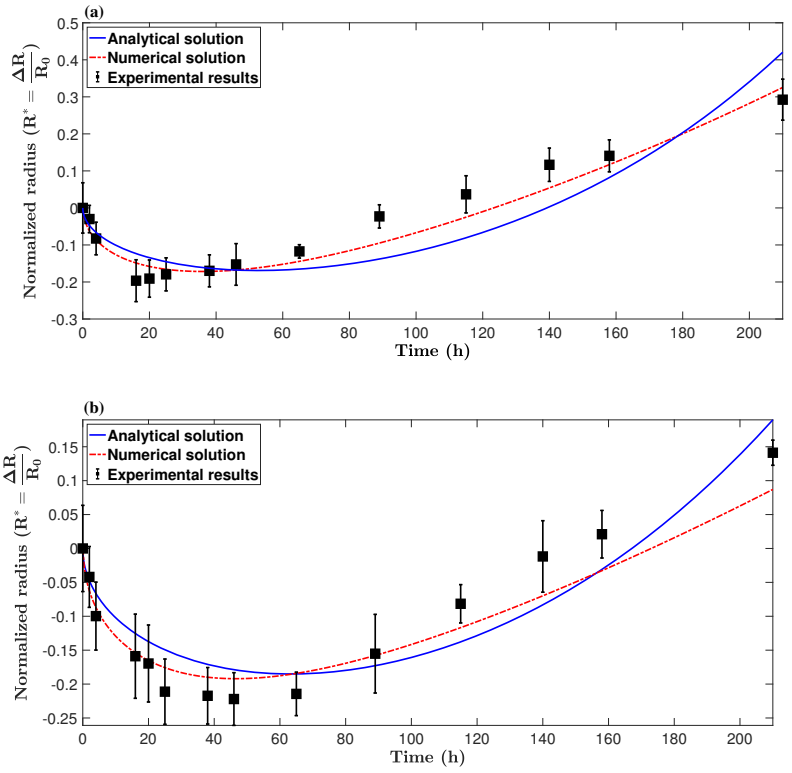

Figure 2.5: Formation of a tumor spheroid over time, obtained by spheroid culture of hGB cancer cell lines (n=3), (a) U251 and (b) U87, and compared with both analytical and numerical predictions. The model is able to predict the formation of tumor spheroids and the minimum diameter, but loses accuracy after approximately 160∼180 hours. This divergence from experimental results is started when the tumor spheroids lose their homogeneity due to hypoxia and/or necrosis initiation.

2.4 Experimental Methodology

2.4.1 Proliferation Rate

HGB cells were cultured in Dulbecco's Modification of Eagle's Medium (DMEM) supplemented with 10% (v/v) Fetal Bovine Serum (FBS) and 1% (v/v) Penicillin/Streptomycin, and incubated at 37°C in 5% CO_2. The umber of cells, N_1 and N_2, was counted using a Trypan blue assay after 24h and 48h, respectively (fresh media was added after 24h). Rates of proliferation (1/h) were calculated, shown in Figure (2.3), for both cell lines as

$$\eta = \frac{N_2 - N_1}{N_1 * 24}. \tag{2.19}$$

2.4.2 Spheroid Culture

For culturing spheroids, cells cultured in Sec. (4.1), were dissociated with Gibco™ Trypsin-EDTA (0.5%) and were centrifuged at 300g for 5min. After removing the supernatant and suspending the cell pellet in 1 mL of medium, the number of cells was counted using a Trypan blue assay. Afterwards, self-filling micro-well arrays (SFMAs) were used to produce uniform tumor spheroids [84]. The desired concentration of cells was loaded dropwise through guiding channels of SFMAs and were gently seeded into the wells. The microwells were kept in an incubator and imaging started 5h after seeding to let the cells fully settle in the wells. Cells were supplemented with fresh medium every 24h to maintain the concentration of nutrients. The formation of spheroids was imaged using optical microscopy (Axio Observer, ZEISS, Oberkochen, Germany) over 210 hours. The size of spheroids was measured using ImageJ [103].

Conclusion

In this work, we have presented an analytical solution for the formation of solid tumor spheroids. The process of tumor spheroid formation includes a preliminary contraction phase where adhesion forces densify cell aggregation. This phase proceeds until the cell concentration reaches a threshold, the so-called "relaxed concentration" at equilibrium. Afterwards, cell proliferation raises concentration and produces pressure which breaks the equilibrium. The tumor spheroid evolves in size to compensate for the generated pressure. This transient phase in formation and growth of tumor spheroids was mathematically modeled using a system of coupled PDE and ODE with

appropriate boundary and initial conditions. To validate model predictions, human glioblastoma cancer cell lines were spheroid cultured and their size was imaged over 210 hours. Results showed that although the model loses accuracy after approximately 160∼180 hours, it can nevertheless provide reliable prediction of the size of the spheroids before they become inhomogeneous. It should be noted that this study is limited to the modeling of solid tumor formation with no access to environmental stimuli such as stroma, immune cells, *etc.* However, our approach has the potential to include the inhibitory effect of drugs using an additional reaction-diffusion equation. The effect of a drug on the tumor development may be expected either to simply extend the contraction phase, or to cause a monotonic contraction after the expansion, in either case due to the apoptotic affect of the drug.

Author Contributions: Conceptualization, M.A. (Meitham Amereh) and B.N.; methodology, all authors contributed; writing—original draft preparation, M.A. (Meitham Amereh) and R.E.; writing— review and editing, all authors contributed; supervision, R.E., M.A. (Mohsen Akbari) and B.N. All authors have read and agreed to the published version of the manuscript.
Funding: Natural Science and Engineering Research Council (NSERC) of Canada. M.A. (Mohsen Akbari) and M.A. (Meitham Amereh) acknowledge BC Cancer Foundation and Canadian Foundation for Innovation (CFI) for supporting this work.
Conflicts of Interest: The authors declare no conflict of interest.

2.5 Appendix

2.5.1 Rate of Change of Spheroid's Volume

In this section, we derive an expression to relate the gradient of concentration at the boundary of a tumor to the time rate of change of its radius.

The rate of change of volume is

$$\frac{dV\left(t\right)}{dt}=\int_{V}\nabla\cdot\mathbf{v}\left(\mathbf{x},t\right)\,dV=-\int_{V}K\,\nabla^{2}C\left(r,t\right)dV=-\int_{\Omega}K\,\nabla C\left(r,t\right)\cdot\mathbf{n}\,d\Omega\,,\quad(2.20)$$

where $\mathbf{n}$ is normal to the surface, *i.e.*, $\mathbf{n}=\hat{\mathbf{e}}_{\mathbf{r}}$. Also, $\nabla C\left(r,t\right)=\dfrac{\partial C\left(r,t\right)}{\partial r}\,\hat{\mathbf{e}}_{\mathbf{r}}$, and $\dfrac{dV\left(t\right)}{dt}=4\pi R^{2}(t)\dfrac{dR\left(t\right)}{dt}$. The surface element on a sphere of radius R is $d\Omega=$

$R^2 \sin(\phi) d\theta d\phi$, where θ and ϕ are azimuthal and polar angles, respectively. Hence, equation (2.20) gives:

$$4\pi R^2(t) \frac{dR\,(t)}{dt} = -\int_0^{\pi} \int_0^{2\pi} K \frac{\partial C\,(r,t)}{\partial r} \hat{\mathbf{e}}_{\mathbf{r}} \cdot \hat{\mathbf{e}}_{\mathbf{r}}\, R^2(t) \sin(\phi)\, d\theta d\phi\,, \tag{2.21}$$

which further simplifies to:

$$\frac{dR\,(t)}{dt} = -K \frac{\partial C\,(r,t)}{\partial r}\bigg|_{r=R(t)}\,. \tag{2.22}$$

2.5.2 Proof of Proposition 1

In this section, the proof of Proposition 1, which was utilized as an intermediate step to solve Equation (2.6), is provided.

Taking derivatives of (2.10) gives:

$$\frac{\partial C\,(r,t)}{\partial r} = -\eta \int_0^t \frac{\partial C_1\,(r,t)}{\partial r} e^{\eta\tau} d\tau + \frac{\partial C_1\,(r,t)}{\partial r} e^{\eta t}\,, \tag{2.23a}$$

$$\frac{\partial^2 C\,(r,t)}{\partial r^2} = -\eta \int_0^t \frac{\partial^2 C_1\,(r,t)}{\partial r^2} e^{\eta\tau} d\tau + \frac{\partial^2 C_1\,(r,t)}{\partial r^2} e^{\eta t}\,, \tag{2.23b}$$

$$\frac{\partial C\,(r,t)}{\partial t} = \frac{\partial C_1\,(r,t)}{\partial t} e^{\eta t}\,. \tag{2.23c}$$

By substitution, it can be shown that (2.23) satisfies Equation (2.6), as follows.

$$\frac{\partial C_1}{\partial t} = \frac{K}{r^2} \frac{\partial}{\partial r} \left(r^2 \frac{\partial C_1}{\partial r} \right) + \eta C_i$$

by assumption. The LHS of (2.6) is

$$\frac{\partial C}{\partial t} = \frac{\partial C_1}{\partial t} e^{\eta t}\,.$$

The RHS of (2.6) is

$$\begin{aligned}
\frac{K}{r^2}\frac{\partial}{\partial r}\left(r^2\frac{\partial C}{\partial r}\right) \;+\; \eta\, C &= \frac{K}{r^2}\frac{\partial}{\partial r}\left(r^2\left[-\eta\int_0^t \frac{\partial C_1}{\partial r}e^{\eta\tau}d\tau + \frac{\partial C_1}{\partial r}e^{\eta t}\right]\right) + \eta C \\
&= \frac{K}{r^2}\frac{\partial}{\partial r}\left(r^2\frac{\partial C_1}{\partial r}\right)e^{\eta t} - \eta\int_0^t \frac{K}{r^2}\frac{\partial}{\partial r}\left(r^2\frac{\partial C_1}{\partial r}\right)e^{\eta\tau}d\tau + \eta C \\
&= \left(\frac{\partial C_1}{\partial t} - \eta C_i\right)e^{\eta t} - \eta\int_0^t \left(\frac{\partial C_1}{\partial \tau} - \eta C_i\right)e^{\eta\tau}d\tau + \eta C \\
&= \frac{\partial C_1}{\partial t}e^{\eta t} - \eta C_i e^{\eta t} - \eta\left[C_1 e^{\eta\tau}|_0^t - \eta\int_0^t C_1 e^{\eta\tau}d\tau\right] + \eta C_i\int_0^t \eta e^{\eta\tau}d\tau + \eta C \\
&= \frac{\partial C_1}{\partial t}e^{\eta t} - \eta C_i e^{\eta t} - \eta\left[C - C_i\right] + \eta C_i(e^{\eta t} - 1) + \eta C \\
&= \frac{\partial C_1}{\partial t}e^{\eta t}\,.
\end{aligned}$$

Hence Equation (2.6) is satisfied.

2.5.3 Solution of $R_1(t)$

Here, we solve Equation (2.11a) and derive an approximate expression for $R_1(t)$.

Using separation of variables, $U(r,t) = P(r)\,T(t)$, one can derive the solution of (2.11a) as

$$U(r,t) = \sum_{n=1}^{\infty} D_n e^{-(\lambda_n^2 - \eta C_i)Kt}\ \frac{\sin(\lambda_n r)}{r}\,, \tag{2.24}$$

where $D_n = 2R(0)\,(C_0 - C_i)\dfrac{(-1)^n}{n\pi}$ and $\lambda_n = \dfrac{n\pi}{R_1(t)}$. Hence,

$$C_1(r,t) = \sum_{n=1}^{\infty} D_n e^{-(\lambda_n^2 - \eta C_i)Kt}\ \frac{\sin(\lambda_n r)}{r} + C_0\,. \tag{2.25}$$

Substitution of (2.25) into (2.22) gives

$$\frac{dR_1(t)}{dt} = \frac{2K(C_i - C_0)}{R_1(t)}\sum_{n=1}^{\infty} e^{-(\lambda_n^2 - \eta C_i)Kt}\,. \tag{2.26}$$

The infinite series in equation (2.26) is convergent and has upper and lower bounds

as follows:

$$\int_1^\infty e^{-(\lambda_n^2-\eta C_i)Kt}dn \leqslant \sum_{n=1}^{\infty} e^{-(\lambda_n^2-\eta C_i)Kt} \leqslant \int_0^\infty e^{-(\lambda_n^2-\eta C_i)Kt}dn\,. \tag{2.27}$$

Using the identity $\int e^{-(\lambda_n^2-\eta C_i)Kt}dn = \dfrac{R_1(t)\,e^{\eta C_i Kt}}{2\sqrt{\pi Kt}}\,\mathrm{erf}\left(\dfrac{n\pi\sqrt{Kt}}{R_1(t)}\right) + \text{constant}$, the inequalities in (2.27) become

$$\begin{aligned}\frac{\sqrt{K}(C_i-C_0)}{\sqrt{\pi}}e^{\eta C_i Kt}\left(\frac{1-\mathrm{erf}\left(\frac{\pi\sqrt{Kt}}{R_1(t)}\right)}{\sqrt{t}}\right) &\leqslant \frac{2K(C_i-C_0)}{R_1(t)}\sum_{n=1}^{\infty} e^{-(\lambda_n^2-\eta C_i)Kt} \\ &\leqslant \frac{\sqrt{K}(C_i-C_0)}{\sqrt{\pi t}}e^{\eta C_i Kt}\,.\end{aligned} \tag{2.28}$$

Here, we observe that the upper and lower bounds in equation (2.28) are very tight, at least for system parameters in a reasonable range. Therefore, considering either bound as an approximate solution for $\dfrac{dR_1(t)}{dt}$ is acceptable. To show this, the solution of $R_1(t)$ using the upper bound, $R_1(t)_{ub}$, and lower bound, $R_1(t)_{lb}$, are found by a finite difference method and the corresponding relative error, $\dfrac{R_1(t)_{ub}-R_1(t)_{lb}}{R_1(t)_{lb}}$, is shown in Figure (2.6). System parameters are adopted in the range of biological properties of tumor spheroids as $K = 10^{-10}$ cm^2/s, $R_0 = 0.01$ cm. We also assume that the initial phase of growth does not take longer than a few days, t_{max} =240 hours, and $\dfrac{C_0}{C_i} = 2$.

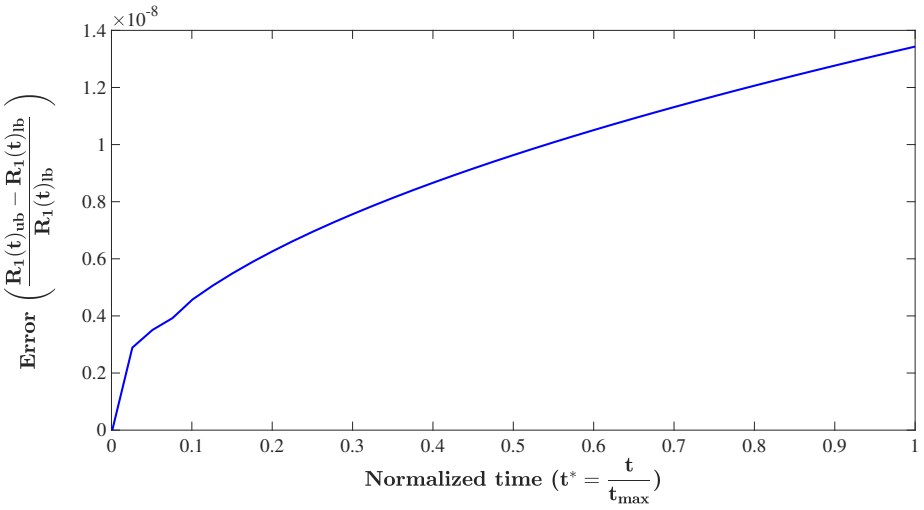

Figure 2.6: The relative error in the solution of $R_1(t)$ in equation (2.26) using the upper bound, $R_1(t)_{ub}$, and lower bound, $R_1(t)_{lb}$, of equation (2.28). Parameters are set as $K = 10^{-10}$, $R_0 = 0.01$ cm, t_{max} =240 hours and $\frac{C_0}{C_i} = 2$.

As can be seen in the figure, the error is very small, indicating that both bounds are acceptable in this range. To reduce the complexity in the analytical solution procedure, we used the upper bound as the solution of $\frac{dR_1(t)}{dt}$, for which the analytical solution is available as

$$R_1(t) = \frac{C_i - C_0}{\sqrt{\eta C_i}} \operatorname{erfi}\sqrt{\eta C_i K t} + R(0)\,. \tag{2.29}$$

2.5.4 Solution of Full RD Equation

In this section, the solution to the full reaction-diffusion equation (2.5) is obtained. By substitution of equation (2.25) into (2.10), one can obtain:

$$\begin{aligned} C\,(r,t) = -\eta f_i R(0) \sum_{n=1}^{\infty} \frac{(-1)^n}{n} \int_0^t e^{-(\lambda_n^2 - \eta C_i)K\tau}\ \frac{\sin(\lambda_n r)}{r}\, e^{\eta\tau} d\tau\ - \eta C_0 \int_0^t e^{\eta\tau} d\tau \\ + R(0) f_i \sum_{n=1}^{\infty} \frac{(-1)^n}{n} e^{-(\lambda_n^2 - \eta C_i)Kt}\ \frac{\sin(\lambda_n r)}{r} e^{\eta t} + C_0\, e^{\eta t}\,, \end{aligned} \tag{2.30}$$

which further simplifies to:

$$\begin{aligned} C\left(r,t\right) = -\eta f_i R(0) \sum_{n=1}^{\infty} \frac{(-1)^n}{n} \int_0^t e^{-(\lambda_n^2 - \eta C_i)K\tau} \ \frac{\sin(\lambda_n r)}{r} \, e^{\eta\tau} d\tau \\ + R(0) f_i \sum_{n=1}^{\infty} \frac{(-1)^n}{n} e^{-(\lambda_n^2 - \eta C_i)Kt} \ \frac{\sin(\lambda_n r)}{r} e^{\eta t} + C_0 \,, \end{aligned} \tag{2.31}$$

where $f_i = \dfrac{2(C_0 - C_i)}{\pi}$. It should be noted that there are two radii in this solution, *i.e.*, $R_1(t)$ and $R(t)$. The former is the radius of the reaction-diffusion form with constant source, equation (2.9), and the latter is the radius of the concentration-dependent reaction-diffusion form, equation (3.1). By substitution of (2.31) into (2.22), the first order differential equation for $R(t)$ is obtained as:

$$\begin{aligned} \frac{dR(t)}{dt} = -K f_i \Bigg(-\eta \sum_{n=1}^{\infty} \frac{(-1)^n}{n} \int_0^t R(0) e^{(\eta - \lambda_n^2 K + \eta C_i K)\tau} F(R(t), n) d\tau \\ + R(0) \sum_{n=1}^{\infty} \frac{(-1)^n}{n} e^{(\eta - \lambda_n^2 K + \eta C_i K)\tau} F(R(t), n) \Bigg) \,, \end{aligned} \tag{2.32}$$

where $F(R,n) = \dfrac{\lambda_n R(t)\cos(\lambda_n R(t)) - \sin(\lambda_n R(t))}{R(t)^2}$.

2.5.5 Model Simplification

Here, steps to simplify Equation (2.15) are provided. Equation (2.15) gives the rate of change of radius as

$$\frac{dR(t)}{dt} = -\pi K f_i \left(-\eta \int_0^t \frac{R(0)}{R^2(\tau)} \sum_{n=1}^{\infty} e^{(\eta - \lambda_n^2 K + \eta C_i K)\tau} d\tau + \frac{R(0)}{R^2(t)} \sum_{n=1}^{\infty} e^{(\eta - \lambda_n^2 K + \eta C_i K)t} \right). \tag{2.33}$$

Using the same identity used in (2.28) and the argument proposed in deriving equation (2.29), equation (2.33) simplifies to

$$\frac{dR(t)}{dt} = -\alpha \left(-\eta \int_0^t \frac{R(0) R_1(\tau)}{R^2(\tau)} \frac{e^{\eta\tau(1 + C_i K)}}{\sqrt{\tau}} d\tau + \frac{R(0) R_1(t)}{R^2(t)} \frac{e^{\eta t(1 + C_i K)}}{\sqrt{t}} \right), \tag{2.34}$$

where $\alpha = \dfrac{f_i \sqrt{\pi K}}{2}$. It should be noted that $C_i K \ll 1$, $(1 + C_i K \approx 1)$. Hence, equation (2.34) simplifies approximately to the following nonlinear integro-differential

equation:

$$\frac{dR(t)}{dt} = -\alpha\left(-\eta\int_0^t \frac{R(0)R_1(\tau)}{R^2(\tau)}\frac{e^{\eta\tau}}{\sqrt{\tau}}d\tau + \frac{R(0)R_1(t)}{R^2(t)}\frac{e^{\eta t}}{\sqrt{t}}\right). \tag{2.35}$$

Note that $R(0)$ is the initial radius, and $R_1(t)$ and $R(t)$ are radii for the constant-source reaction-diffusion equation and the concentration-dependent reaction-diffusion equation, respectively. It can be shown that the term $\dfrac{R(0)R_1(t)}{R^2(t)}$ fluctuates around 1 during the shrinkage and early growth phase as follows:

$$\frac{R(0)R_1(t)}{R^2(t)} = 1, \text{ at } t = 0\,, \tag{2.36a}$$

$$\frac{R(0)R_1(t)}{R^2(t)} > 1, \text{ in the shrinkage phase}\,, \tag{2.36b}$$

$$\frac{R(0)R_1(t)}{R^2(t)} \approx 1, \text{ in the transition phase}\,, \tag{2.36c}$$

$$\frac{R(0)R_1(t)}{R^2(t)} < 1, \text{ in the initial growth phase}\,. \tag{2.36d}$$

Thus, we write $\dfrac{R(0)R_1(t)}{R^2(t)} = 1 + \varepsilon(t)$, where $\varepsilon(t)$ denotes the variation around 1 and depends on the intrinsic properties of the system, such as proliferation rate (η), cell diffusivity (D), *etc.* Although the form of function $\varepsilon(t)$ cannot be specified precisely, we make the approximation $\varepsilon(t) \approx 0$ in order to simplify equation (2.35). This assumption is not accurate, especially for the growth phase. However, the comparison between the analytical solution and both numerical and experimental results in Sections 2.3.1 and 2.3.2 confirms that this approximation provides an acceptable prediction on the formation of spheroids in the range of interest. Using the identity $\displaystyle\int_0^t \frac{e^{\eta\tau}}{\sqrt{\tau}}d\tau = \sqrt{\frac{\pi}{\eta}}\ \mathrm{erfi}(\sqrt{\eta t})$, equation (2.35) then yields:

$$\frac{dR(t)}{dt} = -\alpha\left(-\sqrt{\pi\eta}\ \mathrm{erfi}\,(\sqrt{\eta t}) + \frac{e^{\eta t}}{\sqrt{t}}\right); \quad R(t)\Big|_{t=0} = R_0\,. \tag{2.37}$$

Note that if $C_i = C_0$ then $\alpha = 0$, and the size of the tumor does not change, but experimentally, the initial seeding concentration, C_i, is always less than C_0, since a compact tumor mass has not yet formed, so this can be considered physically

implausible. Using the fact that

$$\int_0^t \text{erfi}(\sqrt{\eta\tau})d\tau = \frac{(2\eta t+1)\text{erfi}(\sqrt{\eta t}) - \frac{2e^{\eta t}\sqrt{\eta t}}{\sqrt{\pi}}}{2\eta}, \tag{2.38}$$

the solution to (2.37) can be obtained as

$$R(t) = \alpha\left(\frac{\sqrt{\pi}\ (2\eta t-1)}{2\sqrt{\eta}}\,\text{erfi}(\sqrt{\eta t}) - \sqrt{t}\,e^{\eta t}\right). \tag{2.39}$$

2.5.6 Numerical Method

The Crank–Nicolson scheme is implicit, unconditionally stable, and gives second-order convergence. Considering temporal (i) and spatial (j) discretizations, the following approximations to temporal and spatial derivatives transform the differential equations (2.6) and (2.8) into an algebraic system of equations.

$$\frac{\partial C(i,j)}{\partial \bar{t}} = \frac{C_j^{i+1} - C_j^i}{\Delta \bar{t}}, \tag{2.40a}$$

$$\frac{dR(i)}{d\bar{t}} = \frac{R^{i+1} - R^i}{\Delta \bar{t}}, \tag{2.40b}$$

$$\frac{\partial C(i,j)}{\partial \bar{r}} = \frac{1}{2}\left(\frac{C_{j+1}^i - C_{j-1}^i}{\Delta \bar{r}} + \frac{C_{j+1}^i - C_{j-1}^i}{\Delta \bar{r}}\right), \tag{2.40c}$$

$$\frac{\partial^2 C(i,j)}{\partial \bar{r}^2} = \frac{1}{2}\left(\frac{C_{j+1}^{i+1} - 2C_j^{i+1} + C_{j-1}^{i+1}}{\Delta \bar{r}^2} + \frac{C_{j+1}^i - 2C_j^i + C_{j-1}^i}{\Delta \bar{r}^2}\right). \tag{2.40d}$$

Substitution of these approximations into (2.17) gives a system of linear algebraic equations in the form of $A\mathbf{x} = \mathbf{b}$, where A is square matrix of coefficients and vector $\mathbf{x}$ contains unknown concentrations at each node. The CN scheme is implicit in both time and space. Based on this method, the $(k+1)^{th}$ iteration of unknown concentrations, $C^{(k+1)}$, is defined as:

$$C^{(k+1)} = A_{lower}^{-1}\left(\mathbf{b} - A_{upper}C^{(k)}\right), \tag{2.41}$$

where A_{lower} and A_{upper} are respectively a lower triangular and strictly upper triangular decomposition of matrix A. As the iterations proceed, the approximations converge until the error reaches a defined tolerance. MATLAB® [104] was used to perform iterations to obtain unknown concentrations at each node. Note that we

used explicit value of $R(t)$ in Equation (2.17a), *i.e.* $R^i(t)$, such that we could solve for the concentrations first and plug them into Equation (2.17b) to obtain $R^{i+1}(t)$.

Chapter 3

Asymmetric Growth of Tumor Spheroids in a Symmetric Environment

Contributions:

Meitham Amereh: Conceptualization, methodology, experiments, validation, formal analysis, investigation, writing—original draft preparation, writing—review and editing

Yakine Bahri: Methodology, formal analysis, writing—original draft preparation, writing—review and editing

Roderick Edwards: Methodology, formal analysis, investigation, writing—review and editing, supervision

Mohsen Akbari: Conceptualization, Validation, resources, writing—review and editing, supervision, funding acquisition

Ben Nadler: Formal analysis, investigation, writing—review and editing, supervision, funding acquisition

Meitham Amereh[1,2,3], Yakine Bahri[4], Roderick Edwards[4], Mohsen Akbari[1,2,3,5] and Ben Nadler [1,*]

[1] Department of Mechanical Engineering, University of Victoria, Victoria, BC V8W 2Y2, Canada; makbari@uvic.ca (M.A.)

[2] Laboratory for Innovations in MicroEngineering (LiME), Department of Mechan-

Mathematics 2022, 1, 0. https://doi.org/10.3390/math1010000 https://www.mdpi.com/journal/mathematics

ical Engineering, University of Victoria, Victoria, BC V8P 5C2, Canada
[3] Centre for Advanced Materials and Related Technologies (CAMTEC), University of Victoria, Victoria, BC V8W 2Y2, Canada
[4] Department of Mathematics and Statistics, University of Victoria, Victoria, BC V8W 2Y2, Canada; edwards@uvic.ca (R.E.)
[5] Biotechnology Center, Silesian University of Technology, Akademicka 2A, 44-100 Gliwice, Poland
*Correspondence: bnadler@uvic.ca; Tel.: (+1) 250-721-6050

Abstract

In this work, we studied the stability of radially symmetric growth in tumor spheroids using a reaction-diffusion model. In this model, nutrient concentration and internal pressure are local variables that implicitly relate the proliferation of cells to the growth of the tumor. The analytical solution of the governing model was presented in an orthonormal spherical harmonic basis. It was shown that the radially symmetric steady-state solution to the growth of tumor spheroids, under symmetric growth conditions, was unstable with respect to small asymmetric perturbations. Such perturbations excited the asymmetric modes of growth, which could grow in time and change the spherical configuration of the tumor. The number of such modes and their rates of growth depended on parameters such as surface tension, external energy and the rate of nutrient consumption. This analysis indicated that the spherical configuration of tumor spheroids, even under experimentally controlled symmetric growth conditions, were naturally unstable. This was confirmed by a comparison between the shapes of in vitro human glioblastoma (hGB) spheroids and the configuration of the first few asymmetric modes predicted by the model.
Keywords: asymmetric growth; instability; human glioblastoma spheroid

3.1 Introduction

Mathematical modeling has great potential in predicting different aspects of tumor progression. The complicated behavior of growing tumors can often be interpreted by understanding the underlying interactions in a mathematical model. In this regard, avascular tumor spheroids have been extensively studied over the past decades [6–10]. The growth of tumor spheroids, in particular, has been mathematically described

from different perspectives such as continuum models, discrete (agent-based) models and hybrid (continuum-discrete) models [11]. Continuum models are generally built upon partial differential equations (PDEs) for mass conservation and evolution of the tumor boundary [105–107]. In some of these models, the concentration of nutrients defines the cell concentration and type at each point in the tumor body. Indeed, these models implicitly determine the concentration of cells. They can also show acceptable qualitative agreement with experimental data. Furthermore, the literature on mathematical models that explicitly consider the concentration of cells as one of the variables is rapidly growing [30, 108–110]. In these models, an additional PDE defines the change in the concentration of cells.

Primary invasive tumors emerge from small aggregations of abnormal cells that possess cancerous characteristics, such as high proliferation potential, mainly due to the mutations in their oncogenes, DNA repair genes and/or tumor suppressors [47]. The progression of these tumors starts with the formation of small avascular tumors, followed by a volumetric growth and also the initiation of cell heterogeneity, due to hypoxic/necrotic formation, and finally leads to the formation of large and complex vascular tumors [111]. Among different aspects, asymmetric growth has gained particular attention. Studies have tried to provide insight into why, and how, possible asymmetric configurations may occur during tumor growth [112–114]. For instance, the response of spherical tumors to asymmetric perturbations was studied by Byrne and Chaplain [17]. They considered the avascular tumor spheroids as an incompressible fluid where the evolution of the radius depends on the change in internal pressure. The stability of the steady-state solution was then evaluated by examining the excited spherical harmonic modes. They have shown that the growth of invasive tumors evolves according to the unstable modes and that the number of unstable modes increases as the energy required to preserve the tumor structure is reduced. They assumed that the rate of nutrient consumption is constant. This is not a realistic assumption; however, experimental evidence shows that the rate of consumption depends on the nutrient concentration [115]. In addition, the asymptotic stability of the radially symmetric growth of tumor spheroids has been studied in [116, 117]. In addition, Li et al. [118], Cristini et al. [119] and Wu et al. [120] carried out numerical simulations of tumor growth in circumstances where a small perturbation can eventually give rise to a radially non-symmetric configuration. The authors investigated the role of a single parameter, such as either nutrient supply or surface tension.

Most of the existing studies either investigated the role of a single parameter in

the stability of radially symmetric growth in tumor spheroids, or they lacked an experimental component. In this work, like that of Byrne and Chaplain, we modeled the tumor as a incompressible continuum medium, in which the local proliferation of cells gave rise to a change in internal pressure and, consequently, to growth. However, we relaxed the assumption of a constant consumption rate, adopting instead a concentration-dependent rate, which affected the stability of the steady-state solutions. To observe the behavior of the tumor in response to asymmetric excitation, a small perturbation was introduced to the steady-state solutions. It was seen that increasing the concentration of nutrients, C_∞, increased the number of growing asymmetric modes. However, increasing the rate of consumption led to a smaller steady-state radius with a smaller number of growing asymmetric modes. In addition, higher surface tension allowed for a smaller steady-state radius and a smaller number of growing asymmetric modes. We also compared the predicted asymmetric growth with experimental results. The growth of in vitro solid tumor spheroids generated from the glioma cell line (U251 hGB cells) was observed over time. It was seen that spheroids in a roughly symmetric environment lost their spherical configuration due to small natural perturbations from perfect symmetry exerted by their environment.

3.2 Model Formulation

We adopted a reaction-diffusion model that considered a tumor as an incompressible continuum medium where the proliferation depended on the presence of nutrients. The system of the governing equation is

$$\frac{\partial C(\mathbf{x},t)}{\partial t} = \nabla^2 C(\mathbf{x},t) - \eta^2 C(\mathbf{x},t)\,, \tag{3.1a}$$

$$\frac{\partial P(\mathbf{x},t)}{\partial t} = \mu \nabla^2 P(\mathbf{x},t) + \zeta\left(C(\mathbf{x},t) - C_d\right), \tag{3.1b}$$

$$\boldsymbol{V}_\Gamma \cdot \boldsymbol{n} = -\mu \operatorname{grad} P(\mathbf{x},t)\Big|_\Gamma \cdot \boldsymbol{n}\,, \tag{3.1c}$$

where $C(\mathbf{x},t)$, $P(\mathbf{x},t)$ are the concentrations of nutrients and the internal pressure, respectively, and $\eta^2 C(\mathbf{x},t)$ is the positive rate of nutrient consumption. A constitutive relation analogous to Darcy's law relates the velocity of cells to the pressure gradient with a constant of proportionality μ that describes cell motility. The pressure is

assumed to be proportional to the cell density, which does not appear explicitly in the equations. However, the pressure production is modulated by the rate of cell proliferation, $\zeta\, C$, which depends linearly on the concentration of nutrients, and the natural rate of cell death ζC_d. The tumor boundary is Γ, $\boldsymbol{V}_\Gamma$ is the boundary velocity and $\boldsymbol{n}$ is the outward normal. Hence, Equation (3.1c) denotes the rate of growth of the tumor boundary, that is, the normal velocity of its boundary. The boundary of the tumor is a two-phase interface (i.e., cells and nutrients), hence, we impose boundary conditions as

$$C(\mathbf{x}, t)\Big|_\Gamma = C_\infty\ (1 - 2\gamma H)\ , \tag{3.2a}$$

$$P(\mathbf{x}, t) = P_\infty\ , \tag{3.2b}$$

where (3.2a) is a thermodynamically consistent boundary condition as proposed in [121], C_∞ is the nutrient supply, γ is the surface tension, H is the mean curvature and P_∞ is the external pressure. Equation (3.2a) allows a nutrient concentration jump of $2\gamma H C_\infty$ across the boundary interface due to the surface tension. It should be noted that the boundary condition (3.2a) couples the system of the governing equations. Next, we present the analytical solution to the governing Equation (3.1a–3.1c), subjected to the boundary conditions (3.2a,3.2b).

3.2.1 Analytical Solutions

Spherical coordinates, which are well suited to represent the spherical configuration of tumors, could be used to our advantage. To study the asymmetric instabilities of tumor growth, we first considered the radially symmetric solutions to the governing equation, Equation (3.1a–3.1c), and the boundary conditions (3.2a,3.2b). The equations can be made more meaningful by the following normalization

$$\bar{C} = \frac{C}{C_d}\ , \quad \bar{C}_\infty = \frac{C_\infty}{C_d}\ , \quad \bar{P} = \frac{P}{P_\infty}\ . \tag{3.3}$$

Note that in spherical coordinates, the position is $\mathbf{x} = r\, \boldsymbol{e_r}(\theta, \phi)$ and the Laplace operator ∇^2 has the form

$$\nabla^2 = \frac{1}{r^2}\frac{\partial}{\partial r}\left(r^2 \frac{\partial}{\partial r}\right) + \frac{1}{r^2 \sin(\theta)}\frac{\partial}{\partial \theta}\left(\sin(\theta)\frac{\partial}{\partial \theta}\right) + \frac{1}{r^2 \sin^2(\theta)}\frac{\partial^2}{\partial \phi^2}\ , \tag{3.4}$$

in the domain $\theta \in [0, \pi]$ and $\phi \in [0, 2\pi]$.

Symmetric Steady-State Solutions

For the radially symmetric case, the fields are only a function of r and t, i.e., $C(r,t)$, $P(r,t)$ and the tumor boundary Γ is defined by $r = R(t)$, and its velocity is $\mathbf{V}_\Gamma = V_R \mathbf{e}_r$. Thus, Equations (3.1c) and (3.2a) read

$$V_R = -\mu \frac{\partial P(r,t)}{\partial r}\bigg|_{r=R(t)}, \tag{3.5a}$$

$$C(r,t)\bigg|_{r=R(t)} = C_\infty \left(1 - 2\gamma R^{-1}(t)\right), \tag{3.5b}$$

where V_R is the velocity of the tumor boundary and $R(t)$ is the radius of the tumor. Note that Equation (3.5b) provides a lower bound for $R(t)$ such that $2\gamma < R(t)$. To eliminate singularities at $r = 0$, we use

$$\frac{\partial C(0,\theta,\phi,t)}{\partial r} = 0\,, \tag{3.6a}$$

$$\frac{\partial P(0,\theta,\phi,t)}{\partial r} = 0\,. \tag{3.6b}$$

The solution for the nutrient concentration is

$$\bar{C}(r,t) = \frac{\bar{C}_\infty (R(t) - 2\gamma)\sinh(\eta r)}{r \sinh(\eta R(t))}\,, \tag{3.7}$$

and substitution into (3.1b,3.1c) yields

$$\frac{\mu P_\infty}{\zeta C_d}\frac{\partial \bar{P}}{\partial r}(r,t) = \frac{\bar{C}_\infty (R(t) - 2\gamma)\sinh(\eta r)}{\eta^2 r^2 \sinh(\eta R(t))} - \frac{\bar{C}_\infty (R(t) - 2\gamma)\cosh(\eta r)}{\eta r \sinh(\eta R(t))} + \frac{r}{3}\,, \tag{3.8a}$$

$$\frac{1}{\zeta C_d}\frac{dR(t)}{dt} = \frac{\bar{C}_\infty \left(R(t) - 2\gamma\right)}{\sinh(\eta R(t))}\left(\frac{1}{\eta R(t)}\cosh(\eta R(t)) - \frac{1}{\eta^2 R(t)^2}\sinh(\eta R(t))\right) - \frac{R(t)}{3}\,. \tag{3.8b}$$

To understand the role of the model parameters, the tumor growth rate V_R was plotted against the tumor radius R for different values of nutrient source C_∞, surface tension γ and rate of consumption η.

Figure 3.1 shows that at most two plausible steady-state solutions, $V_R = 0$ existed.

The plausible steady-state solutions could be stable for $dV_R/dR < 0$ or unstable for $dV_R/dR > 0$. However, in the current context it was necessary for a steady-state solution to be stable. Figure 3.1a shows that no steady-state solution existed for $\bar{C}_\infty \leq 1$ since the net proliferation was negative due to the limited nutrient supply. Thus, the tumor continuously diminished to zero. For sufficient nutrient supply, $\bar{C}_\infty \geq 1.25$, two steady-state solutions existed. Similarly, Figure 3.1b shows that two steady-state solutions existed for the low consumption rate $\eta \leq 3$, and no steady-state solution existed for $\eta \geq 4$ due to the insufficient supply of nutrients. It followed that, for a particular $\eta = \eta_0$ in the range $(3, 4)$, the two solutions coincided into one unstable solution, such that for $0 \leq \eta < \eta_0$ one stable solution existed and for $\eta > \eta_0$ no solutions existed. Figure 3.1c shows that for large surface tension no steady-state solution existed. Recall that $R > 2\gamma$, hence the curves where $R < 2\gamma$ were not physically admissible. When two plausible steady-state solutions existed, the large radius solution was stable, but the small radius solution was unstable. It was also observed that the radius of the stable steady-state solution increased with increasing $\bar{C}_\infty$ and decreased with increasing η and γ. It should be noted that only dimensional stability was investigated above; shape stability is yet to be considered. In what follows, we investigated shape instability in the form of asymmetric instability of the radially symmetric steady-state solutions by introducing asymmetric perturbations. We also explored the growth rate of unstable asymmetric modes to obtain an insight into the perturbed configuration of the tumor.

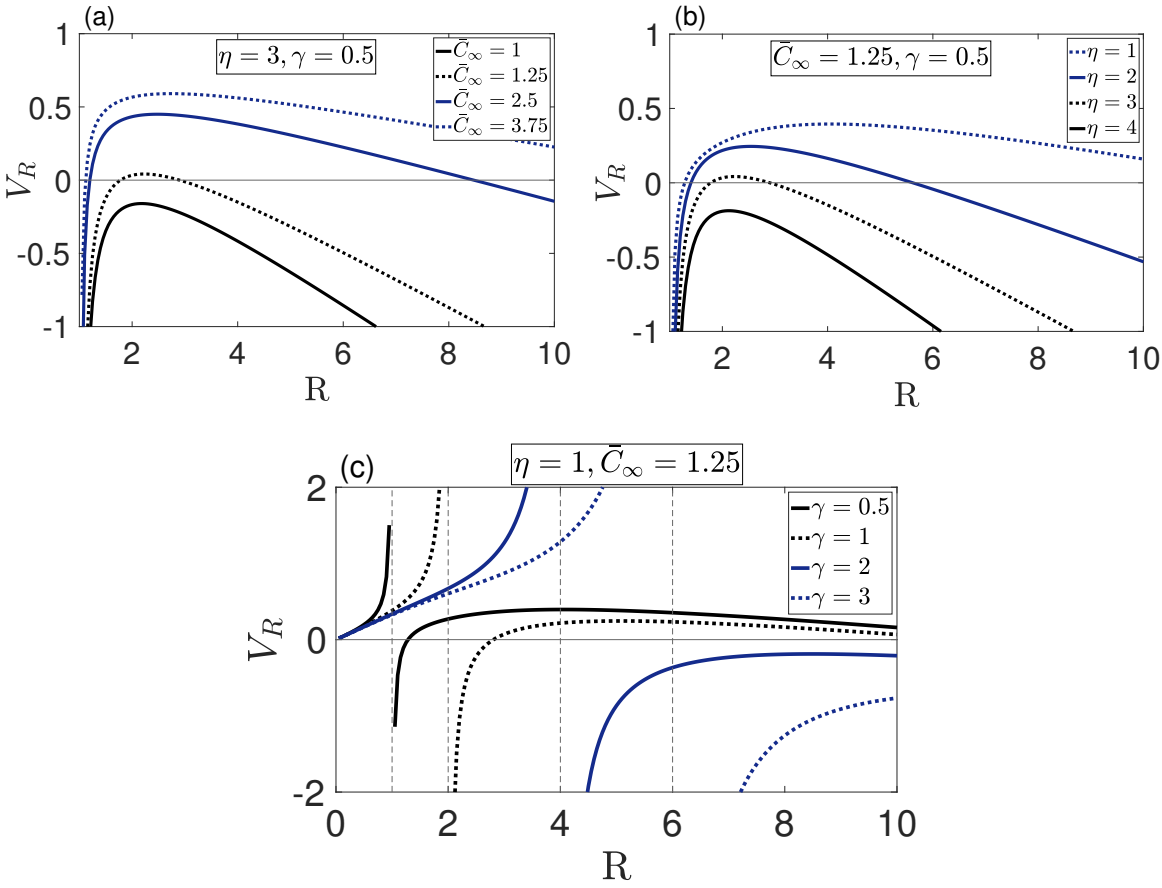

Figure 3.1: Tumor growth rate, V_R, vs. R for various values of nutrient supply $\bar{C}_\infty$ in (**a**), nutrient consumption η in (**b**) and surface tension γ in (**c**). A maximum of two plausible steady-state solutions existed, which could be stable ($dV_R/dR < 0$) or unstable ($dV_R/dR > 0$). It could be seen that the maximum of two steady-state solutions was achieved for sufficient nutrient supply (**a**), low consumption rate (**b**) and low surface tension (**c**).

3.2.2 Instability to Asymmetric Perturbation

A tumor microenvironment can exert external stimuli in various non-symmetric ways. For instance, tumor tissue can apply forces in different directions or cells can be exposed to an asymmetric gradient of chemoattractants, growth factors, etc. In addition, the heterogeneity of the cell population may change the local properties in large tumors and lead to an inhomogeneous structure. Therefore, tumors are susceptible to asymmetric growth. This can be seen in the growth of benign tumors when they eventually lose their close-to-spherical shape. The vast majority of invasive tumors are not spherical [122]. To investigate the stability of the steady-state radially sym-

metric solution, small time-dependent asymmetric perturbations were introduced as

$$C(r,\theta,\phi,t) = \bar{C}(r) + \epsilon\, C_p(r,\theta,\phi,t)\,, \tag{3.9a}$$

$$P(r,\theta,\phi,t) = \bar{P}(r) + \epsilon\, P_p(r,\theta,\phi,t)\,, \tag{3.9b}$$

$$R(\theta,\phi,t) = \bar{R} + \epsilon\, R_p(\theta,\phi,t)\,, \tag{3.9c}$$

where $0 < \epsilon \leqslant 1$, $\bar{C}(r), \bar{P}(r)$ and $\bar{R}$ are the dimensionally stable steady-state radially symmetric solutions of the governing equations (3.1) and C_p, P_p and R_p are the asymmetric perturbations. The substitution of (3.9a,3.9b) into (3.1a,3.1b) immediately yields the governing equations for C_p and P_p, respectively. In order to obtain the equation of R_p, first substitute (3.9c) into (3.1c), which yields

$$\frac{\partial}{\partial t}\left(\bar{R} + \epsilon\, R_p\right) = -\mu \frac{\partial}{\partial r}\left(\bar{P} + \epsilon\, P_p\right)\Big|_{r=\bar{R}+\epsilon\, R_p}\,, \tag{3.10}$$

and then utilize the Taylor series of (3.9b) about $\bar{R}$ in the form

$$\frac{\partial}{\partial r}\left(\bar{P} + \epsilon\, P_p\right)\Big|_{r=\bar{R}+\epsilon R_p} = \frac{\partial \bar{P}}{\partial r}\Big|_{r=\bar{R}} + \epsilon \frac{\partial P_p}{\partial r}\Big|_{r=\bar{R}} + \epsilon R_p \frac{\partial^2 \bar{P}}{\partial^2 r}\Big|_{r=\bar{R}} + O(\epsilon^2)\,. \tag{3.11}$$

Finally, substitution of (3.11) into (3.10) yields the governing equation for C_p. The system of governing equations of the perturbations C_p, P_p and R_p reads

$$\nabla^2 C_p - \eta^2 C_p = 0\,, \tag{3.12a}$$

$$\mu \nabla^2 P_p + \zeta\, C_p = 0\,, \tag{3.12b}$$

$$\frac{\partial R_p}{\partial t} = -\mu \left(\frac{\partial P_p}{\partial r} + R_p \frac{\partial^2 \bar{P}}{\partial r^2}\right)\Big|_{r=\bar{R}}\,. \tag{3.12c}$$

Similarly, substitution of the perturbations into (3.2a,3.2b) yields the perturbed boundary conditions

$$C_p\Big|_{r=\bar{R}} = \frac{\gamma C_\infty}{\bar{R}^2}\left[2R_p + \frac{1}{r^2\sin(\theta)}\frac{\partial}{\partial\theta}\left(\sin(\theta)\frac{\partial R_p}{\partial\theta}\right) + \frac{1}{r^2\sin^2(\theta)}\frac{\partial^2 R_p}{\partial\phi^2}\right] - R_p \frac{\partial C}{\partial r}\Big|_{r=\bar{R}}\,, \tag{3.13a}$$

$$P_p\Big|_{r=\bar{R}} = -R_p \frac{\partial P}{\partial r}\Big|_{r=\bar{R}}\,. \tag{3.13b}$$

Also, the following conditions can be simply inferred from (3.6a,3.6b)

$$\left.\frac{\partial C_p}{\partial r}\right|_{r=0} = 0\,, \tag{3.14a}$$

$$\left.\frac{\partial P_p}{\partial r}\right|_{r=0} = 0\,. \tag{3.14b}$$

Separation of variables $C_p\,(r,\theta,\phi) = R(r)\Theta(\theta)\Phi(\phi)$ is used to solve Equation (3.12a). Substitution gives the following equations for the polar and azimuthal angles

$$\frac{1}{\Phi(\phi)}\frac{d^2\Phi(\phi)}{d\phi^2} = -m^2 \quad \rightarrow \quad \Phi(\phi) = e^{im\phi}\,, \tag{3.15a}$$

$$\frac{d}{dx}\left((1-x^2)\frac{d\Theta(x)}{dx}\right) + \left(l(l+1) - \frac{m^2}{1-x^2}\right)\Theta(x) = 0 \quad \rightarrow \quad \Theta(x) = P_l^m(x)\,, \tag{3.15b}$$

where m is an integer, $x = \cos\theta$ and $P_l^m(x) = \frac{1}{2^l\,l!}(1-x^2)^{\frac{m}{2}}\frac{d^{l+m}}{dx^{l+m}}(x^2-1)^l$ are the Legendre polynomials. Combining $\Theta(\theta)$ and $\Phi(\phi)$ forms the spherical harmonics

$$Y_l^m(\Theta,\phi) = \chi_{lm}\,P_l^m(x)\,e^{im\phi}\,, \tag{3.16}$$

where the coefficients $\chi_{lm}(t)$ are determined by the boundary conditions. The equation for the radial component of $C_p\,(r,\theta,\phi)$ reads

$$r^2\frac{d^2z}{dr^2} + r\frac{dz}{dr} - \left(\eta^2r^2 + \left(l+\frac{1}{2}\right)^2\right)z = 0, \tag{3.17}$$

where $z = R(r)(\eta r)^{\frac{1}{2}}$. The known solutions to Equation (3.17) are the modified spherical Bessel functions of the first kind, $R(r) = i_l^{(1)}(\eta r)$, where $i_l^{(1)}(\eta r) = \sqrt{\left(\frac{\pi}{2r}\right)}\,I_{l+\frac{1}{2}}(\eta r)$; $I_{l+\frac{1}{2}}$ is Bessel's function of the first kind. Gathering all components of the solution yields (note that here we used $i_l^{(1)'}(r) = i_{l+1}^{(1)}(\eta R(t)) + \frac{l}{\eta R(t)}i_l^{(1)}(\eta R(t))$),

$$C_p\,(R(r),\Theta(\theta)\,,\Phi(\phi)) = \sum_{l\geq 0}\sum_{|m|\leq l}\chi_{lm}(t)\;i_l^{(1)}(\eta r)\,Y_l^m(\theta,\phi)\,. \tag{3.18}$$

To solve for the pressure, we multiply (3.12a) by $\frac{s}{\eta^2}$ and add it to (3.12b) to obtain

$$\nabla^2 \left(P_p + \frac{s}{\eta^2 \mu} C_p \right) = 0.$$

It follows that the known solution is

$$P_p + \frac{\zeta}{\eta^2 \mu} C_p = \sum_{l \geq 0} \sum_{|m| \leq l} \Pi_{lm}(t) r^l \, Y_l^m(\theta, \phi) \,,$$

which by (3.18) yields the final solution in the form

$$P_p \left(R(r), \Theta(\theta) \,, \Phi(\phi) \right) = \sum_{l \geq 0} \sum_{|m| \leq l} \left(\Pi_{lm}(t) r^l - \frac{\zeta}{\eta^2 \mu} \chi_{lm}(t) \; i_l^{(1)}(\eta r) \right) Y_l^m(\theta, \phi) \,, \quad (3.19)$$

where the coefficients $\Pi_{lm}(t)$ are determined by the boundary conditions. From (3.14a,3.14b), we infer that

$$\chi_{1m}(t) = 0 \quad \text{and} \quad \Pi_{1m}(t) = 0 \,,$$

and from (3.13b), we find $\rho_{1m}(t) = 0$. For $l \neq 1$ we have

$$\begin{aligned} \chi_{lm}(t) \; i_l^{(1)}(\frac{\eta R(t)}{C_d}) &= \left[\frac{\gamma \bar{C}_\infty}{R^2} (2 - l(l+1)) - \frac{\partial \bar{C}}{\partial r}(R(t)) \right] \rho_{lm}(t) \\ &= \left(-l(l+1) \frac{\gamma}{R(t)^2} - \left(1 - \frac{2\gamma}{R(t)} \right) \eta \coth(\eta R(t)) + \frac{1}{R(t)} \right) \bar{C}_\infty \rho_{lm}(t) \,, \end{aligned} \quad (3.20)$$

and by (3.19)

$$\begin{aligned} &\frac{1}{C_d P_\infty} \left(\Pi_{lm}(t) R(t)^l - \frac{\zeta}{\eta^2 \mu} \chi_{lm}(t) \; i_l^{(1)}(\eta R(t)) \right) = -\frac{\partial \bar{P}}{\partial r}(R(t)) \, \frac{\rho_{lm}(t)}{C_d} \quad (3.21) \\ &= \left(-\frac{\bar{C}_\infty}{\eta^2} \left(\frac{1}{R(t)} - \frac{2\gamma}{R(t)^2} \right) + \frac{\bar{C}_\infty}{\eta} \left(1 - \frac{2\gamma}{R(t)} \right) \coth(\eta R(t)) - \frac{R(t)}{3} \right) \frac{\zeta}{P_\infty \mu} \rho_{lm}(t). \end{aligned}$$

Hence, substitution of (3.20) into (3.21) yields

$$\frac{\mu}{C_d \zeta} \Pi_{lm}(t) R(t)^l = \left((1-l)(l+2) \frac{\gamma \bar{C}_\infty}{\eta^2 R(t)^2} - \frac{R(t)}{3} \right) \rho_{lm}(t). \quad (3.22)$$

By writing the perturbed radius in an orthonormal spherical basis,

$$R_p(t) = \sum_{l\geq 0} \sum_{|m|\leq l} \rho_{lm}(t)\, Y_l^m(\theta,\phi)\,, \tag{3.23}$$

and implementing (3.12c), we conclude that $\frac{d\rho_{1m}}{dt}(t) = 0$ and for $l \neq 1$

$$\begin{aligned}
\frac{1}{C_d\zeta\rho_{lm}(t)}\frac{d\rho_{lm}(t)}{dt} &= -\frac{\mu}{C_d}\left(l\,\Pi_{lm}(t)\,l\,R(t)^{l-1} - \frac{\zeta}{\mu\eta}\chi_{lm}(t)\; i_l^{(1)'}(\eta R(t)) + \frac{\partial^2 P}{\partial r^2}(R(t))\right)\\
&= -\,l\frac{\mu}{C_d\zeta}\Pi_{lm}(t)R(t)^{l-1} + \frac{1}{C_d\eta}\chi_{lm}(t)\;\left(i_{l+1}^{(1)}(\eta R(t)) + \frac{l}{\eta R(t)}i_l^{(1)}(\eta R(t))\right)\\
&\quad - \frac{2\bar{C}_\infty(R(t)-2\gamma)\coth(\eta R(t))}{\eta R(t)^2} + \frac{2\bar{C}_\infty(R(t)-2\gamma)}{\eta^2 R(t)^3} + \frac{\bar{C}_\infty(R(t)-2\gamma)}{R(t)} - \frac{1}{3}\\
&= -\,\frac{l}{R(t)}\frac{\mu}{C_d\zeta}\left(\Pi_{lm}(t)R(t)^l - \frac{1}{\eta}\chi_{lm}(t)\,i_l^{(1)}(\eta R(t))\right) + \frac{1}{C_d\eta}\chi_{lm}(t)\,i_{l+1}^{(1)}(\eta R(t))\\
&\quad - \frac{2\bar{C}_\infty(R(t)-2\gamma)\coth(\eta R(t))}{\eta R(t)^2} + \frac{2\bar{C}_\infty(R(t)-2\gamma)}{\eta^2 R(t)^3} + \frac{\bar{C}_\infty(R(t)-2\gamma)}{R(t)} - \frac{1}{3}\\
&= -\,\frac{l}{R(t)}\left(-\frac{\bar{C}_\infty}{\eta^2}\left(\frac{1}{R(t)} - \frac{2\gamma}{R(t)^2}\right) + \frac{\bar{C}_\infty}{\eta}\left(1 - \frac{2\gamma}{R(t)}\right)\coth(\eta R(t)) - \frac{R(t)}{3}\right)\\
&\quad - \frac{2\bar{C}_\infty(R(t)-2\gamma)\coth(\eta R(t))}{\eta R(t)^2} + \frac{2\bar{C}_\infty(R(t)-2\gamma)}{\eta^2 R(t)^3} + \frac{\bar{C}_\infty(R(t)-2\gamma)}{R(t)} - \frac{1}{3}\\
&\quad + \frac{1}{C_d\eta}\chi_{lm}(t)\,i_{l+1}^{(1)}(\eta R(t))\,.
\end{aligned}$$

Finally, from (3.20) we obtain

$$\begin{aligned}
\frac{1}{C_d\zeta\rho_{lm}(t)}\frac{d\rho_{lm}(t)}{dt} &= (l+2)\frac{\bar{C}_\infty(R(t)-2\gamma)}{\eta^2 R(t)^3} - (l+2)\frac{\bar{C}_\infty(R(t)-2\gamma)\coth(\eta R(t))}{\eta R(t)^2}\\
&\quad + \frac{\bar{C}_\infty(R(t)-2\gamma)}{R(t)} + (l-1)\frac{1}{3}\\
&\quad + \left(-l(l+1)\frac{\gamma\bar{C}_\infty}{R^2} - \bar{C}_\infty\left(1 - \frac{2\gamma}{R(t)}\right)\eta\coth(\eta R(t)) + \frac{\bar{C}_\infty}{R(t)}\right)\frac{i_{l+1}^{(1)}(\eta R(t))}{\lambda i_l^{(1)}(\eta R(t))}\,.
\end{aligned} \tag{3.24}$$

Equation (3.24) describes the growth of asymmetric modes $\rho_{lm}(t)$ in time, which depends on both system parameters $\{C_\infty, C_d, \gamma, \eta\}$ and the system variable $R(t)$. These modes can be either excited or damped for various ranges of $R(t)$. In order

to find these ranges, the evolution equation in (3.24) was plotted against $R(t)$ for particular choices of system parameters in Figure 3.2. Each curve corresponded to a particular asymmetric mode number. The rate of growth $dR(t)/dt$ was also plotted to indicate the steady-state radially symmetric solutions. As discussed in Section 3.2.1, there were at most two steady-state solutions, $0 < R_1 < R_2$, depicted in the figure, identified by $dR/dt = 0$; however, only R_2 was dimensionally stable. Therefore, we carried out asymmetric stability analysis only for R_2.

For a given R_2, high mode numbers were stable, but low mode numbers were unstable as can be seen in Figure 3.2. Note that changing the system parameters changed the number of stable and unstable modes. As can be seen in Figure 3.2a,b, increasing the concentration of nutrients C_∞ increased the number of growing asymmetric modes. This was directly related to the tumor's access to nutrients, which increased tumor activity and proliferation, which in turn enabled them to adopt a new homeostatic equilibrium and become invasive. This allowed the tumor to evolve from a spherical shape, which was energy-wise preferred, and grow along asymmetric modes, called invasion modes. Therefore, a higher concentration of nutrients enabled a tumor to gain invasion modes. On the other hand, as depicted in Figure 3.2c,d, increasing the rate of consumption led to a smaller steady-state radius with a smaller number of invasion asymmetric modes. The same behavior can be seen for the change in surface tension (γ) in Figure 3.2e,f. Higher surface tension allowed for a smaller steady-state radius and a smaller number of growing asymmetric modes.

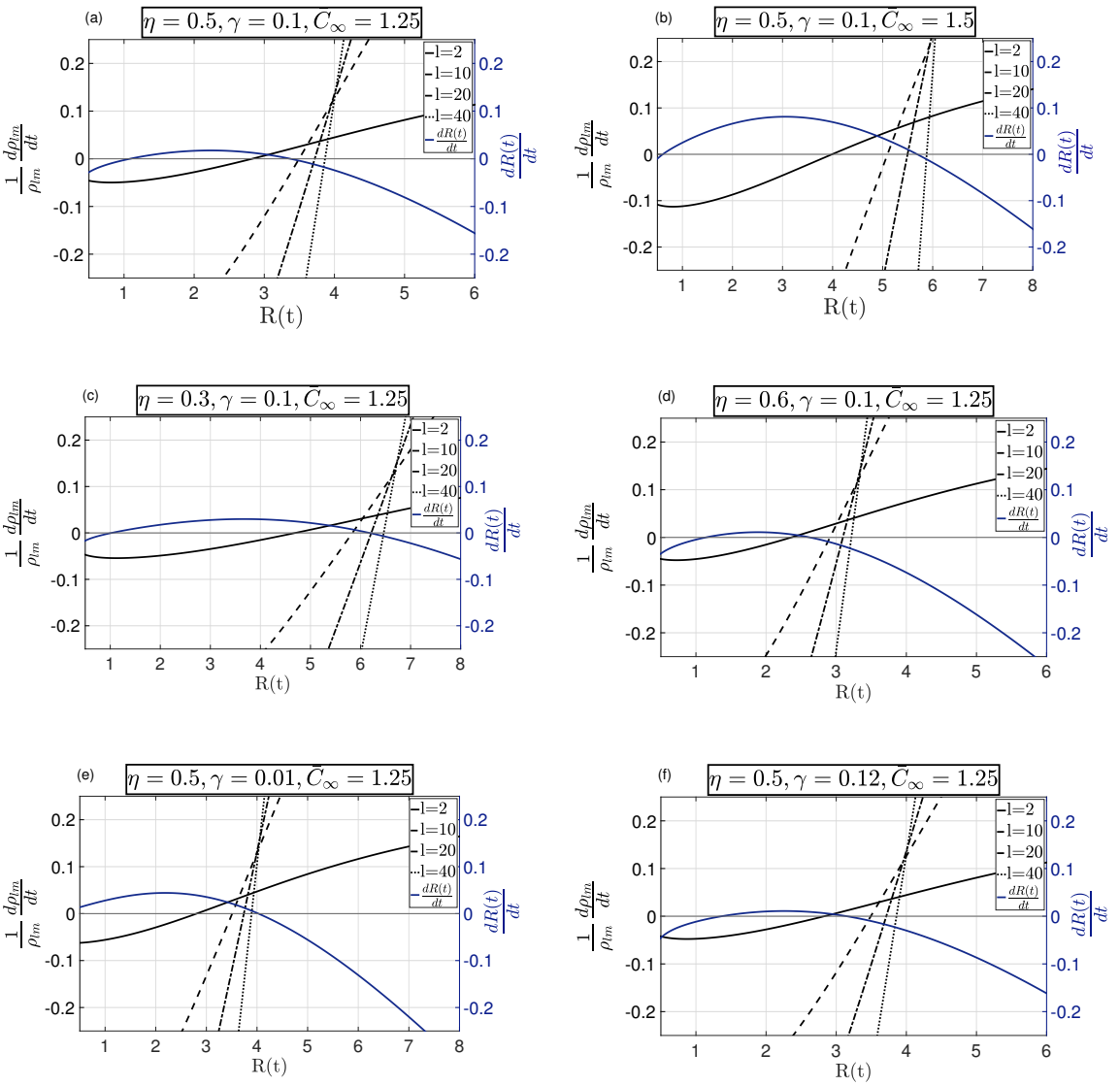

Figure 3.2: Growth rate of asymmetric modes $Y_l^m(\theta, \phi)$ with respect to $R(t)$ for four choices of mode number $l = \{2, 10, 20, 40\}$. In each sub-figure, the radii where the curves cross $\frac{dR}{dt} = 0$ indicate the steady-state solutions, i.e., $R_1 < R_2$. In (**a**) $\bar{C}_\infty = 1.25$ and (**b**) $\bar{C}_\infty = 1.5$; the number of unstable asymmetric modes for R_2 was reduced by lowering the nutrient source $\bar{C}_\infty$. For instance, for $l = 20$, the steady state was unstable in (**b**), while reducing $\bar{C}_\infty$ stabilized it in (**a**). In (**c**) $\eta = 0.3$ and (**d**) $\eta = 0.6$; a higher rate of consumption led to smaller steady-state R_2 with a smaller number of unstable asymmetric modes. In (**e**) $\gamma = 0.01$ and (**f**) $\gamma = 0.12$; reducing the surface tension allowed for larger steady-state R_2, while more asymmetric modes became unstable. In all cases, R_2 was unstable to low-mode numbers, but was stable with respect to sufficiently large mode numbers.

3.2.3 Growing Asymmetric Modes

To achieve insight into the perturbed configuration of the tumor, it was important to find the fastest growing mode, i.e., the dominant mode number l_d. Such mode(s) could determine the long-term change in the shape of the tumor. In addition, the surface tension γ could stabilize the growth of this mode. Therefore, we centered our focus on the variation of l_d for different values of γ, in close proximity to the steady-state solution $R_2(t)$. The steady-state solution of (3.8b), $dR/dt = 0$, takes the form

$$\frac{\bar{C}_\infty(R(t)-2\gamma)}{\eta^2 R(t)^2} - \frac{\bar{C}_\infty(R(t)-2\gamma)}{\eta R(t)}\coth(\eta R(t)) + \frac{R(t)}{3} = 0.$$

Substitution of this into (3.24) gives

$$\begin{aligned}\frac{1}{C_d\zeta\rho_{lm}(t)}\frac{d\rho_{lm}(t)}{dt} &= \frac{\bar{C}_\infty(R-2\gamma)}{R(t)} \\ &\quad + \left((1-l)(l+2)\frac{\gamma\bar{C}_\infty}{R^2} + \frac{\eta^2 R}{3}\right)\frac{i_{l+1}^{(1)}(\eta R)}{\eta i_l^{(1)}(\eta R)} - 1\,.\end{aligned} \tag{3.25}$$

To better understand the role of the surface tension, γ, given a particular choice of system parameters $\{C_\infty, C_d, \eta\}$, Equation (3.24) can be expressed as in Equation (3.25) as a function only of l and γ. Figure 3.3 shows the positive rate of growth of asymmetric modes. Modes with a negative rate of growth (damped modes) were neglected. Mode numbers that had the maximum rate of growth (maximal modes) are marked in red. It can be seen that for $\bar{C}_\infty = 1.5$, by increasing the surface tension the dominant mode dropped from $l = 9$ to $l = 7$; however, it had a fixed value of $l = 3$ for $\bar{C}_\infty = 1.2$. This behavior could be interpreted as the role of nutrients and surface tension on tumor invasiveness, that is, a higher concentration of nutrient source maximized the growth of a higher asymmetric mode number, which dropped to a lower mode number by increasing the surface tension.

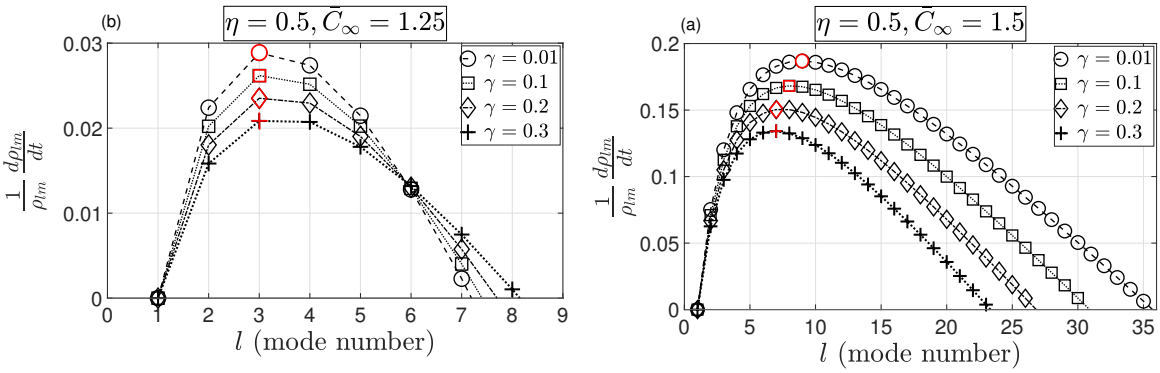

Figure 3.3: Growth rate of asymmetric modes $Y_l^m(\theta, \phi)$ with respect to l (mode number) for $\gamma = \{0.01, 0.1, 0.2, 0.3\}$ and $C_\infty = \{1.25, 1.5\}$. The mode number that maximized the asymmetric growth rate (maximal mode) is marked in red, indicating that increasing surface tension dropped the dominant mode from $l = 9$ to $l = 7$ for $C_\infty = 1.5$; however, it had a fixed value of $l = 3$ for $C_\infty = 1.25$.

3.3 Asymmetric Configuration

The progression of tumors starts with the formation of small symmetric-shaped avascular tumors (spherical configuration) and proceeds with their volumetric growth. However, a tumor microenvironment can exert external stimuli that trigger asymmetric growth and, therefore, tumors lose their symmetric shape and acquire an asymmetric configuration. Here, we present an instability analysis of such responses as associated with tumor invasion modes. We considered asymmetric radius perturbation (3.9c) in terms of a spherical harmonic basis, which has the form of (3.23). The perturbed axisymmetric radius is a superposition of infinitely many modes. However, only the growing modes, and particularly the maximal mode, eventually dominate the tumor configuration. The total radius is

$$R_t(\theta, \phi, t) = \bar{R} + \epsilon \sum_{l \geq 0} \sum_{|m| \leq l} \rho_{lm}(t)\, Y_l^m(\theta, \phi)\,, \tag{3.26}$$

where $\bar{R}$ is the steady-state radius. Integration of (3.25) gives the evolution of coefficients

$$\rho_{lm}(t) = \rho_{lm}^{0} \exp\left(\frac{\zeta}{C_d}\left(\frac{\bar{C}_\infty(R-2\gamma)}{R} + \left((1-l)(l+2)\frac{\gamma\bar{C}_\infty}{R^2} + \frac{\eta^2 R}{3}\right)\frac{i_{l+1}^{(1)}(\lambda R)}{\eta i_l^{(1)}(\eta R)} - 1\right)t\right), \tag{3.27}$$

where ρ_{lm}^{0} are the coefficients corresponding to the initial condition R_{p_0}, i.e.,

$$R_{p_0}(\theta,\phi) = \sum_{l\geq 0}\sum_{|m|\leq l} \rho_{lm}^{0}\, Y_l^m(\theta,\phi).$$

Figure 3.4 depicts the three-dimensional configurations of the tumor (3.26) and (3.27) after sufficient time when only the growing modes were observable. For the two choices of parameters used in Figure 3.2a,b, i.e., $\{\bar{C}_\infty = 1.25, \eta = 0.5, \gamma = 0.1, \bar{R} = 3.37\}$ and $\{\bar{C}_\infty = 1.5, \eta = 0.5, \gamma = 0.1, \bar{R} = 5.69\}$, the corresponding unstable modes were $l = \{0, 2, 3, ..., 7\}$ and $l = \{0, 2, 3, ..., 30\}$, respectively. Implementing these parameters and the unstable modes in (3.26), perturbed radii were obtained to plot the asymmetric configurations.

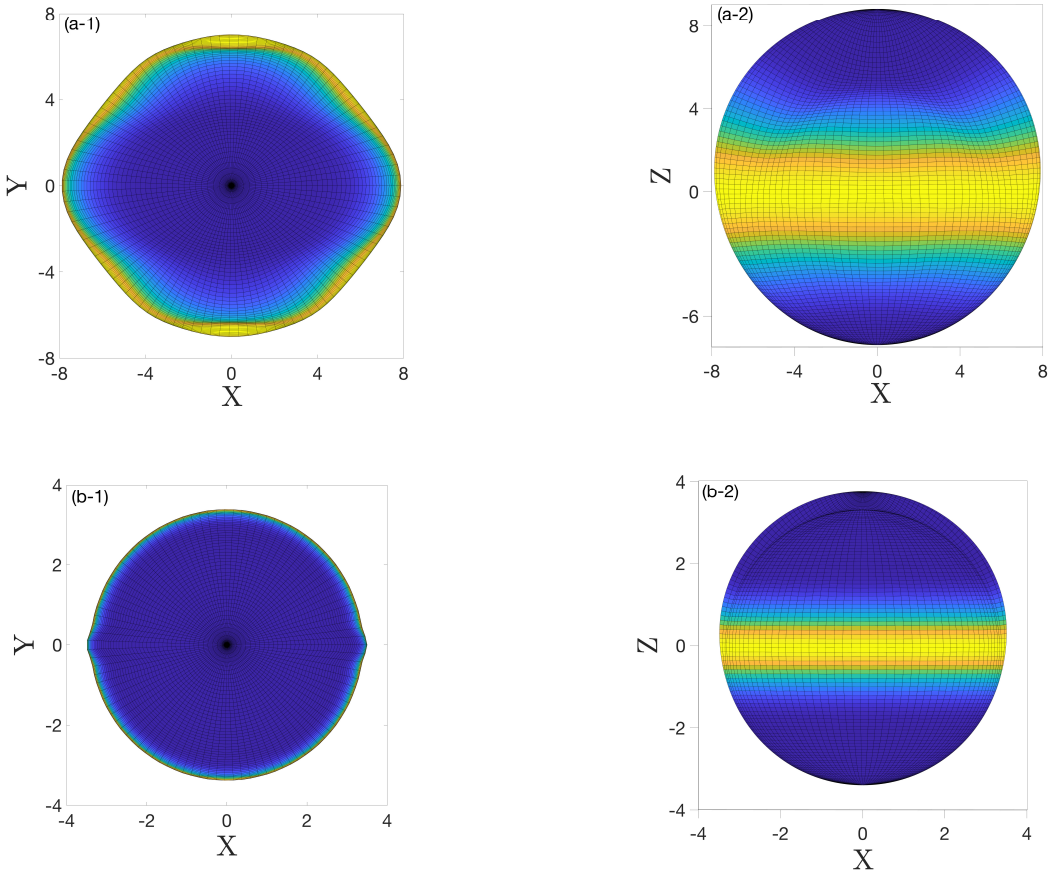

Figure 3.4: The asymmetric configuration of a tumor for two different choices of parameters, (**a-1**,**a-2**) $\{\bar{C}_\infty = 1.25, \eta = 0.5, \gamma = 0.1, \bar{R} = 3.37\}$, the corresponding growing modes $l = \{0, 2, 3, ..., 7\}$, (**b-1**,**b-2**) $\{\bar{C}_\infty = 1.5, \eta = 0.5, \gamma = 0.1, \bar{R} = 5.69\}$ and the corresponding unstable modes $l = \{0, 2, 3, ..., 30\}$. The top (left) and side (right) views are shown in the figure. Colors represent the value of the z component of the radius; yellow means $R_z = 0$.

3.4 Results and Discussion

In this section, experimental results are compared to the model predictions presented in previous sections. To this end, the asymmetric modes were compared against the formation of in vitro solid tumor spheroids generated from a glioma cell line (U251 hGB cells). HGB cells were cultured in Dulbecco's Modification of Eagle's Medium (DMEM) supplemented with 10% (v/v) Fetal Bovine Serum (FBS) and 1% (v/v) Penicillin/Streptomycin and incubated at 37 °C in 5% CO_2. Cells were then dissociated with Gibco^{TM} Trypsin-EDTA (0.5%), centrifuged at 300× g (5 min) and counted

using a Trypan blue assay. Self-filling micro-well arrays (SFMAs) were used to produce tumor spheroids [84]. Spheroids were then supplemented with fresh medium every 24h to maintain the concentration of nutrients. To resemble the conditions considered in the analytical part as closely as possible, only approximately spherical tumor spheroids were selected, and only small spheriods of $\sim$200 μm diameter, to avoid heterogeneity in their cell population, such as hypoxic and necrotic cells. Presence of such heterogeneity violated the adopted assumption of linear nutrient consumption throughout the tumor, $\eta^2 C$, η = constant, as hypoxic cells normally switch their metabolism to anaerobic glycolysis where they consume glucose at a higher rate compared to normal cells. We also provided them with a constant concentration of nutrients C_∞ at their boundary by regularly refreshing the medium. Although the spheroids were kept in a symmetric medium, asymmetric stimuli are always a part of the natural environment of tumors. Images of tumors were obtained using optical microscopy (Axio Observer, ZEISS, Oberkochen, Germany). Figure 3.5 shows images of a few representative examples of aspherical tumors frequently observed in experiments, compared with model predictions of the maximal asymmetric modes. The qualitative comparison showed that the tumor spheroids acquired configurations similar to the model predictions. It should be noted that the experimental results were limited in terms of quantitative measurements due to the complexity in implementation of the parameters of interest. For instance, the real system could only start from an approximately spherical shape. In addition, the environment could not be perfectly uniform. However, reasonable agreement was observed between the experimental results and the model predictions where the salient features of the tumor configurations aligned with the model predictions of configurations dominated by the growth of asymmetric modes.

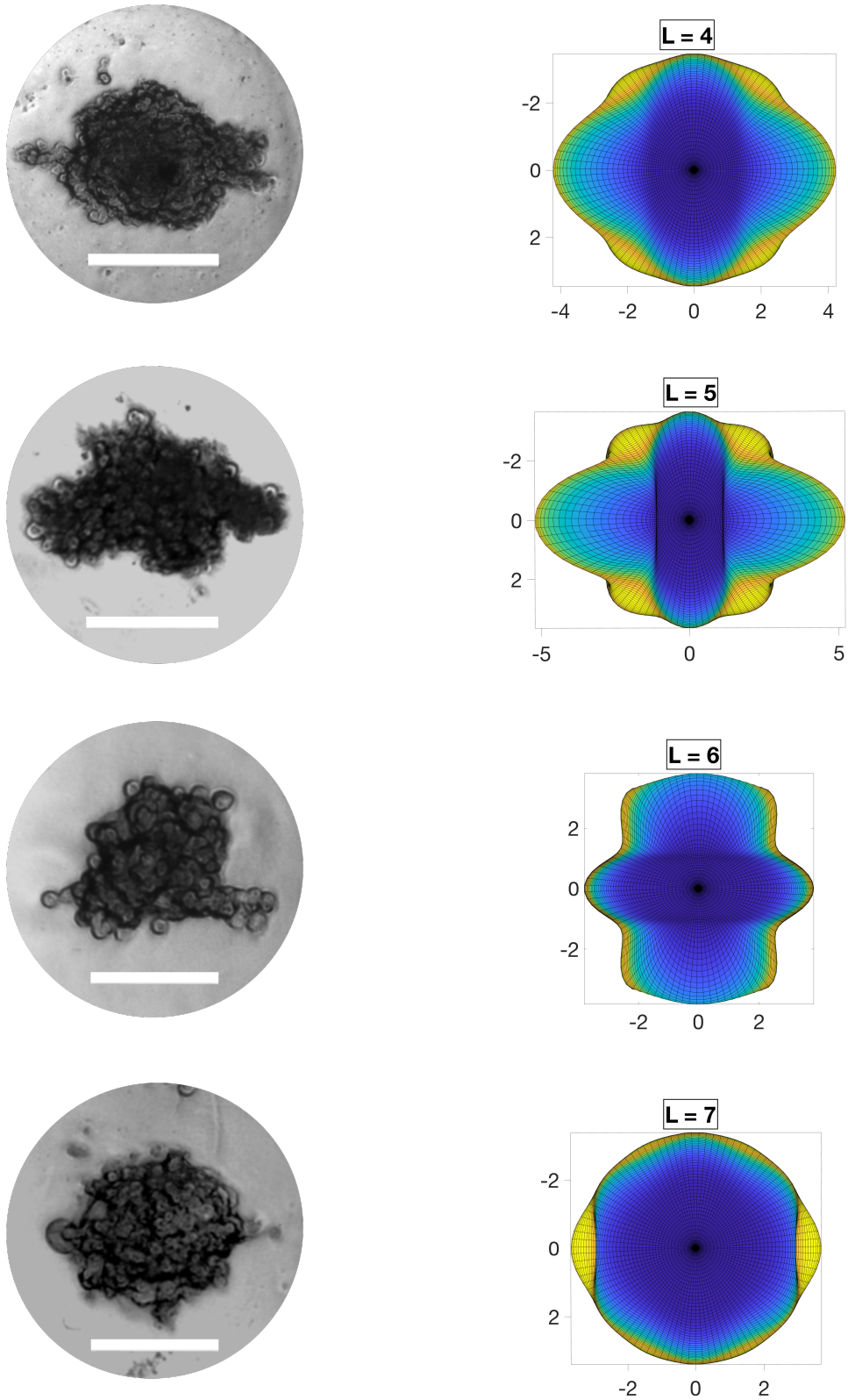

Figure 3.5: Asymmetric configurations of in vitro human glioblastoma (hGB) spheroids (**left column**) compared with the similar configurations of maximal asymmetric modes predicted by the model (**right column**). Nearly spherical tumors with no heterogeneity in their cell population were provided with constant concentration of nutrients C_∞ at their boundary to resemble a symmetric environmental condition. Scale bars are 200 μm.

3.5 Conclusion

The stability of the radially symmetric growth of tumor spheroids was studied by introducing asymmetric perturbations to the symmetric steady-state solution of a reaction-diffusion model in which the rate of nutrient consumption was concentration dependent. The analytical solution, expressed in terms of a spherical harmonic basis, manifested the growth of asymmetric modes. It was shown that the radially symmetric steady-state solution for the growth of tumor spheroids in a symmetric environment was unstable with respect to small asymmetric perturbations. Such perturbations excited asymmetric modes of growth. These modes could grow in time and dominate the tumor configuration. The number of such modes and their rates of growth depended on surface tension, external nutrient sources and the rate of nutrient consumption. A high nutrient source concentration allowed for a large tumor size, which increased the number of unstable excited asymmetric modes. However, high rates of nutrient consumption and surface tension led to a smaller size of the tumor and a smaller number of growing asymmetric modes. In addition, we showed that spherical tumors were unstable since asymmetric growing modes always dominated the tumor configuration. Hence, the spherical configurations of tumors, even under experimentally controlled symmetric conditions, were naturally unstable. These analytic results were in agreement with the configurations of growing in-vitro human glioblastoma (hGB) spheroids.

Author Contributions: Conceptualization, M.A. (Meitham Amereh); methodology, M.A. (Meitham Amereh), Y.B. and R.E.; validation, M.A. (Meitham Amereh) and M.A. (Mohsen Akbari); formal analysis, M.A. (Meitham Amereh), Y.B., B.N. and R.E.; investigation, M.A. (Meitham Amereh), B.N. and R.E.; resources, M.A. (Mohsen Akbari); writing—original draft preparation, M.A. (Meitham Amereh); writing—review and editing, M.A. (Meitham Amereh), B.N., R.E. and M.A. (Mohsen Akbari); supervision, B.N., R.E. and M.A. (Mohsen Akbari); funding acquisition, B.N. and M.A. (Mohsen Akbari). All authors have read and agreed to the published version of the manuscript.

Funding: Funding was provided by the Natural Science and Engineering Research Council (NSERC) of Canada.M.A. (Mohsen Akbari) and M.A. (Meitham Amereh) acknowledges the BC Cancer Foundation and Canadian Foundation for Innovation (CFI) for supporting this work.

Acknowledgments: The authors acknowledge the BC Cancer Foundation and Canadian Foundation for Innovation (CFI) for supporting this work.
Conflicts of interest: The authors declare no conflict of interest.

Chapter 4

In-Silico Study of Asymmetric Remodeling of Tumors in Response to External Biochemical Stimuli

Contributions:
Meitham Amereh: Conceptualization, theory and simulation, methodology, formal analysis, experiments, validation, writing—original draft preparation, writing—review and editing
Mohsen Akbari: Conceptualization, methodology, formal analysis, writing—review and editing, supervision, resources
Ben Nadler: Theory and simulation, formal analysis, writing—review and editing, supervision

Meitham Amereh[1,2,3], Mohsen Akbari[1,2,3,4,5,+] and Ben Nadler [1,*]

[1] Department of Mechanical Engineering, University of Victoria, Victoria, BC V8W 2Y2, Canada; makbari@uvic.ca (M.A.)

[2] Laboratory for Innovations in MicroEngineering (LiME), Department of Mechanical Engineering, University of Victoria, Victoria, BC V8P 5C2, Canada

[3] Centre for Advanced Materials and Related Technologies (CAMTEC), University of Victoria, Victoria, BC V8W 2Y2, Canada

[4] Biotechnology Center, Silesian University of Technology, Akademicka 2A, 44-100 Gliwice, Poland

Scientifc Reports 2023 13:941. https://doi.org/10.1038/s41598-022-26891-8 https://www.nature.com/srep/

[5] Terasaki Institute for Biomedical Innovations, Los Angeles, CA, USA
*Correspondence: bnadler@uvic.ca; Tel.: (+1) 250-721-6050
+Co-corresponding author: makbari@uvic.ca; Tel.: (+1) 250-721-6038

Abstract

Among different hallmarks of cancer, understanding biomechanics of tumor growth and remodeling benefits the most from the theoretical framework of continuum mechanics. Tumor remodeling initiates when cancer cells seek new homeostasis in response to the microenvironmental stimuli. Cells within a growing tumor are capable to remodel their inter- and intra-connections and become more mobile to achieve a new homeostasis. This mobility enables the tumor to undergo large deformation. In this work, we studied the remodeling of homogeneous tumors, at their early stage of growth, in the context of continuum mechanics. We developed an evolution law for the remodeling-associated deformation which correlates the remodeling to a characteristic tensor of external stimuli. The asymmetric remodeling and the induced mechanical stresses were analyzed for different types of biochemical distributions. To experimentally investigate the model, we studied the remodeling of human glioblastoma (hGB) tumoroids in response to the gradient of nutrients. Using a tumoroid-on-a-chip platform, the degree of remodeling was estimated for the ellipsoidal tumoroids over time. It was observed that higher gradient of nutrients induces higher degree of ellipticity suggesting that the gradient of nutrient is a characteristic property of nutrient distribution that derives the remodeling. We also showed that remodeling gives rise to heterogeneity in cell distribution forming circumferentially aligned cells within the tumors. Compared to the existing studies on tumor growth, our work provides a biomechanical module that relates the remodeling to biochemical stimuli, and allows for large deformation. It also includes experimental component, a necessary but challenging step, that connects the theory and reality to evaluate the practicability of the model.

4.1 Introduction

Cancer has been recognized as one the most challenging problems in biology and medicine. Aggressive tumors are lethal type of cancers characterized by high genomic instability, rapid progression, invasiveness and therapeutic resistance [123]. Their

behavior involves complicated molecular biology and consequential dynamics. Diversity of mechanisms involved in cancer progression makes the treatment strategies inevitable to approach from different areas of knowledge. Although tremendous effort has been devoted to developing new therapeutics, there is still a huge need for new insights into the less known aspects of tumors such as evolution of heterogeneity, biomechanical responses, etc. [71]. Mathematical modeling, and continuum mechanics in particular, can play a pivotal role in better understanding the complex behavior of tumors by providing quantitative predictions of biological processes involved in tumor growth and invasion and helping to interpret complicated mechanical interactions between tumor and microenvironment [11]. Having insight into mechanical responses of a growing tumor can contribute in development of cancer therapeutic approaches. Mathematical oncology, for instance, with a broad scope including theoretical studies and mathematical models used to design clinical trials, has become a dominant field of research in personalized medicine [52]. In-silico cancer models have a great potential to help improving therapeutic efficacy and drug design and delivery in clinical oncology. Applications of continuum based in-silico models in simulating the growth of vascularised solid tumours have been reviewed in [53].

The pathophysiology of aggressive tumors is strongly affected by the extracellular cues such as nutrients, growth factors, oxygen and stresses [54]. For instance, a growing tumor can change its homeostasis in response to nutrient supply via different mechanisms [124]. One of such mechanisms is remodeling by breaking and making adherent junctions [55]. During this process, the tumor stops the rapid proliferation and begins to remodel its shape to preserve the homeostatic equilibrium state. To reach this, the tumor in turn upregulates epithelial to mesenchymal transit-inducing transcription factors (EMT-TFs) [125]. These EMT-TFs are involved in various signaling cascades which are often associated with tumor invasiveness and malignancy [126].

The growth of solid tumor spheroids has been mathematically studies from different perspectives such as continuum, discrete and hybrid (continuum-discrete) methods [105–107, 127]. These models built upon partial differential equations (PDEs) for mass conservation and evolution of the tumor boundary, considering the concentrations of cells and nutrients as the main variables that define the local proliferation/death of cells. In addition, the stability of the radially symmetric growth to asymmetric perturbation is explored using the same mathematical framework [56, 128]. These analyses indicated that the spherical configuration of tumor spheroids

are naturally unstable to asymmetric perturbations. Despite the success in exposition of the role of properties such as surface tension and rate of proliferation in the stability of growth, they lack description of several components including the the mechanical stress distribution, anisotropic growth, the role of mechanical forces on the net tumor growth and mechanical interaction between tumor and extracellular matrix (ECM). These aspects of tumor progression are exclusively investigated in the framework of continuum mechanics [57, 58]. For instance, the influence of anisotropic growth on the overall growth and the resultant stress in avascular tumor spheroids is modeled by introducing a growth tensor [129–131]. Analysis of the radial and circumferential stresses on the degree of anisotropy revealed that growth rate is inversely proportional to the magnitudes of stresses. Anisotropic growth was also studied using a biomechanical model for the growth of spinal tumors [132]. The isotropic vs. anisotropic effects on the evolution of stress and interstitial pressure in intramedullary spinal tumours were predicted which revealed a significant difference in tumors shape. Results of these studies provide a direction to the prediction of different growth patterns, yet missing the remodeling module that allows for cell rearrangement and large deformation. Including experimental component is another necessary but challenging step that connects the theory and reality and evaluates the practicability of the models.

Despite the significance of these studies and the important results they provided, they do not account for the remodeling. Tumor progression is a multi-aspect complex process that includes growth, remodeling, etc. Remodeling is one of the important phenomena that occurs in solid tumors in response to external effects. The remodeling process takes place via different biomechanical rearrangements including cell–cell and cell-ECM adhesion bindings and can give rise to large deformation. Hence, study of the remodeling can help elucidate the dynamics of cell-cell and cell-matrix interactions stimulated by external influences. In this study, we proposed a mathematical framework based on the principles of continuum mechanics to better understand the role of biochemical stimuli in tumor remodeling. A volume-preserving evolution of remodeling was obtained that relates the characteristic tensor of external stimuli to the elastic response of tumor and the associated remodeling deformation. The tumor was taken to be hyperplastic material with Ciarlet strain energy function. The asymmetric remodelling and the induced stress distribution were analyzed for linear and quadratic distribution fields of biochemical stimuli. To experimentally validate the model, the shape of human glioblastoma (hGB) tumoroids exposed to the gradient of nutrient was studied over 6 days, using an open-well tumor-on-a-chip platform. We

introduced a gradient of nutrients within a composite hydrogel mimicking the extracellular matrix of hGB, and investigated the asymmetric remodeling of tumoroids in response to the nutrient gradient.

4.2 Biomechanical model

In the theory of material evolution, configurational forces are thermodynamically dual to the evolution rate, driving the growth, remodeling and material evolution [133]. The significance of these forces is explored in different areas of continuum mechanics, including defects [134], interfaces [135] and biological materials [136]. From the study of cell morphology, it is observed that a cluster of cells has the ability to break and form new bonds in the microstructure [137–139]. This mechanism is important when tumors are subjected to external stimuli such as mechanical stress and biological signals. From microstructure and continuum mechanics points of view, one may think of such microstructural rearrangement, analogous to plastic deformation, where the energy spent on remodeling of tumor microstructure dissipates, while the tumor conserves the energy associated with small elastic deformations.

4.2.1 Theory of material evolution

In this work we adopt the theory of material evolution to capture the time-dependent remodeling responses of tumors [140, 141]. We consider the tumor body as a simple evolving material, i.e. defined by their strain energy function, and neglect the thermodynamics effects, such as temperature. The invertible linear deformation gradient $\mathbf{F}$ is defined to map referential vector $\mathbf{X}_r$ from the initial configuration $\mathcal{B}_r$ to the spatial vector $\mathbf{x}_s$ in the current configuration $\mathcal{B}_s$, shown in Figure 4.1. The multiplicative decomposition of $\mathbf{F}$ reads $\mathbf{F} = \mathbf{F}_e\,\mathbf{P}$, where $\mathbf{F}_e$ and $\mathbf{P}$ are elastic and remodelling deformation tensors, respectively. The remodelling, denoted by $\mathbf{P}$, is the time-dependent induced invertible linear map from the initial configuration $\mathcal{B}_r$ to the natural configuration $\mathcal{B}_n$. The natural configuration is taken to be stress-free and used as a reference configuration for the constitutive law.

We assume that the energy supplied to the system includes mechanical power and other form of power flux, that stimulates remodeling by microstructural rearrange-

ment, and has the dissipation inequality form

$$\dot{\overline{J\rho\psi}} - J\mathbf{T}\cdot\mathbf{L} - J_p\rho\mathbf{S}\cdot\mathbf{L}_p \leqslant 0 \ , \tag{4.1}$$

where ψ is free energy per unit mass, ρ is the mass density, $J = \det\mathbf{F}$, $\mathbf{T}$ is Cauchy stress tensor, $\mathbf{L} = \dot{\mathbf{F}}\mathbf{F}^{-1}$ is the velocity gradient, $J_p = \det(\mathbf{P})$, $\mathbf{S}$ is the configurations stress per unit mass associated with external stimuli deriving the remodeling. Also, $\mathbf{L}_p = \dot{\mathbf{P}}\,\mathbf{P}^{-1}$ is the rate of remodeling such that $\mathbf{S}\cdot\mathbf{L}_p$ is the remodeling power where the inner product of two second-order tensors is defined as $\mathbf{S}\cdot\mathbf{L}_p = \mathrm{tr}\,(\mathbf{S}^T\mathbf{L}_p)$. Here, we focus on remodeling while neglecting the growth, that is $J_p = 1$ and $\dot{\overline{J\rho}} = 0$, hence $\dot{\overline{J\rho\psi}} = J\rho\dot{\psi}$.

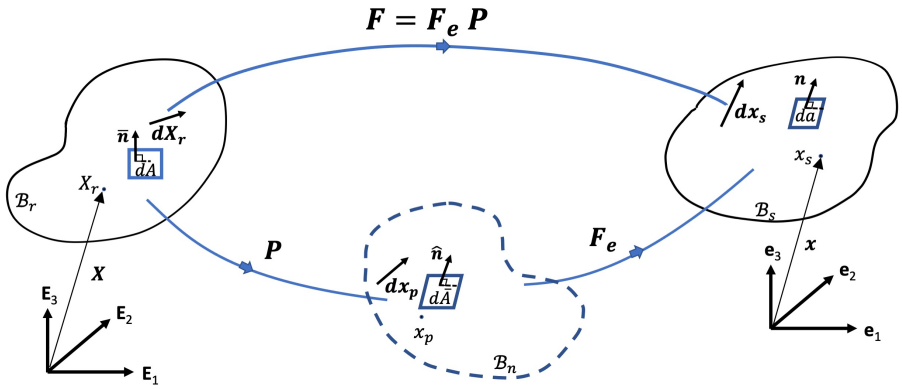

Figure 4.1: Multiplicative decomposition of the deformation $\mathbf{F} = \mathbf{F}_e\,\mathbf{P}$. Initial configuration $\mathcal{B}_r$, natural configuration $\mathcal{B}_n$ and the current configuration $\mathcal{B}_s$ together with their area elements and normal vectors are depicted in the figure. $\mathbf{E}_i$ and $\mathbf{e}_i$, $i = \{1, 2, 3\}$, are orthonormal bases in $\mathcal{B}_r$ and $\mathcal{B}_s$, respectively.

For elastic material the constitutive law states that strain energy is a function of the deformation $\psi = \hat{\psi}(\mathbf{F}_e)$, which yields $\dot{\psi} = (\partial\psi/\partial\mathbf{F}_e)\cdot\dot{\mathbf{F}}_e$. Now, equation (4.1) takes the form

$$J\rho\,\frac{\partial\psi}{\partial\mathbf{F}_e}\cdot\dot{\mathbf{F}}_e \leqslant J\mathbf{T}\cdot\mathbf{L} + \rho\,\mathbf{S}\cdot\mathbf{L}_p\,, \tag{4.2}$$

where the partial derivative $\partial A/\partial\mathbf{B}$ stands for the second-order-tensor-valued spatial derivative of the scalar-valued function A with respect to the second-order tensor

variable $\mathbf{B}$. Rearranging (4.2) into the convenient form yields

$$\begin{aligned} J\rho\,\frac{\partial\psi}{\partial\mathbf{F}_e}\cdot\dot{\mathbf{F}}_e &\leqslant J\mathbf{T}\cdot(\dot{\mathbf{F}}\mathbf{F}^{-1})+\rho\,\mathbf{S}\cdot\dot{\mathbf{P}}\,\mathbf{P}^{-1} \\ &\leqslant J\mathbf{T}\cdot(\dot{\mathbf{F}}_e\mathbf{P}+\mathbf{F}_e\dot{\mathbf{P}})(\mathbf{P}^{-1}\mathbf{F}_e^{-1})+\rho\,\mathbf{S}\cdot\dot{\mathbf{P}}\,\mathbf{P}^{-1} \\ &\leqslant J\mathbf{T}\cdot(\dot{\mathbf{F}}_e\mathbf{P}\mathbf{P}^{-1}\mathbf{F}_e^{-1}+\mathbf{F}_e\dot{\mathbf{P}}\mathbf{P}^{-1}\mathbf{F}_e^{-1}+\rho\,\mathbf{S}\cdot\dot{\mathbf{P}}\,\mathbf{P}^{-1} \\ &\leqslant J\mathbf{T}\mathbf{F}_e^{-T}\cdot\dot{\mathbf{F}}_e+J\mathbf{F}_e^{T}\mathbf{T}\mathbf{F}_e^{-T}\cdot\dot{\mathbf{P}}\,\mathbf{P}^{-1}+\rho\,\mathbf{S}\cdot\dot{\mathbf{P}}\,\mathbf{P}^{-1}\,, \end{aligned}$$

hence

$$\left(J\mathbf{T}\mathbf{F}_e^{-T}-J\rho\,\frac{\partial\psi}{\partial\mathbf{F}_e}\right)\cdot\,\dot{\mathbf{F}}_e+(\mathbf{M}+\rho\mathbf{S})\cdot\,\mathbf{L}_p\,\geqslant 0\,, \tag{4.3}$$

where the Mandel stress is

$$\mathbf{M}=J\mathbf{F}_e^{T}\mathbf{T}\mathbf{F}_e^{-T}\,. \tag{4.4}$$

Since $\dot{\mathbf{F}}$ and$\mathbf{L}_p$ are independent and the elastic part is non-dissipative, inequality (4.3) requires that

$$\left(J\mathbf{T}\mathbf{F}_e^{-T}-J\rho\,\frac{\partial\psi}{\partial\mathbf{F}_e}\right)\cdot\,\dot{\mathbf{F}}_e=0\,, \tag{4.5}$$

$$(\mathbf{M}+\rho\mathbf{S})\cdot\,\mathbf{L}_p\,\geqslant 0\,. \tag{4.6}$$

To satisfy (4.5), it is necessary that

$$\mathbf{T}=\rho\,\frac{\partial\psi}{\partial\mathbf{F}_e}\mathbf{F}_e^{T}\,. \tag{4.7}$$

As $\mathbf{L}_p$ involves pure remodeling, it implies that $\dot{J}_p=\operatorname{tr}\mathbf{L}_p=0$. By (4.6), it follows that only the divatoric part of $(\mathbf{M}+\rho\mathbf{S})$ yields a non-vanishing power, hence, it can be expressed as

$$(\mathbf{M}+\rho\mathbf{S})^{\mathrm{div}}\cdot\,\mathbf{L}_p\,\geqslant 0\,, \tag{4.8}$$

where the superscript div is the deviatoric part of the argument. It follows that the form

$$\mathbf{L}_p=\left(\mathbb{K}\,(\mathbf{M}+\rho\mathbf{S})\right)^{\mathrm{div}}\,, \tag{4.9}$$

automatically satisfies (4.8) given that $\mathbb{K}$ is a positive semi-definite fourth order ten-

sor. Finally, the evolution of the remodeling has the form

$$\dot{\mathbf{P}} = (\mathbb{K}(\mathbf{M} + \rho\mathbf{S}))^{\text{div}}\ \mathbf{P}\,, \tag{4.10}$$

where $(\mathbf{M}+\rho\mathbf{S})$ is the remodeling stimuli and $\mathbb{K}$ represents the anisotropy relationship between the direction of the stimuli and the remodeling.

4.2.2 Governing equations

For solids undergoing large deformation it is convenient to use the known referential configuration, $\mathcal{B}_r$, to express the governing equations, rather than the unknown spatial configuration $\mathcal{B}_s$. The referential forms of the conservation of mass and balance of linear momentum are

$$\rho = J^{-1}\rho_0\,, \tag{4.11}$$

$$\rho_0\dot{V}_R = \rho_0\mathbf{b} + \text{Div}(\mathbf{\Pi})\,, \tag{4.12}$$

where ρ_0 and ρ are the spatial and referential densities, respectively, $\dot{V}_R$ is the material time derivative of the velocity, $\mathbf{b}$ is the body force, $\mathbf{\Pi}$ is the Piola stress, and Div is referential divergence operator. Next step is to utilize a constitutive strain energy for the tumor mass to relate the deformation to the stress.

Observations suggest that small avascular solid tumors, made of single cell type population, behave as isotropic compressible materials [142, 143]. In addition, biological tissues show rate-dependent responses, and hence viscoelastic constitutive equations are used to model their behaviour. However, the solid tumor spheroids have a small relaxation time compared to the time scale of biological evolution such as growth, remodelling, invasion, etc. [144]. Therefore, we consider solid tumor spheroids as hyperelastic isotropic compressible material with strain energy function that depends only on the deformation gradient. It has been shown that the evolution of stress in tumors has limited dependency on the specific hyperelastic constitutive relations [145]. Therefore, we adopt the commonly used Ciarlet strain energy [143]

$$\psi = \frac{\lambda}{4}\left[I_3(\mathbf{B}_e) - \ln I_3(\mathbf{B}_e) - 1\right] + \frac{\mu}{2}\left[I_1(\mathbf{B}_e) - \ln I_3(\mathbf{B}_e) - 3\right], \tag{4.13}$$

where $\mathbf{B}_e = \mathbf{F}_e\,\mathbf{F}_e^T$ is the left Cauchy-Green elastic deformation tensor, $I_1(\mathbf{B}_e)$, $I_3(\mathbf{B}_e)$ are the principal invariants of $\mathbf{B}_e$, and λ and μ are Lame's constants associated with

the tumor. Substitution of (4.13) in (4.7) gives the Cauchy stress tensor

$$\mathbf{T} = \rho\left[\mu\mathbf{B}_e + \frac{\lambda}{2}\left(I_3(\mathbf{B}_e) - 1\right)\mathbf{I} - \mu\mathbf{I}\right]. \tag{4.14}$$

The transformation of the Cauchy stress tensor to the Piola stress tensor is

$$\mathbf{\Pi} = J\,\mathbf{T}\,\mathbf{F}^{-T}. \tag{4.15}$$

Finally, the spatial boundary condition is

$$\mathbf{T}\,\mathbf{n} = \mathbf{t}, \tag{4.16}$$

where $\mathbf{n}$ is the normal and $\mathbf{t}$ is the boundary traction. The boundary normal can be calculated using Nanson's equation expressed as

$$\mathbf{n} = \left(\bar{\mathbf{n}} \cdot \mathbf{C}^{-1}\,\bar{\mathbf{n}}\right)^{-\frac{1}{2}}\mathbf{F}^{-T}\bar{\mathbf{n}}\,. \tag{4.17}$$

where $\bar{\mathbf{n}}$ is the boundary normal in the reference configuration and $\mathbf{C}$ is right Cauchy-Green deformation tensor. Equations (4.12) and (4.16) together with the evolution of remodeling (4.10) form the governing equations. In the next section, we discuss the solution procedure.

4.2.3 Theoretical study of tumor remodelling

The evolution of remodeling and the governing equation for the stress were presented in the previous section. In this section, we extend the correlation between the remodeling and the nutrient distribution. To that end, it is necessary to associate configuration stress $\mathbf{S}$ with the effect of external stimuli.

Gradient of biochemicals such as nutrient and chemo- attractants are among the important biological stimuli that can evoke tumor response. For instance, in chemotaxis, cells change their morphology, break E-cadherin junctions and move toward the gradient of chemo-attractant [146]. Another example is the ability of tumors to remodel their shape in response to external forces that relieves the stress and preserves the homeostatic equilibrium state [55]. A tumor, that is deprived from sufficient nutrients can expand its boundaries by remodeling the microstructure (i.e. binding and unbinding the inter- and intra-cellular junctions) in favor of reaching

new source. Here, we propose that the gradient of nutrient is the main property of nutrient distribution that governs the remodeling. Hence, we take the characteristic tensor associated to the biochemical stimuli in the spatial configuration to be aligned with gradient of nutrients in the form

$$\mathbf{s} = \operatorname{grad} c \otimes \operatorname{grad} c\,, \tag{4.18}$$

where c is the nutrients concentration. The pullback of this stimuli into the natural configuration is

$$\mathbf{S} = J\mathbf{F}_e^T\,\mathbf{s}\,\mathbf{F}_e^{-T}\,. \tag{4.19}$$

Here we take the evolution of the remodeling to be isotropic, that is, the remodeling is aliened with the stimuli $(\mathbf{M} + \rho\mathbf{S})$

$$\mathbb{K} = a\mathbb{I}\,, \tag{4.20}$$

where $a \geq 0$ determines the intensity of stimuli that drives the evolution of the remodeling. Also, this equation shows that the remodeling tensor is aligned with the tensor of stimuli, and $\mathbb{I}$ is the forth order identity. We further assume that there is a constant supply of nutrients and the time scale of the nutrient diffusion is much faster then the evolution of the tumor. Therefore, we take the nutrients field to be time-independent.

Here, we use the mathematical model presented in section 4.2.2 to study the remodeling of tumor spheroids in response to gradient of external stimuli that is generated using tumor-on-a-chip platform. For simplicity, we consider two-dimensional geometry subjected to gradient of nutrients. The tumor is initially circular, hence $\mathbf{X} = R\hat{\mathbf{E}}_R\,(\Theta)$, where $\{R, \Theta\}$ and $\{\mathbf{E}_R, \mathbf{E}_\Theta\}$ are standard polar coordinates and basis in referential configuration, respectively. The position vector in the spatial configuration, i.e. deformed tumor, is $\mathbf{x} = r\,\hat{\mathbf{e}}_r(\theta)$, where $\{r, \theta\}$ and $\{\mathbf{e}_r, \mathbf{e}_\theta\}$ are standard polar coordinates and basis in spatial configuration, respectively. Note that $r(R, \Theta, t)$ and $\theta(R, \Theta, t)$ are invertible mappings between the referential and spatial configurations. It follows that the deformation gradient $\mathbf{F} = \operatorname{Grad}\mathbf{x}$ and the left and right Cauchy-Green deformation tensors read

$$\mathbf{F} = r_{,R}\,\mathbf{e}_r \otimes \mathbf{E}_R + r\,\theta_{,R}\,\mathbf{e}_\theta \otimes \mathbf{E}_R + \frac{1}{R}\,(r_{,\Theta}\,\mathbf{e}_r + r\,\theta_{,\Theta}\,\mathbf{e}_\theta) \otimes \mathbf{E}_\Theta\,, \tag{4.21}$$

$$\mathbf{C} = \mathbf{F}^T\mathbf{F} = \left(r_{,R}^2 + (r\,\theta_{,R})^2\right)\mathbf{E}_R \otimes \mathbf{E}_R + \left((\frac{1}{R}\,r_{,\Theta})^2 + (\frac{r}{R}\,\theta_{,\Theta})^2\right)\,\mathbf{E}_\Theta \otimes \mathbf{E}_\Theta + \left(\frac{1}{R}\,r_{,R}\,r_{,\Theta} + \frac{r^2}{R}\,\theta_{,R}\,\theta_{,\Theta}\right)\,(\mathbf{E}_R \otimes \mathbf{E}_\Theta + \mathbf{E}_\Theta \otimes \mathbf{E}_R)\,, \tag{4.22}$$

$$\mathbf{B} = \mathbf{F}\mathbf{F}^T = \left(r_{,R}^2 + \frac{1}{R}\,(r_{,\Theta})^2\right)\mathbf{e}_r \otimes \mathbf{e}_r + \left((r\,\theta_{,R})^2 + (\frac{r}{R}\,\theta_{,\Theta})^2\right)\,\mathbf{e}_\theta \otimes \mathbf{e}_\theta + \left(\frac{1}{R}\,r_{,R}\,r_{,\Theta} + \frac{r^2}{R}\,\theta_{,R}\,\theta_{,\Theta}\right)\,(\mathbf{e}_r \otimes \mathbf{e}_\theta + \mathbf{e}_\theta \otimes \mathbf{e}_r)\,, \tag{4.23}$$

where the subscript comma represents the partial derivative with respect to the argument. Expressing the velocity and acceleration in polar coordinates as

$$\mathbf{v} = r_{,t}\mathbf{e}_r + r\theta_{,t}\mathbf{e}_\theta\,,\ \mathbf{v}_{,t} = \left(r_{,tt} - r(\theta_{,t})^2\right)\mathbf{e}_r + (r\theta_{,t} + 2r_{,t}\theta_{,t})\,\mathbf{e}_\theta\,, \tag{4.24}$$

the Piola stress and it's divergence has the form

$$\mathbf{\Pi} = \Pi_{rr}\mathbf{e}_r \otimes \mathbf{e}_r + \Pi_{r\theta}\mathbf{e}_r \otimes \mathbf{e}_\theta + \Pi_{\theta r}\mathbf{e}_\theta \otimes \mathbf{e}_r + \Pi_{\theta\theta}\mathbf{e}_\theta \otimes \mathbf{e}_\theta\,, \tag{4.25a}$$

$$\mathrm{Div}\,\mathbf{\Pi} = \left(\Pi_{rr,_r} + \frac{1}{r}\left(\Pi_{\theta r,_\theta} + \Pi_{rr} - \Pi_{\theta\theta}\right)\right)\mathbf{e}_r + \left(\Pi_{r\theta,_r} + \frac{1}{r}\left(\Pi_{\theta\theta,_\theta} + \Pi_{r\theta} + \Pi_{\theta r}\right)\right)\mathbf{e}_\theta\,. \tag{4.25b}$$

The interaction between the tumor and the surrounding tissue defines the boundary condition for (4.12). Here, we simplify this interaction by considering uniform pressure

$$\mathbf{T}\,\mathbf{n} = -p_0\mathbf{n}, \tag{4.26}$$

where p_0 is the pressure due to the interaction between the tumor and the surrounding tissue, and $\mathbf{n}$ is the normal to the boundary in spatial configuration. This simplification is valid when the surrounding tissue is much softer and its size is larger than the tumor such that their interface is not affected by the outer boundary of the tissue.

The governing equations are the balance of linear momentum and the evolution of the remodeling. The balance of linear momentum is obtained by substitution of (4.14), (4.15), (4.23) and (4.25b) into (4.12), and the evolution of the remodeling is obtained by substitution of (4.4), (4.19) into (4.10). The associated initial conditions are taken as

$$\mathbf{P}^i = \mathbf{I}\,,\ \mathbf{T}^i = -p_0\mathbf{I}\,,\ \mathbf{v}^i = \mathbf{0}\,, \tag{4.27}$$

and the boundary conditions are (4.16), where we take p_0 to be uniform and time independent. The system of nonlinear equations are solved numerically using the finite differences method. The referential two dimensional domain is discretized uniformly in radial and angular directions. The numerical solution algorithm starts from a system in equilibrium, such that the stress field is homogeneous with $\mathbf{T}^i = -p_0\mathbf{I}$, which gives rise to initial uniform elastic deformation $\mathbf{F}_e^i$, and $\mathbf{F} = \mathbf{F}_e^i$. The Mandel stress (4.4) and the Piola stress (4.15) are calculated, accordingly. Next, the configuration and the remodeling fields are integrated by (4.12) and (4.10) respectively using explicit forward Euler integration. Convergence of the solution was verified by a sequence of grid refinements. This process is repeated to obtain the time integration of reconfiguration and remodeling processes. The model predictions for different nutrient fields in presented in the next section.

4.3 Results

In this section, we investigate the effect of nutrient distribution on the deformation and remodeling of the tumor. For convenient we use both Cartesian and Polar coordinates to express the nutrient distribution and thus the gradient. The use of Cartesian coordinates gives better understanding of the way such distributions, or gradients, of nutrient can be practically obtained by experiment. We considered two types of nutrient distributions; linear (c_1) and quadratic (c_2) distributions in the x direction. This practically resembles the gradient of nutrients along the microfluidic channels of tumoroid-on-a-chip platforms.

$$c_1 = \sqrt{\alpha}\,\bar{x} + c_0, \qquad \mathbf{s_1} = \alpha\,\boldsymbol{i}\otimes\boldsymbol{i}\,, \tag{4.28a}$$

$$c_2 = \frac{\sqrt{\alpha}}{2}\,\bar{x}^2 + c_0, \qquad \mathbf{s_2} = \alpha\,\bar{x}\,\boldsymbol{i}\otimes\boldsymbol{i}\,, \tag{4.28b}$$

where $\bar{x} = x/R_0$ is normalized length measured from the center of tumor where the nutrient concentration is c_0, $\boldsymbol{i}$ is unit vector in x direction, α is the remodeling coefficient and R_0 is the initial tumor radius. The corresponded representations in

polar coordinates are

$$\mathbf{s_1} = \alpha \left[\left(\cos^2\theta\right)\, \mathbf{e}_r \otimes \mathbf{e}_r + \left(\sin^2\theta\right)\, \mathbf{e}_\theta \otimes \mathbf{e}_\theta - \frac{\sin 2\theta}{2}(\mathbf{e}_r \otimes \mathbf{e}_\theta + \mathbf{e}_\theta \otimes \mathbf{e}_r) \right], \tag{4.29a}$$

$$\mathbf{s_2} = \alpha \bar{r}^2 \left[\left(\cos^4\theta\right)\, \mathbf{e}_r \otimes \mathbf{e}_r + \left(\frac{\sin^2 2\theta}{4}\right)\, \mathbf{e}_\theta \otimes \mathbf{e}_\theta - \frac{\cos^2\theta \sin 2\theta}{2}(\mathbf{e}_r \otimes \mathbf{e}_\theta + \mathbf{e}_\theta \otimes \mathbf{e}_r) \right], \tag{4.29b}$$

where $\bar{r} = r/R_0$. These two cases can approximately represent two setups commonly used in tumor-on-a-chip microfluidic devices. The linear nutrient distribution (4.28a) represents setup with source and sink reservoirs at the two ends of the channel, while the quadratic distribution (4.28b) represents setup with two source reservoirs at the two ends of the channel with a constant sink in the middle. Equations (4.29) are substituted in (4.10) to find the evolution of $\mathbf{P}$. Figure 4.2 shows the simulation results of the deformed boundary of tumor and the ratios of R_{max}/R_{min} for different values of α in both linear and quadratic distributions of nutrients. Note that R_{max} and R_{min} are the vertex (radius of major axis) and the co-vertex (radius of minor axis) of the ellipsoidal geometry of the deformed tumor, respectively. We scale the time by the remodelling coefficient a to obtain the intrinsic remodeling characterization $\bar{t} = \rho a t$ s^2/cm and used the following values for Lama's constants, $\lambda = 0.12$ N/cm^2 and $\mu = 0.19$ N/cm^2 and density, $\rho_0 = 0.01$ kg/cm^3 [147]. As for the boundary pressure, we studied two cases. First, we set the boundary pressure $p_0 = 0$ N/cm^2 to look into only residual stresses developed in the tumor due to remodeling.

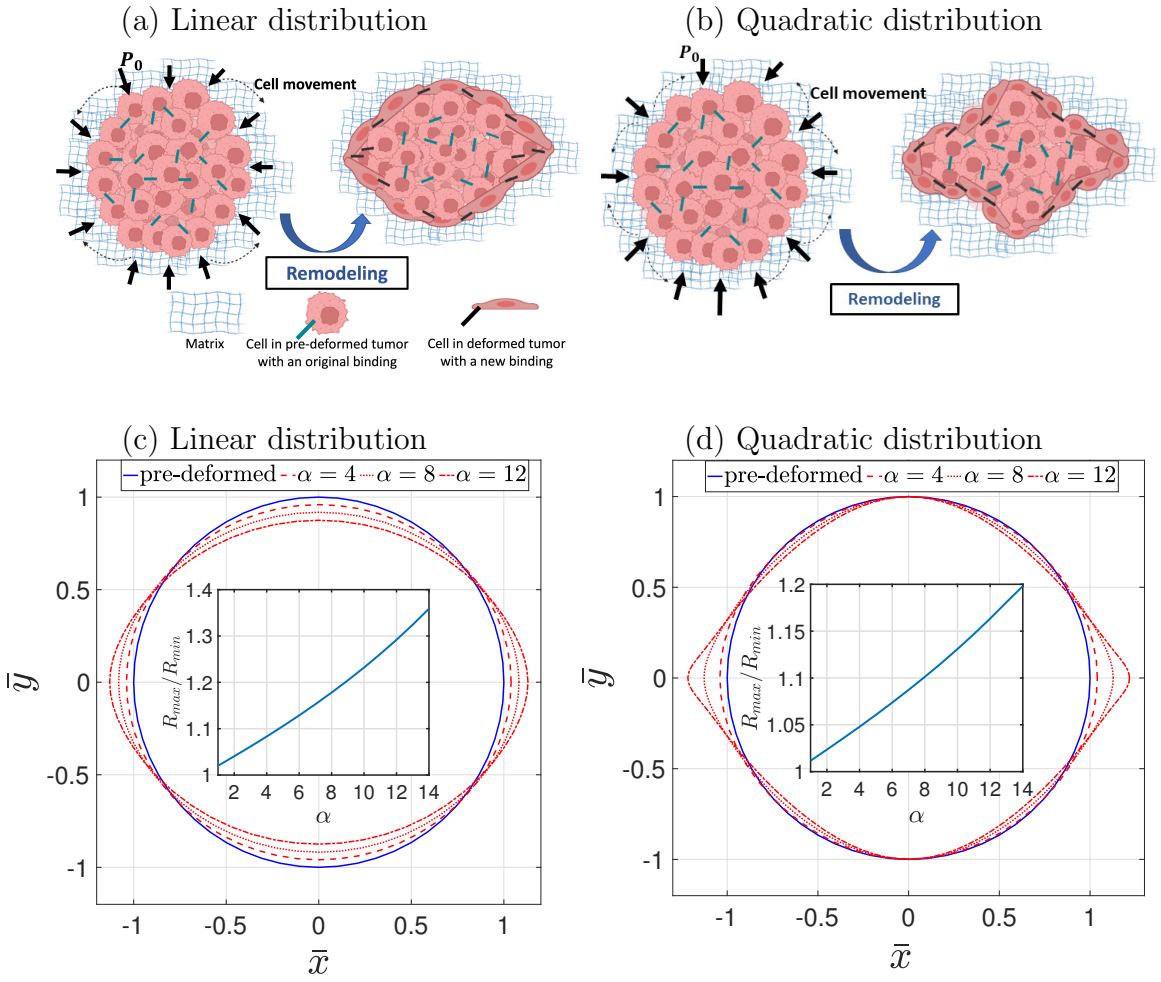

Figure 4.2: Deformation of tumor under gradient of nutrients. Schematic representation of the remodeling in linear distribution of nutrients (a), which lead to ellipsoidal geometry, and quadratic distribution (b), which gives rise to irregular ellipsoidal geometry. The corresponding results of theory for $\alpha = \{4, 8, 12\}$, $p_0 = 0$ and $\bar{t} = 1.5 \times 10^{-4}\text{s}^2/\text{cm}$ are shown in (c) and (d). The inset graphs show the ratios of vertex to covertex R_{max}/R_{min} for range of α. The rate of remodeling is shown to increase with nutrient concentration in both types distributions.

The remodeling occurs when cancer cells at the outer layer of tumor acquire elongated morphology and change their local cell-cell and cell-matrix bindings, Figure 4.2 (a) and (b). This heterogeneity in cells behaviour exhibiting circumferentially aligned cells was shown to be correlated with the mechanical stress field [148]. As can be seen in Figure 4.2 (c) and (d), the presents of nutrient enhance remolding, that is, the rate of remodeling increases with nutrient concentration for both linear and quadratic distributions. However, the shapes of the tumours are different for the two cases. In

linear distribution, the spherical tumour remodels into an ellipsoidal shape, where extension and perpendicular contraction occur along the vertex and covertex, respectively. In quadratic distribution, spherical tumour remodels into a irregular ellipsoidal shape with sharper edges along the vertex and no deformation along the covertex. These differences are contributed to the different remodeling fields which are proportional to nutrient gradient, hence, for the linear case, the remodeling is homogeneous, while for the quadratic distribution, the remodeling is inhomogeneous and increasing with $|\bar{x}|$. The ratio of R_{max}/R_{min} is also depicted in this figure for a range of α where the linear distribution imposes larger ratios compared to the quadratic. This is also supported by the analysis of the residual stress developed in the tumor due to remodeling. Figure 4.3 depicts the pressure p and the magnitude of shear stress τ evaluated by

$$p = -\frac{1}{2}\left(\mathbf{T}\cdot\mathbf{I}\right) \tag{4.30a}$$

$$\tau = \sqrt{\boldsymbol{\tau}\cdot\boldsymbol{\tau}}\,, \tag{4.30b}$$

where $\boldsymbol{\tau} = \mathbf{T} + p\mathbf{I}$ is deviatoric part of the stress tensor. The pressure and the shear stress are invariant measures of the stress and are known to be mechanical stimuli that induce biological responses such as autophagy [149] . It has been observed that direct compression of cancer cells can affect gene expression, hence alter the tumor invasiveness, rate of cancer cell proliferation and death. Shear stress, on the other hand, has less effect on the growth rate, but alters autophagy and apoptosis. Readers are referred to [149] for details of the role of different types of stresses on cell behaviour and the associated signaling mechanochemical pathways. Figure 4.3 shows that for the linear distribution of nutrients the stress is homogeneous indicating homogeneous remodeling due to constant gradient of nutrients. However, for the quadratic case, the stress is inhomogeneous where limited remodeling occurs about the co-vertex, $\bar{x} = 0$, and yields vanishing stresses around that region. This is due to zero gradient of nutrients across the co-vertex. On the other hand, stress concentration is observed at the vertex edges indicating significant local remodeling due to the local increase in the gradient of nutrients. Moreover, the vertex edges are sharper due to the high gradient of nutrients.

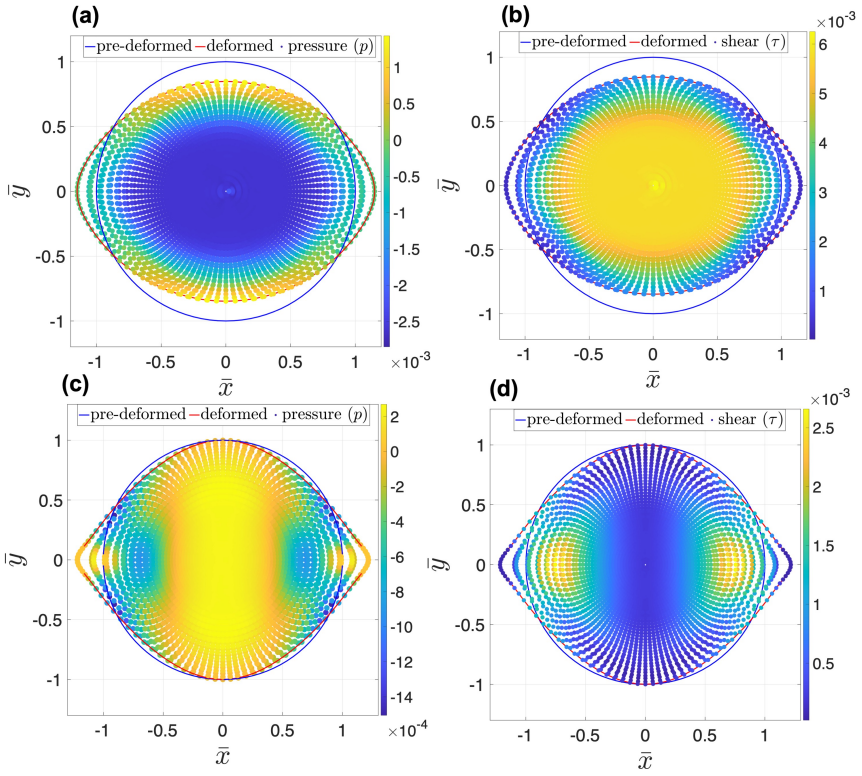

Figure 4.3: Distribution of residual pressure p and shear τ developed in the deformed body of tumor due to remodeling and in response to linear and quadratic distributions of nutrients, for $\alpha = 12$, $p_0 = 0$ and $\bar{t} = 1.5 \times 10^{-4}\text{s}^2/\text{cm}$. Stress distributions are mostly homogeneous in linear nutrient distribution, indicating homogeneous remodeling. In quadratic distribution of nutrient, the stress distribution is inhomogeneous, vanishing around the covertex region. However, stress concentration is observed at the vertex edges indicating significant local remodeling.

Next, we looked into non-zero pressure boundary condition. The interaction between tumor and the surrounding tissue is an important source of mechanical stresses that can trigger biological mechanisms. Different types of tumors, and their surrounding tissues, have different mechanical properties. For instance, human colon adenocarcinoma, glioblastoma and osteosarcoma are types of solid tumors with different mechanical stiffnesses [150]. Besides, acute myeloid leukemia (AML) is generally considered a liquid tumor. The interaction at the interface of tumor and tissue gives rise to stresses inside the tumor. To model a realistic boundary condition, one may model the tissue as a hyperplastic material similar to the tumor, and consider appropriate interaction between the tumor and the tissue, such as zero jumps in displacement and traction across the interface. Here, we simplify this interaction by considering a uniform pressure on the boundary of a tumor. Figure 4.4 shows the radial, tangential

and shear stresses developed in the deformed body of tumor in response to linear and quadratic distributions of nutrients and in presence of constant boundary pressure. In linear nutrient distribution, the radial and tangential stresses are maximum along the covertex and vertex, respectively. The shear stress is maximum along the diagonals. However, in quadratic nutrient distribution, both radial and tangential stresses are maximum around the edges of the covertex where the nutrient gradient is maximum, and zero along the vertex where nutrient gradient is zero. Also, the shear stress is maximum at the edges of the diagonals. As can be seen, the nutrient distribution strongly changes the pattern of stress distributions.

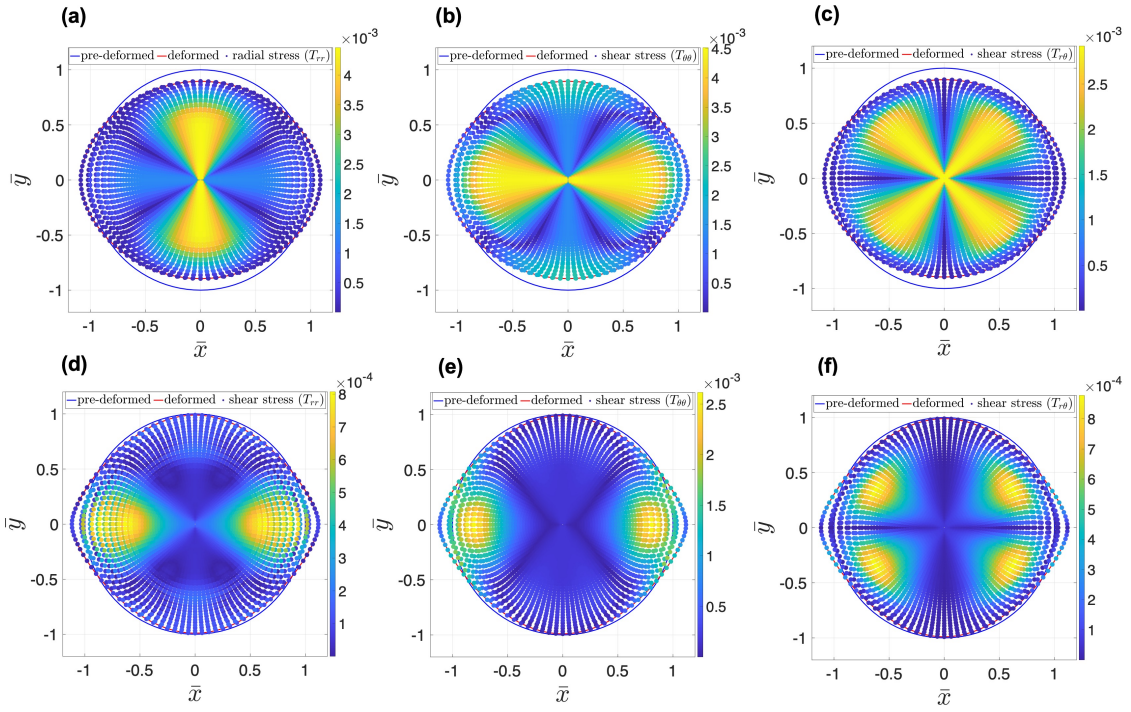

Figure 4.4: Distribution of radial T_{rr}, tangential $T_{\theta\theta}$ and shear $T_{r\theta}$ stresses in deformed body of tumor in response to linear and quadratic distribution of nutrients, for $\alpha = 12$, $p_0 = 0.001$ and $\bar{t} = 1.5 \times 10^{-4}\text{s}^2/\text{cm}$. Radial and tangential stresses are maximum along the covertex and vertex, respectively, in linear nutrient distribution. However, the shear stress is maximum along the diagonals. In quadratic nutrient distribution, both radial and tangential stresses are maximum around the edges of the covertex where the nutrient gradient is maximum, and zero along the vertex where nutrient gradient is zero. Similar to the linear distribution, maximum shear stress in quadratic distribution is seen along the diagonals but only at the edges.

To evaluate the presented theory and simulation results, we designed an experimental model to resemble tumor remodeling. Glioblastoma (GB) multiforme was

selected to investigate the remodeling capability. GB multiforme accounts for 47.1% of malignant tumors in the central nervous system [151]. Highly malignant GB tumors grow and spread rapidly in the CNS and hence significantly affects the patient's physical and cognitive abilities [152]. The importance of better understanding their biomechanical responses makes them a proper candidate for remodeling analysis. To investigate the remodelling behaviour of the GB tumoroids in response to biochemical stimuli, an in-vitro GB tumoroid-on-a-chip model was designed and fabricated. GB tumoroids were generated using EZ-seed culture plate, Figure 4.5(a-1) and (a-2). We used an extrusion 3D bioprinter and printable PDMS resin to fabricate a microfluidic chip with three compartments including a central tumor chamber, where the GB tumoroid-embedded CH was injected, and the two side chambers as the nutrient source and sink reservoirs, as shown in Figure 4.5(b-1). The chip was capable of generating gradient of biochemicals and incorporates GB tumoroids embedded inside the hyaluronic acid (HA)/alginate composite hydrogel (CH) [153]. We replaced matrigel with HA to avoid the common finger-type invasion of the GB tumoroids, while providing freedom for tumor remodeling within the ECM. The difference between the volume of chambers guarantees the gradient of biochemical through the central chamber. As the platform had no control on producing different types of gradient, we focused on generating different levels of gradient for which we fabricated short and long diffusion channels inside the tumor chamber, shown in Figure 4.5(b-2) and (b-3), respectively. Chamber with longer channels can contain more amount and CH, leading to longer diffusion length and hence higher gradient of nutrient. To evaluate the diffusion rate and the generated gradient, the transport profile of fluorescein isothiocyanate-Dextran, (FITC-Dextran, 20 kDa), was measured in both chips. FITC-Dextran solution (1 mg/mL in PBS) was added to the source chambers while the sink chambers were filled with only PBS Figure 4.5(c-1) and (c-2). To quantify the overall diffusion, 20μL of the sink chambers were sampled every two hours and the fluorescent intensity of the diffused FITC was measured using Nano plate reader. The change in the concentration of FITC over 48h is shown in Figure 4.5(d). As can be seen, higher concentration of FITC was diffused in low gradient chip, while the high gradient chip allowed less diffusion but sustained higher level of gradient.

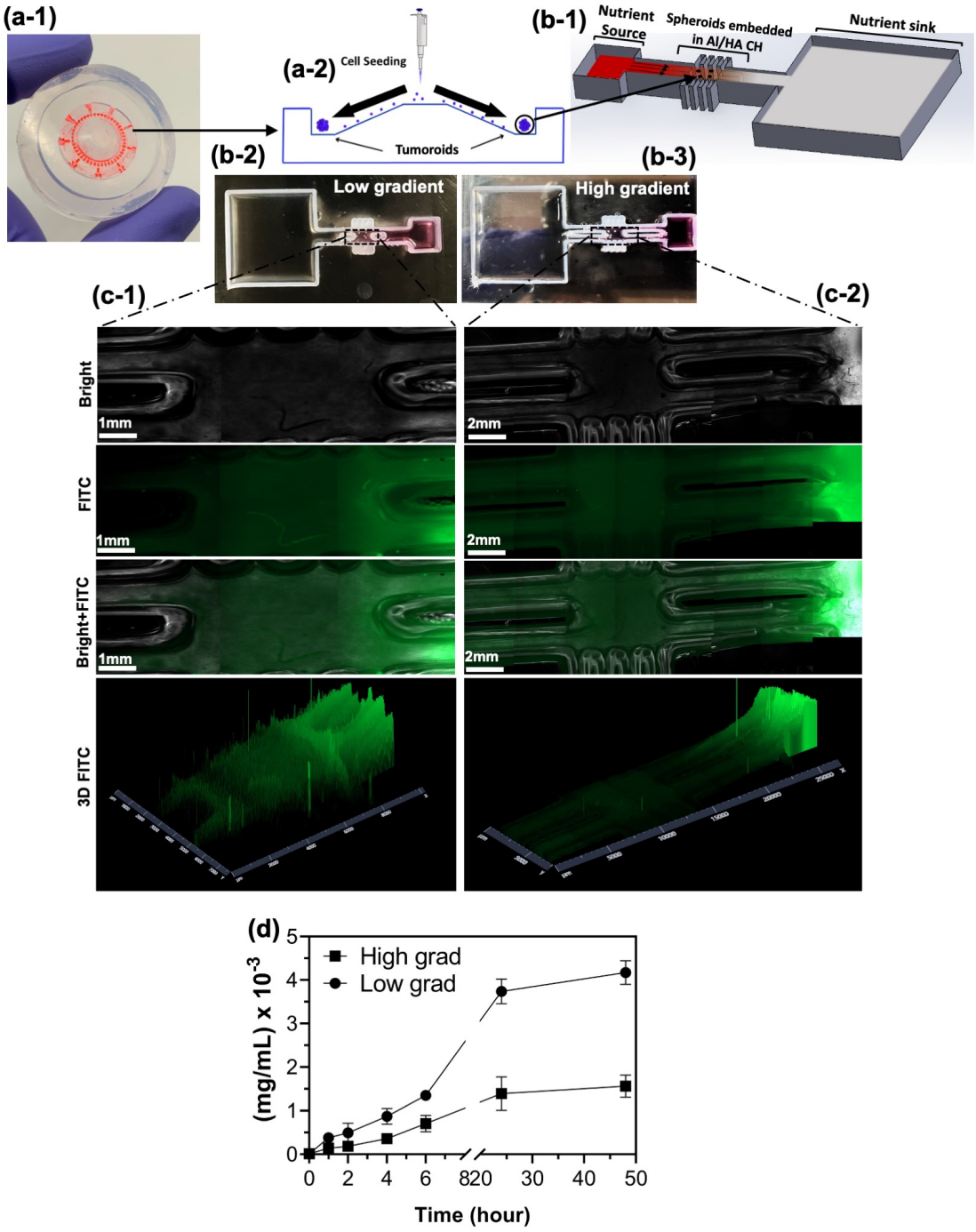

Figure 4.5: EZ-seed culture plate (a-1) and the schematic of the microwells (a-2) are shown. GB tumoroids were generated by seeding single cell suspension in the microwell array. The schematic of open-surface tumoroid-on-a-chip model that induces gradient of biochemicals is shown in (b-1). The chip consists of a central chamber for the GB tumoroid-embedded CH connected to a sink and a source reservoirs. To generate high and low gradients, short (b-2) and long (b-3) channels were designed to vary the diffusion length. Diffusion of FITC through the CH in channels was imaged, (c-1) and (c-2), and measured over time, (d), indicating lower diffusion (higher gradient) in long channels and higher diffusion (lower gradient) in short channels.

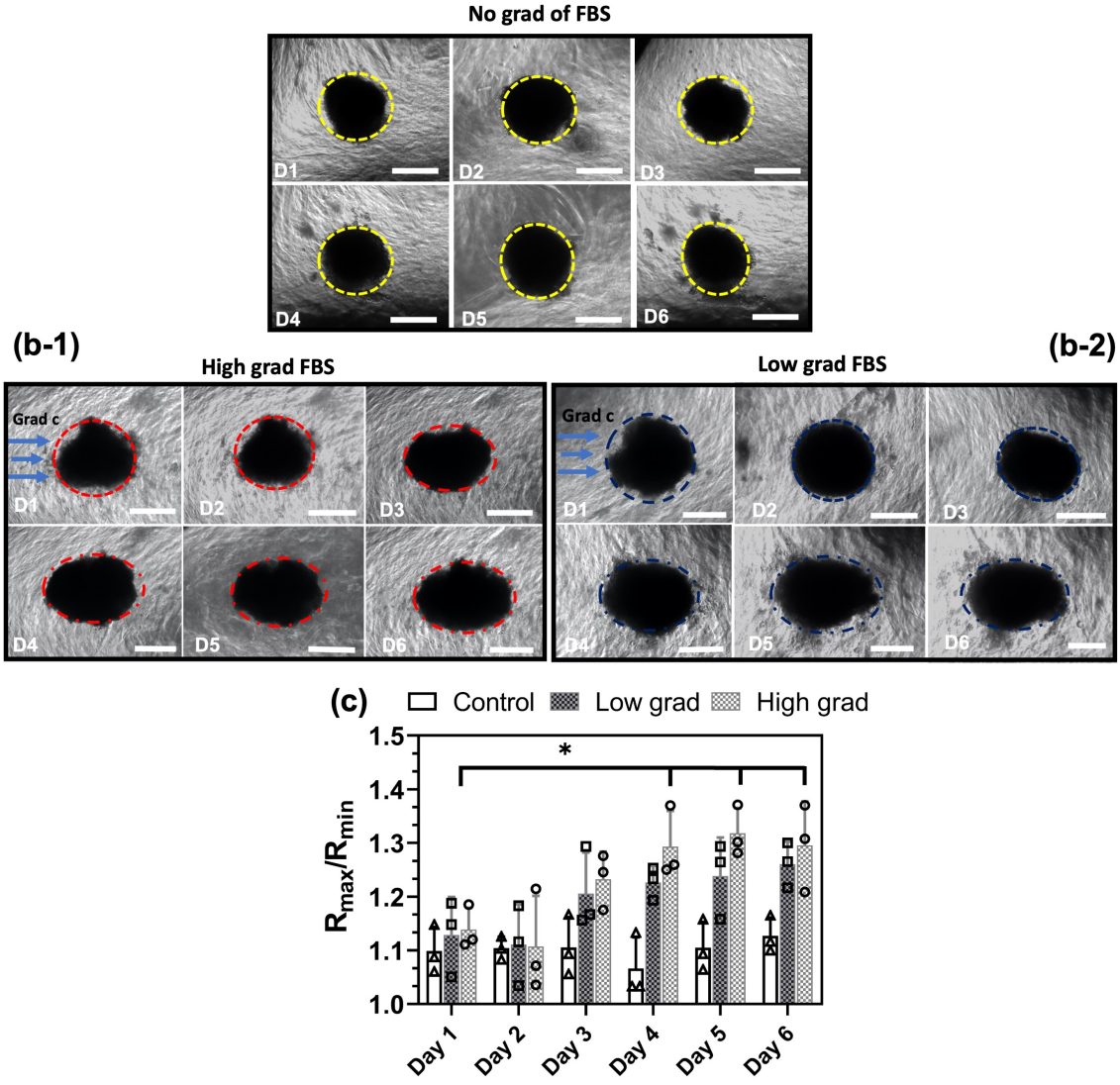

Figure 4.6: Asymmetric remodeling of GB tumoroids in response to high gradient (b-1) and low gradient (b-2) of FBS was imaged over 6 days and compared with the control (a). Spherical tumoroids remodeled to ellipsoidal shapes along the direction of FBS gradient. Measurement of vertex to covertex ratios R_{max}/R_{min} of tumoroids indicated that higher gradient gives rise to higher levels of remodeling (c). Scale bares are 200μm.

Figure 4.6 depicts the remodeling of tumoroids in response to the zero (a), high (b-1) and low (b-2) gradients of FBS. A chip with source and sink chambers of the same size, both filled with the same concentration of FBS and saturated CH with the diffused FBS was used as a control. Tumoroids were imaged over 6 days and the vortex to co-vortex ratios (R_{max}/R_{min}) were measured (c). As can be seen, tumoroids

were able to respond to the gradient of FBS and undergo remodeling configuration. Higher gradient of FBS (high gradient *vs.* low gradient chip) gave rise to higher ratios (R_{max}/R_{min}) indicating that gradient of nutrient is indeed the characteristic property of the biochemical stimuli.

To investigate the effect of remodeling on cell distribution within tumoroids, IHC technique was used to stain the interior part of tumoroids. Figure 4.7 shows the cross-

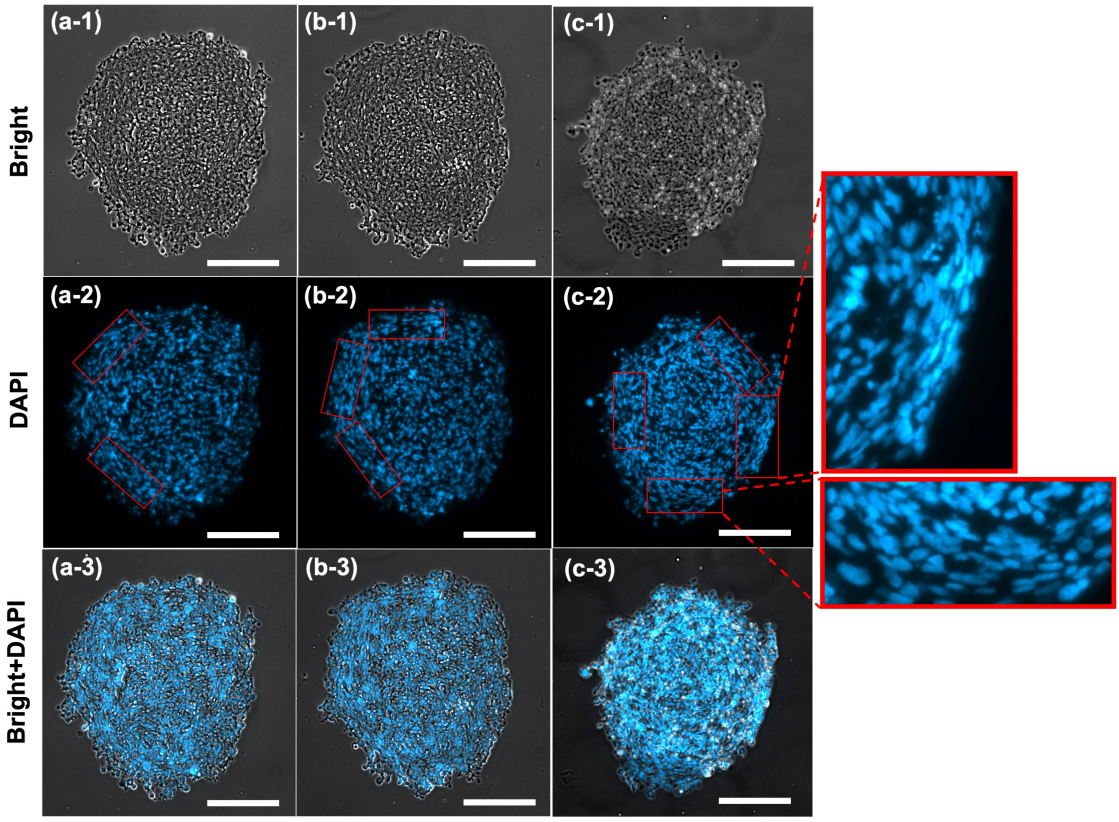

Figure 4.7: Remodeling gives rise to heterogeneity in cell distribution within tumoroids. Cells alignment in cross sections of GB tumoroids with low (a) to high (c) degrees of ellipticity. More alignment zones were observed in (c) indicating the correlation between the degree of remodeling and level of cell alignment. Higher alignments were identified at the circumferential regions of tumoroids where the cells undergo larger displacement and hence tend to further align with themselves. Cells in interior regions have no alignment preference, therefore, acquire isotropic orientation. Scale bars are 200μm

sections of three tumoroids with different degrees of ellipticity due to remodeling. The tumoroid with higher degree of ellipticity (c) contained more circumferentially aligned cells compared to less ellipsoidal tumoroid in (a) and (b). These cells undergo

larger displacement compared to the interior cells, predicted by model and shown in Figure 4.2(c) and (d), as the tumoroid remodels to an ellipsoidal shape. This is depicted in the magnified zones marked by red boxes which qualitatively show the correlation between the degree of remodeling and level of cell alignment. Due to the movement schematically illustrated in Figure 4.2(a) and (b), these cells tend to align with themselves as the remodeling takes place. This pattern identifies a heterogeneity in cell distribution that is corresponded to the remodeling in response to the gradient of biochemical stimuli.

4.4 Discussion

In this work, we studied asymmetric remodeling of tumor in response to biomechanical stimuli. We considered the tumor body as a simple evolving material, i.e. defined by their strain energy function, with a volume-preserving isotropic remodeling evolution. A characteristic tensor associated to the biomechanical stimuli, e.g. gradient of nutrient, was proposed that derives the remodeling. In this framework, principal balance laws were considered for tumor mass and linear momentum. As for the boundary conditions, we studied zero pressure, to investigate the residual stresses due to only the remodeling, and constant pressure to model the tumor-tissue interaction. Two types of nutrient distributions, linear and quadratic, were considered to explore the remodeling response. Results showed that the nutrient distribution strongly changes the remodeling and the stress distributions. Using the experimental platform, we were able to validate our hypothesis that the gradient of nutrient is the main characteristic of nutrient distribution in deriving the remodeling. In addition, we showed that the degree of remodeling is proportional to the magnitude of gradient. It was observed that the remodeled shape and the stress distribution are respectively ellipsoid and homogeneous, while irregular ellipsoid and in-homogeneous, in linear ad quadratic distributions of nutrient, respectively. To evaluate the model, an in-vitro open surface GB tumoroid-on-a-chip platform was designed and fabricated. Tumoroids were embedded in a HA/alginate composite hydrogel, injected inside the chip and exposed to gradient of FBS. Results showed that tumoroids were influenced by the gradient of FBS and undergo asymmetric remodeling. Also, measurement of vertex to covertex ratios over time indicated that higher gradient of FBS induces higher degree of ellipticity. It was also observed that remodeling induced heterogeneity in cell alignment forming circumferentially aligned cells within the tumors. The presented

framework gives a new insight to better understanding the interrelationship between the mechanical stress and biological responses in tumors. Using the proposed model, we were able to study the role of gradient of nutrient, as one of the key factors influencing tumor progressions, on biomechanics of tumor including tumor deformation, asymmetric remodeling, and stress distribution. Future research directions include, but not limited to, experimental measurements of the correlation between the distribution of stresses and the biological responses, such as cell proliferation, autophagy and apoptosis, and calibration of model parameters, such a and p_0, using quantitative biological assays. Another promising research direction can be utilizing the proposed framework to study a more realistic model that includes heterogeneity in terms of cell population and phenotype, and ECM effects.

Acknowledgements: The authors acknowledge the BC Cancer Foundation and Canadian Foundation for Innovation (CFI) for supporting this work. We also acknowledge Apricell biotechnology for providing us with the chips.

Author contributions statement: Theory and simulation M.A. (Meitham Amereh) and B.N.; conceptualization, M.A. (Meitham Amereh) and M.A. (Mohsen Akbari); methodology (Meitham Amereh); resources, M.A. (Mohsen Akbari); writing—original draft preparation, M.A. (Meitham Amereh); writing—review and editing, M.A. (Meitham Amereh), B.N., and M.A. (Mohsen Akbari); supervision, B.N. and M.A. (Mohsen Akbari). All authors have read and agreed to the published version of the manuscript.

4.5 Methods

4.5.1 Cell and tumoroid culture

Human glioblastoma cancer cells (U251) were cultured in Dulbecco's Modified Eagle Medium (DMEM) supplemented with 10% (v/v) fetal bovine serum (FBS), and 1% (v/v) Penicillin/Streptomycin. The U251 cells were incubated at 37°C in a humidified atmosphere of 5% CO_2, and at 90% confluency were trypsinized with Gibco™ Trypsin-EDTA (0.5%) into a single cell suspension. The cell suspension was centrifuged at 300g (5 minutes). After removing the supernatant, cells were suspended in 1 mL of medium and counted using a standard hemocytometer. EZ-seed culture plate from Apricell biotechnology was used to generate U251 tumoroids. 500 μL of

1×10^6 cells/mL cell suspension was loaded dropwise through the guiding channels and was kept in an incubator for 10 minutes to let the cells fill the microwells. Afterwards, the culture medium was aspirated and exchanged with a new medium. U251 tumoroids were monitored over 4 days until the formation stage is completed and they start the volumetric growth with average diameter of 500 μm.

4.5.2 Tumoroid-on-a-chip model

To prepare the GB tumoroids embedded in CH, tumoroids were removed from SFMAs by gentle aspiration of the media from the loading zone of the microwell array and collected in a Petri dish. To make 500μL of CH, 62.5μL of 5mg/mL alginate, 200μL of 4mg/mL HA and 234.5μL of DMEM were mixed and crosslinked with 3μL of 1M $CaCl_2$. The CH solution was pipetted inside the central chamber of the microfluidic chips. GB Tumoroids in 2 uL media were pipetted inside the CH at the center of the tumor chambers. The source and sink reservoirs were filled with basal media. 10% FBS was added to the source chambers while the sink chambers were kept FBS-free. Every 24h the source chambers were refilled with fresh media containing 10% FBS and the sink chambers refilled with FBS-free media.

4.5.3 IHC staining

Tumoroids were fixed with 10% neutral buffered formalin for 45 minutes, washed twice with Dulbecco's phosphate-buffered saline (DPBS), embedded in 2% agarose solution and kept in room temperature for 30 min. Agarose-embedded tumoroids were dehydrated by 10 min of submerging in 70%, 90% and 100% ethanol, respectively, followed by twice submerging in 100% Xylene for 20 min. Samples were then embedded in melted paraffin wax for four hours and placed in cassette for sectioning. Paraffin blocks were then sliced to approximately 5μm thickness using microtome device and deparaffinized by two minutes wash with 100% Xylene, 100% ethanol, 90% ethanol and distilled water, respectively. Tumoroids sections were then counterstained with 4', 6-diamidino-2-phenylindole (DAPI) and imaged using fluorescent microscopy.

4.5.4 Statistical analysis

All experiments were repeated three times and the average and the standard deviation are reported. Significance analysis was performed using two-way ANOVA analysis.

Differences were considered statistically significant at P-value < 0.05.

4.6 Data availability

The datasets generated for the current study are available upon the publication.

Chapter 5

Mathematical Modeling of Spherical Shell-Type Pattern of Tumor Invasion

Contributions:
Meitham Amereh: Theory and simulation, conceptualization, methodology, formal analysis, writing—original draft preparation, writing—review and editing
Henning Struchtrup: Theory, conceptualization, methodology, formal analysis, writing—review and editing, supervision
Ben Nadler: Theory, conceptualization, methodology, formal analysis, writing—review and editing, supervision

Meitham Amereh, Henning Struchtrup, and Ben Nadler*
Department of Mechanical Engineering, University of Victoria, Victoria, BC, V8P 5C2, Canada (M.A.); struchtr@uvic.ca (H.S.)
*Correspondence: bnadler@uvic.ca; Tel.: +1-250-721-6050

Abstract

Cancer cell migration, as the principal element of tumor invasion, involves different cellular mechanisms. Various modes of cell migration including single and collective

Symmetry 2023, 15, 283. https://doi.org/10.3390/sym15020283 https://www.mdpi.com/journal/symmetry

motions contribute to the invasion patterns. The competition between adhesive cell–cell and cell–matrix forces is a key factor that determines such patterns. In this paper, we study a distinct shell-type mode of tumor invasion observed in brain and breast tumors. In this mode, cells at the outer layer of the tumor collectively move away from the core and form a shell-type shape. Both the core and the shell sustain a sharp interface between cells and the surrounding matrix. To model the preserved interface, we adopted a Cahn–Hilliard-type free energy relation with the contribution of the interfacial stress. This nonconvex form of free energy allows for cells to remain together and preserve the tumor core via adhesive cell–cell forces while separating the core from the surrounding matrix across a continuous sharp interface. In addition, the motion of the shell was modeled using the chemotactic migration of cells in response to the gradient of nutrients. The associated fluxes of cells were implemented in a general form of balance law. A non-Michaelis–Menten kinetics model was adopted for the proliferation rate of cells. The flux of nutrients was also modeled using a simple diffusion equation. The comparison between the model predictions and experimental observations indicates the ability of the model to manifest the salient features of the invasion pattern.
Keywords: tumor modeling; shell-type invasion; chemotaxis

5.1 Introduction

Cancer cell migration is the primary component of tumor invasion and metastasis, which are the main cause of death in patients [60]. Cell migration starts when cells attain a malignant morphology enabling them to detach the tumor body and move along the extracellular matrix (ECM) [61]. Cancer cell migration in three-dimensional tissue involves different cellular mechanisms; hence, various invasion patterns have been observed [62, 63]. In general, cancer cells show two main migration patterns in histological sections: single and collective. In single-cell migration, e.g., in breast cancer, cells break intercellular contacts and acquire mobility via either mesenchymal or amoeboid morphology.

Details of this invasion mode, the corresponding cell morphology characteristics, and the cellular mechanisms were reviewed in [64]. In collective cell migration, cells maintain intercellular adhesion and form an invading front sheet of cells that extend into the tissue and may or may not maintain their contact with the trailing cells and the primary tumor [65, 66]. This group of cohesive cells maintains polarity, and ex-

presses higher level of integrins and matrix metalloproteases (MMPs). Experimental studies using microfluidic platforms showed that the plasticity of tumor invasion modes depends on the tissue context, biochemical signals, and mechanical properties [154, 155]. Collective migration is evidenced by human cancer pathology as the primary pattern of invasion in most epithelial cancers [69]. The tumor microenvironment (TME) plays an important role in the invasion pattern [70]. For example, collagen IV stimulates collective migration, while fibronectin triggers single-cell migration [67, 68]. Collective migration can lead to a distinct pattern of invasion in which a cluster of cells start to break away from the tumor and form a precursor layer of moving cells. For instance, Koh et al. [1] showed that the ECM microenvironment can significantly impact patient-derived glioblastoma mutiforme (pdGBM) invasion and dissemination, as shown in Figure 5.1a. Another study, by Ling et al. [2], showed that altering cell–cell adhesion and contact in collagen-embedded MCF10AT1 cell-derived spheroids cocultured with adipose stromal cells (ASCs) isolated from human breast adipose tissue can lead to a collective invasion, shown in Figure 5.1b. These studies suggested that collective cell migration may give rise to a distinctive pattern of invasion in various types of tumors.

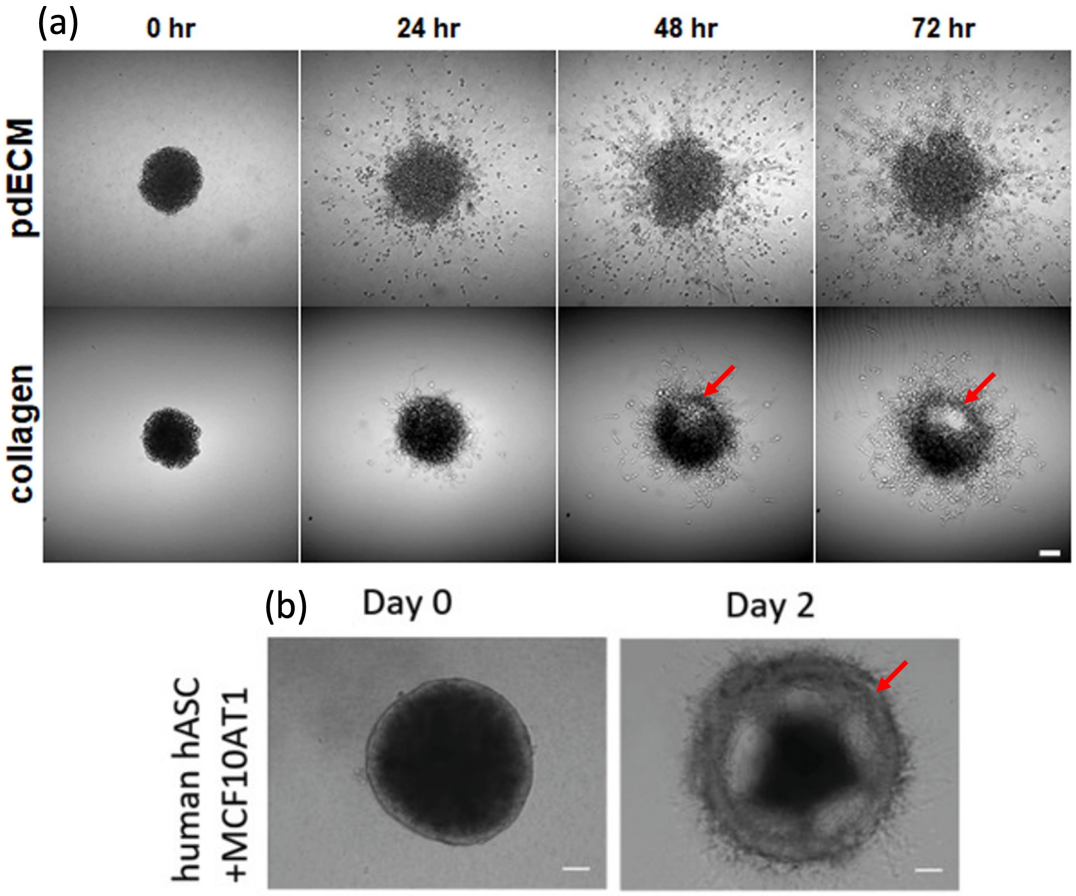

Figure 5.1: Three-dimensional tumor model to study tumor invasion and dissemination. (**a**) Invasion of patient-derived glioblastoma mutiforme (pdGBM) into patient-derived extracellular matrix (pdECM) and collagen; reproduced with permission [1]. PdECM facilitates the dissemination of cells into the matrix while collagen enhances the collective migration of cells. (**b**) Invasion of MCF10AT1 spheroids cocultured with patient-derived adipose stromal cells (ASCs) in collagen; reprinted with permission from [2]. 2020, John Wiley and Sons. Both cases show that the collective migration of cells led to the formation of a cluster of cells that preserved a distinct interface with the tumor core and the surrounding matrix, shown by red arrows.

The diversity of mechanisms involved in tumor invasion requires different areas of knowledge to contribute to the development of treatment strategies [71, 72]. Mathematical modeling can provide both qualitative and quantitative information to better understand the complex behavior of biological tissues, particularly tumors [156–158]. That information helps in interpreting the complicated interactions between tumors and their microenvironment. Tumor growth and invasion were mathematically studied from different perspectives: continuum, discrete, and hybrid (continuum-discrete)

[11]. Continuum models, which are typically built upon partial differential equations (PDEs) to determine the concentrations of cells and nutrients, showed acceptable agreement with experimental observations [106, 127, 128, 159]. These models correlate the growth and invasion with kinetic interactions between the key components, such as the rates of nutrient/oxygen consumption, cell proliferation, and diffusion for transport phenomena [16, 88]. The ability of tumors to maintain a compact aggregation of cells was modeled by introducing adhesive cell–cell forces [17]. Further studies investigated other factors, e.g., level of PH, to predict the growth and invasion of tumors [19, 160]. Other aspects of tumor progression, such as anisotropic growth and mechanical stress distribution, were also investigated in the framework of continuum mechanics [58, 129, 130, 161]. On the other hand, discrete mathematical modeling incorporates signaling pathways, and inter- and intracellular interactions in tumor progression.

These models are capable of predicting tumor progression at the subcellular level. For instance, a lattice Monte Carlo model was utilized to predict the dynamics of avascular tumor growth, and the effects of microenvironmental conditions and growth promoters/inhibitors on tumor cell survival [30]. Another example of discrete models is cellular automata (CA), which predict the collective behavior of self-organizing systems, such as tumors, by focusing on the interactions between the components [31].

To relate the cellular mechanisms with tissue-level responses, hybrid mathematical models integrate continuum and discrete approaches, and allow for descriptions of discrete cellular interactions together with macroscopic variables [11]. The effects of cellular pathways and interactions on the clinical-size morphology of tumors can be studied using hybrid models [37].

The results of these studies provide the prediction of various growth and invasion patterns, including the standard dissemination of cells, anisotropic growth, and asymmetric invasion, but are missing the exposition of the spherical-shell-type invasion pattern observed in breast and brain tumors.

Tumors exhibit different patterns of invasion, among which the spherical shell-type pattern is a distinct mode that is less studied. In this work, we study this unique mode of invasion in which cancer cells collectively migrate away from the tumor, forming the precursor layer of a moving shell. The interplay between cell–cell and cell–matrix adhesion allows for the shell and the tumor to develop and preserve sharp interfaces. To capture this, we adopted a nonconvex free energy that allowed for phase separation.

The motion of the shell was also modeled using chemotactic migration in response to the nutrient gradient. The role of various parameters in the invasion pattern, such as cell and nutrient diffusion, cell proliferation, and nutrient uptake, were investigated. The model was able to predict the formation and movement of the spherical shell pattern. The novelty of the presented work is in incorporating the interplay between cell–cell and cell–matrix adhesion using a nonconvex free energy in which the capillary stress allowed for a continuous transition between low and high concentrations across the interface

5.2 Model Formulation

Different forces may induce cell migration within a tumor microenvironment. A typical form of cell migration is due to the nonuniform distribution of cells within tumor aggregation, which governs uniform distribution via random motions. This form of cell migration is correlated to the gradient of concentration, and the corresponding cell flux may be obtained using a standard Fick's law relationship. In contrast, adhesive forces due to cell–cell and/or cell–matrix bindings prevent cell diffusion, hence maintaining the structure of a tumor. Another stimulus that may regulate cell migration either collectively or individually is the gradient of chemoattractants such as nutrients and growth factors. In this form of motion, cells break their cell–cell bindings, e.g., E-cadherin junctions, change their morphology, and move in response to the gradients of chemoattractants, so-called chemotaxis [146, 162]. The competition among diffusive, adhesive, and chemotactic forces determines the ultimate pattern of cell migration.

To model the contribution of different forces, we adopted a general form of balance equations for cells and nutrient concentrations,

$$\frac{\partial C}{\partial t} + \operatorname{div} \mathbf{J}_C = \zeta \,, \tag{5.1a}$$

$$\frac{\partial N}{\partial t} + \operatorname{div} \mathbf{J}_N = \eta \,, \tag{5.1b}$$

where C and N are the concentrations of cells and nutrients, i.e., mass per volume ($\mathrm{kg{\cdot}m^{-3}}$), $\mathbf{J}_C$ and $\mathbf{J}_N$ are the cell and nutrient fluxes ($\mathrm{kg{\cdot}m^{-2}{\cdot}\,s^{-1}}$), η is the rate of nutrient consumption ($\mathrm{kg{\cdot}m^{-3}{\cdot}\,s^{-1}}$), and ζ is the rate of cell proliferation ($\mathrm{kg{\cdot}m^{-3}{\cdot}\,s^{-1}}$).

The flux of nutrients in the tumor microenvironment can be described with a standard Fick's law equation. However, cell flux is mainly generated according to the interplay between diffusive and adhesive forces, and the directional motion due to chemotaxis. As observed in experimental studies, when cell–cell adhesive forces are dominant, tumors are able to maintain their compact structure, while highly invasive tumors could exhibit a long trace of cell migration [163]. In addition, the composition of the ECM surrounding the tumor is an important stimulus that may switch the invasion mode [1].

To account for the overall flux of cells, we considered a nonconvex form of free energy and a standard chemotactic model. The total flux of cells and nutrients can be expressed as follows:

$$\mathbf{J}_C = \mathbf{J}_f + \mathbf{J}_d \,, \tag{5.2a}$$

$$\mathbf{J}_N = -D_N \operatorname{grad} N \,, \tag{5.2b}$$

where $\mathbf{J}_f$ is the flux due to the free energy, $\mathbf{J}_d$ is the chemotactic flux and D_N is nutrient diffusivity coefficient. In the next section, we study both fluxes and present a full formulation for Equation (5.1).

5.2.1 Free Energy and Interfacial Flux

The pattern of invasion in Figure 5.1 shows that the tumor's sharp interface with the surrounding gel was sustained. The continuous transition from high to low concentrations across the interface required a distributed surface tension. The surface tension of the diffusive layer between the regions with different concentrations generated a form of capillary stress. This implies that the properties must depend on the interface contribution, i.e., $\Psi = (\operatorname{grad} \bar{C} \cdot \operatorname{grad} \bar{C})/2$, as proposed by Anderson et al. [164]. Hence, the free energy could take the form $f = \hat{f}(\bar{C}) + \check{f}(\Psi)$. We adopted a nonconvex form of free energy, similar to Cahn–Hilliard interfacial free energy [165], which allowed for phase separation:

$$f = \left(-\bar{C} + \bar{C}^2/10 - \bar{C}^3/6 + \bar{C}^4/12\right) + \beta\Psi \,, \tag{5.3}$$

in which $\bar{C}$ is the dimensionless cell concentration, and β is a coefficient related to the length of transition that should be determined on the basis of the nature of the interaction between the cells and the ECM. Other coefficients were selected

such that the corresponding flux retained two nontrivial roots as the equilibrium states in the domain $0 \leq \bar{C} \leq 1$. This form of free energy allows for cells to remain together and form the tumor body due to cell–cell adhesive forces with a continuous transition across the interface that could form a sharp edge and separate the tumor from the surrounding matrix. According to [164], the cell flux takes the following form:

$$\mathbf{J}_f = -D_f \operatorname{grad}\left[\frac{\partial f}{\partial \bar{C}} - \operatorname{div}\left(\frac{\partial f}{\partial \Psi} \operatorname{grad} \bar{C}\right)\right], \tag{5.4}$$

where D_f is a diffusion coefficient. We considered the isothermal process and neglected the dependency on temperature. The substitution of (5.3) into (5.4) yields

$$\mathbf{J}_f = -D_f \operatorname{grad}\left[\left(\frac{\bar{C}}{5} - \frac{\bar{C}^2}{2} + \frac{\bar{C}^3}{3}\right) - \beta \operatorname{div}\left(\operatorname{grad} \bar{C}\right)\right]. \tag{5.5}$$

The proposed form of free energy allows for an equilibrium state of separated phases, as the term $\partial \hat{f}/\partial \bar{C}$ in (5.4) had two extrema, and the corresponding flux function
$\hat{\mathbf{J}} = -D_f \operatorname{grad}(\partial \hat{f}/\partial \bar{C})$ had two nontrivial roots, as depicted in Figure 5.2a.

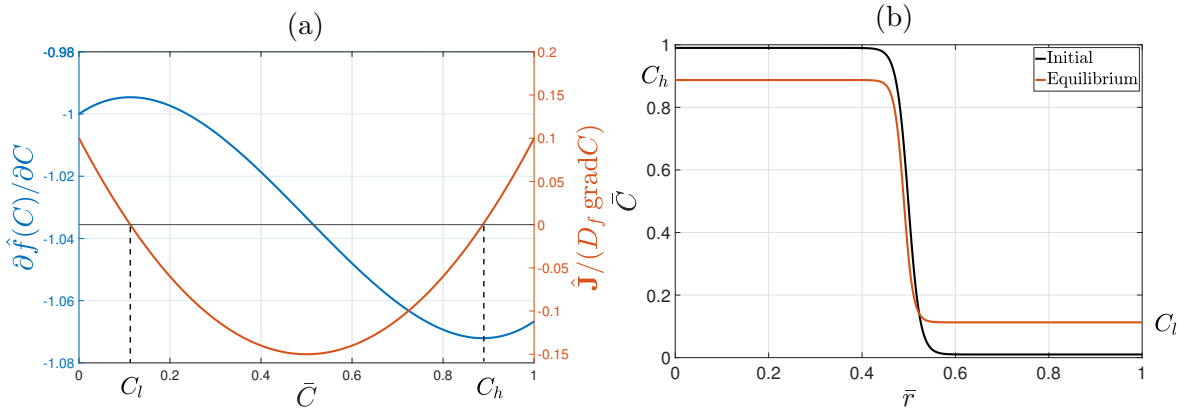

Figure 5.2: The equilibrium state of separated phases was acquired as $\partial \hat{f}/\partial \bar{C}$ and had two extrema, (**a**) left axis, and the corresponding flux function $\hat{\mathbf{J}} = -D_f \operatorname{grad}(\partial \hat{f}/\partial \bar{C})$ had two nontrivial roots, (**a**) right axis. This allowed for the coexistence of high C_h and low C_l concentrations with a continuous transition (**b**).

Cell distribution at equilibrium in the absence of nutrients is shown in Figure 5.2b. The initial distribution of cells, that is, the initial tumor consisting of a concentrated core and a sharp interface with the matrix, reached an equilibrium state of high C_h and low C_l concentrations coexisting with a continuous transition. The values of C_h

and C_l were determined on the basis of the coefficients in Equation (5.3).

Next, we describe the role of nutrients in cell proliferation and chemotactic flux.

5.2.2 Chemotactic Flux and Cell Proliferation

Cellular migration mechanisms depend on cell morphology and external stimuli. Invasive tumor cells become morphologically polarized and develop membrane protrusions, allowing for them to migrate forward, the so-called mesenchymal motion, when cells move via traction and adhesion to the ECM [166]. In addition, cells squeeze through the pores in the ECM, i.e., amoeboid motion, which is relatively fast and does not require strong cell–matrix adhesive forces [167]. Nutrients also play a significant role in inducing directional motion, i.e., chemotaxis [168]. Observations suggest that the gradient of nutrients is the characteristic property of nutrient distribution that can drive chemotaxis. Therefore, we adopted a simple form of the chemotactic flux:

$$\mathbf{J}_d = \mu C \operatorname{grad} N \,, \tag{5.6}$$

where μ is the chemotactic coefficient, and the flux was towards larger values of nutrient concentration. In addition, the rate of cell proliferation depends on the local concentrations of nutrients, as they are the main components of cellular metabolism and essential for cell growth. Cells nonlinearly consume nutrients, i.e., the higher the concentration of the supplied nutrient is, the higher the consumption rate and hence the higher the rate of proliferation, which saturates at a certain nutrient level. In addition to the nutrients, cells require intercellular proteins and enzymes for their growth. The local concentrations of these components are proportional to the concentration of cells. The cellular metabolisms in which nutrients and intercellular components are involved take place through cooperative enzymatic reactions [169]. Therefore, we adopted a non-Michaelis–Menten kinetics model for the proliferation rate ζ that included two substrates, nutrient N and cells C concentrations:

$$\zeta = V_{max} \frac{1}{1 + (k_1/C)^{c_1}} \frac{1}{1 + (k_2/N)^{c_2}} \,, \tag{5.7}$$

where V_{max} is the maximal (saturated) rate, k_1, k_2 are reaction constants, and c_1, and c_2 are the Hill coefficients. We took $c_1 = c_2 = c$ for the sake of simplicity. The nutrient consumption rate is also concentration-dependent. For simplicity, we took the linear form $\eta = \eta_0 CN$, where η_0 is the consumption coefficient.

5.2.3 Problem Statement

In vitro studies of tumors often involve using microfluidic chips comprising a main chamber for the tumor-embedded hydrogel and side channels to supply the nutrients, as shown in Figure 7.2. In such experiments, tumors are either mixed with the hydrogel and injected into the chamber or placed within the hydrogel already filling the chamber. In either case, the initial condition of tumors is essentially a compact aggregation of cells preserved by adhesive cell–cell forces that start responding to the matrix and the nutrient when placed inside the chamber. To simulate such a condition, we set the initial condition of cells to be a uniform axisymmetric spherical distribution that accounted for the tumor, followed by a sharp interface with the surrounding matrix. For nutrients, we took uniform initial concentration. The radius of the chamber R_∞ is typically much larger than that of tumor R_0; hence, we considered zero flux at the boundary, shown by $\mathbf{J}_c = \mathbf{0}$ in the figure. Nutrients are constantly and symmetrically provided via the microfluidic channels; therefore, we set a constant concentration of nutrient supply at the boundary, $N_0 = N_s$. The simulation was performed over a spherical domain, as shown in the figure.

5.2.4 Governing Equations

Balance Equations (5.1) can be expressed using dimensionless parameters. Scaling the distance with the domain radius R_∞, time with total time τ, and cell and nutrient concentrations with initial cell concentration C_0 and the nutrient source concentration N_s, respectively, yields

$$\frac{\partial \bar{C}}{\partial \bar{t}} = \alpha \operatorname{div}\left[\operatorname{grad}\left(\bar{f}(\bar{C}) - \bar{\beta}\operatorname{div}(\operatorname{grad}\bar{C})\right) - \gamma \bar{C}\operatorname{grad}\bar{N}\right] + \frac{\bar{V}}{(1+(\bar{k}_1/\bar{C})^c)(1+(\bar{k}_2/\bar{N})^c)}, \tag{5.8a}$$

$$\frac{\partial \bar{N}}{\partial \bar{t}} = \psi \operatorname{div}\left(\operatorname{grad}\bar{N}\right) - \bar{\eta}\,\bar{C}\bar{N}, \tag{5.8b}$$

with dimensionless parameters introduced as $\bar{C} = C/C_0, \bar{N} = N/N_s, \bar{t} = t/\tau, \bar{r} = r/R_\infty$, $\alpha = \tau D_f/R_\infty^2, \bar{\beta} = \beta R_\infty^2, \gamma = N_s\mu/D_f, \bar{V} = \tau V_{max}/C_0, \bar{k}_1 = k_1/C_0, \bar{k}_2 = k_2/N_s$, $\bar{f} = f/C_0$, $\psi = \tau D_n/R_\infty^2$ and $\bar{\eta} = \tau\eta_0 C_0$. Using spherical coordinates and assuming axisymmetric distributions, cell and nutrient concentrations were only a function of t and r. The system of equations presented in (5.8) was subjected to the initial and boundary conditions followed by Section 5.2.3. We took the uniform initial con-

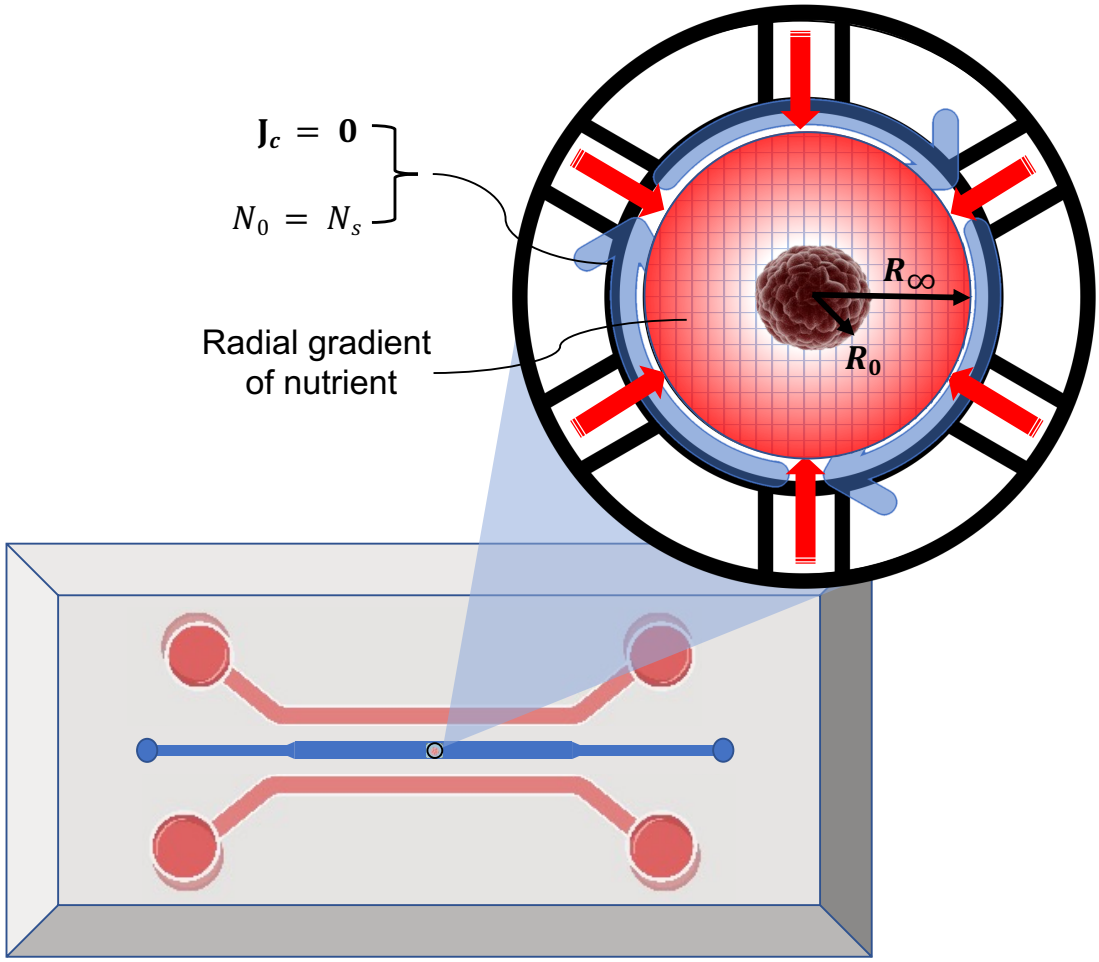

Figure 5.3: Schematic representation of a typical in vitro tumor platform used to study the growth and invasion of tumors. Tumor-embedded hydrogels were injected into the chamber of a microfluidic chip supplied with nutrients via microchannels that resembled the vasculatures. The size of the chip is typically in the order of a few centimeters, and the smallest dimension of the channels is around a few millimeters.

centrations of cells $C_0 = \text{const.}$ within R_∞ and $C_0 = 0$ elsewhere, and nutrients $N_0 = N_s$:

$$C(r, t = 0) = \begin{cases} C_0, & 0 < r < R_0 \\ 0, & \text{elsewhere} \end{cases} \qquad \text{and} \qquad N(r, t = 0) = N_s \,, \tag{5.9}$$

where R_0 is the initial radius of the tumor. At the boundary, we took the cell flux to be zero and applied a fixed nutrient source concentration $N_s = \text{const.}$; hence, boundary conditions were

$$\left.\frac{\partial C(r,t)}{\partial r}\right|_{r=R_\infty} = 0 \,, \tag{5.10a}$$

$$N(r = R_\infty, t) = N_s \,. \tag{5.10b}$$

The symmetry condition at the center of the tumor applied to both cells and nutrients:

$$\left.\frac{\partial C(r,t)}{\partial r}\right|_{r=0} = \left.\frac{\partial N(r,t)}{\partial r}\right|_{r=0} = 0 \,. \tag{5.11}$$

The nonlinear system of Equations (5.8) was numerically solved with the finite differences method. Considering radially symmetric solutions, a uniform spatial discretization of 1000 grid points was applied, and the Euler method was implemented for forward integration in time using 5000 time steps. The convergence of the solution was verified with a sequence of grid refinements. We took the following baseline values for the parameters, $C_0 = 1 \times 10^{-2}$ kg/cm^3, $N_s = 1 \times 10^{-3}$ kg/cm^3, $R_\infty = 1 \times 10^{-1}$ cm, $R_0 = 5 \times 10^{-2}$ cm, $D_f = 1 \times 10^{-8}$ cm^2/s, $\mu = 1 \times 10^{-7}$ cm^2/s, $D_n = 1 \times 10^{-6}$ cm^2/s, $k_1 = 5 \times 10^{-3}$, $k_2 = 5 \times 10^{-4}$ and $\tau = 24$ h.

In the following section, we study the role of dimensionless parameters in tumor invasion pattern. First, we obtained the steady-state solution to Equation (5.8a) in the absence of nutrients. Next, the sustainability of the tumor's sharp interface, the distribution of the migrated cells, and the shape and the formation of the shell are demonstrated in response to the variation of the dimensionless parameters $\bar{\beta}, \gamma, \bar{V}, \bar{\eta}, \psi$ and c by solving the full system of Equations (5.8a,b) subjected to (5.9)–(5.11).

5.3 Results

To better understand the role of free energy and the interfacial stress proposed in Section 5.2.1, we first look into the steady-state axisymmetric spherical form of Equation (5.8a):

$$\nabla \cdot \left[\nabla \left(\bar{f}(\bar{C}) - \bar{\beta} \nabla \cdot (\nabla \bar{C}) \right) \right] = 0 \,, \tag{5.12}$$

where $\nabla(\cdot) = \partial(\cdot)/\partial r$ and $\nabla \cdot (\cdot) = (2/r)\partial(\cdot)/\partial r + \partial^2(\cdot)/\partial r^2$. This equation, in the absence of nutrients, represents the steady state cell distribution when the adhesive and diffusive forces are balanced. This equilibrium was determined with parameter $\bar{\beta}$, as shown in Figure 5.4.

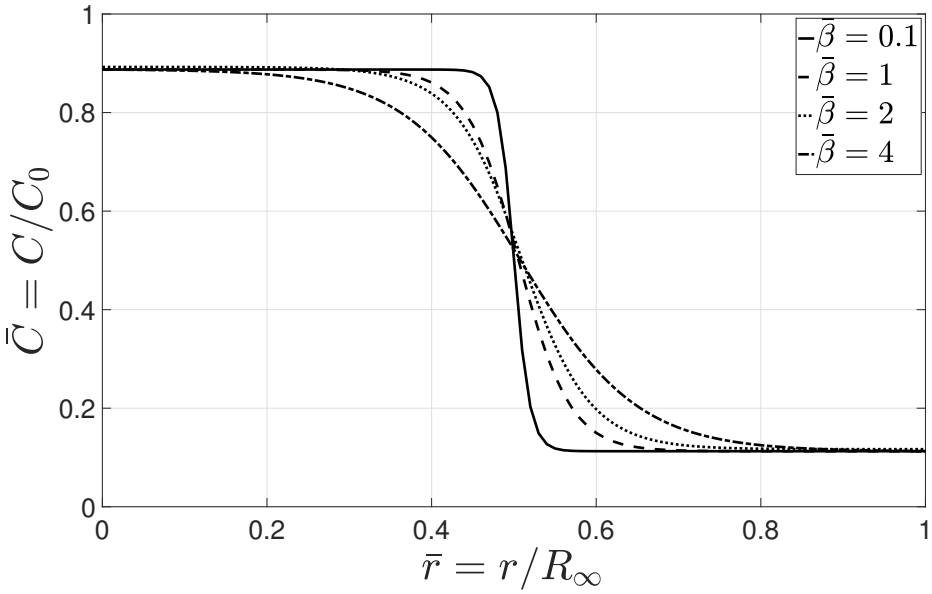

Figure 5.4: Steady state distribution of cells in absence of nutrients for $\bar{\beta} = \{0.1, 1, 2, 4\}$.

Dimensionless parameter $\bar{\beta}$ controls the transitional length between the high- and low-concentration regions. Higher values of $\bar{\beta}$ led to a smooth edge where the balance of diffusive and adhesive forces occurred at a longer transitional length. However, lower values of $\bar{\beta}$ allowed for the tumor to sustain a sharp continuous interface. The physical interpretation of $\bar{\beta}$ could be explained by considering the role of ECM in cell migration. An ECM composition that allows for strong cell–matrix adhesion and facilitates the mesenchymal motion corresponds to higher values of $\bar{\beta}$. In this case, cells migrated through the matrix and exhibited a typical finger-type invasion pattern where the tumor interface was generally indistinct. However, lower values

of $\bar{\beta}$ are associated with the ECM composition that regulates weak adhesive bindings with invasive cells. In this case, invasion is either inhibited or limited to the amoeboid motion of cells through the matrix pores. In addition, amoeboid-mesenchymal plasticity comprises both migration patterns that could be regulated by a specific ECM composition, and allows for a switch between the aforementioned modes.

Next, we study the role of dimensionless parameters $\gamma, \bar{V}, \bar{\eta}, \psi$, and c for the baseline values presented in Section 5.2.4, depicted in Figure 5.5.

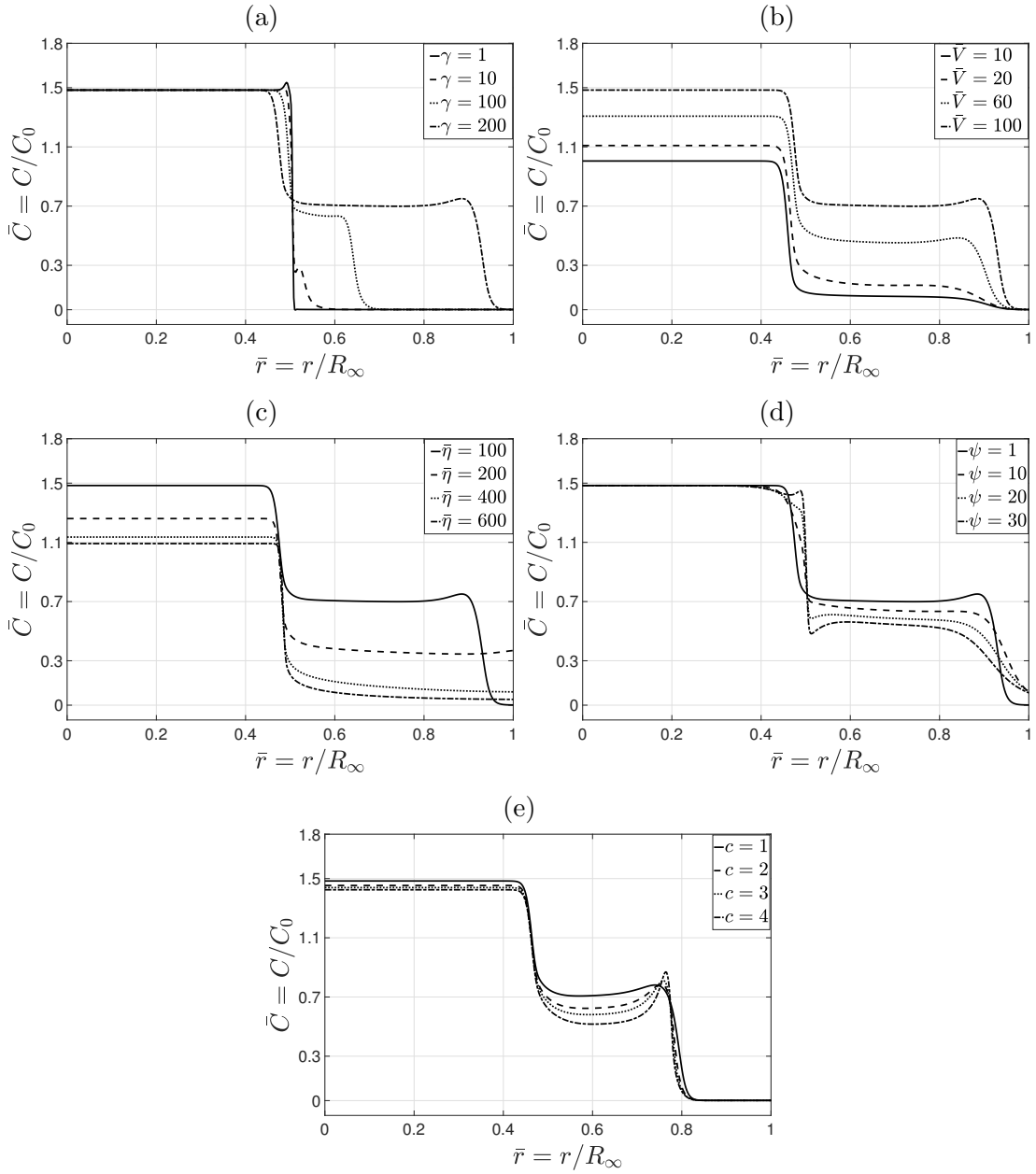

Figure 5.5: Cell distribution corresponding to different values of $\gamma, \bar{V}, \bar{\eta}, \psi$ and c. (**a**,**b**) Higher values of γ and $\bar{V}$ increased the growth of cells moving outward the tumor core, yielding a peak in cell concentration with a distinct interface. (**c**,**d**) Higher values of $\bar{\eta}$ and ψ reduced cell concentration and eliminated the peak. Parameter c controlled the formation of a peak and the concentration of cells within the invasion zone. (**e**) A higher c corresponds to a higher sensitivity of the proliferation rate to the gradient of nutrients giving rise to a larger peak at the leading interface.

Dimensionless cell diffusion number $\gamma = N_s\mu//D$ represents the ratio of chemotac-

tic flux to the diffusive flux, for particular values of nutrient source concentration N_s. Higher values of γ correspond to higher chemotactic effects that derive cells migrating toward the gradient of nutrients and initiate the formation of a peak in the cell concentration at the precursor cells, as shown in Figure 5.5a. Increasing γ gave rise to a higher level of chemotactic invasion with a less distinct interface between the tumor core and the matrix, while the leading cluster of cells still preserved the interface.

A similar effect related to $\bar{V}$, i.e., dimensionless cell growth number, can be seen in Figure 5.5b, where a higher growth number $\bar{V}$ increased cell concentration and led to the formation of a peak in cell concentration. A comparison between the effects of γ and $\bar{V}$ indicates that a variation in γ only changed the concentration of cells outside the tumor core, while variation in $\bar{V}$ changed cell concentration everywhere. Dimensionless nutrient consumption number $\bar{\eta}$ had an opposite effect to that of growth number γ. Higher consumption led to a uniform decrease in cell concentration and eliminated the leading interface, as shown in Figure 5.5c.

Dimensionless nutrient diffusion number ψ plays a dual role in cell migration, as shown in Figure 5.5d. Higher values of ψ led to the formation of a more distinct tumor edge separating the tumor core and migrated cells, but removing the peak and the leading edge. Higher diffusion reduced the nutrient gradient; hence, less chemotactic migration occurred within the invasion zone.

Hill coefficient c determines the formation of a peak in the cell concentration at the leading edge. As depicted in Figure 5.5e, c alters the sensitivity of migrating cells to the change in cell and nutrient concentrations. Higher values of c reduce the concentration of cells in the invasion zone due to a significant change in the proliferation rate while leading to the formation of a notable peak at the leading interface. The peak observed in the axisymmetric radial solution corresponded a spherical-shell-type cluster of cells in the three-dimensional domain.

Lastly, the dynamic progression of the invasion and the nutrient distribution are shown in Figure 5.6. As captured by the model, a cluster of cells at the outer layer of the tumor broke away and formed a shell-type layer of cells moving up the gradient of nutrients while preserving a notable interface, as the experimental data in Figure 5.1 show. This can be explained as the interplay between adhesive cell–cell and cell–matrix forces that led to the separation of a cell cluster in the form of a shell layer diffusing into the surrounding matrix. As discussed in the previous section, we modeled this phenomenon by adopting nonconvex free energy and accounting

for the interfacial properties, which allowed for the equilibrium states of high and low concentrations. We also adopted a simple reaction–diffusion model for the chemotactic migration of cells. The formation of the shell was predicted as a peak in the cell concentration over a small interval followed by a drop denoting the interface. This peak corresponded to the cell aggregation seen as a ring and marked by red arrows in Figure 5.1. As shown in the figure, the tumor and the invading cells preserved their interfaces with the surrounding gel while the invasion proceeded. The same behavior was predicted by the model, as shown in Figure 5.6, where the shell-type cluster of cells preserved a sharp continuous interface and broke away. The gradient of nutrients due to the consumption by the precursor cells evoked the chemotactic migratory response, hence inducing the radial motion of the shell over time.

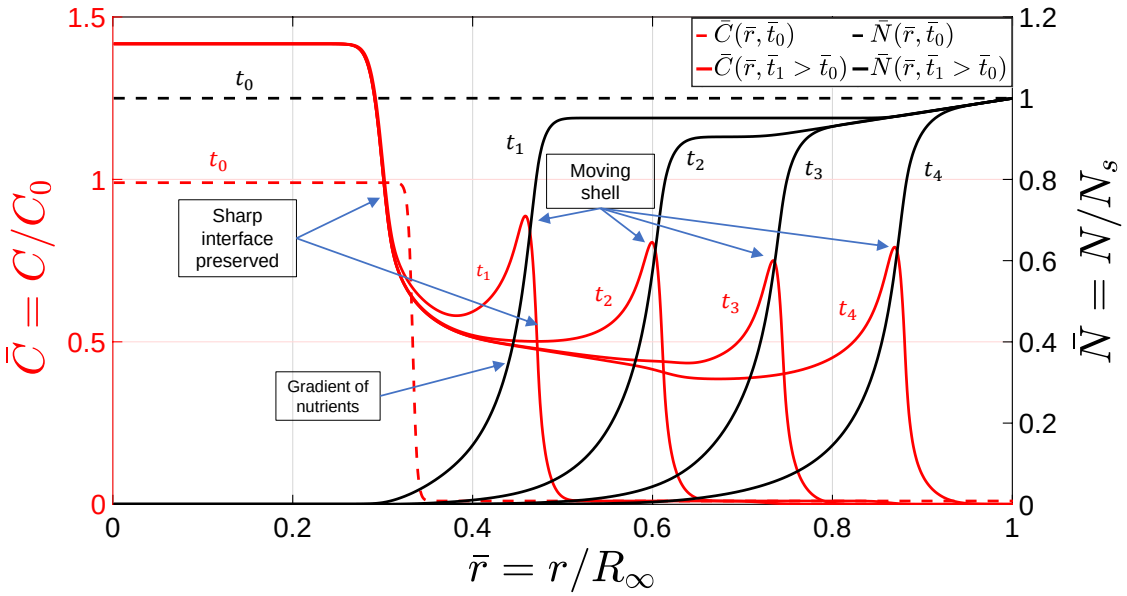

Figure 5.6: The dynamic progression of tumor invasion within a hydrogel matrix in the form of the shell-type motion of invasive cells over time. The shell-type cluster of cells moved up the gradient of nutrients due to chemotaxis while sustaining its structure due to adhesive cell–cell forces. The ability of cells to preserve the shell as they move was modeled with nonconvex free energy that included interfacial stress.

The proposed model presents a mathematical framework that translates biological phenomena, such as cell–cell/–matrix adhesion, chemotaxis, proliferation and consumption rates, into the context of free energy and capillary stress. Using this model, we were able to interpret the interplay between various biological factors that influenced tumor invasion and their effects on inducing a distinctive pattern of inva-

sion observed in different tumors. In this invasion mode, a cluster of cells migrated into the surrounding matrix, with a preserved interface exhibiting a spherical-shell-type layer moving away from the tumor core. This pattern may be perceived as a ring in experimental studies due to the projection of tumor images onto a two-dimensional plane in microscopic imaging. The results presented here are limited to the axisymmetric invasion of tumors with a homogeneous cell population. Anisotropic tumor invasion may occur due to different stimuli, such as heterogeneity in a cell population, e.g., hypoxic and normoxic cell phenotypes, and fiber-embedded tumor ECM.

5.4 Conclusion

In this work, we developed a continuum model to study the distinctive mode of tumor invasion resulting from the interplay between cell–cell and cell–matrix adhesion. A nonconvex free energy is integrated with a standard chemotactic model to predict the collective migration of cells in the form of a shell-type invasion. The adopted Cahn–Hilliard-type free energy with the contribution of the interfacial stress allowed for the cells to remain together and preserve the tumor core via adhesive cell–cell forces while separating the shell from the core and the surrounding matrix across continuous sharp interfaces. Cells moved in response to the gradient of nutrients, i.e., chemotaxis, while preserving the shell layer. This indicates that the adhesive cell–cell force was strong enough to maintain the structure of the shell throughout the migration. Due to nutrient consumption, the chemotactic effect was reduced as the shell passed along, leaving behind a region with fewer cells. The effects of different parameters, such as diffusion, growth, and consumption numbers, on cell distribution were studied. Higher values of cell diffusion and growth numbers increased the growth of cells moving outwards from the tumor core, yielding a peak in cell concentration with a distinct interface. Higher values of nutrient consumption and diffusion numbers reduced cell concentration and eliminated the peak. In addition, the formation of the peak was controlled by the Hill coefficient, c, which determined the sensitivity of the proliferation rate to the gradient of nutrients, giving rise to a larger peak at the leading interface. The proposed model could demonstrate the principal features of the invasion pattern, including the formation, shape, and movement of the shell, and the continuous interface separating the tumor from the surrounding matrix. Nevertheless, empirical studies are required to calibrate the model parameters for quantitative predictions. Future research directions include experimental studies on tu-

mor invasion patterns using tumor-on-a-chip platforms that enable testing different hydrogel compositions, and help in understanding the role of cell/matrix adhesion. This further helps in the calibration of model parameters to enhance quantitative predictions. In addition, the model can be integrated with a discrete mathematical framework to include cellular interactions. This improves the accuracy of predictions in the case of anisotropic invasion.

Author contributions: Conceptualization, M.A., H.S. and B.N.; methodology, M.A., H.S. and B.N.; formal analysis, M.A., H.S. and B.N.; software, M.A.; writing—original draft preparation, M.A.; writing—review and editing, M.A., H.S. and B.N.; supervision, B.N. and H.S.; funding acquisition, B.N. All authors have read and agreed to the published version of the manuscript.

Funding: funding was provided by the Natural Science and Engineering Research Council (NSERC) of Canada.

Data availability: Data will be available upon request.
Conflicts of interest: The authors declare no conflict of interest.

Chapter 6

Unveiling the role of metabolic rates variation in driving glioblastoma multiforme (GBM) heterogeneity and controlling growth and invasion: insights from an integrated multiscale in-vitro in-silico framework

Contributions:

Meitham Amereh: Conceptualization, theory and simulation, methodology, experiments, formal analysis, validation, writing—original draft preparation, writing—review and editing

Shahla Shojae: Conceptualization, methodology, experiments

Tavia Walsh: Methodology, writing—review and editing

Prashant Dogra: Writing—review and editing

Vittorio Cristini: Writing—review and editing

Mohsen Akbari: Conceptualization, methodology, writing—review and editing, su-

Communications Engineering. https://doi.org/10.21203/rs.3.rs-2828746/v1 https://www.nature.com/commseng/journal-information

pervision, resources
Ben Nadler: Theory, writing—review and editing, supervision

Meitham Amereh[1,2,3], Shahla Shojaei[1,4], Tavia Walsh[1], Prashant Dogra[5,6], Vittorio Cristini[5,7,8,9], Ben Nadler[1], Mohsen Akbari[1,2,3,10,*]

[1] Department of Mechanical Engineering, University of Victoria, 3800 Finnerty Road, Victoria, V8P 5C2, BC, Canada

[2] Laboratory for Innovations in MicroEngineering (LiME), University of Victoria, 3800 Finnerty Road, Victoria, V8P 5C2, BC, Canada

[3] Centre for Advanced Materials and Related Technologies (CAMTEC), University of Victoria, 3800 Finnerty Road, Victoria, V8P 5C2, BC, Canada

[4] Department of Anatomy and Cell Sciences, University of Manitoba, 66 Chancellors Cir, Winnipeg, R3B 2E9, MB, Canada

[5] Mathematics in Medicine Program, Department of Medicine, Houston Methodist Research Institute, 6670 Bertner Ave., Houston, 77030, TX, USA

[6] Department of Physiology and Biophysics, Weill Cornell Medical College, 300 York Ave., New York, 10065, NY, USA

[7] Neal Cancer Center, Houston Methodist Research Institute, 6670 Bertner Ave., Houston, 77030, TX, USA

[8] Department of Imaging Physics, University of Texas M.D. Anderson Cancer Center, 1515 Holcombe Blvd, Houston, 77030, TX, USA

[9] Physiology, Biophysics, and Systems Biology Program, Graduate School of Medical Sciences, Weill Cornell Medicine, 1300 York Ave., New York, 10065, NY, USA

[2] School of Biomedical Engineering, University of British Columbia, 2329 West Mall, Vancouver, V6T 1Z4, BC, Canada

*Correspondence: makbari@uvic.ca; Tel.: (+1) 250-721-6038

Abstract

The three-dimensional (3D) structure of solid tumors inherently limits oxygen and nutrient diffusion to deeper cells, resulting in morphological and metabolic variations. Non-physiological levels of oxygen and nutrients within the tumors result in heterogeneous cell populations that exhibit distinct necrotic, hypoxic, and proliferative zones. Among these zonal cellular properties, metabolic rates strongly affect the overall growth and invasion of tumors. Here we report on a hybrid discrete-

continuum (HDC) mathematical framework that uses data from a biomimetic two-dimensional (2D) in-vitro cancer model to accurately predict three-dimensional (3D) tumor growth, invasion, and treatment response. The mathematical model integrates modules of continuum, discrete, and neurons. Model predictions are compared to the growth and invasion of human glioblastoma (hGB) non-resistant and chemo-resistant tumoroids co-cultured with healthy neurons within a hydrogel matrix using an in-vitro tumoroid on-a-chip model. The in-vitro model is composed of tumor organoids (called tumoroids) co-cultured with healthy neurons all embedded within a hydrogel matrix. Results indicated that the HDC model is capable of quantitatively predicting volumetric growth and invasion length and tracking the asymmetric finger-type invasion pattern in hGB tumors. Additionally, the model could predict the resulting reduction in invasion length of hGB tumoroids in response to temozolomide (TMZ) by utilizing the viability variation observed in 2D-cultured hGB cells treated with TMZ. This model has the potential to incorporate additional modules, including immune cells and the corresponding signaling pathways governing cancer/immune cell interactions. Moreover, the model can be used to investigate targeted therapies, such as aberrant glucose metabolism in hGB tumors, as a potential therapeutic strategy.
Keywords: tumor growth and invasion; in-silico modeling; metabolic rates

6.1 Introduction

Tumor heterogeneity arises from genetic mutations, epigenetic modifications, environmental factors, and selective pressures, playing a crucial role in cancer diagnosis, treatment, and prognosis. For instance, cells acquire a hypoxia-induced phenotypic heterogeneity due to change in their metabolism caused by the spatial distribution of oxygen and nutrients within solid tumors [78, 79, 170–172]. Hypoxic cells over-express proteins involved in growth signaling pathways such as epidermal growth factor receptor (EGFR), promoting cell division and invasion [173–175]. Tumor heterogeneity poses substantial challenges for cancer treatment, given that distinct cells within the tumor may respond disparately to therapies, with certain cells demonstrating greater resistance to treatment. To address these challenges, there is considerable interest in creating personalized and precision medicine approaches that take into account individual tumors' unique genetic and phenotypic features. This can include using genomic profiling and other indicators to identify cell subpopulations within the tumor and tailoring treatment accordingly.

The cross-disciplinary approach of combining mathematical and biological models of cancer has great potential to enhance treatment strategies. By giving insights into the underlying biological processes governing tumor formation and progression, mathematical modeling plays an essential role in advancing and refining cancer treatment approaches [83]. Solid tumors have been extensively studied from continuum and discrete perspectives in the field of mathematical biology [6, 8–10, 176, 177]. In the continuum approach, partial differential equations (PDEs) incorporate growth and kinetic interactions between components, along with diffusion [12, 127, 128]. Discrete methods instead focus on intra- and intercellular interactions providing a more accurate representation of cellular and sub-cellular behaviors, especially in predicting single cell responses [11]. However, the computational cost substantially increases for large systems such as biological tissues and tumors [32]. Hybrid Discrete-Continuum (HDC) models integrate continuum and discrete approaches to interrelate the cellular mechanisms with tissue-level responses allowing for the analysis of discrete cellular interactions alongside macroscopic variables. Therefore, HDC models combine the precision of discrete descriptions with the computational efficiency of continuum approaches, providing a comprehensive understanding of complex biological systems [11].

Mathematical models have been previously used to simulate and study the effects of cell heterogeneity on tumor growth and response to therapy, as well as to identify potential strategies for mitigating these effects. Notably, the variation in cellular metabolism—a key regulator of tumor morphology and invasion of multicellular human glioblastoma (hGBM) tumors has been studied using HDC models [178]. In addition, the correlation of the interactions between different phenotypes and the level of malignancy was modeled using evolutionary game theory [80]. It was shown that cancer cells initially in growth phenotype can switch to an anaerobic or invasive phenotypes [81]. Several mathematical models include the preferential invasion direction of cancer cells via an anisotropic diffusion tensor [179, 180]. The metabolic modeling method is another technique used in the context of tumor invasion. These models are typically steady-state stoichiometric models that predict the distribution of fluxes, but lack the transient aspects such as time-dependent metabolite concentrations as well as the description of spatial heterogeneity in cancer cell populations [82, 181, 182]. Despite the rich literature on mathematical modeling of solid tumor growth invasion, there is a lack of integration with multiscale experimental platforms that can provide more realistic model parameters and monitoring techniques. For instance, many ex-

isting models consider the rates of proliferation and nutrient uptake to be constant or a linear functions while they are inherently non-linear parameters [173, 175, 183–187]. Cellular metabolism is altered when cancer cells change phenotype, generally following a nonlinear fashion [188]. Additionally, the hypoxic population of cells were commonly considered passive and quiescent with either negligible or simplified linear proliferation and consumption rates [38, 175, 183].

Current in-vitro models, particularly drug resistant models, rely mainly on two-dimensional (2D) culture systems, xenografts, and genetically engineered animal models that are either unable to recapitulate the complex TME or have physiological differences and ethical concerns [189–191]. Three-dimensional (3D) tumoroid culture via tumor-on-a-chip platform is an alternative to traditional models that can simulate TME characteristics such as cell-cell adhesion, heterogeneity, and diffusion properties of nutrients in TME [84]. In addition, it is necessary to include the GBM-neurons interaction for developing realistic in-vitro models [86]. While GBM is more commonly associated with white matter, its invasive nature can lead to infiltration into surrounding brain tissue, which includes both white and gray matter [192]. GBM-neuron synaptic interactions in TME have a pivotal role in tumor growth and invasion [87]. We have recently shown that these interactions significantly change the secretome profile of inflammatory and invasion cytokines [163]. More interestingly, the variation in cytokine profile strongly depends on the state of hGBM cells (i.e., non-resistant or TMZ-resistant) and plays a dual effect. Additionally, the growth and the finger-pattern invasion have been observed in in-vitro platforms [193], and is simulated via simulate Gompertzian model based on probabilistic model parameters [194]. However, they lack a comprehensive framework integrating underlying cellular and subcellular interactions.

In this paper, we present an HDC model to quantitatively assess tumor growth and invasion. Compared to the existing models, our model offers a more realistic scheme of metabolic rates by measuring the rate of cell proliferation and glucose uptake in normoxia and hypoxia, as well as their dependency on glucose concentration. This extension from the common practice of assuming linear or constant functions allows us to capture the non-linear heterogeneity of tumoroids' behaviour more accurately. This inclusion is essential for modeling solid tumors characterized by a diverse cellular distribution, wherein cellular metabolism significantly responds to fluctuations in oxygen and nutrient levels. Additionally, incorporating the hypoxic cells as an active subpopulation of tumoroid with their nonlinear proliferation and consumption rates is

another key feature of our model. Moreover, the discrete module captures the effect of hif1-alpha expression by hypoxic cells in invasiveness of GBM, by including a simplified representation of the associated signaling pathway. It also considers the effects of cancer cell-neuron inter- actions on GBMs growth and invasion that is missing from previous studies on GBMs progression. The model focuses on glucose and oxygen metabolism, both modulate various signaling pathways and provide energy for the synthesis of nucleic acids, proteins, and lipids [195]. Moreover, quantitative measurement of the interrelation between glucose and oxygen uptake is especially significant for hypoxic cells due to the Warburg Effect [196]. To overcome the drawbacks of previous approaches, a tumoroid-on-a-chip platform was developed to resemble TME and monitor tumoroid responses over time, where simultaneous growth and invasion are observed upon integration with the HDC model. This model identifies the invasion zone by tracking the moving boundary of tumor by incorporating a mechanism for constantly updating the spatial location of tumor boundaries. Capturing the moving boundary of tumoroids is important in order to quantitatively distinguish the growth and invasion. The migration of invasive cells into the matrix is modeled via a random walk module and includes the interaction of single cells with the continuum field of variables. We developed a comprehensive framework integrating underlying cellular and subcellular interactions, providing a quantitative basis for predicting the finger-pattern invasion. The incorporation of these detailed interactions enhances the predictive capabilities of our model beyond existing in-vitro demonstrations. Our model relies on a deterministic scheme of cellular interactions. We experimentally measure growth, consumption, and conversion, linking these factors to a discrete module that considers mechanical pressure, proliferation time, oxygen, and nutrient availability, as well as cancer-neuron interactions. Additionally, our model uniquely predicts finger-type invasion patterns, which was not present in the previous works. Moreover, the inclusion of chemo-resistant cells with varying metabolic rates allows us to identify their distinctive growth and invasion behavior compared to non-resistant cells. Finally, to validate this model, the growth and invasion of hGBM (non-resistant and temozolomide (TMZ)-resistant) were monitored over time and compared with the model predictions.

6.2 Results

In this section, we present the in-vitor in-silico framework including experimental and HDC ccomponents, model formulation, parameter measurments, and model validation. While the main focus of this study is not to validate biological hypothesis, it aims to (i) formulate these hypotheses into mathematical frameworks consistent with physical laws, (ii) solve the resulting governing equations with incorporating appropriate boundary conditions reflective of biological settings, and finally (iii) derive quantitative predictions, such as growth and invasion patterns of tumoroids. It's essential to note that although the presented framework has the capability to implement and validate biological hypotheses, our immediate focus is on achieving accurate quantitative predictions. Figure 6.1 elucidates the workflow and data acquisition process, highlighting in-vitro components, experimental timeline, 2D culture data extraction and integration into the HDC model, and comparisons drawn between in-vitro observations and model predictions. This visual illustrates intricacies of the experimental design and the seamless connection between empirical data and computational modeling.

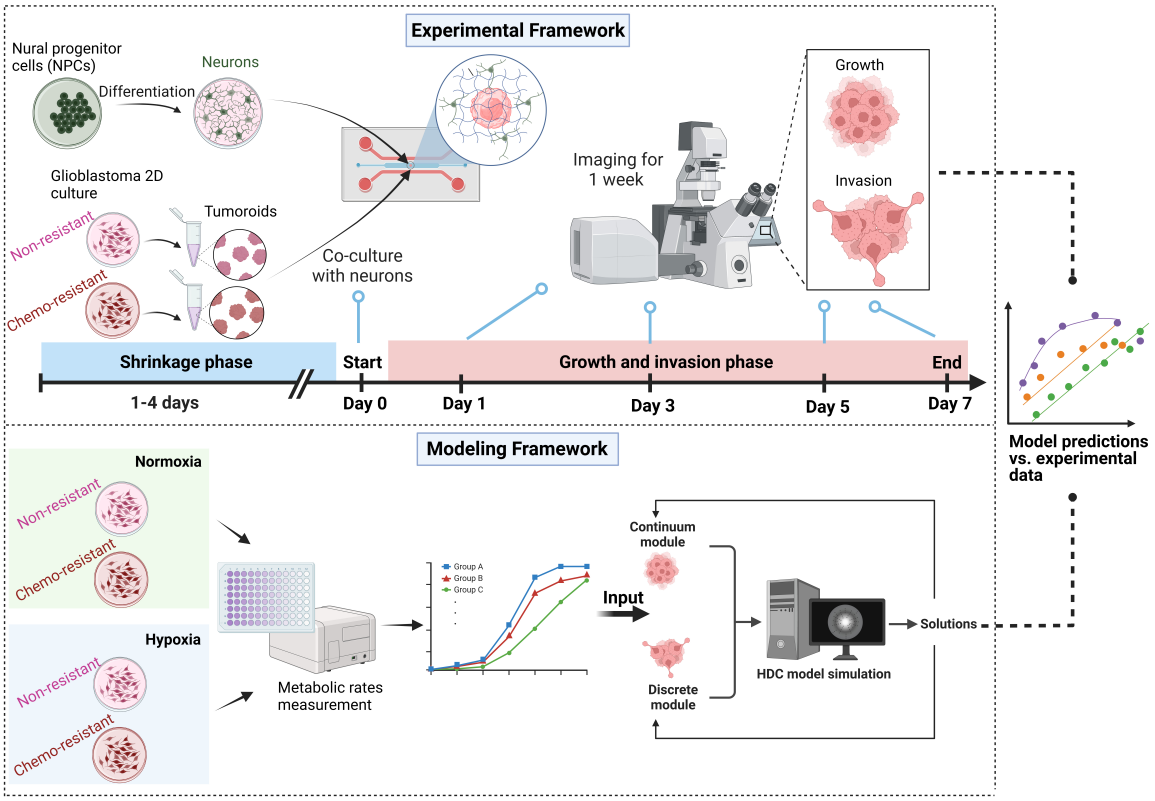

Figure 6.1: The workflow and data acquisition process in experimental and HDC modeling frameworks. In experimental module, non-resistant and TMZ-resistant hGB cells were tumoroid-cultured using SFMAs. After four days, allowing to form a compact solid tumor structure, tumoroids were co-cultured with NPC-differentiated neurons in a hydrogel matrix within a microfluidic chip. The growth and invasion of tumoroids were monitored over 7 days and were quantified via ImageJ. In the HDC framework, non-resistant and TMZ-resistant cells were 2D cultured, their metabolic rates were extracted and input to the model, and predictions were validated by comparing with the experimental data. Created with BioRender.com.

6.2.1 Diffusion of external components contributes to tumor heterogeneity

Tumor evolution can be described as the changes in the properties of a continuous system in which the local points, i.e., cells, react to the presence of external components that diffuse into the 3D structure of the tumor. These reactions that change the local properties of a tumor depend on the characteristics of cells in the infinitesimal neighborhood. When the tumor size exceeds a certain level, the diffusion limit deprives internal tumor cells of the nutrients necessary for normal metabolism. Oxygen

and glucose have critical physiological roles in cell growth and survival, modulating various signaling pathways and providing energy for the synthesis of proteins, nucleic acids, and lipids. The threshold of normal oxygenation varies among organs, and is around 4.4% in brain [197]. Hypoxia initiates below this threshold, leading to the stabilization of hypoxia-related genes such as HIF-1-alpha. Hypoxic cells with the altered proliferation and consumption rates form a hypoxic zone in the center of tumor. Moreover, insufficiency of adequate growth factors may induce a necrotic zone. Large tumors are therefore susceptible to developing two distinct interior zones (hypoxic and necrotic) beneath a proliferative layer of cells, as shown in Figure 6.2.

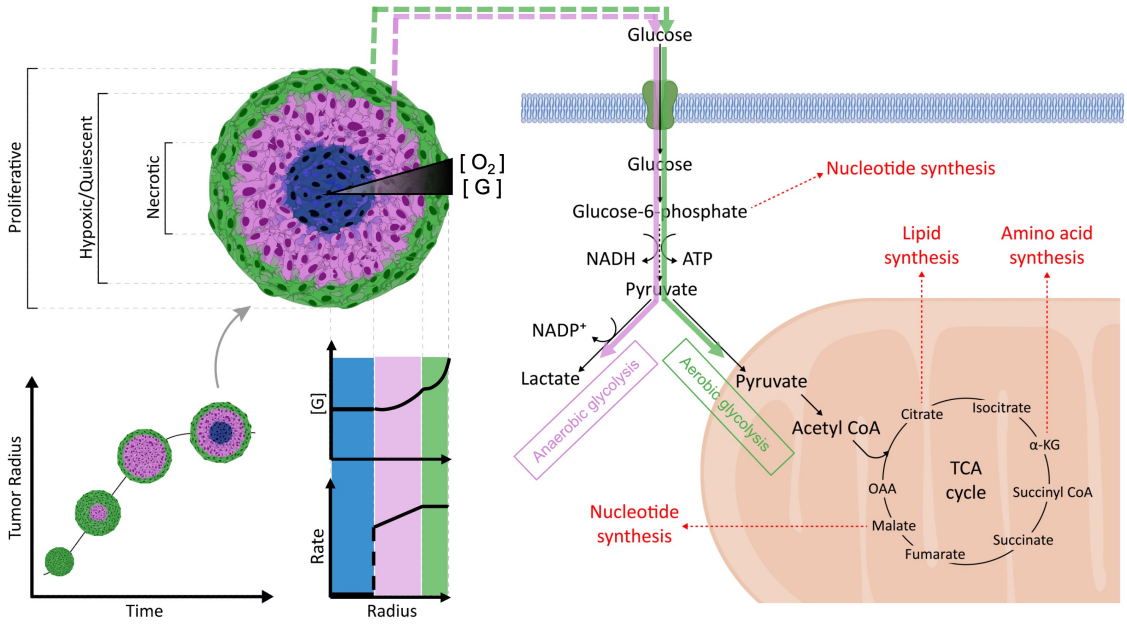

Figure 6.2: The non-uniform distribution of oxygen [O_2] and glucose [G] within the three-dimensional structure of tumors gives rise to the formation of proliferative, hypoxic, and necrotic zones. This inhomogeneity results in nonuniform glucose consumption and distribution. Compared to normoxia, hypoxic cells switch their metabolism to anaerobic glycolysis and uptake glucose faster to compensate for the low efficiency of ATP production.

The external growth factors required for cell metabolism were subdivided into two representative components to model the function of external growth factors in tumors. Critically, non-physiological levels of oxygen tension in hypoxia can change cancer cell metabolism and lead to angiogenesis, epithelial-to-mesenchymal transition (EMT), and upregulation of pro-inflammatory cytokines [198]. In addition, amongst various nutrients, glucose has a critical physiological role in cell growth and survival.

Glucose metabolism modulates various signaling pathways and provides energy for the synthesis of macromolecules such as proteins, nucleic acids, and lipids, as shown in Figure 6.2. Cancer cells also have the ability to switch their metabolism to aerobic glycolysis, so-called the Warburg Effect, by increasing glucose uptake to promote proliferation and long-term survival [196]. Cell growth and survival therefore strongly rely on the concentration of glucose in the hypoxic zone.

Formation of distinct zones within the 3D structure of a tumor mainly results from the diffusion of external components such as glucose and oxygen, as shown in Figure 6.2. The proliferative zone, which includes normoxic cancer cells, is the outer layer of cells within the tumor that receives enough oxygen and glucose for normal metabolism. Cells at the peripheral rim have access to a high level of diffused components, hence their rate of uptake is generally constant, while the interior rim may receive levels of nutrients below a certain threshold, resulting in concentration-dependent uptake rates. The concentration of oxygen and glucose drops inwardly, reaching the hypoxic zone, where the concentration of oxygen is below a critical level required for oxidative phosphorylation. In this zone, cells acquire a hypoxia-induced phenotype, switch their metabolism to anaerobic glycolysis (consequently producing less ATP), and take up glucose faster. This further reduces the concentration of glucose, ultimately depriving the interior cells of the minimum nutrient requirements for survival. These central cells undergo necrosis, forming a necrotic zone. A continuum reaction-diffusion model for the evolution of tumor heterogeneity and diffusion of external components is presented in Section 6.4.1.

Hypoxia significantly alters concentration-dependent rates of glucose uptake and proliferation

At low glucose concentrations, the cancer cell uptake rate is concentration-dependent and increases by raising the supplied glucose to a threshold, after which the rate remains constant [199]. The same concentration-dependent property is expected for the rate of proliferation. At very low glucose concentrations, cells cannot maintain the energy required for homeostatic synthesis of proteins, nucleic acids, and lipids. Among various pathways that may lead to necrosis in glioblastoma [200, 201], alterations in cellular metabolism, particularly glucose deprivation, can induce metabolic stress and energy depletion, leading to oxidative stress and potentially triggering various forms of cell death, including necrosis [202]. Moreover, glucose withdrawal

activates a positive feedback loop involving the generation of reactive oxygen species (ROS) by NADPH oxidase and mitochondria, ultimately resulting in ROS-mediated cell death [203]. A minimum glucose concentration is required for cell proliferation, while cells provided with higher concentrations proliferate at faster rates until they reach maximum proliferation capacity [204]. This nonlinear behavior is significant in 3D tumors where their geometry imposes nonuniform oxygen and glucose distributions. Although hypoxic cells consume glucose at a higher rate with anaerobic glycolysis, they proliferate at a lower rate [205]. Therefore, the distinct zones shown in Figure 6.2 eventually balance and stop overall volumetric tumor growth. To inves-

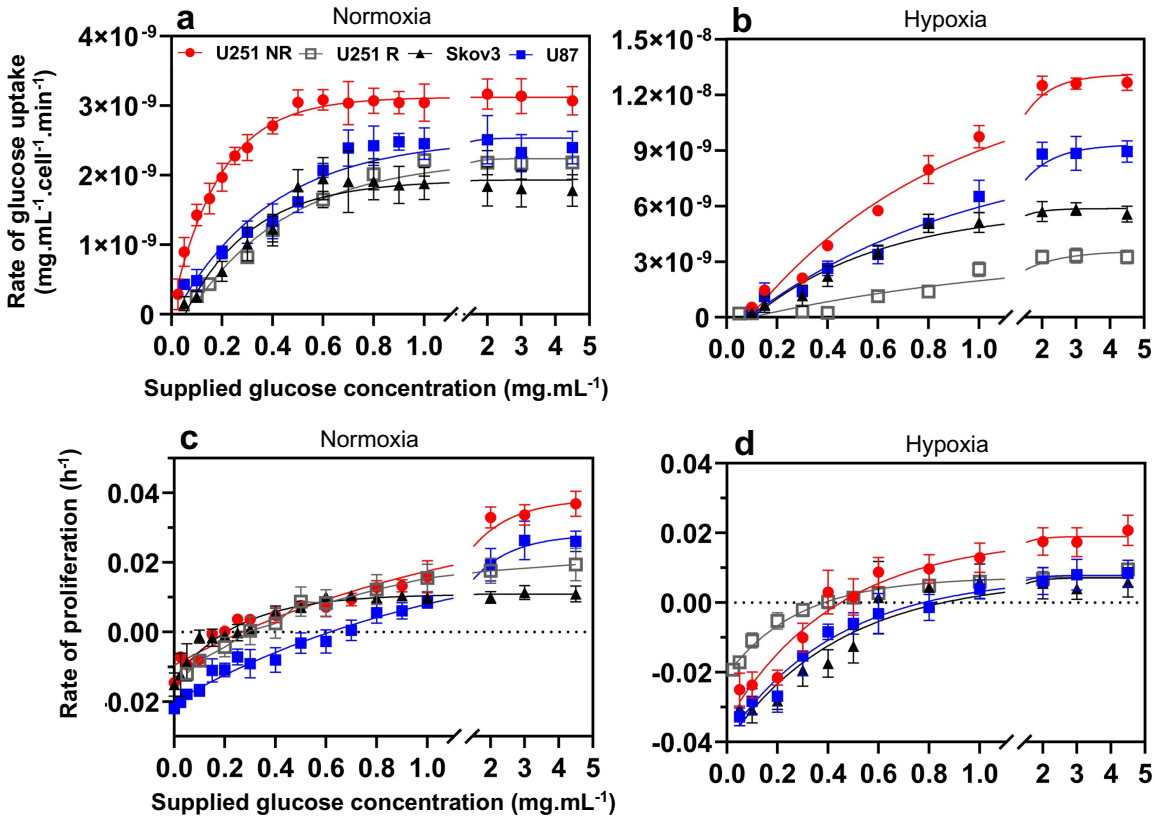

Figure 6.3: Concentration-dependent glucose uptake and proliferation rates in hGBM U251 (non-resistant and TMZ-resistant), U87, and Skov3 cells. Glucose uptake rates in response to a range of supplied glucose in normoxic (a) and hypoxic (b) conditions are measured using glucose uptake and trypan blue assays. Hypoxic cells consume glucose at significantly higher rates as they switch their metabolism to anaerobic glycolysis. Proliferation rates are glucose concentration dependent in normoxia (c) and hypoxia (d). Solid lines represent non-linear interpolations of experimental data points.

tigate rates dependency on glucose concentration, we measured the rates of glucose uptake and proliferation in three glioma cell lines (U251 non-resistant, U251 TMZ-resistant, and U87), and one ovarian cell line (Skov3), to a range of supplied glucose concentrations in normoxia and hypoxia, shown in Figure 6.3. The associated critical values such as saturated glucose uptake and proliferation rates are presented in Table 6.1 (supplementary data). In brief, hypoxia increased the saturated uptake rates of U251 non-resistant, U87, Skov3, and U251 TMZ-resistant by 4, 3.6, 3.1, and 1.5 fold, respectively, compared to normoxia (Figure 6.3(a) and (c)). Also, the maximum proliferation rates dropped by 2, 3, 2 and 1.2 fold in U251 non-resistant, U87, U251 TMZ-resistant, and Skov3 cell, respectively, in hypoxia (Figure 6.3(b) and (d)).

To formulate model parameters, including rates of proliferation and glucose uptake in normoxia and hypoxia, nonlinear interpolation was obtained for the data in Figure 6.3. The following exponential plateau function was adopted.

$$f(X) = V_{max} - (V_{max} - V_{min})\, e^{-KX}\,. \tag{6.1}$$

where X represents the concentration of supplied glucose, $f(x)$ is the approximated rates of glucose uptake or proliferation, V_{max} is the maximum rate at saturated glucose concentration, V_{min} is the minimum rate, and K is the rate constant. The units for V_{max} and V_{min} corresponded to the uptake rate is mg.mL^{-1}.cell^{-1}.min^{-1}, and corresponded to the proliferation rate is h^{-1}. K is in mg.mL^{-1}. Table 6.2 (supplementary data) includes the values of these constants for U251 non-resistant, U251 TMZ-resistant, U87, and Skov3, obtained from Figure 6.3. These non-linear rates were incorporated into the HDC model as inputs.

In-silico model predicts the evolution of tumor heterogeneity and the growth rates of different tumoroids

To ensure the applicability of feeding 2D data into a 3D model and validate the results, glucose consumption and growth rates in 3D tumoroids were experimentally measured. The rate of normoxic-to-hypoxic conversion was quantified through flow cytometry analysis and subsequently incorporated into the model to predict hypoxia development in tumoroids (Fig. 6.4(a)). 24 hour exposure of U251 non-resistant, U251 TMZ-resistant, U87, and Skov3 cells to 2% oxygen in a hypoxic chamber resulted in the conversion of 69%, 51%, 62%, and 53% of normoxic cells to a hypoxic state, respectively. These rates were considered as the maximum conversion rates

in Michaelis-Menten-type kinetic model. The amount and rate of glucose uptake by U251 non-resistant, U251 TMZ-resistant, U87, and Skov3 tumoroids was measured using a glucose assay. Using the continuum model and experimental uptake rates from Figure 6.3, we calculated the overall uptake rates by accounting for tumoroid heterogeneity (Section 6.4.2). Figure 6.4(b) compares the predicted rates of glucose uptake with the experimental data for U251 non-resistant, U251 TMZ-resistant, U87, and Skov3 tumoroids. U251 non-resistant and U251 TMZ-resistant tumoroids had the highest and the lowest rates of glucose uptake, respectively. The comparison between experimental data and model predictions, demonstrated the model's accuracy despite potential differences between 2D and 3D cultures.

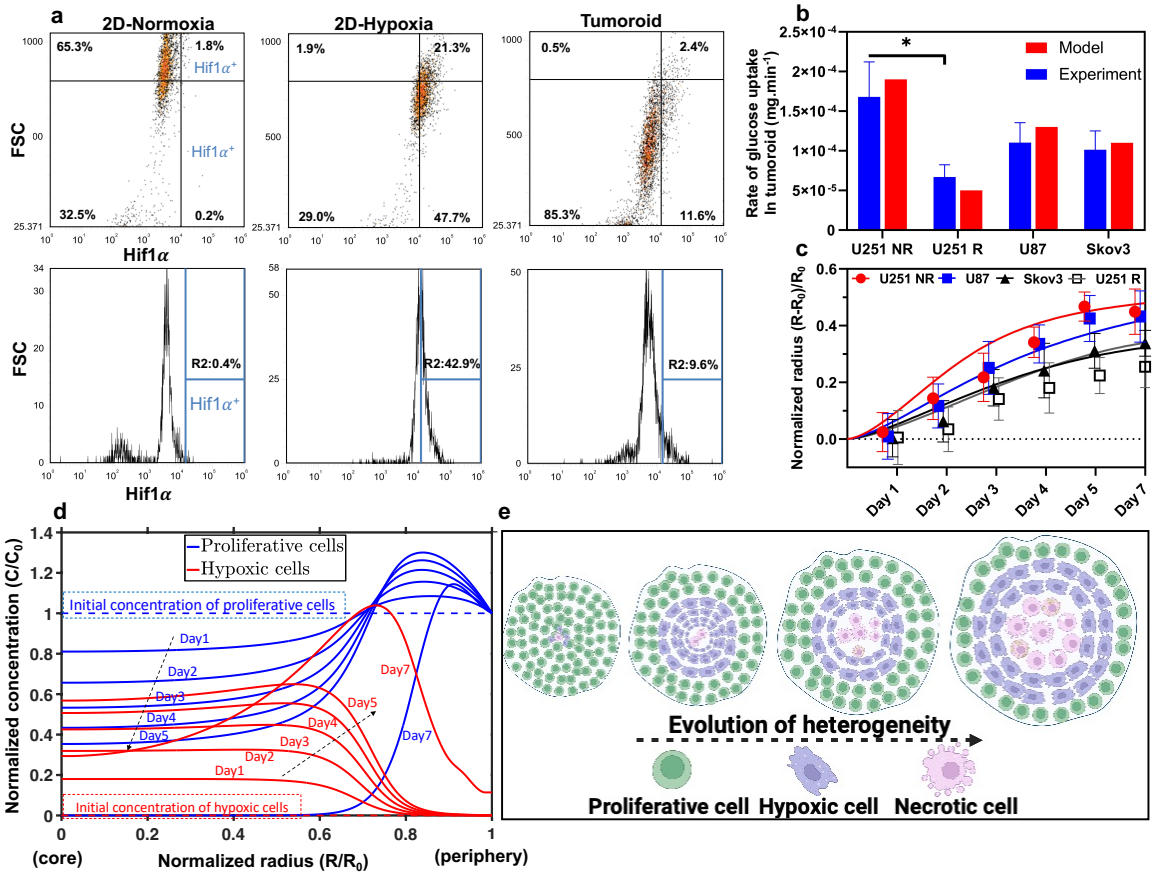

Figure 6.4: In-silico model predicts the rates of growth and glucose uptake in different tumoroids. Rate of normoxic-to-hypoxic conversion in monolayer cell culture was obtained using flow cytometry, and implemented to determine the formation of tumoroid hypoxic zones (a). Rates of glucose uptake and growth of hGBMs (U251 non-resistant, U251 TMZ-resistant, and U87) and Skov3 tumoroids measured experimentally and predicted by the proposed RD model (solid lines). U251 non-resistant and U251 TMZ-resistant tumoroids have the highest and the lowest rates of glucose uptake (b), and the highest and the lowest rates of growth, respectively (c). The distribution of proliferative and hypoxic cells in U251 non-resistant tumoroids is shown in (d). The schematic representation of the tumoroid heterogeneity evolution is shown in (e).

The model was validated against the free growth of in-vitro solid tumoroids generated from hGBMs, U251 non-resistant, U251 TMZ-resistant, U87, and Skove3 cells. The diameter of tumoroids was measured for seven days and compared with model predictions. Figure 6.4(c) shows the size of tumoroids over time measured within the microwell arrays and predicted by the model, where U251 non-resistant and U251 TMZ-resistant cells display the highest and the lowest growth rate, respectively. The

Pearson correlation coefficient is 0.97 for U251 non-resistant and 0.99 for U251 TMZ-resistant, U87, and Skov3 tumoroids. The distribution of normoxic and hypoxic cells over time is depicted in Figure 6.4(d). As predicted by the model, proliferative cell concentrations internal to the tumoroids decrease over time due to the diffusion limit. Conversely, the concentration of hypoxic cells increases within the tumoroid near the center due to low oxygen levels, followed by a reduction in concentration due to cell necrosis. This leads to the formation of a secondary hypoxic rim behind the proliferative rim, shown by a peak on day seven. Normoxic cells require a higher concentration of glucose and oxygen for sustained metabolism. Therefore, their concentration at the outer boundary of tumoroids increases as they receive a high concentration of nutrients and proliferate at a higher rate, while their concentration decreases centrally due to a lack of nutrients. Conversely, the oxygen gradient causes normoxic to hypoxic conversion at the internal regions of tumoroids, leading to a heterogeneity in cells population within the tumoroids, as illustrated in Figure 6.4(e).

6.2.2 Discrete model links modules of random walk, cellular processes, and cell-neuron interaction to the continuum model

Volumetric tumor growth is limited due to environmental restrictions, resulting in different patterns of invasion. Various stimuli such as mechanical stress, hypoxia, chemoattractants, and nutrient gradients can trigger such invasion [206]. For instance, the expression of genes that induce matrix degradative enzymes (MDE), metalloproteinases (MMP), and epithelial-mesenchymal-transition (EMP) proteins can be upregulated in hypoxia (Figure 6.5(a)).

In particular, hypoxia-induced reactive oxygen species (ROS) influence integrin binding to ECM by activating pro-MMPs [207, 208]. These proteins alter cell adhesion properties regulated through surface receptors such as CD-44 and integrins that down-regulate cell motility. The proteolytic degradation of ECM components by MDE and MMP can upregulate cell motility [209]. Cellular migration mechanisms depend on cell morphology and external stimuli. Invasive tumor cells may become morphologically polarized and develop membrane protrusions allowing them to reach forward [155]. This mesenchymal motion is slow and requires strong adhesion between ECM and cells via integrins. On the other hand, amoeboid motion is the process of cells squeezing through pores in the ECM; this is relatively fast and does not require

strong adhesion forces. The former type of migration is directional (haptotaxis) and the latter can be both directional and random (chemokinesis) (Figure 6.5 (b)). The two mechanisms are captured by our HDC model (see 6.4.3). Changes take place at a cellular scale and require a discrete mathematical model to capture the cellular migration mechanisms. Moreover, these cellular processes strongly depend on the local properties of the system, such as nutrient concentrations and external stimuli, which are obtained by a continuum model as field variables.

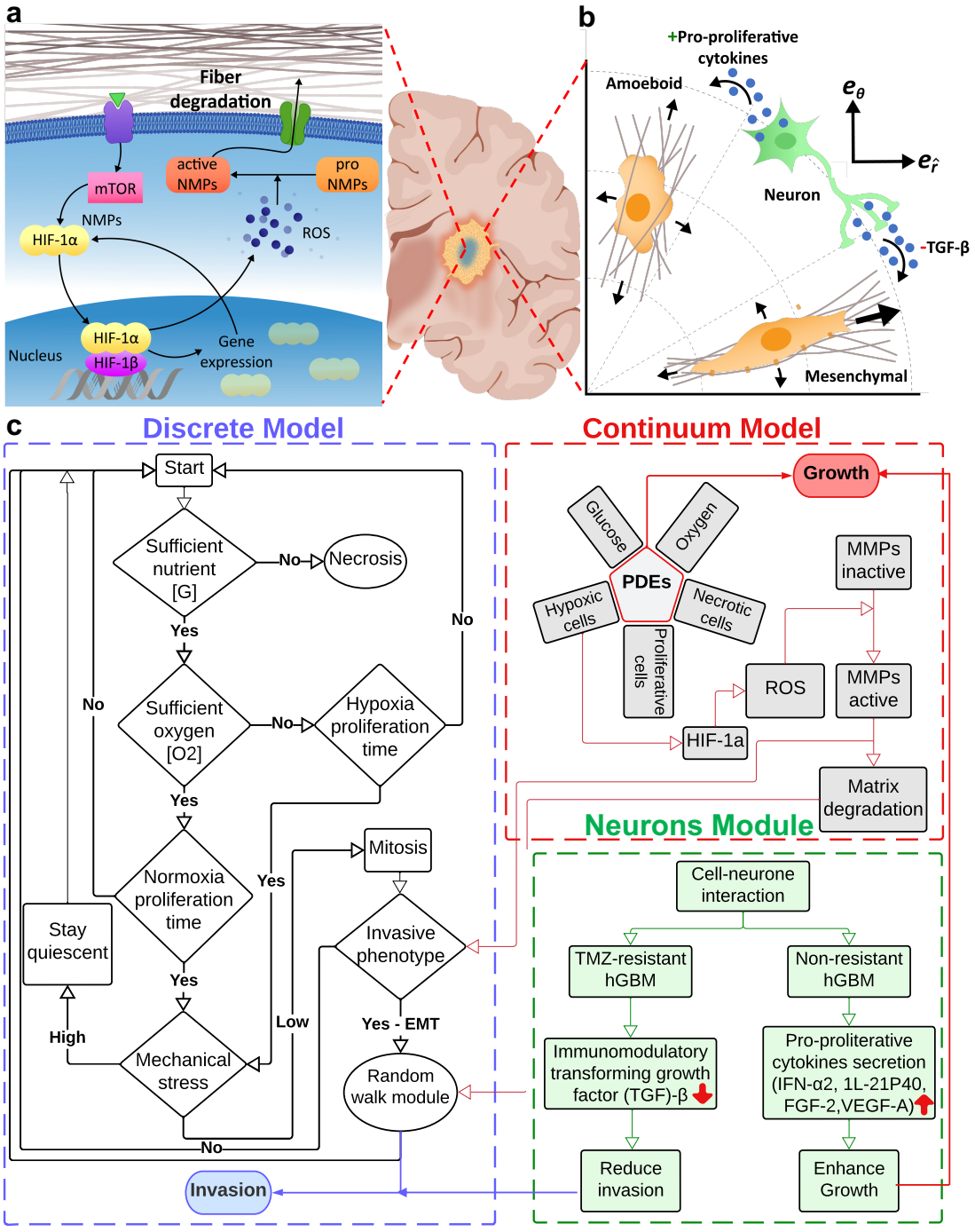

Figure 6.5: The HDC model includes continuum, discrete, and neuron modules, and links their components, e.g., random walk for cell migration, cellular process for individual cell progress, and neurons for cell-neuron interaction. Hypoxia upregulates matrix degradative enzymes such as MMPs that induce haptotactic gradients and facilitate cell migration (a). The cellular migration mechanism of invasive cells is comprised of directional (mesenchymal) and random (amoeboid) motions (b). Mesenchymal cells move via traction and adhesion to the fibers within the ECM, while amoeboid cells squeeze through pores. The simulation flowchart displays the interrelation between continuum variables and cellular processes to account for the evolution of a single invading cell, including cellular age, proliferation, migration, cell-neuron interaction. (c).

GBM-neuron synaptic interactions in the TME play a pivotal role in GBM growth and invasion. Our secretome analysis has demonstrated significant alterations in the secretion profile of inflammatory and invasion cytokines due to these interactions [163]. More importantly, results revealed that TMZ-resistant hGBM cells exhibited a distinct profile compared to non-resistant hGBMs, underscoring the importance of incorporating such interactions as a key variable in our HDC model. The secretome analysis indicated changes in the secretion profile of ECM remodeling cytokines such as IFN-α2 and IL-21P40, as well as growth factors FGF-2 and VEGF-A, in non-resistant hGBMs cocultured with neurons, suggesting enhanced growth potential in the presence of neurons. Conversely, in TMZ-resistant hGBMs, the secretion of the immunomodulatory transforming growth factor (TGF)-β family increased. We integrated these dual effects into the HDC model by randomly dispersing the initial concentration of neurons within the simulation domain (see 6.4.3). These neurons were considered fixed, with a time-independent secretion of cytokines. A single partial differential equation (PDE) was employed to capture the diffusion of pro-proliferative cytokines, including growth factors FGF-2 and VEGF. For invasion, cell-neuron interaction was deemed inactive unless cells were spatially close enough, reducing the probability of migrating cells remaining stationary due to the effect of secreted cytokines such as TGF-β

To simulate the complex dynamics of the system, the discrete model, which captures the cellular processes, is coupled with the continuum model. By linking these two models, the system receives updated information on field variables and implement them in the discreet model, which allows for more accurate predictions. Additionally, the neurons module is incorporated into both models to account for cell-neuron interactions, which play a crucial role in GBMs growth and invasion.

Overall, the distribution of field variables such as oxygen, nutrients, and concentration of cells, used in discrete module is continuously updated via the continuum model. Information on these variables were utilized as criteria in the discrete module determining cell proliferation, conversion to a hypoxic state, etc. Cell concentrations obtained by continuum module were used in random walk simulation. Additionally, continuum module provides information on the hypoxic cell population and subsequent upregulation of MMPs production and diffusion. ECM degradation by MMPs was then used in the discrete model as a pro-invasiveness component contributing to the haptotactic motion of invasive cells. The border of the bulk tumor and the discrete domain are continuously updated. This process involves obtaining the radii

of the tumoroid from the continuum solution and updating the reference location of invasion. The flowchart in Figure 6.5 (c) provides a detailed illustration of the interplay between the components of the HDC model and clarifies the point connections between the three modules.

6.2.3 Hybrid discrete-continuum model is capable of predicting the growth and invasion of tumoroids in recapitulated TME

In-vitro growth and invasion of tumoroids in the TME is mathematically modeled using an HDC technique that utilizes the information provided by the continuum model for the derivation of a discrete model. The volumetric growth of tumoroids and concentration fields of glucose and oxygen are predicted by the continuum model. Additionally, the random and directional migration of invasive cells are predicted by a discrete model. This model utilizes cellular processes to update the state of individual cells. Details of these models are described in Sections 6.4.3 and 6.4.3.

To study the growth and invasion of hGBMs U251 non-resistant and TMZ-resistant tumoroids, self-filling micro-well arrays (SFMAs) were used to initially generate uniform tumoroids Figure 6.6(a) for a tumoroid-on-a-chip platform. A central tumoroid-embedded hydrogel matrix chamber was bounded by two side channels for nutrient delivery Figure 6.6(b). To mimic the ECM of the brain, a combination of alginate, Matrigel, and a chemical cross-linker, $CaCl_2$ was used. This composition has been shown to recapitulate human brain ECM [153]. U251 non-resistant and TMZ-resistant tumoroids were mixed with the hydrogel matrix injected with and without neurons into the central chamber. After incubation for 10min, side channel reservoirs were filled with media and refreshed every 24hr to support long-term diffusion. Tumoroids began to exhibit a finger-type pattern of invasion while their volumetric growth decreased compared to free-growth samples. The growth and invasion of hGBM tumoroids was imaged using bTright-field and confocal microscopy Figure 6.6(c). ImageJ software was used to measure the tumor diameter and invasion lengths [210]. Results were compared with the HDC model predictions.

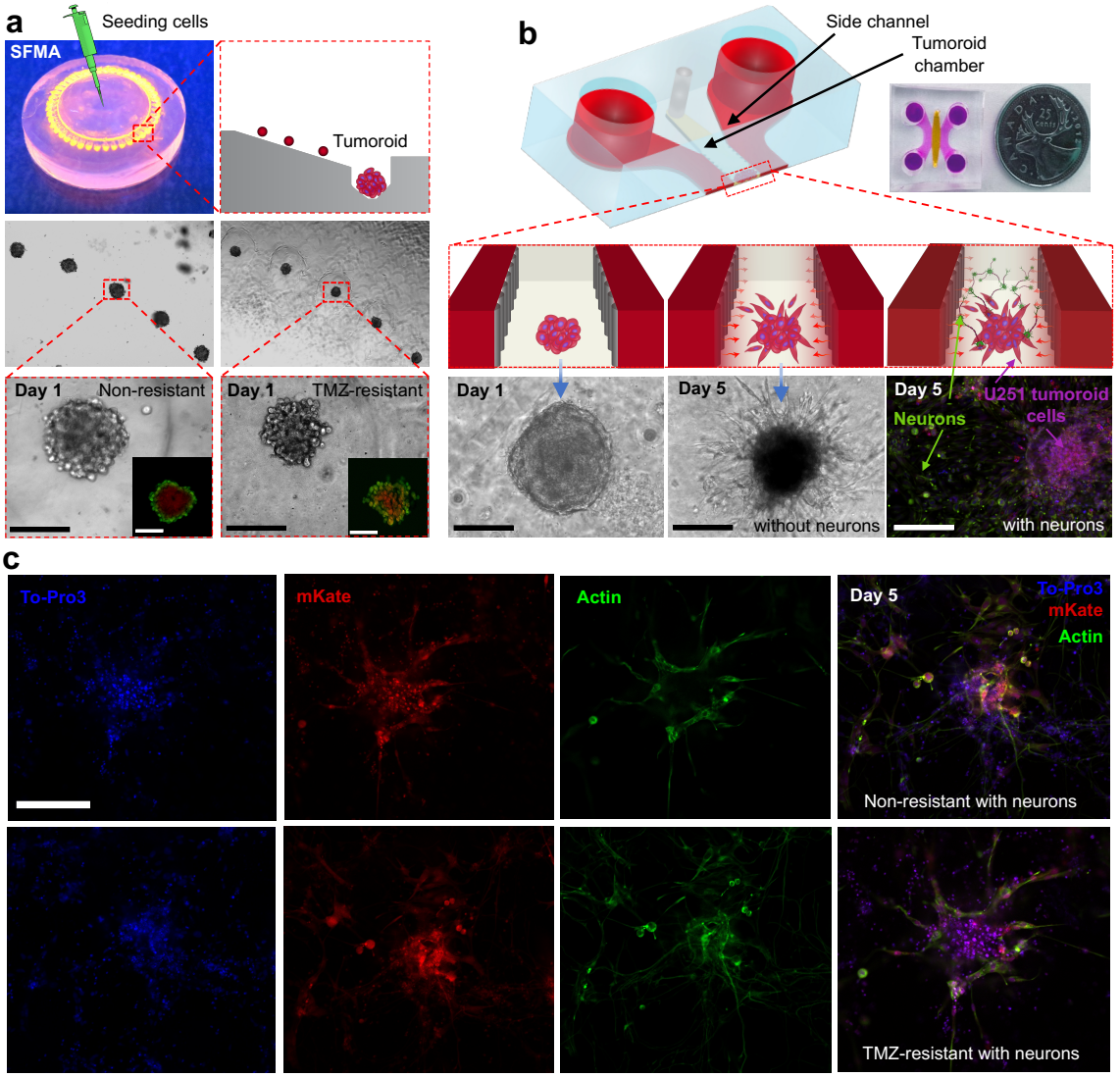

Figure 6.6: A tumoroid-on-a-chip platform recapitulates the TME comprised of U251 non-resistant and TMZ-resistant tumoroids co-cultured with neurons embedded in a hydrogel matrix. SFMAs (a) used to generate uniform tumoroids of U251 non-resistant and TMZ-resistant hGBMs. Tumoroids were mixed with an alginate/Matrigel hydrogel matrix and injected into the microfluidic chip, displaying a finger-type pattern of invasion (b). Tumoroids were co-cultured with neurons to quantify the variation in their growth and invasion due to cell-neuron interactions. The growth and invasion of non-resistant and TMZ-resistant tumoroids were monitored by stained with phalloidin and To-pro3 to visualize actin filaments (green) and nuclei (blue) (c). Scale bars are 250 μm.

The growth and finger-type invasion pattern of hydrogel matrix-embedded hGBM non-resistant and TMZ-resistant tumoroids were monitored over time (Figure 6.7).

The free growth of tumoroids within microwells involved no invasion (a), however, matrix-embedded tumoroids exhibited invasion characteristic (b, c). Fluorescent microscopy imagining of tumoroids, expressing red fluorescent protein mKate, co-cultured with neurons distinguished the invading cells from neurons (c). Although TMZ-resistant tumoroids exhibited a lower growth rate, they displayed longer invasion lengths. Compared to non-resistant cells, the resistant cells undergo morphological changes featured by elongation, a frequently reported mesenchymal characteristic [211–213]. This indicates higher invasiveness in TMZ-resistant tumoroids versus non-resistant. To implement this characteristic in the HDC model, we assigned the resistant cells a higher haptotaxis coefficient. In addition, resistant cells acquire other characteristics such as mitotic quiescence and OXPHOS metabolism, all of which infer a lower growth rate [214, 215].

Despite the radially symmetric distribution of nutrients and homogeneous TME, the in-vitro invasion pattern shown in Figure 6.7 reveals an asymmetric direction. This invasion pattern is attributed to the stochastic or random movement of cells within the TME influenced by factors such as Brownian motion, intercellular interactions with neurons, and complex architecture of TME [216, 217]. In addition, GBMs are often characterized by heterogeneity contributing to the random migratory patterns [218]. This behavior is incorporated in the HDC model by involving a certain level of randomness in determining the direction of migration for individual cells, with restrictions by other specific factors presented in 6.4.3.

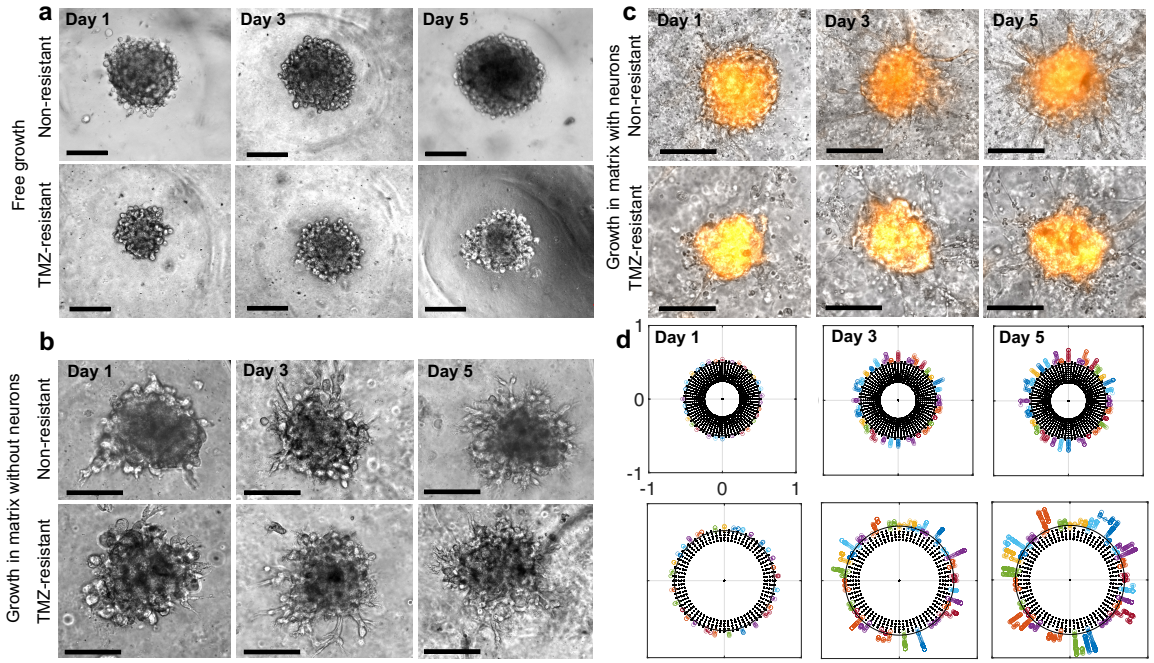

Figure 6.7: The growth and invasion pattern of U251 non-resistant and TMZ-resistant tumoroids. The free growth within microwell arrays and growth/invasion patterns within the alginate/Matrigel hydrogel matrix were imaged over five days using a tumoroid-on-a-chip platform (b, c). The invasion pattern of U251 non-resistant and TMZ-resistant tumoroids predicted by HDC model (d). Scale bars are 250 μm.

As seen in Figure 6.8(a), the model is capable of predicting the overall pattern of GBM tumoroids invasion. The pattern of invasion demonstrated in Figure 6.8(a)-right, has similarities with the in-vitro invasion observed in the tumor-on-a-chip platform shown in Figure 6.8(a)-left. Within the proliferative zone, the probability of stasis is higher than that of moving forwards or backwards Figure 6.8(b). At the interface of the tumor and the surrounding matrix, the probability of forwards motion increases as cells are free to migrate into the surroundings, enhanced by the stimulatory haptotactic effects of the matrix. The quantitative seven day measurement (Figure 6.8(c)) of growth and invasion of U251 non-resistant and TMZ-resistant tumor-on-a-chip platforms, together with the predictions of the HDC model, are respectively shown in Figure 6.8(d) and (e), similarly for tumoroids co-cultured with neurons (Figure 6.8(f) and (g)). The initial radii of tumoroids considered in the HDC model were set according to the experimental results. The hydrogel matrix-embedded TMZ-resistant tumoroids had an initially larger size but similar hypoxic zone size to the non-resistant counterparts.

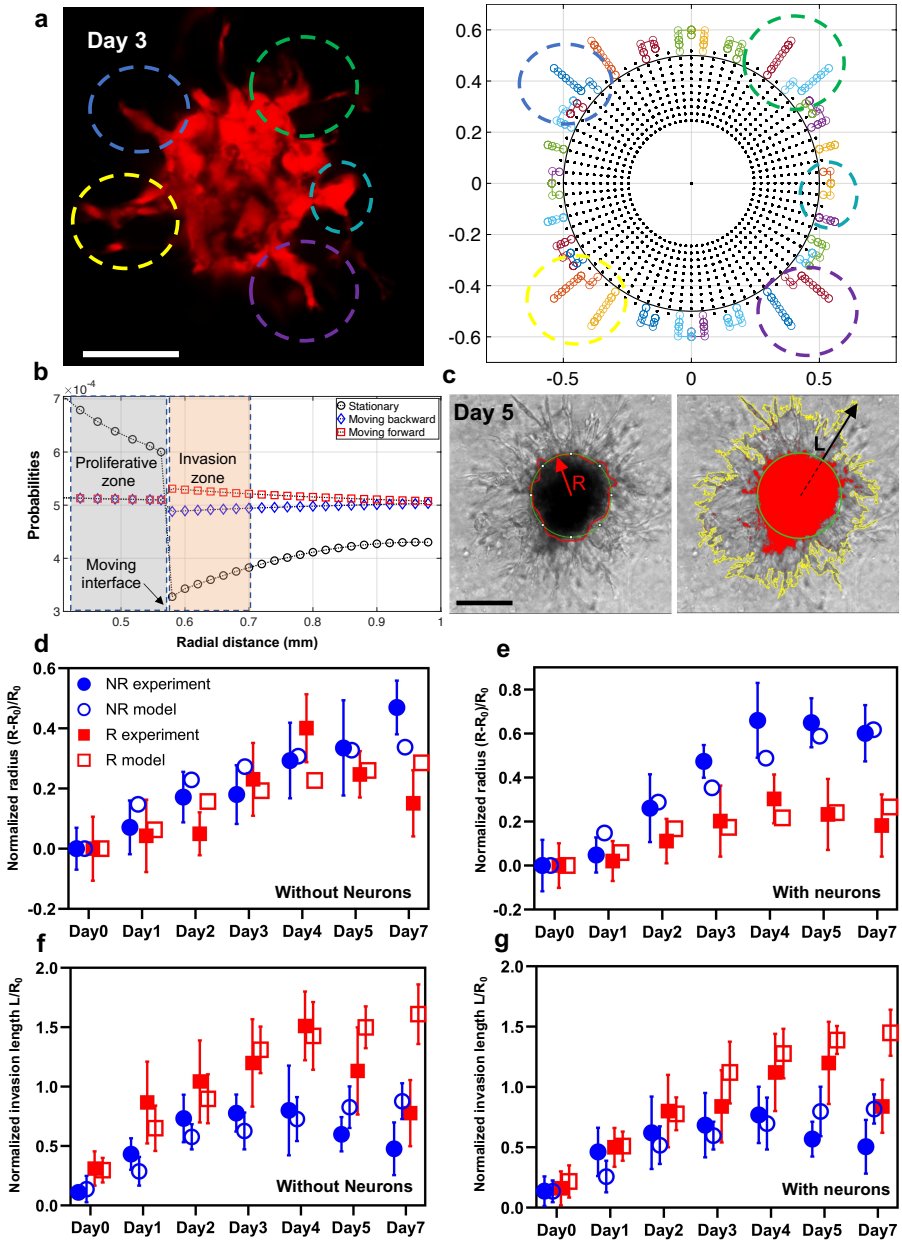

Figure 6.8: HDC model accurately predicted the growth and invasion length of tumoroids. In-vitro finger-type invasion pattern of GBM tumoroid vs. HDC model predictions (a). Radial probability distribution of invasive cells staying stationary, moving forward vs. moving backward (b). Invasion of GBM tumoroids embedded in a hydrogel matrix, with and without neurons, using a tumor-on-a-chip model compared to the pattern of cell invasion using the HDC model. Growth was estimated by measuring the tumoroid radius and invasion length was measured as the longest trace of cell migration (blue arrows) (c). The in-vitro growth and invasion were measured using a tumor-on-a-chip model over seven days. The radius of tumoroids (d, f) and length of invasion (e, g) were measured every 24hr and normalized with the initial radius compared with the model predictions. Scale bars are 250 μm.

Model predictions were in acceptable agreement with the experimental measurements. U251 non-resistant tumoroids showed faster volumetric growth, but smaller invasion length compared to U251 TMZ-resistant tumoroids. It should be noted that the HDC model lost the accuracy of prediction for invasion after day five when the invasion length significantly dropped. The Pearson correlation coefficient in growth, excluding day seven, for U251 non-resistant and TMZ-resistant were 0.89 and 0.71, and 0.83 and 0.90 in invasion, respectively. This coefficient for tumoroids co-cultured with neurons were 0.95 and 0.86 in growth, and 0.82 and 0.97 in invasion.

The performance of the HDC model was also evaluated by comparing its predictions of drug inhibitory effects with experimental data. To achieve this, we measured the viability variation in 2D-cultured non-resistant and TMZ-resistant hGB cells in response to various concentrations of TMZ. Using this data as input, the model's predictions regarding the length of invasion were compared to the invasion observed in TMZ-treated tumoroids, utilizing an EZ-seed-96 platform from Apricell Biotechnology Inc. Tumoroids were created in SFMA inserts within a 6-well culture plate and were embedded in an ECM matrix. Their invasive behavior was monitored over time. Figure 6.9(a, b) show the reduction in invasion length of non-resistant and TMZ resistant tumoroids treated with 50-500 μM of TMZ over five days, with the highest reduction caused by 500 μM. The variation in viability was shown in Figure 6.9(c) denoting the resistance of TMZ-resistant cells to the drug, and susceptibility of non-resistant cells. Using these data as model input (see 6.4.10), the invasion length of tumoroids was predicted and compared with experimental observation (Figure 6.9(d)).

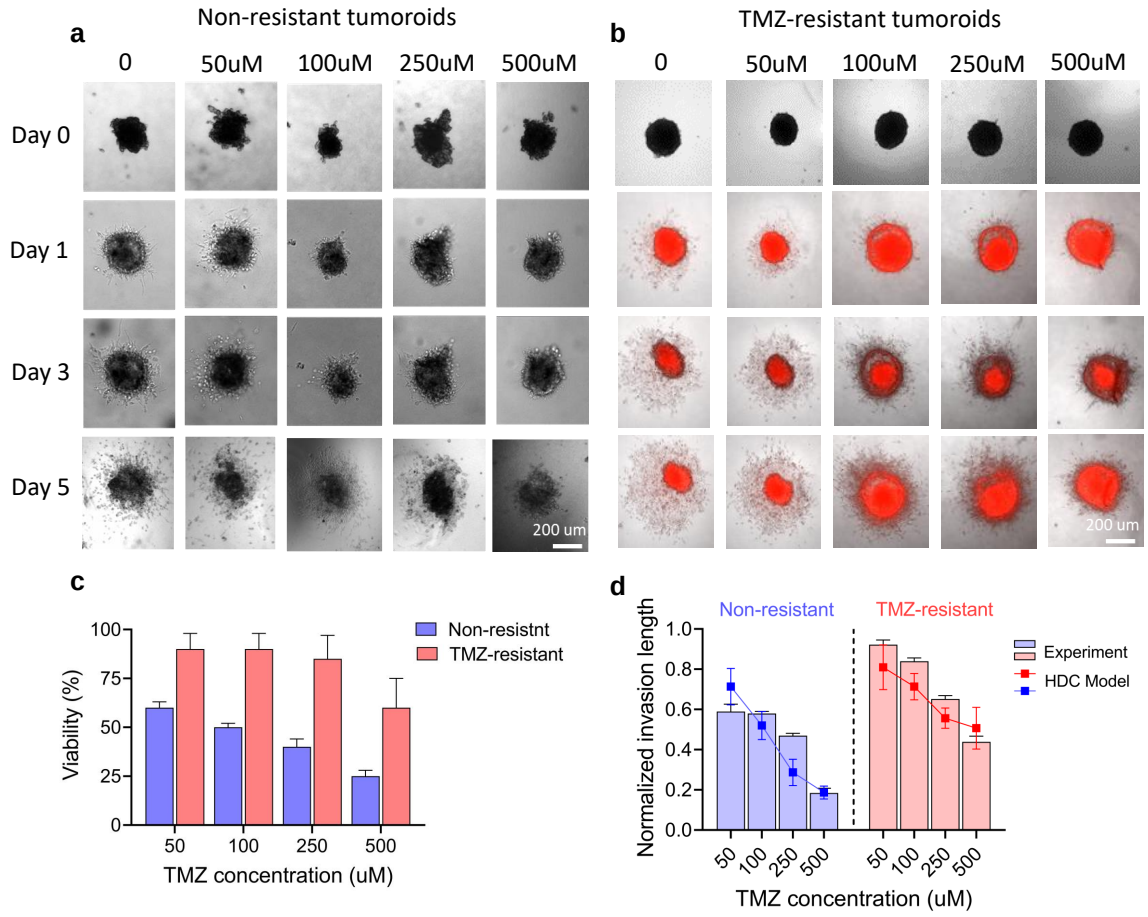

Figure 6.9: The HDC model predicts the inhibitory effect of TMZ on GB invasion. Inhibition of invasion in (a) non-resistant and (b) TMZ-resistant tumoroids treated with TMZ. (c) Viability variation in 2D-cultured non-resistant and TMZ-resistant GB cells in response to TMZ. (d) Model predictions on the invasion lenghth of GB compared to the invasion observed in TMZ-treated tumoroids in a tumor-on-a-chip platform.

6.3 Conclusion and Discussion

In this work, we integrated an HDC model with an in-vitro tumor-on-a-chip device to predict the 3D behaviour of hGBM such as growth, invasion, and drug response using 2D data acquisition. To that aim, the model integrates the continuum field of variables with a discrete approach, that includes modules of random walk and cellular processes. Model parameters such as rate of proliferation and glucose uptake were experimentally measured for 2D-cultured hGBM (U251 non-resistant and TMZ-

resistant) cell lines. GBM-neuron synaptic interactions were incoorporated to the model according to the cytokine profile of GB-neuron coculturs. The performance of the continuum model was checked by comparing the predictions on the rate of glucose uptake in tumoroids with the experimental measurements. Next, model predictions on the growth, invasion length, and drug response of hGBMs were compared with the in-vitro growth and invasion of hGB tumoroids cocultured with neurons in a tumoroid-on-a-chip platform. Results showed that the HDC model was able to quantitatively predict the characteristic of GBMs, i.e., U251 non-resistant tumoroids acquiring a higher growth rate, but lower invasion length, compared to U251 TMZ-resistant cells. Additionally, the stochastic approach utilized in the discrete module enabled the HDC model to capture the asymmetric finger-type invasion pattern. Future research directions include the incorporation of additional modules, including immune cells and the corresponding signaling pathways governing cancer/immune cell interactions, angiogenesis, and autophagy. This integration aims to recapitulate a more realistic TME. The formulation of each component and its interactions with others may necessitate the development of new assumptions and hypotheses. Understanding the dynamics of these hypothesis-driven components will require comprehensive local and global sensitivity analyses. Additionally, the model can be used to investigate metabolism-targeted cancer therapies. For instance, hGBMs exhibit an aberrant glucose metabolism that could be targeted as a potential therapeutic strategy [219].

6.4 Methods

6.4.1 Continuum reaction-diffusion model for tumor growth

A tumor is considered an nonhomogeneous system of particles (i.e. cells) that displays continuous changes in properties such as local concentration, velocity, and kinetic rate. To account for these changes, the distribution of key external components such as oxygen and glucose, and to moderate the common assumptions of constant proliferation rate and cell mobility, we propose a general form of reaction-diffusion

model

$$\frac{\partial C_p}{\partial t} = \nabla \cdot \left(\frac{C_p}{C} D_c \nabla C_p \right) + C_p \Big(\eta_p(G) + \phi(P) - S(g) \Big) , \tag{6.2}$$

$$\frac{\partial C_h}{\partial t} = \nabla \cdot \left(\frac{C_h}{C} D_c \nabla C_h \right) + C_h \eta_h(G) + C_p S(g) , \tag{6.3}$$

$$\frac{\partial C_n}{\partial t} = \nabla \cdot \left(\frac{C_n}{C} D_c \nabla C_n \right) - (C_p \eta_p + C_h \eta_h) , \quad \text{if } \eta_p < 0 \text{ and } \eta_h < 0 \tag{6.4}$$

$$\frac{\partial G}{\partial t} = \nabla \cdot (D_G \nabla G) - C_p \lambda_p(G) - C_h \lambda_h(G) , \tag{6.5}$$

$$\frac{\partial g}{\partial t} = \nabla \cdot (D_g \nabla g) - C_p \theta_p(g) - C_h \theta_h(g) , \tag{6.6}$$

$$\frac{\partial P}{\partial t} = \nabla \cdot (D_P \nabla P) + \kappa_g(N_0) - \kappa_d P , \tag{6.7}$$

in which $C_p(\mathbf{x}, t), C_h(\mathbf{x}, t), C_n(\mathbf{x}, t)$, $G(\mathbf{x}, t)$, $g(\mathbf{x}, t)$ and $P(\mathbf{x}, t)$ are concentrations of proliferative cells, hypoxic cells, necrotic cells, glucose, oxygen, and neuron-secreted cytokines, respectively. $\mathbf{x}$ is the position vector and $\partial(\cdot)/\partial t$ is material time derivative when the particle location is held fixed. The diffusion of cells C_i is proportional to the gradient of cell concentrations ∇C_i, where $i = \{p, h, n\}$ corresponds to prolifertive, hypoxic, and necrotic cells, respectively. $C = C_p + C_h + C_n$ is total cell concentration, implying that all three populations can coexist in the same location. Necrotic cells undergo a process of functional cessation and no longer function, but their physical entity persists. This persistence is particularly relevant in the tumor context, as necrotic cells are primarily located at the center of the tumor and are less exposed to environmental degradation. In line with the biological understanding, the model does not remove the population of necrotic cells from the structure of the tumor. D_c, D_G, D_g, D_P are the diffusivities of cells, glucose, oxygen, and cytokines. The mobility of each population is proportional to the ratio of the population to the total concentration of cells. For example, $K_i = (C_i/C)\, D_c$ where $i = \{p, h, n\}$ describes the influence of the coexistence of different populations on the cell diffusivity. $\eta_p(g)$ and $\eta_h(G)$ are proliferation rates of proliferative and hypoxic cells, respectively. $S(g)$ is the rate of proliferative-to-hypoxic conversion (PHC). $\lambda_p(n), \lambda_h(n), \theta_p(g)$ and $\theta_h(g)$ are rates of glucose and oxygen uptake by proliferative and hypoxic cells, respectively. The nutrient-corresponding rates are taken to be independent of oxygen concentration, and vice versa. $\phi(P)$ represents the pro-proliferative effect of cytokines, and their rates of production and degradation are presented by κ_g and κ_d, respectively. We assume a fixed time-independent concentration of neurons, i.e., the initial concentration

N_0, at the boundary for the purpose of the continuum model. In the discrete module, however, we dispersed the neurons randomly within the simulation domain to include single cell-neuron interactions. A Michaelis–Menten-type kinetic model is adopted for rates of oxygen consumption and PHC where θ_{max} and S_{max} are the maximum uptake and PHC rates, and θ_{cr} and g_{cr} are the corresponding critical concentrations of oxygen and glucose, respectively. We take a constant rate for oxygen consumption in hypoxia.

$$\theta_p = \frac{\theta_{max}}{1+\theta_{cr}/g}\,, \qquad S = S_{max}\left(1-\frac{1}{1+(g_{cr}/g)^2}\right). \tag{6.8}$$

To solve the system of equations, spherical coordinates are well suited to represent the spherical shape of tumors. We consider axisymmetric solutions, hence $\mathbf{x} = r\mathbf{e}_r$, $\nabla(\cdot) = \partial(\cdot)/\partial r\,\mathbf{e}_r$ and $\nabla\cdot(\cdot) = (2/r)\partial(\cdot)/\partial r + \partial^2(\cdot)/\partial r^2$. Following the procedure in [127] and by denoting the free surface boundary by $\Omega(t) = \{\mathbf{x}\in\mathbb{R}^3 \mid r - R(t) = 0\}$, the size of tumor can be obtained by

$$\frac{dR(t)}{dt} = -\mu\, D_c \frac{\partial C_p(r,t)}{\partial r}\bigg|_{r=R(t)}\,; \quad \text{where} \quad \mu = 1-\frac{p}{p+p_{cr}} \quad \text{and} \quad p = \epsilon E\,, \tag{6.9}$$

where $R(0) = R_0$ is the initial radius, μ represents the proportionality of the volumetric growth to the gradient of proliferative cells, $p = \epsilon E$, and P_{cr} is the critical pressure limiting the growth. μ is subject to variation due to the growth limit imposed by the pressure from the surrounding tissue. As a tumor grows, the increased volume applies pressure to the surrounding tissue, and vice versa. This pressure restricts growth and is influenced by factors such as the radial strain of the growing tumor and the mechanical properties of the tissue. We adopt a simple form for μ where either $\mu = 1$ for free growth condition, e.g., in-vitro tumoroids inside the micro-well array surrounded by media, or $\mu = 1 - \frac{p}{p+p_{cr}}$ for tumoroids embedded in a hydrogel matrix. Therefore, μ becomes a function of the mechanical properties of tissue (i.e., Young's modulus E, and the radial strain ϵ). Symmetry condition $\frac{\partial\square}{\partial r} = 0$ applies to the concentration of cells, nutrient, and oxygen at the center of tumor denoting zero changes at the center. Constant concentrations $C_p = C_p^{BC}, G = G_0$, and $g = g_0$ are imposed at the radius of tumor for proliferative cells, nutrients, and oxygen, respectively [127]. Zero gradient $\frac{\partial C_{\{h,n\}}}{\partial r} = 0$ is applied to concentration of hypoxic and necrotic cells at the radius of tumor R(t) defining zero flux at the boundary of tumor. Therefore, equations (6.2) to (6.7) in spherical coordinates are subjected to the following boundary and symmetry

conditions

$$\left.\frac{\partial C_p(r,t)}{\partial r}\right|_{r=0} = 0\,, \quad \left.C_p(r,t)\right|_{r=R(t)} = C_p^{BC}\,, \tag{6.10}$$

$$\left.\frac{\partial C_h(r,t)}{\partial r}\right|_{r=0} = \left.\frac{\partial C_n(r,t)}{\partial r}\right|_{r=0} = 0\,, \tag{6.11}$$

$$\left.\frac{\partial C_h(r,t)}{\partial r}\right|_{r=R(t)} = \left.\frac{\partial C_n(r,t)}{\partial r}\right|_{r=R(t)} = 0\,, \tag{6.12}$$

$$\left.\frac{\partial G(r,t)}{\partial r}\right|_{r=0} = 0\,, \quad \left.G(r,t)\right|_{r=R(t)} = G_0\,, \tag{6.13}$$

$$\left.\frac{\partial g(r,t)}{\partial r}\right|_{r=0} = 0\,, \quad \left.g(r,t)\right|_{r=R(t)} = g_0\,. \tag{6.14}$$

Initial concentration of cells within the tumor is taken to be C_p^{IC}, defining a homogeneity in initial cell populations, and G^{IC}, g^{IC} for nutrients and oxygen, respectively. Hence, the fallowing initial conditions (IC) apply to the system

$$C_p(r,t=0) = \begin{cases} C_p^{IC}, & 0 < r < R(0) \\ 0, & \text{elsewhere} \end{cases} \quad \text{and} \quad C_n(r,t=0) = C_h(r,t=0) = 0\,, \tag{6.15}$$

$$G(r,t=0) = G^{IC}\,, \quad g(r,t=0) = g^{IC}\,. \tag{6.16}$$

6.4.2 Rate of glucose uptake in tumoroids

To simplify the calculation, we considered a linear relationship between the concentration of glucose and the rate of glucose uptake in hypoxia, and in normoxia below the saturation. This approximation method facilitates the derivation of analytical solutions for the spatial distribution of glucose. In hypoxia, this is an acceptable approximation as the tumoroids are supplied with 1 mg/mL of glucose, therefore the concentration of diffused glucose in the tumoroids is always below 1mg/mL. According to Figure 6.3 (B), the rate of glucose consumption is below the saturation point at this range, making the linear approximation an acceptable simplification. To obtain analytical solutions for this equation, a practical approach was taken by dividing the tumor into four distinct zones characterized by radii as denoted in (6.17), in which the rate of glucose consumption was approximated by either a constant or a linear

function of G.

$$\frac{\partial G(r,t)}{\partial t} = D\nabla^2 G(r,t) - \eta(G\,(r,t))\ ,$$

$$\eta(G) = \begin{cases} \bar{\eta}_0 & G_{c_1} \leqslant G_1(r,t) \leqslant G_0 \qquad (R_{c_1} \leqslant r \leqslant R_0) \\ \bar{\eta}_0\, G_2(r,t)/G_{c_1} & G_{c_2} \leqslant G_2(r,t) < G_{c_1} \qquad (R_{c_2} \leqslant r \leqslant R_{c_1}) \\ kG_3(r,t) & G_{c_3} \leqslant G_3(r,t) < G_{c_2} \qquad (R_{c_3} \leqslant r \leqslant R_{c_2}) \\ 0 & G_4(r,t) = G_{c_3} \qquad (0 \leqslant r \leqslant R_{c_3}) \end{cases} \tag{6.17}$$

The corresponding axisymmetric steady-state solutions of (6.17) are given below.

$$G_1(r) = \frac{\eta_0}{6D}\, r^2 - \frac{C_1}{r} + C_2\,, \tag{6.18}$$

$$G_2(r) = \frac{C_3}{r}\, \cosh\sqrt{\frac{\eta_0}{DG_{c_1}}}\, r + \frac{C_4}{r}\, \sinh\sqrt{\frac{\eta_0}{DG_{c_1}}}\, r\,, \tag{6.19}$$

$$G_3(r) = \frac{C_5}{r}\, \cosh\sqrt{\frac{k}{D}}\, r + \frac{C_6}{r}\, \sinh\sqrt{\frac{k}{D}}\, r\,, \tag{6.20}$$

$$G_4(r) = C_7\,. \tag{6.21}$$

The corresponding axisymmetric steady-state solutions are subjected to the following boundary and continuity equations, where G_1 and G_2 are concentrations of glucose in the proliferative zone, corresponding to the constant and linear uptake rates, respectively. G_3 and G_4 are concentrations of glucose in hypoxic and necrotic zones, respectively. G_0 is the concentration at the boundary, G_{c_i} are critical concentrations at R_{c_i} (critical radii), η_0 is the rate of glucose consumption at saturated concentration, and D is glucose diffusivity.

$$G_1(R_0) = G_0\,, \qquad \frac{\partial G_1(R_{c_1})}{\partial r} = \frac{\partial G_2(R_{c_1})}{\partial r}\,, \tag{6.22}$$

$$G_1(R_{c_1}) = G_2(R_{c_1})\,, \qquad \frac{\partial G_2(R_{c_2})}{\partial r} = \frac{\partial G_3(R_{c_2})}{\partial r}\,, \tag{6.23}$$

$$G_2(R_{c_2}) = G_3(R_{c_2})\,, \qquad \frac{\partial G_3(R_{c_3})}{\partial r} = \frac{\partial G_4(R_{c_3})}{\partial r}\,, \tag{6.24}$$

$$G_3(R_{c_3}) = G_4(R_{c_3})\,. \tag{6.25}$$

To maintain the proper dimensionality of (6.17), the uptake rate η_0, obtained experimentally (see Figure 6.3 (A) and (B)) must be expressed in mg.min^{-1} per mL of tissue. Following previous research [199], we approximate a median tumoroid-derived cell vol-

ume of 1200 μm^3 (or 1.2 $\times 10^{-9}$cm^3) in tissue where 16.2% of the total volume is extracellular space. We consider a correction factor ($\alpha = 0.71$) for sphere packing (mean of face-centered cubic-factor $\alpha = 0.74$ and body centered cubic factor $\alpha = 0.68$). Hence, $\bar{\eta}_0 = \eta_0$ (mg.mL^{-1}.cell^{-1}.min^{-1}) $\times (1/1.2 \times 10^{-9}\text{cm}^3) \times (83.8/100) \times 0.71 = 4.9 \times 10^8$(mg.mL^{-1}.min^{-1}). The unknowns C_1 to C_7 can be obtained by substitution of (6.18)-(6.21) into (6.22)-(6.25). The total amount of glucose taken up by tumoroids can be found by integrating the uptakes at different zones.

$$\int_{R_{c_3}}^{R_{c_2}} kG_3(r)4\pi r^2 dr + \int_{R_{c_2}}^{R_{c_1}} \eta_0 \frac{G_2(r)}{G_{c_1}} 4\pi r^2 dr + \int_{R_{c_1}}^{R_0} \eta_0 4\pi r^2 dr = G_t\,. \tag{6.26}$$

6.4.3 HDC mathematical model for tumor invasion

Here, we use the reaction-diffusion model described in the previous section to predict the growth of tumoroids with a system of PDEs that form the governing equations. To include the TME, we introduce 2 equations that capture the change in the concentrations of matrix degradative enzymes $M(\mathbf{x}, t)$, such as MDE and MMP, and the concentration of macromolecules $f(\mathbf{x}, t)$ such as laminin and fibronectin in the surrounding tissue.

$$\frac{\partial M(\mathbf{x},t)}{\partial t} = D_M \nabla^2 M(\mathbf{x},t) + \gamma C_h(\mathbf{x},t) - \lambda M(\mathbf{x},t) f(\mathbf{x},t)\,, \tag{6.27}$$

$$\frac{\partial f(\mathbf{x},t)}{\partial t} = -\delta M(\mathbf{x},t) f(\mathbf{x},t)\,, \tag{6.28}$$

where D_M is the diffusivity of MDEs, γ is the rate of enzyme production by hypoxic cells, λ is the rate at which enzymes bind to the tissue, and δ is the rate of degradation of tissue by enzymes. The ECM repair is a relatively slow process compared to the degradation within the tumor microenvironment, hence, the repair term is neglected [220, 221]. We then take $M_i = 0$, the initial concentration of MDEs, and the boundary conditions to determine the following, and equations (6.27)-(6.28) together with the equations (6.2)-(6.7) form the continuum model.

$$\left.\frac{\partial M\,(r,t)}{\partial r}\right|_{r=0} = 0\,, \quad \left. M\,(r,t)\right|_{r=R_\infty} = 0\,. \tag{6.29}$$

To capture both haptotaxis and chemokinesis mechanisms, we write the cell flux J as the combination of random and directional fluxes where $C_{in}(\mathbf{x}, t)$ is the concentration of invasive cells, and D_{in} and χ_{hap} are the associated coefficients. The first term on

the right hand side of equation (6.30) represents the random motion of cells, while the second term accounts for the cell migration in the direction of the collagen gradient.

$$J = -D_{in}\nabla C_{in} + \chi_{hap} C_{in} \nabla f \,. \tag{6.30}$$

To model cell-neuron interactions in a discrete model, we randomly dispersed the initial concentration of neurons within the solution domain. The number of neurons selected for random placement within the discretized domain was determined by the concentration ratio of neurons to tumoroid cells. For example, if a tumoroid with concentrations of C_0 and an area of A_0 (2D projection on the simulation domain) was co-cultured with N_0 neurons within a domain of area A_t and n_t grids, then we considered $n_{dis} = n_t \times (A_0/A_t) \times (N_0/C_0)$ neurons. Empty grids were then numbered, and we randomly selected n_{dis} locations for the neurons. If an invading cell approaches a neuron, the probability of that cell moving in each direction decreased by 10% and the probability of staying stationary increased by 40% .

Module of random walk

The motion of a single invasive cell is tracked by a discrete method originally developed by Anderson et al. [34], where it is present for Cartesian coordinates. Here, we use polar coordinates $\mathbf{x} = r\,\mathbf{e}_r\,(\theta)$ to represent the circular shape of tumors. Considering temporal (i), radial (j), and angular (k) discretizations, the finite difference approximations (see supplementary) transform the PDEs (6.30) into an algebraic system of equations where $C^i_{j,k}$ is cell concentration at time i and point (j,k), obtained from continuum module. Equation (6.30) is used to find the probabilities of cell motions in different directions on the discretized plane. Implementing central finite differences technique to the equation (6.30) and solving for $C^{i+1}_{j,k}$ gives

$$C^{i+1}_{j,k} = P_0\, C^i_{j,k} + P_1\, C^i_{j+1,k} + P_2\, C^i_{j-1,k} + P_3\, C^i_{j,k+1} + P_4\, C^i_{j,k-1}\,, \tag{6.31}$$

where P_0, P_1, P_2, P_3, and P_4 are proportional to probabilities of cell staying stationary, moving in directions of $+r$ (forward), $-r$ (backward), $+\theta$ counter-clockwise and $-\theta$ clockwise, respectively (see supplementary). These movement probabilities are a function of cell position, collagen gradient, and diffusivity of invasive cells and hence link the discrete model to the continuum model. Therefore, the discrete model governs the migration of individual cells based on their interactions with the ECM.

Module of cellular process

The evolution of a single cell including the age, proliferation rate, phenotype (normoxic and hypoxic), mitosis, etc. is captured as the cell migrates through the ECM. The model is capable of incorporating cellular processes for individual cells, summarized in Figure 6.5(C). Each individual cell starts at a checkpoint where sufficient nutrient concentrations allow the process to continue, while low nutrient concentrations for an extended period leads to necrosis. The next checkpoint relates to local oxygen concentration; if the concentration is below 6%, the cell will be labeled with hypoxic status, otherwise the process continues. Cells are then assessed based on age (depending on the time step of simulation); a cell at proliferation age continues to the next checkpoint. This checkpoint is performed to see if the criteria for cell doubling is satisfied, i.e., whether the cell is reached maturity and if there is sufficient space surrounding the parent cell (the four neighbors) for the daughter cells to occupy. The latter condition is imposed by contact inhibition effect [222]. In the case of two or more available spaces, the positions of the new daughter cells are selected randomly. If no space is available, doubling is postponed until the next cycle. The local concentration of MMPs to the cell will then be checked. If the cell is experiencing a high concentration as evaluated by the continuum model, it will be able to go through EMT and labeled as invasive to assess by the random walk module. The cyclic process will then continue for the next cell.

Simulation process

Simulation processes were carried out in MATLAB. The first step of the simulation procedure is labeling individual and newborn cells with a unique identification number (ID). At each time step of the simulation, the position of invasive cells is first updated based on the random walk results as follows. The continuum model presented in Equations (6.2)-(6.7) is used to obtain concentrations of proliferative, hypoxic, and necrotic cells, as well as the concentrations of oxygen, nutrient, collagen, MMPs, and fibers within the ECM. This system of equations, subjected to the initial and boundary conditions, was solved using the finite difference method (see supplementary). In each time step, the five coefficients $P_0 - P_4$ were obtained at each location based on concentrations surrounding that point. Afterwards, five probability ranges, X_0 to X_4,

are generated by normalizing the five coefficients.

$$X_0 = 0 - \frac{P_0}{\sum_{n=0}^{4} P_n}\,, \tag{6.32a}$$

$$X_m = \left[\sum_{n=0}^{m-1} P_n - \sum_{n=0}^{m} P_n\right] / \sum_{n=0}^{4} P_n\,; \qquad m = 1, 2, 3, 4 \tag{6.32b}$$

Five probability ranges were calculated based on probability coefficients $P_0 - P_4$ to determine the invasion direction. A random number between 0 and 1 is then generated to determine the direction of cell motion, depending on the range where the number sits. A higher probability coefficient yields a broader range within which the generated number may fall. Consequently, cell motion in that direction is more likely. The continuum model therefore determines the probability of migration in each direction, and the selected direction restricts cell migration. The next step of the simulation is to update the cellular process based on the flowchart in Figure 6.5 (C). Nutrient and oxygen availability, age, possibilities of doubling, and the interplay between discrete and continuum models through MMP concentration are evaluated for each cell and the status and position of each cell is updated. The simulation then moves on to the next time step to re-update the migration and cellular process information. It should be noted that the volumetric growth of tumoroids was determined by evaluating the moving boundary using Equation (6.9). The time step of simulation was set to 1hr.

6.4.4 TMZ resistance cells

TMZ-resistant hGBM U251 cells were established using a pulsed-selection strategy [223]. U251 cells were cultured in Dulbecco's Modification Eagle Medium (DMEM) (Gibco; Cat#: 11965092), supplemented with 10% (v/v) Fetal Bovine Serum (FBS) (Gibco; Cat#: 10437-036),) and 1% (v/v) Penicillin/Streptomycin (Gibco, Cat#:15140122) and were incubated (37 °C, 7.5% CO_2) in a humidified incubator. After reaching approximately 80% confluence, cells were treated with 10 μM of TMZ (Sigma-Aldrich, CAS#:85622-93-1)over three weeks and recovered in TMZ-free media for four weeks. Cells were then provided with 250 μM TMZ in their media for three weeks and four weeks of recovery. Finally, the population of cells resistant to the 250 μM TMZ was selected and cultured in TMZ-free media for four weeks.

6.4.5 Rates of proliferation and glucose uptake in normoxia and hypoxia

Rates of proliferation and glucose uptake were measured for hGBM U251 non-resistant, U251 TMZ-resistant, U87, and Skov3 cells for different values of glucose concentrations. To simplify the model, these parameters were considered to be independent of oxygen concentration except for hypoxic cells. 20×10^3 cells were cultured in 24 well plates with DMEM supplemented with 10% (v/v) FBS and 1% (v/v) Penicillin/Streptomycin, and incubated (37°C, 5% CO_2). After reaching desired confluence, the media was removed from the wells and media with desired glucose concentrations (0.025, 0.05, 0.1, 0.15, 0.2, 0.25, 0.3, 0.4, 0.5, 0.6, 0.7, 0.8, 0.9, 1 mg/mL) were added to each well. The rate of change in glucose concentration in each well was monitored over 10hr. Glucose oxidase (GOD) (Sigma-Aldrich, CAS#: 9001-37-0) assay was used to monitor the glucose concentration, where glucose oxidase enzyme catalyses the oxidation of glucose to hydrogen peroxide (H_2O_2). The peroxidase (POD) (Sigma-Aldrich, CAS#: 9003-99-0), reaction was then used to colorimetrically visualize the formed H_2O_2 [224].

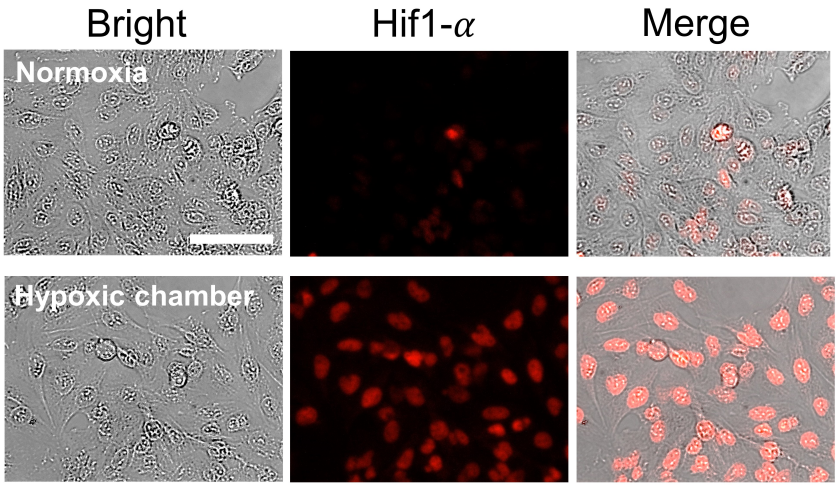

Figure 6.10: Twenty-four hours of culturing hGB cells in hypoxic chamber stabilized hif1-α. Scale bar is 100 μm.

The number of cells in each well was counted to normalize the uptake rate, and it was found that the uptake rate is constant above a threshold. Below this threshold, the rate becomes dependent on the glucose concentration. To measure the proliferation rate, the number of live cells was counted using trypan blue assay after adding

desired concentrations of glucose at different time points to obtain the doubling time. To measure the rates of glucose uptake and proliferation of hypoxic cells, cultured cells were transferred to a hypoxic chamber (Stemcell Technologies, Cat#: 27310) filled with a pre-mixed gas of 2% O_2, 5% CO_2, and 93% N_2. After 48hr, a glucose oxidase assay and trypan blue assay were used to measure the rates of glucose uptake and proliferation, as described previously. Figure 6.10 shows Hif1-α stabilization in non-resistant and TMZ-resistan cells.

6.4.6 Formation of tumoroids

In-vitro solid tumoroids were generated from hGBM U251 non-resistant, U251 TMZ-resistant, U87, and Skov3 cell lines. Cells were cultured in DMEM supplemented with 10% (v/v) FBS and 1% (v/v) Penicillin/Streptomycin, and incubated (37 °C, 5% CO_2). Cells were then dissociated with Gibco^{TM} Trypsin-EDTA (0.5%) (Sigma-Aldrich, P#: T4049), centrifuged at 300$\times g$ for five minutes and counted using a trypan blue assay (Sigma-Aldrich, CAS#: 72-57-1). Self filling arrays of non-cell adherent microwell inserts from Apricell Biotechnology Inc. (EZ-seed Plate, LOT #3101) were used to produce tumoroids. 500 μM of 10^6 cell ml^{-1} of cells were gently added to the loading chamber of SFMAs [84] and kept in a CO_2 incubator for four days to ensure the complete formation of tumoroids [127]. On day four, U251 non-resistant, U87 and Skov3 tumoroids were provided with TMZ-free media, and U251 TMZ-resistant tumoroids was provided with TMZ 250 μM cell media.

6.4.7 Tumoroid-on-a-chip-platform

A microfluidic chip with a central channel (15000 μm long, 1500 μm wide, and 400 μm hight) and side channels (15000 μm long, 3000 μm wide, and 400 μm high) with PDMS posts (300 μm high) was fabricated using two-layer photolithography. 400 μm of SU-8 100 layers were coated onto a microscope slide. One minute of corona treatment and 1300 RPM spin coating was followed by a 30 minute pre-bake at 65 °C and 90 minute bake at 95 °C to form the first layer. The second layer of SU-8 100 was formed similarly. 300sec of 350 Watt ultra-violate (UV) exposure was used to cross-link the layers. The master mold was built by a SU-8 developer (MicroChem) for 10 minutes and completed by washing with isopropanol. The ratio of 1:10 PDMS elastomer to cross-linker (Sylgard 184 Silicone Elastomer Kit, Ellsworth Adhesives) was used to cast the chip out of the master mold. The inlets and the outlets of the

chip were punched for the side channels. The chip was soaked in 70% ethanol for 20 minutes, followed by 30 minutes of UV exposure for sterilization.

6.4.8 Tumoroid-neurons co-culture

iPSC-derived neural progenitor cells (NPC) (ATCC, ACS-5003TM) were differentiated to neurons following the ATCC protocol. In brief, sodium alginate was dissolved in a medium containing 150 mM NaCl and incubated at 37°C for six hours. The solution was filtered through a 0.22 μm filter and kept on ice. Tumoroids were separated from the SFMAs and resuspended in DMEM-F12 (ATCC, 30-2006). Neuronal axons are primarily found in the white matter of the brain while gray matter contains the cell bodies of neurons. Considering that, we cocultured small number of neurons with tumoroids making sure the hydrogel is not packed with neurons resembling brain tumor microenvironment. 10^5 neurons were added to 12.5 μL of the tumoroids, and the mixture was combined with 65 μL of Matrigel, 4% alginate, and 1.2 μL $CaCl_2$ (1M) to create a tumoroid-neuron combination. 10 μL of the mixture was injected into the central chamber of the tumoroid-on-a-chip-platform and incubated. After 45 minutes, complete differentiation media (DMEM-F12 containing Dopaminergic Neuron Differentiation Kit, ATCC ACS-3004) was added and the chips were returned to the incubator.

6.4.9 Growth and invasion assay

The tumoroid diameter and invasion lengths were measured using ImageJ [10]. Imaging was initiated after day four, given the tumoroid size reduction observed during the early stages of formation studied in [127]. This occurs due to dominant intercellular adhesion forces that pull the cells together. When the pressure due to cellular proliferation balances out the adhesion forces and becomes dominant, tumoroids stop shrinking and start a monotonic growth phase after day four. The boundary of the tumoroid was marked to exclude the tumor from the invasion area. A circle was fitted on the boundary of the marked area to approximate tumoroid diameter. The average of the largest and smallest diameters was considered for non-spherical tumoroids. To measure the invasion length, images were converted to 32-bit grayscale, enabling the software to segment the images into features of interest. The boundary of the invasion was then highlighted and the invasion length was measured.

6.4.10 Drug inhibitory

Drug inhibitory effect on the invasion was incorporated into the model for both non-resistant and TMZ-resistant tumoroids through two analyses. Firstly, considering the viability of 2D-cultured cells under treatment, we establish the concentration of TMZ that reduces viability below 50% as the threshold. This threshold is utilized to eliminate invasive cells from the discrete model. Secondly, for concentrations below this threshold, we decrease the probability of movement in all directions. This reduction is proportional to the ratio of the concentration to the viability threshold. Consequently, the probability of staying stationary will increase. For instance, suppose a cell with moving probabilities of P_0, P_1, P_2, P_3, and P_4 (see 6.4.3) is exposed to m (μM) of TMZ. The following PDE obtains the distribution of TMZ,

$$\frac{\partial m}{\partial t} = \nabla \cdot (D_d \nabla m) - \lambda_{Cp} C_p m - \lambda_{Ch} C_h m \,, \tag{6.33}$$

where D_d is the diffusivity of TMZ, λ_{Cp} and λ_{Ch} are rates of TMZ absorption by proliferative C_p and hypoxic C_h cells. Given the viability threshold m_0 (μM), the following adjustments occur: (i) if $m \geq m_0$, the cell will be removed from the model, (ii) if $m < m_0$, the new probabilities will reduce to $P_i^* = [1 - (m/m_0)]\, P_i$, where $i = \{1, 2, 3, 4\}$ represents the direction of movement. Afterwards, the new probability ranges X_0, X_1, X_2, X_3, and X_4, will be obtained following the procedure in 6.4.3 to determine the movement of the invasive cell.

6.4.11 Immunofluorescence imaging

Flow cytometry was used for semi-quantitative analysis of hypoxia-inducible factor-1 alpha (Hif1-α). Prior to analysis, the cells were subjected to a series of preparatory steps, including washing in phosphate-buffered saline (PBS), trypsinization with trypsin-EDTA, resuspension in culture media, and centrifugation at 400 g for three minutes. These steps were done on ice to prevent Hif1-α degradation. The resulting pellet was subsequently resuspended in 90% methanol and incubated at -20°C for 15 minutes to fix the cells. All steps were performed on ice to prevent non-specific interactions and maintain sample integrity. The methanol was then neutralized with excess PBS, and the cells were washed and centrifuged to remove any remaining methanol. The resulting cell pellet was resuspended in PBS, and Hif1-α monoclonal antibody (Mgc3) PE-conjugated (Cat#: 12-7528-82) was added according to the man-

ufacturer's protocol for protein detection. To eliminate any non-specific interactions, a mouse IgG1 kappa isotype control PE (Cat#: 12-4714-41) was employed as a negative control.

To prepare the tumoroid and neuron cells for immunostaining, they were treated with 3.7% formaldehyde (VWR) and left at room temperature for 30 minutes. The samples were washed three times with Dulbecco's phosphate-buffered saline (DPBS) for five minutes each time. The fixed samples were then treated with a blocking buffer containing 5% bovine serum albumin (BSA; Jackson ImmunoResearch) and 0.3% Triton X-100 (Bio Basic) in DPBS and left to incubate at 4°C overnight. After that, an antibody solution containing 1% BSA and 0.3% Triton X-100 in DPBS was added and left to incubate overnight at 4°C in the dark, with phalloidin (Thermo Fischer Scientific, A12379) at dilution ratio of 1:1000. The samples were washed three times with DPBS and treated with To-pro3 (Thermo Fischer Scientific, T3605) solution (1:1000) to stain the nuclei, which was left to incubate for 30 minutes at room temperature in the dark. The nuclei staining solution was removed, and the samples were washed three times with DPBS and incubated for five minutes. The samples were then kept at 4°C in the dark until imaging was performed, and all staining solutions were introduced to tumoroids through the blood channels.

Live/Dead kit (Invitrogen, MP03224) was used to prepare the staining solution by mixing 1 μM calcein and 4 μM ethidium homodimer-1. Tumoroids were washed from SFMAs, transferred to 96 well plates, and 100 μL of Live/Dead solution was added to the wells. After 2hr incubation at room temperature and protection from light, tumoroids were imaged using confocal microscopy.

6.4.12 Statistical analysis

All experiments were independently repeated at least three times. Simulations involving randomness, e.g., invasion length, were repeated 10 times. Average values and standard deviations are reported. Significance analysis was performed using two-way ANOVA in GraphPad Prism with a p-value of 0.05. Average values and standard deviations are reported.

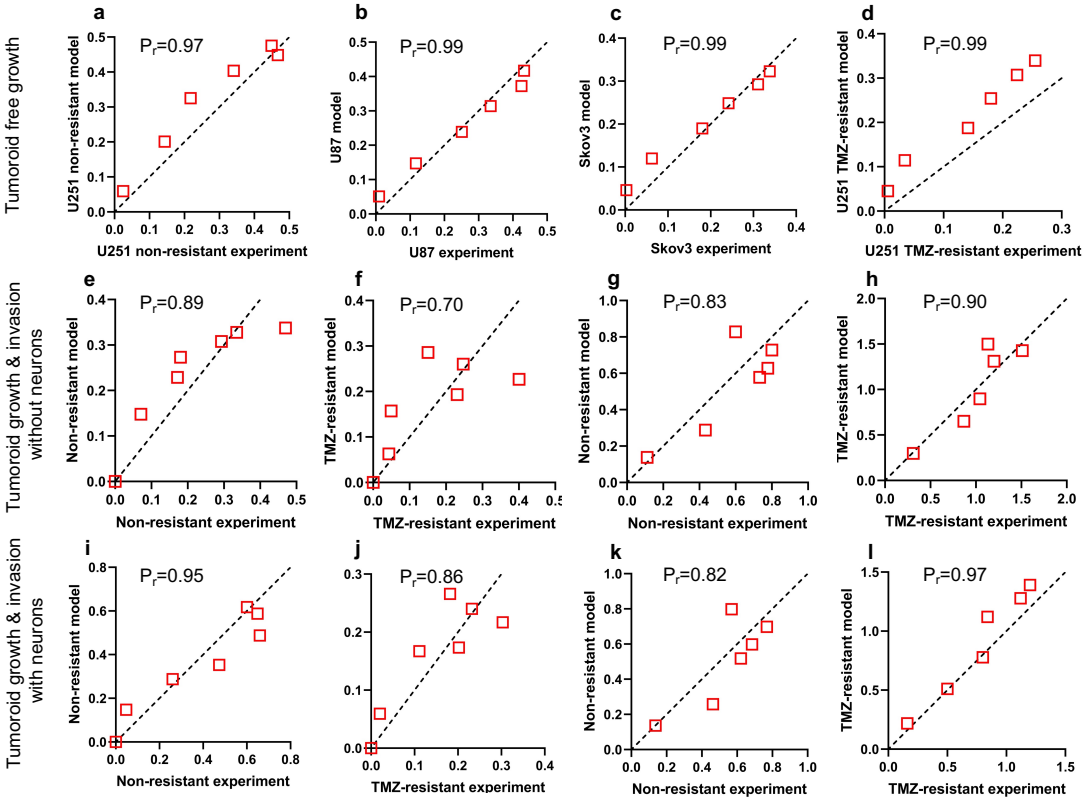

Figure 6.11: Linear correlations between experimental result and HDC model predictions. Pearson correlation coefficient for the free growth is 0.97 for U251 non-resistant (a) and 0.99 for U87 (b), Skov3 (c), and U251 TMZ-resistant (d) tumoroids. The coefficient for tumoroids embedded in hydrogel matrix without neurons is 0.89 and 0.70 for the growth (e, f), and 0.83 and 0.90 (g, h) for the invasion, respectively for U251 non-resistant and U251 TMZ-resistant tumoroids. The coefficient for tumoroids embedded in hydrogel matrix with neurons is 0.95 and 0.86 for the growth (i, j), and 0.82 and 0.97 (k, l) for the invasion, respectively for U251 non-resistant and U251 TMZ-resistant tumoroids.

The pearson correlation coefficient was calculated to measure the linear correlation between the experimental results and model predictions of free growth (Figure 6.11 (a), (b), (c), and (d)), growth and invasion in hydrogel matrix without neurons (Figure 6.11 (e), (f), (g), and (h)), and with neurons (Figure 6.11 (i), (j), (k), and (l)).

Acknowledgments: The authors would like to acknowledge the BC Cancer Foundation, Canadian Foundation for Innovation (CFI), and Natural Sciences and Engineering Research Council of Canada (NSERC) for supporting this work.

Competing interests: The authors declare no competing interests.

Author contributions: M.A. (Meitham Amereh), M.A. (Mohsen Akbari) and V.C. developed the concept and the methodology. M.A. (Meitham Amereh) and B.N. developed the theory. M.A. (Meitham Amereh) carried out the overal analysis and the simulation. M.A. (Meitham Amereh) and S.S. performed the experiments. M.A. (Meitham Amereh), T.W. and P.D. performed the biological data analysis. M.A. (Meitham Amereh) and M.A. (Mohsen Akbari) prepared the original draft. All authors contributed in reviewing and editing the manuscript.

6.5 Supplementary Information

Model parameters

To formulate model parameters, including rates of proliferation and glucose uptake in normoxia and hypoxia, nonlinear interpolation was obtained for the data in Figure 6.3. The following exponential plateau function was adopted.

$$f(X) = V_{max} - (V_{max} - V_{min})\, e^{-KX}\,, \tag{6.34}$$

where X represents the concentration of supplied glucose, $f(x)$ is the approximated rates of glucose uptake or proliferation, V_{max} is the maximum rate at saturated glucose concentration, V_{min} is the minimum rate, and K is the rate constant. The units for V_{max} and V_{min} corresponded to the uptake rate is mg.mL^{-1}.cell^{-1}.min^{-1}, and corresponded to the proliferation rate is h^{-1}. K is in mg.mL^{-1}. Table 6.2 (supplementary data) includes the values of these constants for U251 non-resistant, U251 TMZ-resistant, U87, and Skov3, obtained from Figure 6.3. These non-linear rates were incorporated into the HDC model as inputs. Model parameters obtained from the literature are shown in Table 6.3.

Finite difference approximation

Spherical coordinates and discretized PDEs in the r and θ direction were used, with the following operators.

$$\nabla \square = \frac{\partial \square}{\partial r}\, \boldsymbol{e}_r + \frac{1}{r}\frac{\partial \square}{\partial \theta}\, \boldsymbol{e}_\theta\,, \tag{6.35}$$

$$\nabla^2 \square = \frac{1}{r^2}\frac{\partial}{\partial r}(r^2\, \frac{\partial \square}{\partial r}) + \frac{1}{r^2 \sin\theta}\frac{\partial}{\partial \theta}\,(\sin\theta\, \frac{\partial \square}{\partial \theta})\,. \tag{6.36}$$

Table 6.1: Critical values associated to the rates glucose uptake and proliferation in normoxia and hypoxia for hGBMs, U251 non-resistant, U251 TMZ-resistant, U87, and Skov3 cells.

Condition	Normoxia				Hypoxia			
Concentrations Rates	Glucose uptake			Proliferation	Glucose uptake			Proliferation
	Saturated		Critical	Saturated	Saturated		Critical	Saturated
	[G] ($mg.mL^{-1}$)	Uptake ($mg.cell^{-1}.min^{-1}$)	[G] ($mg.mL^{-1}$)	η (h^{-1})	[G] ($mg.mL^{-1}$)	Uptake ($mg.cell^{-1}.min^{-1}$)	[G] ($mg.mL^{-1}$)	η (h^{-1})
U251 (non-resistant)	0.6	3×10^{-9}	0.1-0.3	0.04	2	1.2×10^{-8}	0.3-0.5	0.02
U251 (TMZ-resistant)	0.7	2×10^{-9}	0.1-0.3	0.02	1.9	3×10^{-9}	0.3-0.5	0.01
U87	0.7	2.5×10^{-9}	0.5-0.7	0.03	2	9×10^{-9}	0.7-0.8	0.01
Skov3	0.6	1.9×10^{-9}	0.1-0.3	0.01	1.5	6×10^{-9}	0.5-0.7	0.008

Table 6.2: Rates of glucose uptake and proliferation in normoxia and hypoxia for hGBMs, U251 non-resistant, U251 TMZ-resistant, U87, and Skov3 cells. Data obtained experimentally shown in Figure 6.3 and formulated by an exponential plateau function. V_{max} and V_{min} are in mg.cell^{-1}.min^{-1} for uptake rates, and h^{-1} for proliferation rates. K is mL.mg^{-1}.

Conditions	Normoxia						Hypoxia					
Rates	Uptake rate			Proliferation rate			Uptake rate			Proliferation rate		
Parameters	V_{max} 10^{-9}	V_{min} 10^{-10}	K	V_{max} 10^{-2}	V_{min} 10^{-2}	K	V_{max} 10^{-9}	V_{min} 10^{-10}	K	V_{max} 10^{-2}	V_{min} 10^{-2}	K
U251 non-resistant	3.123	0.473	5.239	3.83	-0.955	0.835	13.110	-16.310	1.276	1.89	-3.42	2.293
U251 TMZ-resistant	2.2	-4.204	2.541	1.910	-1.525	2.049	3.590	-3.202	0.884	0.732	-2.073	3.497
U87	2.535	-0.851	2.598	2.81	-2.012	0.877	9.335	-9.462	1.111	0.78	-3.90	2.303
Skov3	1.930	-4.285	3.780	1.09	-1.369	3.971	5.866	-13.180	1.952	0.71	-4.03	2.221

Using central finite differences technique, the differential equations were transformed into an algebraic system of equations where j, k and i are radial, angular and temporal indices of material points.

$$\frac{\partial \square}{\partial t} = \frac{\square_{j,k}^{i+1} - \square_{j,k}^{i}}{\Delta t}, \tag{6.37}$$

$$\frac{\partial \square}{\partial r} = \frac{\square_{j+1,k}^{i} - \square_{j-1,k}^{i}}{2dr}, \quad \frac{\partial \square}{\partial \theta} = \frac{\square_{j,k+1}^{i} - \square_{j,k-1}^{i}}{2d\theta}, \tag{6.38}$$

$$\frac{\partial^2 \square}{\partial r^2} = \frac{\square_{j+1,k}^{i} - 2\square_{j,k}^{i} + \square_{j-1,k}^{i}}{2dr^2}, \quad \frac{\partial^2 \square}{\partial \theta^2} = \frac{\square_{j,k+1}^{i} - 2\square_{j,k}^{i} + \square_{j,k-1}^{i}}{2d\theta^2}. \tag{6.39}$$

Substitution in (6.30) and rearrangement of the terms gives the following, where P_0, P_1, P_2, P_3 and P_4 are respectively probabilities of cell staying stationary, moving backward, forward, clockwise and counter-clockwise, and obtained by the following.

$$C_{j,k}^{i+1} = P_0\, C_{j,k}^{i} + P_1\, C_{j+1,k}^{i} + P_2\, C_{j-1,k}^{i} + P_3\, C_{j,k+1}^{i} + P_4\, .C_{j,k-1}^{i} \tag{6.40}$$

$$\begin{aligned} P_0 = 1 + \tau dt \Bigg[& \frac{2D_{c_i}}{R(t)^2} \left(-\frac{1}{dr^2} - \frac{1}{\theta^2 r_{j,k}^2 d\theta^2} \right) \\ & + \frac{\chi_{hap}}{R(t)^2} \left(\frac{(f_{j+1,k}^{i} - f_{j-1,k}^{i})^2}{4dr^2} + \frac{1}{\theta^2 r_{j,k}^2} \frac{(f_{j,k+1}^{i} - f_{j,k-1}^{i})^2}{4d\theta^2} \right) \\ & - \frac{\chi_{hap}}{R(t)^2} \Bigg(\frac{f_{j+1,k}^{i} - 2f_{j,k}^{i} + f_{j-1,k}^{i}}{dr^2} + \frac{1}{r_{j,k}} \frac{f_{j+1,k}^{i} - f_{j-1,k}^{i}}{2dr} \\ & + \frac{1}{\theta^2 r_{j,k}^2} \frac{f_{j,k+1}^{i} - 2f_{j,k}^{i} + f_{j,k-1}^{i}}{d\theta^2} \Bigg) + \eta_p \Bigg], \end{aligned} \tag{6.41a}$$

$$P_1 = \tau dt \left[\frac{D_{c_i}}{R(t)^2} \left(\frac{1}{dr^2} + \frac{1}{2r_{j,k}dr} \right) - \frac{\chi_{hap}}{R(t)^2} \frac{f_{j+1,k}^{i} - f_{j-1,k}^{i}}{4dr^2} \right], \tag{6.41b}$$

$$P_2 = \tau dt \left[\frac{D_{c_i}}{R(t)^2} \left(\frac{1}{dr^2} + \frac{1}{2r_{j,k}dr} \right) + \frac{\chi_{hap}}{R(t)^2} \frac{f_{j+1,k}^{i} - f_{j-1,k}^{i}}{4dr^2} \right], \tag{6.41c}$$

$$P_3 = \tau dt \left[\frac{D_{c_i}}{R(t)^2} \frac{1}{\theta^2 r_{j,k}^2 d\theta^2} - \frac{\chi_{hap}}{R(t)^2} \frac{f_{j,k+1}^{i} - f_{j,k-1}^{i}}{4\theta^2 r_{j,k}^2 d\theta^2} \right], \tag{6.41d}$$

$$P_4 = \tau dt \left[\frac{D_{c_i}}{R(t)^2} \frac{1}{\theta^2 r_{j,k}^2 d\theta^2} + \frac{\chi_{hap}}{R(t)^2} \frac{f_{j,k+1}^{i} - f_{j,k-1}^{i}}{4\theta^2 r_{j,k}^2 d\theta^2} \right]. \tag{6.41e}$$

These probabilities link the discrete method to the continuum model.

Table 6.3: Model parameters used in the HDC model.

Model parameters				
Parameter	Definition	Value	Ref.	Note
D_c	Cell diffusivity	$1 \times 10^{-8}\,\mathrm{cm^2{\cdot}s^{-1}}$	[14]	
D_n	Glucose diffusivity	$4.2 \times 10^{-6}\,\mathrm{cm^2{\cdot}s^{-1}}$	[183]	
D_g	Oxygen diffusivity	$1.6 \times 10^{-6}\,\mathrm{cm^2{\cdot}s^{-1}}$	[183]	
D_m	Diffusivity of MDEs	$1 \times 10^{-9}\,\mathrm{cm^2{\cdot}s^{-1}}$	[220]	
E	Young's modulus of alginate/Matrigel hydrogel matrix	$1 \times 10^{-1}\,\mathrm{kPa}$	[153]	
P_{cr}	Critical stress	1kPa	[142]	Maximum allowable stress is 5 kPa [142]
θ_{max}	Maximum oxygen uptake rate	$2.7 \times 10^{-2}\,\mathrm{mol{\cdot}m^{-3}{\cdot}s^{-1}}$	[183]	
θ_{cr}	Critical concentration in oxygen uptake	$4.6 \times 10^{-3}\,\mathrm{mol{\cdot}m^{-3}}$	[183]	
θ_h	Oxygen uptake rate in hypoxia	$2.7 \times 10^{-3}\,\mathrm{mol{\cdot}m^{-3}{\cdot}s^{-1}}$	[183]	10% of the rate in normoxia
C_0	Initial concentration of cells	$1 \times 10^{4}\,\mathrm{mg.mL^{-1}}$	[147]	
n_0	Glucose supply concentration	$4.5\,\mathrm{mg{\cdot}mL^{-1}}$	Gibco DMEM	
g_0	Oxygen supply	$177\,\mu\mathrm{M}$	[225]	
f_0	Initial concentration of matrix fibers	$1 \times 10^{-9}\,\mathrm{M}$	[220]	
g_{cr}	Critical concentration of oxygen in PHC	$20\,\mu\mathrm{M}$	[225]	
χ_{hap}	Haptotaxis coefficients	$2.6{\times}10^3$ (non-resistant) $5{\times}10^3$ (TMZ-resistant) $\mathrm{cm^2{\cdot}s^{-1}{\cdot}M^{-1}}$	[38]	
γ	Rate of MDEs production	$1{\times}\ 10^{-5}\,\mathrm{s^{-1}}$	N/A	Value is proposed
λ	Rate of MDEs binding	$1{\times}\ 10^{-6}\,\mathrm{s^{-1}{\cdot}M^{-1}}$	N/A	Value is proposed
δ	Rate of macromolecules degradation	$1{\times}\ 10^{-2}\,\mathrm{s^{-1}{\cdot}M^{-1}}$	N/A	Value is proposed
κ_p	Rate of cytokines production	$1{\times}\ 10^{-5}\,\mathrm{s^{-1}}$	N/A	Value is proposed
κ_d	Rate of cytokines degradation	$1{\times}\ 10^{-6}\,\mathrm{s^{-1}}$	N/A	Value is proposed

Chapter 7

3D-Printed Tumor-on-a-Chip Model for Investigating the Effect of Matrix Stiffness on Glioblastoma Tumor Invasion

Contributions:
Meitham Amereh: Conceptualization, theory and simulation, methodology, validation, formal analysis, experiments, writing—original draft preparation, writing—review and editing
Amir Seyfoori: Conceptualization, experiments, methodology, experiments
Briana Dallinger: Experiments, writing—review and editing
Mostafa Azimzadehh: Writing—review and editing
Evan Stefanek: Experiments, writing—review and editing
Mohsen Akbari: Conceptualization, methodology, writing—review and editing, supervision, resources

Meitham Amereh[1,2,3], [1,2,3], Briana Dallinger[2], Mostafa Azimzadehh[1,2], Evan Stefanek[2] and Mohsen Akbari[1,2,3,4,*]

[1] Department of Mechanical Engineering, University of Victoria, Victoria, BC V8P 5C2, Canada

Biomimetics 2023, 8, 421. https://doi.org/10.3390/biomimetics8050421 https://www.mdpi.com/journal/biomimetics

[2] Laboratory for Innovations in MicroEngineering (LiME), Department of Mechanical Engineering, University of Victoria, Victoria, BC V8P 5C2, Canada
[3] Centre for Advanced Materials and Related Technologies (CAMTEC), University of Victoria, Victoria, BC V8W 2Y2, Canada
[4] Terasaki Institute for Biomedical Innovations, Los Angeles, CA 91367, USA
*Corresponding author: makbari@uvic.ca; Tel.: (+1) 250-721-6038

Abstract

Glioblastoma multiform (GBM) tumor progression has been recognized to be correlated with extracellular matrix (ECM) stiffness. Dynamic variation of tumor ECM is primarily regulated by a family of enzymes which induce remodeling and degradation. In this paper, we investigated the effect of matrix stiffness on the invasion pattern of human glioblastoma tumoroids. A 3D-printed tumor-on-a-chip platform was utilized to culture human glioblastoma tumoroids with the capability of evaluating the effect of stiffness on tumor progression. To induce variations in the stiffness of the collagen matrix, different concentrations of collagenase were added, thereby creating an inhomogeneous collagen concentration. To better understand the mechanisms involved in GBM invasion, an in silico hybrid mathematical model was used to predict the evolution of a tumor in an inhomogeneous environment, providing the ability to study multiple dynamic interacting variables. The model consists of a continuum reaction–diffusion model for the growth of tumoroids and a discrete model to capture the migration of single cells into the surrounding tissue. Results revealed that tumoroids exhibit two distinct patterns of invasion in response to the concentration of collagenase, namely ring-type and finger-type patterns. Moreover, higher concentrations of collagenase resulted in greater invasion lengths, confirming the strong dependency of tumor behavior on the stiffness of the surrounding matrix. The agreement between the experimental results and the model's predictions demonstrates the advantages of this approach in investigating the impact of various extracellular matrix characteristics on tumor growth and invasion.
Keywords: 3D-printing; tumor-on-a-chip; glioblastoma; in silico model

7.1 Introduction

Glioblastoma, an aggressive form of primary brain cancer with a low survival rate and limited treatment options, is one of the deadliest types of cancer. Despite advances in

treatment, patients typically survive less than 15 months after diagnosis. This is because it is difficult to surgically remove the tumor due to its rapid growth and invasion into adjacent regions of the brain [73, 74]. Understanding tumor invasion mechanisms may reveal therapeutic targets to stop or slow tumor progression, improving patient outcomes and leading to improved treatments. There are four different routes or patterns that the invasion of GBM can take: through the leptomeningeal space, the brain parenchyma, the white matter tracts, or the perivascular space. Depending on the invasion route, the GBM cells can produce varying degrees of heterogeneity when they invade other parts of the brain. This can make it more difficult to determine the prognosis and appropriate treatments for GBM [75, 226].

Invasion is one of the key hallmarks of tumors [227]. Gaining insights into tumor invasion mechanisms facilitates the development of combination therapies designed to disrupt key invasion pathways in the primary tumor [228]. In addition, invasion mechanisms and patterns may be specific to cancer type. Therefore, understanding tumor invasion may help develop a personalized approach which not only targets the cancer's unique characteristics but also enables early detection through diagnostic tools that are capable of identifying invasive behavior [229]. Moreover, targeted therapy can benefit from knowledge of tumor invasion, as these therapies can then be optimized using knowledge of how tumors invade surrounding tissues, ensuring that drug delivery systems effectively reach and target invasive cells, including those resistant to conventional treatments [230].

Overall, understanding the mechanism of cancer invasion enhances comprehensive strategies and treatment efficacy by addressing multiple aspects of cancer growth and spread, simultaneously.

Tumor modeling has revealed that the invasion and formation of invasive structures in glioblastoma cells varies depending on the stiffness of their matrix [77]. Recent research has demonstrated a direct connection between the ECM of the brain and its modifications surrounding the GBM niche [76]. In the initial phases of GBM, local changes in the ECM occur throughout the brain [231]. As the disease progresses, these changes also facilitate the invasive behavior of the tumor. The variations observed in the ECM of GBM primarily involve modifications in the expression levels of multiple components. They can influence rapid biological and physiological shifts within cellular functions and give rise to the development and progression of tumors [232]. Therefore, stiffness of the ECM represents a key mechanical factor that influences the progression of GBM.

Understanding this mechanism of invasion may help treat invasive tumors cells and improve patient prognoses [233, 234]. Recently, there has been an increasing focus on creating three-dimensional cancer models using spheroids, which involves forming clusters of tumor cells with a spherical shape. Spheroids recapitulate cell–cell interactions, ECM remodeling, and intercellular signaling [235, 236]. Creating tumoroids can be done using novel approaches, such as 3D bioprinting with different cells, extracellular matrices, and blood vessel networks [237, 238]. Refs. [239, 240] show advantages over earlier methods, such as hanging drops [241] and microwells [242]. There are many different 3D bioprinting methods, and digital light processing (DLP) 3D bioprinting can be a high resolution, fast, and high-throughput choice producing highly vascularized microstructures similar to those found in native tumors using cells and photocurable biomaterials [85, 243, 244].

Mathematical models are transforming our comprehension of biological systems through in silico modeling. This enables us to understand the interactions that underlie complex behavior in invasive tumors [127, 128]. These models can be generally categorized into either continuum or discrete individual-based models [245, 246]. Over the past several years, a third category that has the advantages of continuum and discrete models, the so-called Hybrid Discrete-Continuum (HDC) model, has been developed [240]. HDC models use continuum fields to build up the discrete approach; therefore, the process is at both micro and macro scales. The continuum part provides information on the field variables, such as densities and velocities, which are inputted into a discrete part to update the cellular interactions. In addition, tumor heterogeneity and TME components are key factors in developing realistic in silico models [247].

In this study, we investigated how the stiffness of the matrix influences the invasive behavior of human glioblastoma tumoroids. An open surface tumor-on-a-chip platform was 3D printed using a photocurable poly-(ethylene glycol) diacrylate (PEGDA) hydrogel. The chip models the human glioblastoma tumoroid microenvironment in separate chambers with embedded collagen. The current tumor-on-a-chip platform consists of microchannels that flow around a central chamber. This chamber is where tumoroids are embedded in the ECM. The microchannel around the ECM chamber is multifunctional and can either deliver localized therapy or generate a vascularized lumen network that surrounds the microtumor tissue. Additionally, this platform can conduct four experimental conditions at once in a single well, which is compatible with common well-plate tissue cultures. The platform creates a symmetrical distribution

of MMP1 through the ECM, resulting in a gradient of ECM stiffness for invasion analysis. This even distribution allows for the study of the effect of stiffness gradient on tumoroid invasion patterns, such as finger and ring types, from all directions. The microfluidic platform created a gradient of extracellular matrix stiffness within the collagen matrix. The impact of this gradient on the tumoroid's invasion behavior under varying gradients was investigated. To better interpret the experimental data, a hybrid mathematical model based on a continuous reaction–diffusion model was used to model tumor growth. In contrast, a discrete model was used to model cell movement into the surrounding tissue. This study uses experimental and computational methods to show how the matrix's stiffness affects the glioblastoma tumoroid's invasion pattern.

7.2 Materials and Methods

7.2.1 Materials

PEGDA (Mw 700 Da), LAP, and tartrazine were purchased from Sigma-Aldrich (St. Louis, MO, USA). Fetal bovine serum (FBS), phosphate-buffered saline (PBS), Dulbecco's modified Eagle's medium (DMEM) and penicillin were purchased from Gibco (Grand Island, NE, USA). The 10× phosphate buffered saline (PBS), 0.5 N NaOH and bovine collagen type 1 (10 mg/mL) were purchased from Advanced BioMatrix Inc. (San Diego, CA, USA). Collagenase type 2 was purchased from Worthington Biochemical Corporation (Lakewood, NJ, USA). Tumoroids culture plate was purchased from Apricell Biotechnology Inc. (Victoria, BC, Canada). The rest of the suppliers are indicated throughout the text.

7.2.2 DLP Stereolithography Apparatus

The bioprinting apparatus used was a DLP stereolithography printer (Lumen X, Cellink, San Carlos, CA, US). The main hardware components of the printing apparatus were the DLP projector, and the z-axis stage and motor. The projector power output can be varied from 10–30 mW/cm^2 and the wavelength of the projected light was 405 nm (visible light). The XY pixel resolution of the projector was 50 µm, the Z resolution of the motor was 5 µm, and the minimum printable layer height was 50 µm. The total build volume is 64 × 40 × 50 mm. Additional components of the

device are the build platform and vat. The hydrogels are built in a layer-by-layer fashion on the build platform, which attaches to the Z stage. The vat that contains the prepolymer solution is a petri dish coated with a layer of poly(dimethyl-siloxane) (PDMS). The PDMS prevented the construct from sticking to the vat during the crosslinking process.

7.2.3 3D Printing PEGDA Hydrogel

The prepolymer solution is composed of 15% v/v PEGDA (700 Da, Sigma Aldrich), 0.6% w/v lithium phenyl-2,4,6-trimethylbenzoylphosphinate (LAP; Sigma Aldrich), and 2.5 mM tartrazine (Sigma Aldrich) in distilled water. The components are measured into a falcon tube and dissolved by heating to 65 °C and by vortexing. The design that is to be printed is made in SolidWorks and converted to an STL file. To print, first the surface of the build platform is sonicated in ethanol for three minutes and set aside to dry. Next, the PDMS vat is cleaned with isopropanol and distilled water. With the build platform and vat in place, the printer Z stage is calibrated. The exposure time per layer is five seconds per layer and the power intensity of the projector is 21.5 mW. The first layer time scale value is lesser (3×) for smaller constructs and higher (5×) for larger constructs. The added exposure time given to the first layer of the print helps the construct adhere to the build platform. After the print is complete, the build platform is removed from the Z stage and the construct is carefully removed using a plastic razor. The construct is placed in a beaker containing distilled water, and this water is exchanged periodically to remove excess tartrazine from the construct.

7.2.4 Optimization of PEGDA Photoink

The prepolymer PEGDA solution was optimized for printing small horizontal channels. A systematic set of experiments were conducted to optimize each component of the prepolymer solution individually. The parameters of interest were LAP concentration, tartrazine concentration, and projector power, while the PEGDA concentration was maintained at 15%. One at a time, each component was varied (three values) while the other components were kept constant, and the best performing formulation was maintained for the next component test. Ideal exposure time per layer varied widely depending on the components in the prepolymer solution, so set values could not be predetermined prior to testing and a few values were tested with each for-

mulation. Performance of the printed hydrogel was based on material integrity and the smallest printable channel diameter. A horizontally oriented channel model with varying channel sizes (1.0, 0.50, 0.40, 0.30, 0.20, and 0.10 mm) was printed with each hydrogel formulation to test its performance. The values tested were 1.02, 2.04, and 3.06 mM LAP, 1.0, 2.5, and 4.0 mM tartrazine, and 14.0, 21.5, and 25.0 mW/cm^2 projector power. The optimized formulation consisted of 15% PEGDA, 2.04 mM LAP, and 2.5 mM tartrazine printed with projector power of 21.5 mW/cm^2 and 5 s per layer exposure time.

7.2.5 Glioblastoma Cell Culture and Tumoroid Preparation

Human glioblastoma (hGB) U251 cell lines expressing mKate, a red fluorescent protein (developed by Dr. Marcel Bally, Experimental Therapeutics, British Columbia Cancer Agency, Vancouver, BC, Canada) were cultured in DMEM supplemented with 10% FBS, 100 IU/mL penicillin and 100 mg/mL streptomycin. The U251 cells were incubated at 37 °C in a humidified atmosphere of 5% CO_2, and the culture medium was replaced every other day. At 90% confluency, cells were trypsinized into a single cell suspension for 5 min and, to neutralize trypsin, 6 mL of growth medium was added. The cell suspension was centrifuged at 1000 rpm for 5 min to avoid dead cell sedimentation. After removing the supernatant, cells were suspended in 1 mL of medium and counted using a standard hemocytometer. U251 multicellular tumoroid were grown in EZ-seed 3D culture plate from Apricell Biotechnology Inc. In the 3D tumoroid culture plate, U-shaped microwells made of agarose hydrogel served as self-filing microwell arrays (SFMA). To generate tumoroids, agarose microwells were firstly submerged into 1.2 mL culture media per well in 12 well plates, followed by cell seeding with a concentration of 500 $\times$ 10^3 cells/200 µL. Cell-loaded microwells were incubated for 4 days to form compact and round tumoroids.

7.2.6 3D Tumoroids Culture On-a-Chip

The four-day old cultured U251 tumoroids were collected from the SFMA platform by gentle washing with culture media. To mimic the tumor ECM condition of glioblastoma, bovine fibril collagen with a concentration of 4 mg/mL was used as the main hydrogel component of the model. To prepare the hydrogel/tumoroids suspension, first the pH and ionic concentrations of the collagen solution were adjusted by adding 10$\times$ PBS and 0.5 N NaOH to the stock solution of collagen with a ratio of 1:1:8.

Afterwards, a certain volume of culture media containing one tumoroid was immediately mixed with collagen solution to achieve the desired concentration. The final collagen solution was gently introduced into the central chamber of the 3D printed microfluidic device and then incubated in an incubator at 37 °C for 45 min to complete crosslinking.

7.2.7 Enzyme Treatment and Cell Invasion Analysis

Effect of collagenase on the invasion length of the tumoroids inside the ECM hydrogel was studied using two different concentrations of collagenase type I, 0.001 and 0.01 mg/mL. Collagenase solutions with each concentration were made in culture media and introduced symmetrically through the inlet of the microfluidic platform and filled the side chamber of the device. For the invasion studies, the treatment was started immediately after tumoroid seeding and enzyme treatment lasted over three days. The effect of collagenase with different concentrations on tumoroid invasion was analyzed and quantified every day by fluorescent imaging using the Zeiss microscope.

7.2.8 Mechanical Properties of the Collagen Hydrogel

Rheological properties of the collagen hydrogel with and without treatment with collagenase was studied using an Anton Paar (MCR 302 Rheometer, Graz, Austria) rheometer with 25 mm diameter sandblasted plate-to-plate geometry (PP25/s) with 1 mm gap. An amplitude sweep test at the frequency of 1 Hz was performed and the linear viscoelastic region was determined for all gel formulations. Variations in shear stress as well as the viscoelastic parameters such as storage modulus, loss modulus, and complex modulus as a function of shear strain were recorded over the range of 0.1–10%. Oscillatory frequency sweep measurement was carried out at a 0.1–100 rad·s^{-1} in the viscoelastic region (0.5%) for all conditions to further characterize viscoelastic properties. Variations of the storage modulus (G′), loss modulus (G″), complex modulus (G*), and complex viscosity (η^*) against angular frequency sweep were also recorded.

7.2.9 Statistical Analysis

All experiments were repeated three times and the average and the standard deviation were reported. Significance analysis was performed using two-way ANOVA analysis.

Differences were considered statistically significant at p–value ≤ 0.05.

7.3 Results and Discussion

7.3.1 PEGDA Bioprinting Parameters Optimization

The Lumen X DLP printer was used to print the tumor-on-a-chip platform, Figure 7.1a. To optimize channel printing, horizontal and vertical channels were printed for ranges of variables. The prepolymer PEGDA solution was optimized to print small, horizontally aligned channels. The variables to be optimized were the LAP concentration, tartrazine concentration, projector power, and exposure time per layer (Figure 7.1b). Each variable was tested sequentially with three different test values while all other components were kept constant except for exposure time per layer which had to be adjusted for each test case. PEGDA concentration was not a variable that was tested and was maintained at 15% during the optimization process. For each variable, a horizontal channel model with varying channel sizes from 1.0 mm to 0.1 mm in diameter was printed with each PEGDA formulation. The smallest channel that could be printed was recorded from each test, with the goal being to print the smallest possible channels (Figure 7.1c). LAP concentration was the first variable to be tested, once the best LAP concentration was determined, it was carried forward and then tartrazine concentration was tested, and once the best tartrazine concentration was determined, it was carried forward to the projector power testing. At the end of this optimization process, the PEGDA formulation which produced the smallest channel diameter was 15% PEGDA, 2.04 mM LAP, 2.5 mM tartrazine, 5 s/layer exposure, and 21.5 mW/cm^2 power intensity. This optimal formulation produced hollow horizontal channels as small as 0.3 mm in some tests, and consistently produced hollow 0.4 mm diameter channels. The relationship between LAP and tartrazine concentration in the PEGDA formulation is shown in the figure. When the tartrazine concentration was too low, 1 mM tartrazine with 1.02 mM and 2.04 mM LAP, none of the channels printed hollow. LAP concentration did not have much effect on channel printing, but overall made the printed gel stiffer at higher concentrations. To test the accuracy of printing, a microfluidic chip with ten channel diameters from 1.0 to 0.1 mm was 3D printed, the diameter of each channel was measured using ImageJ, and the measured values were compared to the nominal diameters,i.e., horizontal lines (Figure 7.1d).

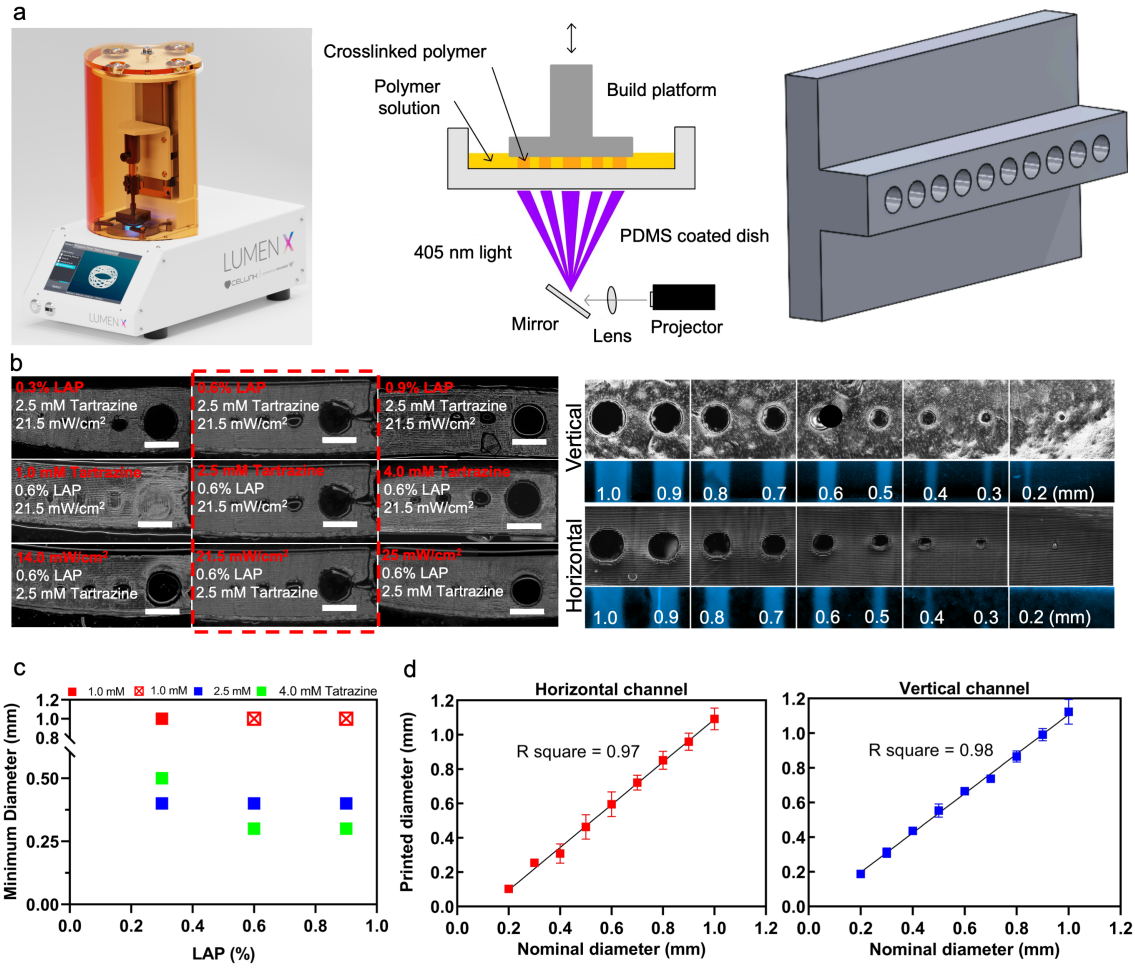

Figure 7.1: Optimizing printing variables for horizontal and vertical channels. (a) Image of the Lumen X DLP printer (left), schematic of basic DLP printer in operation (middle), and an example of a CAD model that was used to print vertically oriented channels of different sizes (right). (b) The change in printable channel diameter when a single component is varied in each row, such as LAP concentration, tartrazine concentration, or projector power, from the optimized prepolymer 15PEGDA solution of 2.04 mM LAP, 2.5 mM tartrazine, 21.5 mW/cm^2 power intensity, and 5 s/layer exposure time (left). Microscope images were taken of the sliced cross sections of the PEGDA channel constructs which featured channels with diameters of 1.0, 0.50, 0.40, 0.30, 0.20, and 0.10 mm. Channel cross-sections and top view of vertically printed and horizontally printed PEGDA channels (right). Purple fluorescent dye was injected into the channels to confirm that they were hollow. (c) Graph demonstrating the effects of tartrazine and LAP concentration in 15% PEGDA, 21.5 mW/cm^2 power intensity, and 5 s/layer exposure time. When tartrazine concentration was too low, hollow channels could not be printed, as demonstrated in the case of 1 mM tartrazine with 2.04 mM and 3.06 mM LAP (red crosses). (d) Ten channel diameters from 1.0 to 0.1 mm were printed in optimal condition and compared with nominal diameters. Scale bars are 1 mm.

7.3.2 Tumor-on-a-Chip Platform

Directional migration of the GBM is a biological phenomenon dependent on multiple factors including chemotaxis and hapto-taxis [166–168]. Collagenase type I (MMP1) as a member of the MMP family secreted in the tumor microenvironment has a massive effect on changes to local mechanical properties of the tumor ECM and subsequent migration of the tumor cells [248]. In this regard, we aimed to measure the effect of collagenase on the invasion behavior of U251 glioma tumoroids inside the fibril collagen hydrogel which mimics the main component of the ECM of the brain tumor microenvironment. Using a tumor-on-a-chip platform with multiple chambers, we cultured U251 tumoroids in collagen, with the capability of separately inducing each chamber, with different concentrations of collagenase (Figure 7.2a). This platform can conduct four experimental conditions at once in a single well, which is compatible with common well-plate tissue cultures. The microfluidic chip has a perfused round microchannel surrounding the central chamber. Tumoroids will be embedded within ECM inside the chamber, and they are perfused with the media and collagenase included media through the surrounding channel. This design creates a symmetrical distribution of MMP1 through the ECM, resulting in a gradient of ECM stiffness for invasion analysis. Each chamber contains an inlet and outlet channel, and collagenase solution with different concentrations was added to the microchannels from the inlet of the device. The microchannel around the ECM chamber is multifunctional and can potentially either deliver localized therapy or generate a vascularized lumen network that surrounds the microtumor tissue. A self-filling microwell array (SFMA) from Apricell Biotechnology Inc. was utilized to generate uniform tumoroids, which were then mixed with collagen and placed inside chambers (Figure 7.2b,c) [84]. The thin floor of the chambers enables clear microscopy imaging of growth and invasion of tumoroids over time (Figure 7.2d). Collagenase type I solutions with concentrations of 0.01 and 0.001 mg/mL were introduced to the collagen embedded tumoroids in the model through the peripheral channels of the microfluidic platform and incubated for 48 h. This platform enables the quantitative analysis of the tumoroid invasion over time. Our developed 3D printed microfluidic platform models how solid tumors behave in their extracellular matrix. Our platform can potentially employ various strategies that consider gradient physio–mechanical properties in cancer studies. The circular microchannels surrounding the central ECM chamber are designed to serve as a localized depot for chemo attractants. This enables us to model how tumor cells

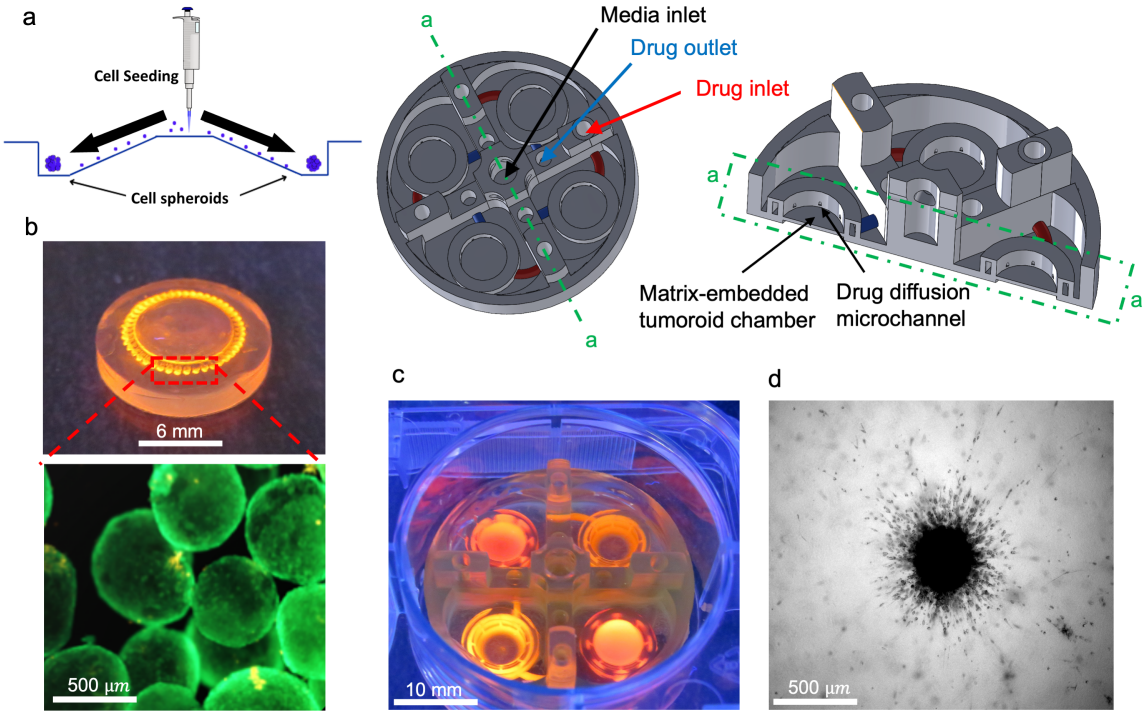

Figure 7.2: In vitro tumoroid invasion platform. (a) Single cell suspension seeded through the loading zone of a self-filling microwell array. (b) Tumoroids were formed after four days of culture and were transferred into the tumor-on-a-chip platform. (c) The platform was capable of growing tumoroids in four different chambers, each addressed separately, with an inlet and outlet for collagenase treatment. (d) Tumoroids embedded in bovine fibril collagen hydrogel were loaded into the open surface tumoroid-on-a-chip platform and their growth and invasion were monitored over time.

invade outward from the core tissue. Our platform can be used as an in vitro model to evaluate therapeutic payloads that trap invaded tumor cells. This leads to more efficient cancer therapy for invasive solid tumors.

7.3.3 Mathematical Modeling

Cancer cell migration, which plays a pivotal role in tumor invasion, encompasses diverse cellular mechanisms [61–63]. Multiple modes of cell migration, including individual and collective motions, contribute to the overall patterns of invasion. These types of migration can potentially give rise to finger-type and ring-type invasion patterns, respectively [206, 249]. The former accounts for the migration of single cells into the surrounding tissue and the latter corresponds to the collective motion of cells in the form of a ring. In single cell motion, cells gain the ability to move by

adopting either a mesenchymal or amoeboid morphology [64]. However, in the case of collective cell migration, cells retain their connections with neighboring cells by maintaining intercellular adhesion and form a leading edge that extends into the surrounding tissue [66]. In this section, the evolution of the tumor is mathematically modeled using an HDC technique which utilizes a continuum model for the derivation of a discrete model [249]. The cell flux, diffusion of nutrients and collagenase, as well as the degradation of collagen, are predicted using a continuum model. The generation of cell flux primarily occurs through the interplay of diffusive and adhesive forces, as well as the directional movement resulting from chemotaxis. We adopted a nonconvex form of free energy and a standard chemotactic model presented in [206] to model the collective motion of cells (Figure 7.3a). Additionally, the motion of single invasive cells, including random and directional motions, was predicted by a discrete model (Figure 7.3b). A reaction–diffusion model that consists of a system of partial differential equations (PDEs) represented the collective motion of cells. In this model, state variables, such as concentrations of cells, nutrients, collagen, and collagenase, were assumed to be continuous, and their local changes are obtained by the following governing equations [249].

$$\frac{\partial C_p}{\partial t} = \nabla \cdot (\mathbf{J}_f + \mathbf{J}_d) + C_p \eta_p \,, \tag{7.1}$$

$$\frac{\partial n}{\partial t} = D_n \nabla^2 n - C_p \lambda_p \,, \tag{7.2}$$

$$\frac{\partial M}{\partial t} = D_M \nabla^2 M - \zeta M f \,, \tag{7.3}$$

$$\frac{\partial f}{\partial t} = -\delta M f. \tag{7.4}$$

where t is time, and C_p, n, f, M are concentrations of proliferative cells, nutrient, collagenase and collagen, respectively. Not that potential inhomogeneity in cells population within the tumoroids was neglected. This assumption, which simplifies the model, becomes more precise as the size of tumoroids becomes smaller, since they do not develop hypoxia. We should also note that all components in the experimental part, including tumoroids, media, collagen, and collagenase, are continuum materials, which is aligned with the assumption in the continuum model. $\mathbf{J}_f$ and $\mathbf{J}_d$ are the free energy and chemotaxis fluxes. Dn, DM are diffusivity coefficients of nutrient and collagenase, and $C_p\eta_p$ and $C_p\lambda_p$ are rates of proliferation and nutri-

ent consumption, respectively. Following [249], we assumed that the rate of collagen degradation is linearly proportional to the concentration of collagenase and, likewise, collagenase degradation is proportional to the collagen concentration, where ζ and δ denote the linear proportionalities. Denoting the tumor domain by Ω and the free boundary by $\delta\Omega$, Equations (7.1)-(7.4) are subjected to the following boundary and initial conditions:

Boundary Conditions (BCs):

$$C_p(\mathbf{x},t)\big|_{\delta\Omega} = C_0, \quad n(\mathbf{x},t)\big|_{\delta\Omega} = n_0, \quad M(\mathbf{x},t)\big|_{\delta\Omega} = M_0. \tag{7.5}$$

Initial Conditions (ICs):

$$C_p(\mathbf{x},t=0) = C_i, \quad n(\mathbf{x},t=0) = n_i, \quad M(\mathbf{x},t=0) = 0, \quad f(\mathbf{x},t=0) = f_0\,, \tag{7.6}$$

where x is the position, $\{C_0, n_0, M_0\}$ are the boundary conditions of cells, nutrient, and collagenase, and $\{C_i, n_i, M_i\}$ are the initial concentrations of cells, nutrient and collagen, respectively. Here, we only considered the axisymmetric solutions due to the symmetric boundary and initial conditions. The governing equations of the continuum model predict the ring-type invasion of tumor and the distribution of nutrients, collagen, and collagenase densities. The next section presents the discrete technique which employs the state variable fields obtained from the continuum model to derive cellular interactions such as single cell migration.

Cellular migration mechanisms depend on morphology and external stimuli. Invasive tumor cells become morphologically polarized and develop membrane protrusions, allowing them to reach forward [155]. This motion is called mesenchymal when cells move via traction and adhesion to the ECM. On the other hand, the motion can be amoeboid when cells squeeze through the pores in the ECM, which is relatively fast and does not require strong adhesion forces [250]. The former type of migration is directional (hapto-taxis) and the latter can be both directional and random (chemokinesis) [251, 252] (Figure 7.3a). To capture both mechanisms, we write the cell flux Ji as a combination of random and directional fluxes

$$\mathbf{J}_i = -D_i \nabla C_i + \chi_{\text{hap}} C_i \nabla f, \tag{7.7}$$

where D_i and χ_{hap} are coefficients of random and haptotactic migrations. Polar coordinates, $\mathbf{x} = r\mathbf{e}_r\,(\theta)$, are used as they well suited to represent the shape of tu-

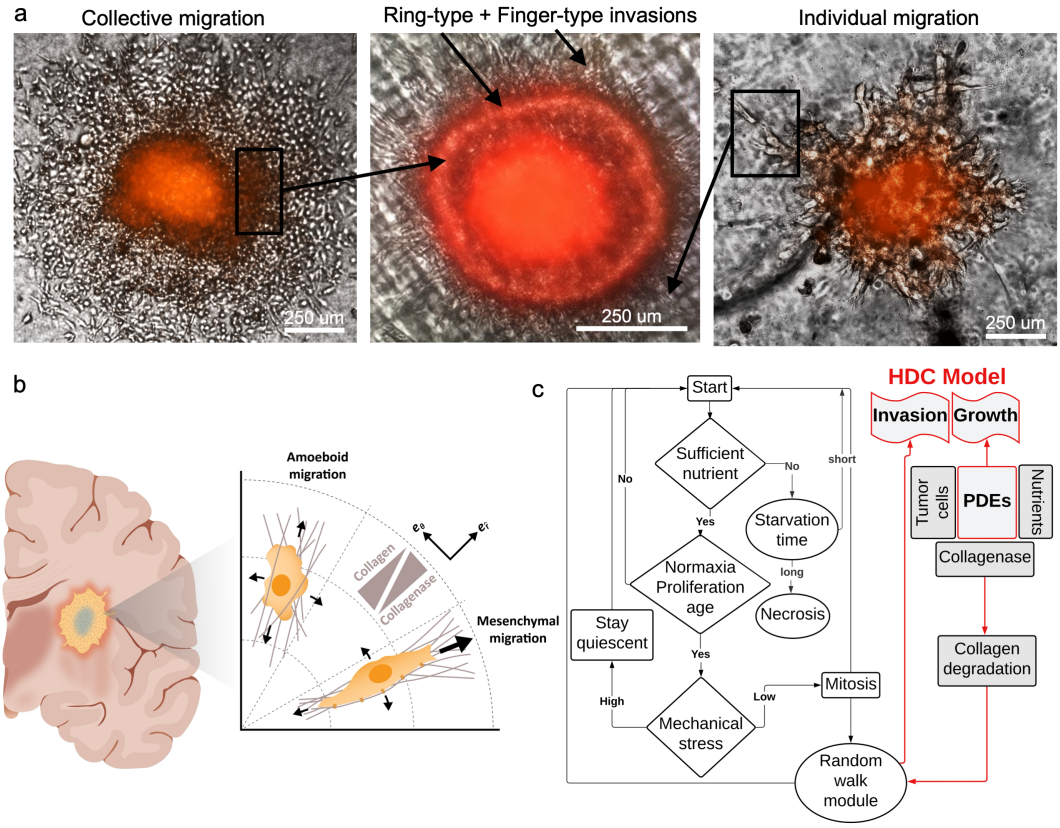

Figure 7.3: Patterns of hGB invasion. (a) Individual and collective migrations contribute to the invasion patterns. Finger-type pattern is mainly derived from individual cells migrating via mesenchymal motion, and ring-type pattern manifests the collective migration mainly via amoeboid motion. (b) Mechanism of cellular migration includes directional (mesenchymal) and random (amoeboid) motions, which is captured using a hybrid discrete-continuum model (HDC). (c) The model combines modules of cellular processes and random walk with continuum fields of variables, such as cell and nutrient concentrations.

moroids. Considering temporal (i), radial (j) and angular (k) discretizations, finite difference approximations transform the differential equations into an algebraic system of equations where $C^i_{j,k}$ is the discretized cell concentration [39]. Equation (8) is used to find the probabilities of cell motions in different directions on the discretized plane. Implementing central finite differences technique and solving for $C^{i+1}_{j,k}$ gives

$$C^{i+1}_{j,k} = P_0\, C^i_{j,k} + P_1\, C^i_{j+1,k} + P_2\, C^i_{j-1,k} + P_3\, C^i_{j,k+1} + P_4\, C^i_{j,k-1}\,, \tag{7.8}$$

where P_0, P_1, P_2, P_3 and P_4 are proportional to probabilities of the cell staying stationary, or moving in directions of $+r$ (forward), $-r$ (backward), $+\theta$ counterclockwise and $-\theta$ clockwise, respectively [249]. These movement probabilities are functions of the cell's random motion and the collagen gradient and link the discrete model to the continuum model. Therefore, the discrete model governs the migration of individual cells based on their interactions with the ECM. The complex dynamics of the system of the discrete model, which captures the cellular processes, is coupled with the continuum model. The simulation flowchart depicts the relationship between continuum variables and cellular processes, such as proliferation, cellular age, mechanical stress, etc. Using this model, the system receives updated information from the continuum model and applies this in the discreet model (Figure 7.3c). Model parameters are presented in Table 7.1.

As shown in Figure 7.4a, there is a gradual and time-dependent increase in invasion length of the tumoroids with no collagenase treatment. It is also demonstrated that the invasion area after 72 h is significantly increased in both collagenase treatment conditions compared to the non-treated sample. Quantification of the invasion area did not show any significant difference between the treated and non-treated conditions at day 0, while the invasion length of the tumoroids treated with 0.01 mg/mL collagenase is significantly increased in comparison with less concentration of collagenase (0.001 mg/mL) at day 1 (Figure 7.4b). The difference in invasion potential of treated and non-treated samples remained consistent at day 3 while there was no statistical significance between the invasion length of the tumoroids with 0.01 and 0.001 mg/mL collagenase. In the current model, we observed that tumoroids embedded with collagen and treated with varying concentrations of collagenase showed both finger-type and ring-type invasion patterns, previously observed in glioblastoma tumors [249, 254]. It was reported that collagen enhances collective migration in glioblastoma cells, whereby a cluster of cells can invade into the surrounding gel

Table 7.1: HDC model parameters.

Parameter	Definition	Value	Ref.	Note
D_i	Cell diffusivity	$1 \times 10^{-8}\,\mathrm{cm}^2 \cdot \mathrm{s}^{-1}$	[14]	
D_n	Nutrient diffusivity	$4.2 \times 10^{-6}\,\mathrm{cm}^2 \cdot \mathrm{s}^{-1}$	[183]	
D_M	Collagenase diffusivity	$1 \times 10^{-9}\,\mathrm{cm}^2 \cdot \mathrm{s}^{-1}$	[220]	
C_0	Initial concentration of cells	$1 \times 10^{4}\,\mathrm{mg} \cdot \mathrm{mL}^{-1}$	[147]	
n_0	Nutrient supply concentration	$4.5\,\mathrm{mg} \cdot \mathrm{mL}^{-1}$	Gibco DMEM	Glucose is taken as the main component of nutrients
f_0	Initial concentration of matrix fibers	$1 \times 10^{-9}\,\mathrm{M}$	[220]	
χ_{hap}	Hapto-taxis coefficients	$2.6 \times 10^{3}\,\mathrm{cm}^2 \cdot \mathrm{s}^{-1} \cdot \mathrm{M}^{-1}$	[38]	
P_{cr}	Critical stress	$1\,\mathrm{kPa}$	[253]	Maximum allowable stress is $5\,\mathrm{kPa}$
η_p	Rate of cell proliferation	Function is taken from ref.	[249]	
λ_p	Rate of nutrient consumption	Function is taken from ref.	[249]	
ζ	Rate of collagenase binding	$1 \times 10^{-6}\,\mathrm{s}^{-1} \cdot \mathrm{M}^{-1}$	N/A	Value is proposed
δ	Rate of collagen degradation	$1 \times 10^{-2}\,\mathrm{s}^{-1} \cdot \mathrm{M}^{-1}$	N/A	Value is proposed

[147]. Moreover, finger-type migration in glioblastoma tumoroids was shown to be the main invasion pattern [61]. Here, we observed the same invasion patterns; (i) cluster migration of cells which manifests a ring, due to the symmetry of model, moving away from the tumoroid, and (ii) individual cells migrating from the ring and forming a finger-type pattern. We conducted quantitative analyses of these two patterns and found that finger-type invasion was more dominant than ring-type invasion in our in vitro model (Figure 7.4c). Moreover, by increasing the concentration of collagenase treatment, tumor cells invaded under the finger-type pattern showed a faster rate than the cells invaded under the ring-type pattern.

The process of invasion involves the local degradation of collagen molecules in the ECM by MMP1 secretion, increasing the porosity of the ECM hydrogel network

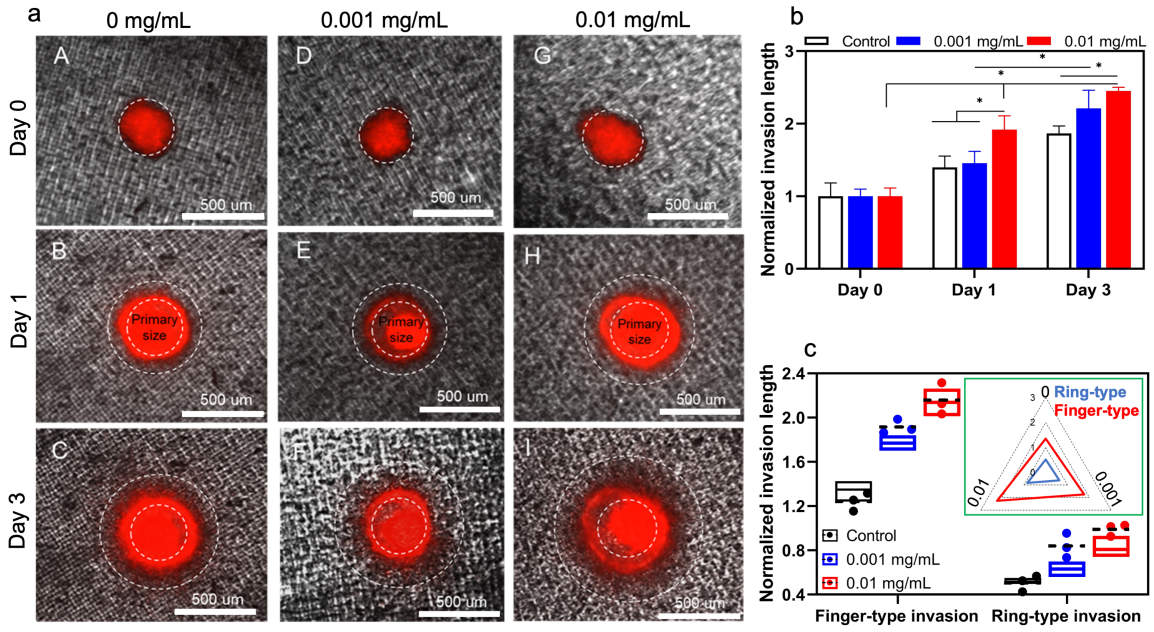

Figure 7.4: The in vitro invasion of hGB tumoroids. (a) Tumoroids exhibit both ring- and finger-type invasion patterns in response to different concentrations of collagenase; 0 mg/mL (A–C), 0.001 mg/mL (D–F), and 0.01 mg/mL (G–I). (b,c) Effects of collagenase concentration on overall invasion length and invasion pattern are quantified and compared with model predictions (i.e., circles with dashed lines). The inserted figure shows a higher increase in finger-type invasion compared to ring-type invasion length.

[255]. To investigate the effect of MMP1 on the invasion pattern of tumoroids, matrix stiffness was used as an indication of changes in the mechanical properties of the ECM after the secretion of collagenase from tumor cells or other elements in the tumor microenvironment during invasion. Our aim was to demonstrate how changing the ECM stiffness in an in-vitro model can complementarily explain our findings, which have been added to the manuscript. To quantify the effect of collagenase on tumoroid ECM, we measured the variation of viscoelastic properties of collagen. Storage modulus (elastic modulus) and loss modulus are representative mechanical properties of viscoelastic materials, such as hydrogels [256]. Storage modulus (G') represents a material's ability to store and recover elastic energy when subjected to an applied force or deformation, and loss modulus (G'') represents the viscous or damping behavior of a material. These two properties together provide insights into the mechanical behavior of a material across a range of deformation. The interplay between them defines how the material responds to different mechanical forces and environments. Therefore, they are crucial for designing biomaterials. Invasion behavior of tumoroids was aligned with the mechanical properties trend of the collagen hydrogel in the presence of different collagenase concentrations (Figure 7.5). Higher concentration of collagenase significantly reduced both storage and loss moduli. According to previous results in the literature, upregulation of matrix metalloproteinase 9 (MMP-9) and enhanced tumor cell invasion are the downstream consequence of TGF-β1 secretion through autocrine signaling from glioma cells [257]. The stiffness of the extracellular matrix (ECM) in solid tumors is a critical physical factor that affects their ability to invade healthy tissue. Observations in vivo show that the ECM's stiffness changes during carcinogenesis stemming from ECM remodeling, resulting from the diverse compositions and densities of collagen [255]. Integrin receptors play a crucial role in transmitting physical cues from the ECM's stiffness to tumor cells, prompting mechano-transduction events that modify their invasive potential. Studies indicate that changes in tumor tissue matrix stiffness substantially impact how tumor cells respond to chemotherapy and immunotherapy [258]. In vitro model findings are consistent with in vivo observations of the tumor microenvironment's mechanical behavior during progression and invasion within the ECM. These results could be valuable for cancer biologists and oncologists seeking to understand the significant impact of ECM stiffness on tumor behavior. Hereby, our in vitro model can be used to predict the migration behavior of the glioma tumor cells in a 3D microenvironment in response to localized TME mechanical stiffness alterations. This model can provide

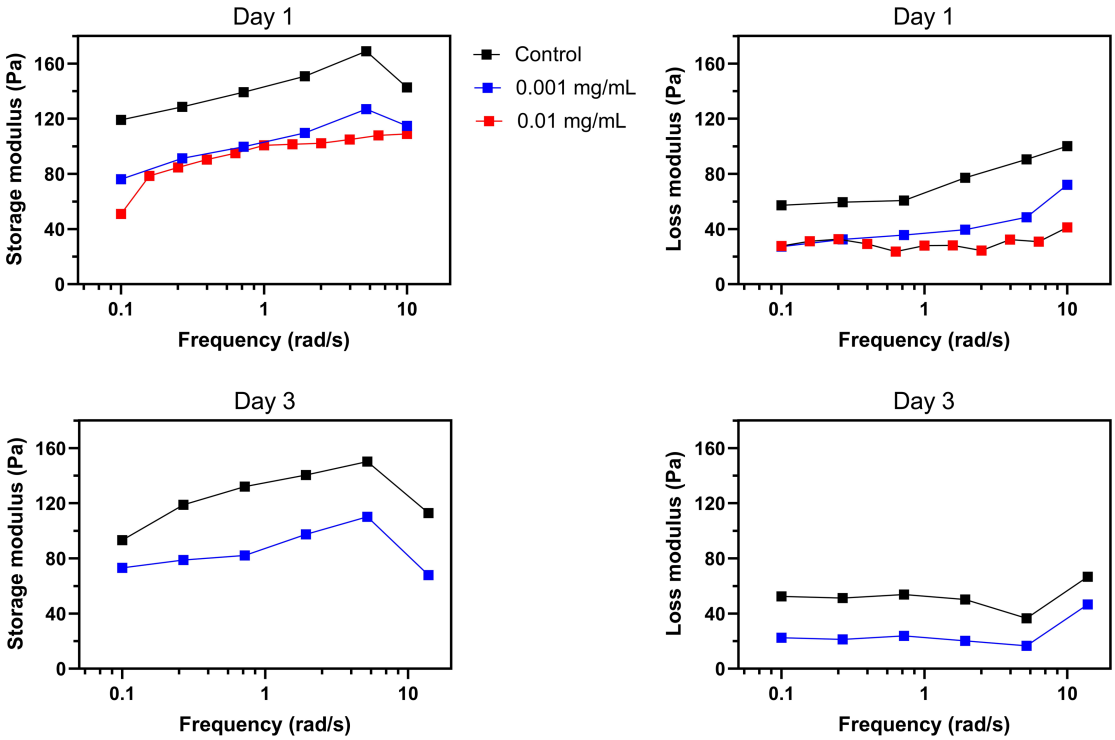

Figure 7.5: Effect of collagenase on mechanical properties of collagen. A decrease in storage and loss moduli was observed in response to 24 h of 0.001 and 0.01 mg/mL collagenase. Further reductions were observed after 72 h of treatment with 0.001 mg/mL of collagenase. Missing results for 72 h of 0.01 mg/mL collagenase is due to the significant degradation of collagen.

an opportunity for studying the effect of TME associated signaling pathways on the function of the tumor cells in ECM and their crosstalk with the other components of the tumor microenvironment. Moreover, this 3D model opens a new venue to study our hypothesis on directing the migration of the tumor cells from the deeper area of the white matter within the brain tissue toward the external source of the anticancer drug. We tested this hypothesis by using MMP 1 with the aim of making a gradient of the collagenase concentration within the hydrogel, leading to partial degradation of the collagen ECM. This model could facilitate measurement of the tumor cells' invasion from the stiffer areas to the less stiff zone of ECM.

Similar to other mathematical techniques, hybrid discrete-continuum (HDC) models come with certain limitations [259]. For instance, they often demand sophisticated numerical techniques to integrate the discrete and continuous components, leading to increased computational complexity. They sometimes require a large number of model

parameter estimations, which can be difficult, and validating the model against both discrete and continuous experimental data is complex. Additionally, bridging different scales and granularities while considering data requirements and assumptions can present significant technical hurdles. Despite the above mentioned limitations, HDC models are valuable tools in mathematical biology for studying complex biological phenomena that involve both discrete entities and continuous fields, such as tumor growth and invasion.

7.4 Conclusions

In this study we investigated the influence of matrix stiffness on the growth and invasion of human glioblastoma tumoroids using a PEGDA-printed tumor-on-a-chip platform. By incorporating varying concentrations of collagenase to create an inhomogeneous collagen matrix, the study successfully demonstrated the strong dependency of tumor behavior on the stiffness of the surrounding extracellular matrix. The results showed that tumoroids exhibited higher growth rates and invasion lengths in response to higher concentrations of collagenase. These findings highlight the potential of investigating the impact of various matrix characteristics on tumor growth and invasion. Furthermore, the study employed a hybrid modeling technique that combined a continuum reaction–diffusion model and a discrete model to accurately capture the growth and invasion in an inhomogeneous environment. The agreement between the experimental results and the model predictions further confirmed the validity and potential of this approach. Extending the tumor-on-a-chip platform to incorporate other components of the tumor microenvironment could offer a more comprehensive representation of the complex tumor–stroma interactions. This advancement would enable the study of how different cellular and extracellular components contribute to glioblastoma progression in response to varying matrix characteristics. Ultimately, such investigations may unveil novel therapeutic targets and strategies for combatting glioblastoma's aggressive behavior in a more physiologically relevant context.

Author contributions: Conceptualization, M.A. (Meitham Amereh), A.S. and M.A. (Mohsen Akbari); methodology, M.A. (Meitham Amereh) and A.S.; validation, M.A. (Meitham Amereh) and A.S.; formal analysis, M.A. (Meitham Amereh), A.S. and M.A. (Mostafa Azimzadeh); experiments, M.A. (Meitham Amereh), A.S., B.D. and E.S.; resources, M.A. (Mohsen Akbari); supervision, M.A. (Mohsen Ak-

bari); All authors contributed in writing—review and editing; funding acquisition, M.A. (Mohsen Akbari). All authors have read and agreed to the published version of the manuscript.

Funding: Funding was provided by the Natural Science and Engineering Research Council (NSERC, RGPIN-2016-04024) of Canada

Data availability: Data will be made available on request.

Acknowledgements: We would like to acknowledge BC cancer Foundation, NSERC and Canada Foundation for Innovation (CFI). We also acknowledge Apricell biotechnology "https://www.apricell.com/ (accessed on 15 August 2023)" for providing us with the chips.

Conflicts of Interest: The authors declare no conflict of interest.

Chapter 8

Conclusion

In this thesis, we have addressed various aspects of tumor progression, employing diverse mathematical models and experimental platforms to deepen our understanding of the underlying mechanisms governing solid tumor behavior.

First, we studied the transient formation of tumor spheroids. A mathematical model with the analytical and numerical solutions was presented, elucidating the intricate interplay between adhesion forces, cell proliferation, and pressure-induced growth. The model's validation through the cultivation of human glioblastoma cancer cell lines underscores its reliability, particularly in predicting spheroid size before the onset of inhomogeneity.

Expanding our investigation into the growth of tumors, we analyzed the stability of radially symmetric growth to asymmetric perturbations. Using a mathematical model, we showed that spherical tumor configurations are inherently unstable under controlled symmetric conditions. The analytical results were in agreement with experimental observations of in-vitro hGB spheroids. Results showed the significance of external factors such as nutrient source concentration, consumption rates, and surface tension in shaping tumor morphology.

We further investigated tumors response to external factors by studying biomechanical stimuli-induced remodeling of tumor. To model this phenomenon, we considered a tumor body as an evolving material subject to volume-preserving isotropic remodeling. The evolution of remodeling and stress distribution were obtained using principles of continuum mechanics. The proposed model was validated through an in-vitro tumoroid-on-a-chip platform, and establishes a crucial link between nutrient gradients and configurational remodeling of tumors. The observed asymmetry in remodeling and cell alignment within tumoroids highlights the pivotal role of nutrient

gradients in influencing tumor biomechanics.

Next, we studied invasion as one of the key hallmarks of tumors. We introduced a continuum model that integrates cell–cell and cell–matrix adhesion with chemotaxis to predict a distinctive shell-type invasion pattern. The model's ability to capture key features of invasion, such as shell formation, shape, and continuous interfaces, provided valuable insights into the interplay of adhesion forces, nutrient gradients, and proliferation rates. The model's predictions aligned with empirical observations, paving the way for future calibration and integration with discrete mathematical frameworks for enhanced accuracy.

Building upon these foundations, we presented a hybrid discrete-continuum (HDC) model integrating experimental measurements and in-vitro tumor-on-a-chip platforms to study the growth and invasion of tumors. The HDC model, validated against experimental data, exhibited promise in predicting volumetric growth, invasion length, and finger-type invasion patterns. The incorporation of randomness in the model captured the inherent variability in cellular behavior, offering a more realistic representation of the invasion process. Additionally, we introduced a drug component to the model to investigate the inhibitory effect of temozolomide (TMZ) on tumor invasion, contributing further insights into the model's applications in drug-related investigations. Moreover, we studied the influence of matrix stiffness on tumor growth and invasion using a PEGDA-printed tumor-on-a-chip platform. This study demonstrated the important role of the extracellular matrix in tumor behavior.

In conclusion, our multifaceted approach, encompassing analytical modeling, experimental validation, and hybrid modeling techniques, contributed to a comprehensive understanding of solid tumor progression. This work lays the groundwork for future investigations into therapeutic interventions and strategies that consider the intricate interplay between biological and mechanical factors in the tumor microenvironment.

8.1 Future works

Our investigation of tumor progression has shown various application of mathematical modeling, continuum and discrete schemes, integrated with experimental studies, paving the way for future works that extend our understanding of tumor progression. The following routes represent promising directions for continued research.

While our current work covered modeling tumors' transient formation, growth, sta-

bility, remodeling, invasion, and metabolic heterogeneity, there is room for extending the model's dynamic capabilities. Future efforts could involve:

- Incorporating time-dependent parameters to simulate the growth over extended periods.
- Including potential factors influencing stability of tumor growth such as heterogeneity to identify the stability criteria.
- Exploring additional factors influencing tumor remodeling, such as cellular mechano-sensitivity and dynamic changes in the microenvironment, to enhance the accuracy of predictions and further validate the model against diverse experimental setups.
- Expanding the application of HDC model by calibrating model parameters with additional experimental data and incorporating more intricate drug-response mechanisms to enhance the model's predictive capabilities and provide a versatile tool for drug-related investigations.
- Combining the influence of multiple factors on tumor invasion, such as matrix composition, stiffness gradients, and dynamic changes in the extracellular matrix, to offer a more comprehensive understanding of their impact on tumor behavior.
- Applying our findings to develop innovative therapeutic interventions that consider the intricate interplay between biological and mechanical factors in the tumor microenvironment

Finally, our current research provides a strong foundation for ongoing and future investigations into solid tumor progression. Further incorporation of the complexity of the tumor microenvironment can contribute to the development of targeted and effective therapeutic strategies, leading to deeper understanding and better solutions in cancer treatment.

Bibliography

[1] IlKyoo Koh, Junghwa Cha, Junseong Park, Junjeong Choi, Seok-Gu Kang, and Pilnam Kim. The mode and dynamics of glioblastoma cell invasion into a decellularized tissue-derived extracellular matrix-based three-dimensional tumor model. *Scientific Reports*, 8(1):1–12, 2018.

[2] Lu Ling, Jeffrey A Mulligan, Yunxin Ouyang, Adrian A Shimpi, Rebecca M Williams, Garrett F Beeghly, Benjamin D Hopkins, Jason A Spector, Steven G Adie, and Claudia Fischbach. Obesity-associated adipose stromal cells promote breast cancer invasion through direct cell contact and ecm remodeling. *Advanced functional materials*, 30(48):1910650, 2020.

[3] Aleksandra Karolak, Dmitry A Markov, Lisa J McCawley, and Katarzyna A Rejniak. Towards personalized computational oncology: from spatial models of tumour spheroids, to organoids, to tissues. *Journal of The Royal Society Interface*, 15(138):20170703, 2018.

[4] Renee Brady and Heiko Enderling. Mathematical models of cancer: when to predict novel therapies, and when not to. *Bulletin of mathematical biology*, 81:3722–3731, 2019.

[5] Triantafyllos Stylianopoulos, Lance L Munn, and Rakesh K Jain. Reengineering the physical microenvironment of tumors to improve drug delivery and efficacy: from mathematical modeling to bench to bedside. *Trends in cancer*, 4(4):292–319, 2018.

[6] CP Please, G Pettet, and DLS McElwain. A new approach to modelling the formation of necrotic regions in tumours. *Applied mathematics letters*, 11(3):89–94, 1998.

[7] Philipp M. Altrock, Lin L. Liu, and Franziska Michor. The mathematics of cancer: integrating quantitative models. *Nature Reviews Cancer*, 15(12):730–745, 2015.

[8] R. P. Araujo and D. L. S. McElwain. A history of the study of solid tumour growth: The contribution of mathematical modelling. *Bulletin of Mathematical Biology*, 66(5):1039, 2004.

[9] K. A. Landman and C. P. Please. Tumour dynamics and necrosis: surface tension and stability. *Mathematical Medicine and Biology: A Journal of the IMA*, 18(2):131–158, 06 2001.

[10] J. P. WARD and J. R. KING. Mathematical modelling of avascular-tumour growth. *Mathematical Medicine and Biology: A Journal of the IMA*, 14(1):39–69, 03 1997.

[11] Vittorio Cristini and John Lowengrub. *Multiscale modeling of cancer: an integrated experimental and mathematical modeling approach*. Cambridge University Press, 2010.

[12] Thomas S Deisboeck, Zhihui Wang, Paul Macklin, and Vittorio Cristini. Multiscale cancer modeling. *Annual review of biomedical engineering*, 13:127–155, 2011.

[13] Dorothy Wallace and Xinyue Guo. Properties of tumor spheroid growth exhibited by simple mathematical models. *Frontiers in oncology*, 3:51, 2013.

[14] Hana LP Harpold, Ellsworth C Alvord Jr, and Kristin R Swanson. The evolution of mathematical modeling of glioma proliferation and invasion. *Journal of Neuropathology & Experimental Neurology*, 66(1):1–9, 2007.

[15] J. P. WARD and J. R. KING. Mathematical modelling of avascular-tumour growth ii: Modelling growth saturation. *Mathematical Medicine and Biology: A Journal of the IMA*, 16(2):171–211, 1999.

[16] H. P. Greenspan. Models for the growth of a solid tumor by diffusion. *Studies in Applied Mathematics*, 51(4):317–340, 1972.

[17] H.M. Byrne and M.A.J. Chaplain. Modelling the role of cell-cell adhesion in the growth and development of carcinomas. *Mathematical and Computer Modelling*, 24(12):1–17, 1996.

[18] J. J. Casciari, S. V. Sotirchos, and R. M. Sutherland. Mathematical modelling of microenvironment and growth in emt6/ro multicellular tumour spheroids. *Cell Proliferation*, 25(1):1–22, 1992.

[19] Joseph J. Casciari, Stratis V. Sotirchos, and Robert M. Sutherland. Variations in tumor cell growth rates and metabolism with oxygen concentration, glucose concentration, and extracellular ph. *Journal of Cellular Physiology*, 151(2):386–394, 1992.

[20] A. Ramírez-Torres, R. Rodríguez-Ramos, J. Merodio, J. Bravo-Castillero, R. Guinovart-Díaz, and J.C.L. Alfonso. Mathematical modeling of anisotropic avascular tumor growth. *Mechanics Research Communications*, 69:8–14, 2015.

[21] D. Ambrosi, L. Preziosi, and G. Vitale. The interplay between stress and growth in solid tumors. *Mechanics Research Communications*, 42:87–91, 2012.

[22] A. Ramírez-Torres, R. Rodríguez-Ramos, J. Merodio, J. Bravo-Castillero, R. Guinovart-Díaz, and J.C.L. Alfonso. Action of body forces in tumor growth. *International Journal of Engineering Science*, 89:18–34, 2015.

[23] Ariel Ramírez-Torres, Reinaldo Rodríguez-Ramos, José Merodio, Raimondo Penta, Julián Bravo-Castillero, Raúl Guinovart-Díaz, Federico J. Sabina, Catherine García-Reimbert, Igor Sevostianov, and Aura Conci. The influence of anisotropic growth and geometry on the stress of solid tumors. *International Journal of Engineering Science*, 119:40–49, 2017.

[24] Larry A. Taber and Jay D. Humphrey. Stress-Modulated Growth, Residual Stress, and Vascular Heterogeneity . *Journal of Biomechanical Engineering*, 123(6):528–535, 2001.

[25] Helen M. Byrne. Dissecting cancer through mathematics: from the cell to the animal model. *Nature Reviews Cancer*, 10(3):221–230, 2010.

[26] Daniela Loessner, J. Paige Little, Graeme J. Pettet, and Dietmar W. Hutmacher. A multiscale road map of cancer spheroids – incorporating experimen-

tal and mathematical modelling to understand cancer progression. *Journal of Cell Science*, 126(13):2761–2771, 2013.

[27] Vittorio Cristini and John Lowengrub. *Multiscale Modeling of Cancer: An Integrated Experimental and Mathematical Modeling Approach*. Cambridge University Press, 2010.

[28] Katarzyna A Rejniak and Alexander R A Anderson. Hybrid models of tumor growth. *Wiley interdisciplinary reviews. Systems biology and medicine*, 3(1):115–125, Jan-Feb 2011.

[29] Jin Chen, Qiang Lu, and Joseph P Balthasar. Mathematical modeling of topotecan pharmacokinetics and toxicodynamics in mice. *Journal of pharmacokinetics and pharmacodynamics*, 34:829–847, 2007.

[30] Yi Jiang, Jelena Pjesivac-Grbovic, Charles Cantrell, and James P Freyer. A multiscale model for avascular tumor growth. *Biophysical journal*, 89(6):3884–3894, 2005.

[31] Haralambos Hatzikirou, Georg Breier, and Andreas Deutsch. Cellular automaton modeling of tumor invasion. *Complex Social and Behavioral Systems: Game Theory and Agent-Based Models*, pages 851–863, 2020.

[32] Zhihui Wang and Thomas S Deisboeck. Computational modeling of brain tumors: discrete, continuum or hybrid? *Scientific modeling and simulations*, pages 381–393, 2009.

[33] Azim Rivaz, Mahdieh Azizian, and Madjid Soltani. Various mathematical models of tumor growth with reference to cancer stem cells: a review. *Iranian Journal of Science and Technology, Transactions A: Science*, 43(2):687–700, 2019.

[34] Alexander RA Anderson and Mark A J Chaplain. Continuous and discrete mathematical models of tumor-induced angiogenesis. *Bulletin of mathematical biology*, 60(5):857–899, 1998.

[35] Katarzyna A Rejniak and Alexander RA Anderson. Hybrid models of tumor growth. *Wiley Interdisciplinary Reviews: Systems Biology and Medicine*, 3(1):115–125, 2011.

[36] Alexander Anderson and Katarzyna Rejniak. *Single-cell-based models in biology and medicine*. Springer Science & Business Media, 2007.

[37] Yangjin Kim, Magdalena A Stolarska, and Hans G Othmer. A hybrid model for tumor spheroid growth in vitro i: theoretical development and early results. *Mathematical Models and Methods in Applied Sciences*, 17(supp01):1773–1798, 2007.

[38] Alexander RA Anderson. A hybrid mathematical model of solid tumour invasion: the importance of cell adhesion. *Mathematical medicine and biology: a journal of the IMA*, 22(2):163–186, 2005.

[39] Cynthia L Stokes and Douglas A Lauffenburger. Analysis of the roles of microvessel endothelial cell random motility and chemotaxis in angiogenesis. *Journal of theoretical biology*, 152(3):377–403, 1991.

[40] Yoonseok Kam, Katarzyna A Rejniak, and Alexander RA Anderson. Cellular modeling of cancer invasion: integration of in silico and in vitro approaches. *Journal of cellular physiology*, 227(2):431–438, 2012.

[41] ML Martins, SC Ferreira Jr, and MJ Vilela. Multiscale models for the growth of avascular tumors. *Physics of Life Reviews*, 4(2):128–156, 2007.

[42] RM Sutherland. Cell and environment interactions in tumor microregions: the multicell spheroid model. *Science*, 240(4849):177–184, 1988.

[43] LEONI A. KUNZ-SCHUGHART, MARINA KREUTZ, and RUTH KNUECHEL. Multicellular spheroids: a three-dimensional in vitro culture system to study tumour biology. *International Journal of Experimental Pathology*, 79(1):1–23, 1998.

[44] W. V. Mayneord. On a law of growth of jensen's rat sarcoma. *The American Journal of Cancer*, 16(4):841–846, 1932.

[45] L. H. Gray, A. D. Conger, M. Ebert, S. Hornsey, and O. C. A. Scott. The concentration of oxygen dissolved in tissues at the time of irradiation as a factor in radiotherapy. *The British Journal of Radiology*, 26(312):638–648, 1953. PMID: 13106296.

[46] Archibald Vivian Hill. The diffusion of oxygen and lactic acid through tissues. *Proceedings of the Royal Society of London. Series B, Containing Papers of a Biological Character*, 104(728):39–96, 1928.

[47] Douglas Hanahan and Robert A. Weinberg. Hallmarks of cancer: The next generation. *Cell*, 144(5):646–674, 2011.

[48] Yong Chen, Hengtong Wang, Jiangang Zhang, Ke Chen, and Yumin Li. Simulation of avascular tumor growth by agent-based game model involving phenotype-phenotype interactions. *Scientific reports*, 5:17992, 2015.

[49] James P. Freyer. Role of necrosis in regulating the growth saturation of multicellular spheroids. *Cancer Research*, 48(9):2432–2439, 1988.

[50] James P. Freyer and Robert M. Sutherland. Proliferative and clonogenic heterogeneity of cells from emt6/ro multicellular spheroids induced by the glucose and oxygen supply. *Cancer Research*, 46(7):3513–3520, 1986.

[51] James P. Freyer and Robert M. Sutherland. Regulation of growth saturation and development of necrosis in emt6/ro multicellular spheroids by the glucose and oxygen supply. *Cancer Research*, 46(7):3504–3512, 1986.

[52] Russell C Rockne, Andrea Hawkins-Daarud, Kristin R Swanson, James P Sluka, James A Glazier, Paul Macklin, David A Hormuth, Angela M Jarrett, Ernesto ABF Lima, J Tinsley Oden, et al. The 2019 mathematical oncology roadmap. *Physical biology*, 16(4):041005, 2019.

[53] Myrianthi Hadjicharalambous, Peter A Wijeratne, and Vasileios Vavourakis. From tumour perfusion to drug delivery and clinical translation of in silico cancer models. *Methods*, 185:82–93, 2021.

[54] Fabian Spill, Daniel S Reynolds, Roger D Kamm, and Muhammad H Zaman. Impact of the physical microenvironment on tumor progression and metastasis. *Current opinion in biotechnology*, 40:41–48, 2016.

[55] D Ambrosi, L Preziosi, and G Vitale. The interplay between stress and growth in solid tumors. *Mechanics Research Communications*, 42:87–91, 2012.

[56] Helen M Byrne and Mark AJ Chaplain. Modelling the role of cell-cell adhesion in the growth and development of carcinomas. *Mathematical and Computer Modelling*, 24(12):1–17, 1996.

[57] D Ambrosi and F23256051149 Guana. Stress-modulated growth. *Mathematics and mechanics of solids*, 12(3):319–342, 2007.

[58] Firas Bou Daher, Yuanjie Chen, Behruz Bozorg, Jack Clough, Henrik Jönsson, and Siobhan A Braybrook. Anisotropic growth is achieved through the additive mechanical effect of material anisotropy and elastic asymmetry. *Elife*, 7, 2018.

[59] Jia-shun Wu, Jian Jiang, Bing-jun Chen, Ke Wang, Ya-ling Tang, and Xin-hua Liang. Plasticity of cancer cell invasion: Patterns and mechanisms. *Translational oncology*, 14(1):100899, 2021.

[60] Franziska van Zijl, Georg Krupitza, and Wolfgang Mikulits. Initial steps of metastasis: cell invasion and endothelial transmigration. *Mutation Research/Reviews in Mutation Research*, 728(1-2):23–34, 2011.

[61] Daniela Spano, Chantal Heck, Pasqualino De Antonellis, Gerhard Christofori, and Massimo Zollo. Molecular networks that regulate cancer metastasis. In *Seminars in cancer biology*, volume 22, pages 234–249. Elsevier, 2012.

[62] Peter Friedl. Prespecification and plasticity: shifting mechanisms of cell migration. *Current opinion in cell biology*, 16(1):14–23, 2004.

[63] Shuiping Liu, Qiujie Li, Ke Chen, Qin Zhang, Guohua Li, Lvjia Zhuo, Bingtao Zhai, Xinbing Sui, Xiaotong Hu, and Tian Xie. The emerging molecular mechanism of m6a modulators in tumorigenesis and cancer progression. *Biomedicine & Pharmacotherapy*, 127:110098, 2020.

[64] Mahmut Yilmaz, Gerhard Christofori, and Francois Lehembre. Distinct mechanisms of tumor invasion and metastasis. *Trends in molecular medicine*, 13(12):535–541, 2007.

[65] Yael Hegerfeldt, Miriam Tusch, Eva-B Bröcker, and Peter Friedl. Collective cell movement in primary melanoma explants: plasticity of cell-cell interaction, β1-integrin function, and migration strategies. *Cancer Research*, 62(7):2125–2130, 2002.

[66] Cornelis J Weijer. Collective cell migration in development. *Journal of cell science*, 122(18):3215–3223, 2009.

[67] Javier Rey-Barroso, Daniel S Calovi, Maud Combe, Yolla German, Mathieu Moreau, Astrid Canivet, Xiaobo Wang, Clément Sire, Guy Theraulaz, and Loïc Dupré. Switching between individual and collective motility in b lymphocytes is controlled by cell-matrix adhesion and inter-cellular interactions. *Scientific Reports*, 8(1):1–16, 2018.

[68] J Plou, Y Juste-Lanas, V Olivares, C Del Amo, C Borau, and JM García-Aznar. From individual to collective 3d cancer dissemination: roles of collagen concentration and tgf-β. *Scientific Reports*, 8(1):1–14, 2018.

[69] P Bronsert, K Enderle-Ammour, M Bader, S Timme, M Kuehs, A Csanadi, G Kayser, I Kohler, D Bausch, J Hoeppner, et al. Cancer cell invasion and emt marker expression: a three-dimensional study of the human cancer–host interface. *The Journal of Pathology*, 234(3):410–422, 2014.

[70] Yamicia Connor, Yonatan Tekleab, Sarah Tekleab, Shyama Nandakumar, Divya Bharat, and Shiladitya Sengupta. A mathematical model of tumor-endothelial interactions in a 3d co-culture. *Scientific Reports*, 9(1):1–14, 2019.

[71] Ash A Alizadeh, Victoria Aranda, Alberto Bardelli, Cedric Blanpain, Christoph Bock, Christine Borowski, Carlos Caldas, Andrea Califano, Michael Doherty, Markus Elsner, et al. Toward understanding and exploiting tumor heterogeneity. *Nature medicine*, 21(8):846–853, 2015.

[72] Yuan Gao, Hang Zhang, Frédéric Lirussi, Carmen Garrido, Xiang-Yang Ye, and Tian Xie. Dual inhibitors of histone deacetylases and other cancer-related targets: A pharmacological perspective. *Biochemical Pharmacology*, 182:114224, 2020.

[73] T.S. van Solinge, L. Nieland, E.A. Chiocca, and M.L.D. Broekman. Advances in local therapy for glioblastoma—taking the fight to the tumour. *Nat. Rev. Neurol.*, 18:221–236, 2022.

[74] A.C. Tan, D.M. Ashley, G.Y. López, M. Malinzak, H.S. Friedman, and M. Khasraw. Management of glioblastoma: State of the art and future directions. *CA Cancer J. Clin.*, 70:299–312, 2020.

[75] M.C. de Gooijer, M.G. Navarro, R. Bernards, T. Wurdinger, and O. van Tellingen. An experimenter's guide to glioblastoma invasion pathways. *Trends Mol. Med.*, 24:763–780, 2018.

[76] K. Khandwala, F. Mubarak, and K. Minhas. The many faces of glioblastoma: Pictorial review of atypical imaging features. *Neuroradiol. J.*, 34:33–41, 2021.

[77] M. Khoonkari, D. Liang, M. Kamperman, F.A.E. Kruyt, and P. van Rijn. Physics of brain cancer: Multiscale alterations of glioblastoma cells under extracellular matrix stiffening. *Pharmaceutics*, 14:1031, 2022.

[78] Hermann B Frieboes, Xiaoming Zheng, Chung-Ho Sun, Bruce Tromberg, Robert Gatenby, and Vittorio Cristini. An integrated computational/experimental model of tumor invasion. *Cancer research*, 66(3):1597–1604, 2006.

[79] Hoibin Jeong, Sehui Kim, Beom-Ju Hong, Chan-Ju Lee, Young-Eun Kim, Seoyeon Bok, Jung-Min Oh, Seung-Hee Gwak, Min Young Yoo, Min Sun Lee, et al. Tumor-associated macrophages enhance tumor hypoxia and aerobic glycolysis. *Cancer research*, 79(4):795–806, 2019.

[80] Sabine Hummert, Katrin Bohl, David Basanta, Andreas Deutsch, Sarah Werner, Günter Theißen, Anja Schroeter, and Stefan Schuster. Evolutionary game theory: cells as players. *Molecular BioSystems*, 10(12):3044–3065, 2014.

[81] David Basanta, Matthias Simon, Haralambos Hatzikirou, and Andreas Deutsch. Evolutionary game theory elucidates the role of glycolysis in glioma progression and invasion. *Cell proliferation*, 41(6):980–987, 2008.

[82] Mahya Mehrmohamadi, Xiaojing Liu, Alexander A Shestov, and Jason W Locasale. Characterization of the usage of the serine metabolic network in human cancer. *Cell reports*, 9(4):1507–1519, 2014.

[83] Dominique Barbolosi, Joseph Ciccolini, Bruno Lacarelle, Fabrice Barlési, and Nicolas André. Computational oncology—mathematical modelling of drug regimens for precision medicine. *Nature reviews Clinical oncology*, 13(4):242–254, 2016.

[84] Amir Seyfoori, Ehsan Samiei, Neda Jalili, Brent Godau, Mehdi Rahmanian, Leila Farahmand, Keivan Majidzadeh-A, and Mohsen Akbari. Self-filling microwell arrays (sfmas) for tumor spheroid formation. *Lab on a Chip*, 18(22):3516–3528, 2018.

[85] Z. Wang, H. Kumar, Z. Tian, X. Jin, J.F. Holzman, F. Menard, and K. Kim. Visible light photoinitiation of cell-adhesive gelatin methacryloyl hydrogels for stereolithography 3d bioprinting. *ACS Appl. Mater. Interfaces*, 10:26859–26869, 2018.

[86] Varun Venkataramani, Dimitar Ivanov Tanev, Christopher Strahle, Alexander Studier-Fischer, Laura Fankhauser, Tobias Kessler, Christoph Körber, Markus Kardorff, Miriam Ratliff, Ruifan Xie, et al. Glutamatergic synaptic input to glioma cells drives brain tumour progression. *Nature*, 573(7775):532–538, 2019.

[87] Varun Venkataramani, Dimitar Ivanov Tanev, Thomas Kuner, Wolfgang Wick, and Frank Winkler. Synaptic input to brain tumors: clinical implications. *Neuro-oncology*, 23(1):23–33, 2021.

[88] David Robert Grimes, Pavitra Kannan, Alan McIntyre, Anthony Kavanagh, Abul Siddiky, Simon Wigfield, Adrian Harris, and Mike Partridge. The role of oxygen in avascular tumor growth. *PloS one*, 11(4):e0153692, 2016.

[89] Lewis Wolpert, Cheryll Tickle, and Alfonso Martinez Arias. *Principles of development*. Oxford university press, 2015.

[90] EJ Crampin, WW Hackborn, and PK Maini. Pattern formation in reaction-diffusion models with nonuniform domain growth. *Bulletin of mathematical biology*, 64(4):747–769, 2002.

[91] JD Murray. *Mathematical biology II: spatial models and biomedical applications*. Springer New York, 2001.

[92] Rebecca H Chisholm, Barry D Hughes, and Kerry A Landman. Building a morphogen gradient without diffusion in a growing tissue. *PloS one*, 5(9):e12857, 2010.

[93] Robin N Thompson, Christian A Yates, and Ruth E Baker. Modelling cell migration and adhesion during development. *Bulletin of mathematical biology*, 74(12):2793–2809, 2012.

[94] Jack D Hywood and Kerry A Landman. Biased random walks, partial differential equations and update schemes. *The ANZIAM Journal*, 55(2):93–108, 2013.

[95] Christian A Yates. Discrete and continuous models for tissue growth and shrinkage. *Journal of theoretical biology*, 350:37–48, 2014.

[96] Donald F Newgreen, Sylvie Dufour, Marthe J Howard, and Kerry A Landman. Simple rules for a "simple" nervous system? molecular and biomathematical approaches to enteric nervous system formation and malformation. *Developmental biology*, 382(1):305–319, 2013.

[97] Heather M Young, Annette J Bergner, Matthew J Simpson, Sonja J McKeown, Marlene M Hao, Colin R Anderson, and Hideki Enomoto. Colonizing while migrating: how do individual enteric neural crest cells behave? *BMC biology*, 12(1):23, 2014.

[98] Kerry A Landman, Graeme J Pettet, and DF Newgreen. Mathematical models of cell colonization of uniformly growing domains. *Bulletin of mathematical biology*, 65(2):235–262, 2003.

[99] Matthew J Simpson. Exact solutions of linear reaction-diffusion processes on a uniformly growing domain: Criteria for successful colonization. *PloS one*, 10(2), 2015.

[100] J. Crank and P. Nicolson. A practical method for numerical evaluation of solutions of partial differential equations of the heat-conduction type. *Advances in Computational Mathematics*, 6(1):207–226, 1996.

[101] Stanley Gu, Gargi Chakraborty, Kyle Champley, Adam M Alessio, Jonathan Claridge, Russell Rockne, Mark Muzi, Kenneth A Krohn, Alexander M Spence, Ellsworth C Alvord Jr, et al. Applying a patient-specific bio-mathematical model of glioma growth to develop virtual [18f]-fmiso-pet images. *Mathematical medicine and biology: a journal of the IMA*, 29(1):31–48, 2012.

[102] Li Dao Ke, Yue-Xi Shi, Seock-Ah Im, Xiashan Chen, and W. K. Alfred Yung. The relevance of cell proliferation, vascular endothelial growth factor, and basic fibroblast growth factor production to angiogenesis and tumorigenicity in human glioma cell lines. *Clinical Cancer Research*, 6(6):2562–2572, 2000.

[103] Caroline A Schneider, Wayne S Rasband, and Kevin W Eliceiri. Nih image to imagej: 25 years of image analysis. *Nature Methods*, 9(7):671–675, 2012.

[104] MATLAB. *9.7.0.1190202 (R2019b)*. The MathWorks Inc., Natick, Massachusetts, 2019.

[105] MAJ Chaplain and NF Britton. On the concentration profile of a growth inhibitory factor in multicell spheroids. *Mathematical biosciences*, 115(2):233–243, 1993.

[106] H M_ Byrne and MAJ Chaplain. Growth of necrotic tumors in the presence and absence of inhibitors. *Mathematical biosciences*, 135(2):187–216, 1996.

[107] John A Adam. A mathematical model of tumor growth. iii. comparison with experiment. *Mathematical biosciences*, 86(2):213–227, 1987.

[108] JJ Casciari, SV Sotirchos, and RM Sutherland. Mathematical modelling of microenvironment and growth in emt6/ro multicellular tumour spheroids. *Cell proliferation*, 25(1):1–22, 1992.

[109] Joseph J Casciari, Stratis V Sotirchos, and Robert M Sutherland. Variations in tumor cell growth rates and metabolism with oxygen concentration, glucose concentration, and extracellular ph. *Journal of cellular physiology*, 151(2):386–394, 1992.

[110] Meitham Amereh, Roderick Edwards, Mohsen Akbari, and Ben Nadler. In-silico modeling of tumor spheroid formation and growth. *Micromachines*, 12(7), 2021.

[111] Didier Bresch, Thierry Colin, Emmanuel Grenier, Benjamin Ribba, and Olivier Saut. Computational modeling of solid tumor growth: the avascular stage. *SIAM Journal on Scientific Computing*, 32(4):2321–2344, 2010.

[112] Young Dong Yoo and Yong Tae Kwon. Molecular mechanisms controlling asymmetric and symmetric self-renewal of cancer stem cells. *Journal of Analytical Science and Technology*, 6(1):1–6, 2015.

[113] Sebastien Benzekry, Clare Lamont, Dominique Barbolosi, Lynn Hlatky, and Philip Hahnfeldt. Mathematical modeling of tumor–tumor distant interactions supports a systemic control of tumor growth. *Cancer research*, 77(18):5183–5193, 2017.

[114] Pietro Mascheroni, M Carfagna, Alfio Grillo, DP Boso, and Bernhard A Schrefler. An avascular tumor growth model based on porous media mechanics and evolving natural states. *Mathematics and Mechanics of Solids*, 23(4):686–712, 2018.

[115] Conan K. N. Li. The glucose distribution in 9l rat brain multicell tumor spheroids and its effect on cell necrosis. *Cancer*, 50(10):2066–2073, 1982.

[116] Shangbin Cui. Analysis of a mathematical model for the growth of tumors under the action of external inhibitors. *Journal of Mathematical Biology*, 44(5):395–426, 2002.

[117] Shangbin Cui and Avner Friedman. Analysis of a mathematical model of the effect of inhibitors on the growth of tumors. *Mathematical Biosciences*, 164(2):103–137, 2000.

[118] Xiangrong Li, Vittorio Cristini, Qing Nie, and John S Lowengrub. Nonlinear three-dimensional simulation of solid tumor growth. *Discrete & Continuous Dynamical Systems-B*, 7(3):581, 2007.

[119] Vittorio Cristini, John Lowengrub, and Qing Nie. Nonlinear simulation of tumor growth. *Journal of mathematical biology*, 46(3):191–224, 2003.

[120] Junde Wu and Shangbin Cui. Asymptotic behaviour of solutions of a free boundary problem modelling the growth of tumours in the presence of inhibitors. *Nonlinearity*, 20(10):2389, 2007.

[121] James S Langer. Instabilities and pattern formation in crystal growth. *Reviews of modern physics*, 52(1):1, 1980.

[122] Brook K Byrd, Venkataramanan Krishnaswamy, Jiang Gui, Timothy Rooney, Rebecca Zuurbier, Kari Rosenkranz, Keith Paulsen, and Richard J Barth. The shape of breast cancer. *Breast Cancer Research and Treatment*, 183(2):403–410, 2020.

[123] Douglas Hanahan and Robert A Weinberg. The hallmarks of cancer. *cell*, 100(1):57–70, 2000.

[124] Andreas Menzel and Ellen Kuhl. Frontiers in growth and remodeling. *Mechanics research communications*, 42:1–14, 2012.

[125] Elena Prieto-Garcia, C Vanesa Díaz-García, Inmaculada García-Ruiz, and M Teresa Agulló-Ortuño. Epithelial-to-mesenchymal transition in tumor progression. *Medical Oncology*, 34(7):1–10, 2017.

[126] Michèle Sabbah, Shahin Emami, Gérard Redeuilh, Sylvia Julien, Grégoire Prévost, Amazia Zimber, Radia Ouelaa, Marc Bracke, Olivier De Wever, and Christian Gespach. Molecular signature and therapeutic perspective of the epithelial-to-mesenchymal transitions in epithelial cancers. *Drug resistance updates*, 11(4-5):123–151, 2008.

[127] Meitham Amereh, Roderick Edwards, Mohsen Akbari, and Ben Nadler. In-silico modeling of tumor spheroid formation and growth. *Micromachines*, 12(7):749, 2021.

[128] Meitham Amereh, Yakine Bahri, Roderick Edwards, Mohsen Akbari, and Ben Nadler. Asymmetric growth of tumor spheroids in a symmetric environment. *Mathematics*, 10(12):1955, 2022.

[129] A Ramírez-Torres, R Rodríguez-Ramos, José Merodio, Julián Bravo-Castillero, R Guinovart-Díaz, and Juan Carlos López Alfonso. Mathematical modeling of anisotropic avascular tumor growth. *Mechanics Research Communications*, 69:8–14, 2015.

[130] Ariel Ramírez-Torres, Reinaldo Rodríguez-Ramos, José Merodio, Raimondo Penta, Julián Bravo-Castillero, Raúl Guinovart-Díaz, Federico J Sabina, Catherine García-Reimbert, Igor Sevostianov, and Aura Conci. The influence of anisotropic growth and geometry on the stress of solid tumors. *International Journal of Engineering Science*, 119:40–49, 2017.

[131] A Ramírez-Torres, R Rodríguez-Ramos, José Merodio, Julián Bravo-Castillero, R Guinovart-Díaz, and Juan Carlos López Alfonso. Action of body forces in tumor growth. *International Journal of Engineering Science*, 89:18–34, 2015.

[132] Ioanna Katsamba, Pavlos Evangelidis, Chrysovalantis Voutouri, Alkiviadis Tsamis, Vasileios Vavourakis, and Triantafyllos Stylianopoulos. Biomechanical modelling of spinal tumour anisotropic growth. *Proceedings of the Royal Society A*, 476(2238):20190364, 2020.

[133] Marcelo Epstein and Marek Elzanowski. *Material inhomogeneities and their evolution: A geometric approach*. Springer Science & Business Media, 2007.

[134] John Douglas Eshelby. The force on an elastic singularity. *Philosophical Transactions of the Royal Society of London. Series A, Mathematical and Physical Sciences*, 244(877):87–112, 1951.

[135] Morton E Gurtin. *Configurational forces as basic concepts of continuum physics*, volume 137. Springer Science & Business Media, 1999.

[136] Marcelo Epstein. *The elements of continuum biomechanics*. John Wiley & Sons, 2012.

[137] Dani L Bodor, Wolfram Pönisch, Robert G Endres, and Ewa K Paluch. Of cell shapes and motion: the physical basis of animal cell migration. *Developmental cell*, 52(5):550–562, 2020.

[138] Sharona Even-Ram and Kenneth M Yamada. Cell migration in 3d matrix. *Current opinion in cell biology*, 17(5):524–532, 2005.

[139] TJ Mitchison and LP Cramer. Actin-based cell motility and cell locomotion. *Cell*, 84(3):371–379, 1996.

[140] Antonıo DiCarlo and Sara Quiligotti. Growth and balance. *Mechanics Research Communications*, 29(6):449–456, 2002.

[141] K.R. Rajagopal and A.R. Srinivasa. A thermodynamic frame work for rate type fluid models. *Journal of Non-Newtonian Fluid Mechanics*, 88(3):207–227, 2000.

[142] Gabriel Helmlinger, Paolo A Netti, Hera C Lichtenbeld, Robert J Melder, and Rakesh K Jain. Solid stress inhibits the growth of multicellular tumor spheroids. *Nature biotechnology*, 15(8):778–783, 1997.

[143] Albrecht Bertram. Plasticity. In *Elasticity and Plasticity of Large Deformations*, pages 253–315. Springer, 2008.

[144] Dominique P Pioletti and Lalao R Rakotomanana. Non-linear viscoelastic laws for soft biological tissues. *European Journal of Mechanics-A/Solids*, 19(5):749–759, 2000.

[145] Chrysovalantis Voutouri, Fotios Mpekris, Panagiotis Papageorgis, Andreani D Odysseos, and Triantafyllos Stylianopoulos. Role of constitutive behavior and tumor-host mechanical interactions in the state of stress and growth of solid tumors. *PloS one*, 9(8):e104717, 2014.

[146] Shannon K Hughes-Alford and Douglas A Lauffenburger. Quantitative analysis of gradient sensing: towards building predictive models of chemotaxis in cancer. *Current opinion in cell biology*, 24(2):284–291, 2012.

[147] Tiina Roose, Paolo A Netti, Lance L Munn, Yves Boucher, and Rakesh K Jain. Solid stress generated by spheroid growth estimated using a linear poroelasticity model. *Microvascular research*, 66(3):204–212, 2003.

[148] Mahvash Jebeli, Samantha K Lopez, Zachary E Goldblatt, Dannel McCollum, Sebastian Mana-Capelli, Qi Wen, and Kristen Billiar. Multicellular aligned bands disrupt global collective cell behavior. *bioRxiv*, 2022.

[149] Joyjyoti Das, Suman Chakraborty, and Tapas K Maiti. Mechanical stress-induced autophagic response: A cancer-enabling characteristic? In *Seminars in Cancer Biology*, volume 66, pages 101–109. Elsevier, 2020.

[150] Paolo A Netti, David A Berk, Melody A Swartz, Alan J Grodzinsky, and Rakesh K Jain. Role of extracellular matrix assembly in interstitial transport in solid tumors. *Cancer research*, 60(9):2497–2503, 2000.

[151] Quinn T Ostrom, Haley Gittleman, Jordan Xu, Courtney Kromer, Yingli Wolinsky, Carol Kruchko, and Jill S Barnholtz-Sloan. Cbtrus statistical report: primary brain and other central nervous system tumors diagnosed in the united states in 2009–2013. *Neuro-oncology*, 18(suppl_5):v1–v75, 2016.

[152] Sabine Hombach-Klonisch, Maryam Mehrpour, Shahla Shojaei, Craig Harlos, Marshall Pitz, Ahmed Hamai, Krzysztof Siemianowicz, Wirginia Likus, Emilia Wiechec, Brian D Toyota, et al. Glioblastoma and chemoresistance to alkylating agents: Involvement of apoptosis, autophagy, and unfolded protein response. *Pharmacology & therapeutics*, 184:13–41, 2018.

[153] Halil Tekin, Sean Simmons, Beryl Cummings, Linyi Gao, Xian Adiconis, Cynthia C Hession, Ayan Ghoshal, Danielle Dionne, Sourav R Choudhury, Volkan

Yesilyurt, et al. Effects of 3d culturing conditions on the transcriptomic profile of stem-cell-derived neurons. *Nature biomedical engineering*, 2(7):540–554, 2018.

[154] Wei Yang, Chunxiong Luo, Luhua Lai, and Qi Ouyang. A novel microfluidic platform for studying mammalian cell chemotaxis in different oxygen environments under zero-flow conditions. *Biomicrofluidics*, 9(4):044121, 2015.

[155] Katarina Wolf, Yi I Wu, Yueying Liu, Jörg Geiger, Eric Tam, Christopher Overall, M Sharon Stack, and Peter Friedl. Multi-step pericellular proteolysis controls the transition from individual to collective cancer cell invasion. *Nature Cell Biology*, 9(8):893–904, 2007.

[156] Anyue Yin, Dirk Jan AR Moes, Johan GC van Hasselt, Jesse J Swen, and Henk-Jan Guchelaar. A review of mathematical models for tumor dynamics and treatment resistance evolution of solid tumors. *CPT: pharmacometrics & systems pharmacology*, 8(10):720–737, 2019.

[157] Rajneesh Kumar Chaudhary, Vikas Chaurasiya, and Jitendra Singh. Numerical estimation of temperature response with step heating of a multi-layer skin under the generalized boundary condition. *Journal of Thermal Biology*, page 103278, 2022.

[158] Rajneesh Kumar Chaudhary, Vikas Chaurasiya, Mohamed M Awad, and Jitendra Singh. A numerical study on the thermal response in multi-layer of skin tissue subjected to heating and cooling procedures. *The European Physical Journal Plus*, 137(1):1–18, 2022.

[159] Huicong Li, Rui Peng, and Zhi-an Wang. On a diffusive susceptible-infected-susceptible epidemic model with mass action mechanism and birth-death effect: analysis, simulations, and comparison with other mechanisms. *SIAM Journal on Applied Mathematics*, 78(4):2129–2153, 2018.

[160] Anderson LA de Araujo, Artur C Fassoni, and Luís F Salvino. An analysis of a mathematical model describing acid-mediated tumor invasion. *Mathematical Methods in the Applied Sciences*, 42(18):6686–6705, 2019.

[161] Meitham Amereh, Mohsen Akbari, and Ben Nadler. In-silico study of asymmetric remodeling of tumors in response to external biochemical stimuli. *Scientific Reports*, 2022.

[162] Ping Liu, Junping Shi, and Zhi-An Wang. Pattern formation of the attraction-repulsion keller-segel system. *Discrete & Continuous Dynamical Systems-B*, 18(10):2597, 2013.

[163] Shahla Shojaei, João Basso, Meitham Amereh, Javad Alizadeh, Tania Dehesh, Simone De Silva Rosa, Courtney Clark, Misha Hassan, Mateuz Tomczyk, Laura Cole, et al. A multi-omics analysis of glioma chemoresistance using a hybrid microphysiological model of glioblastoma. *bioRxiv*, pages 2022–10, 2022.

[164] Daniel M Anderson, Geoffrey B McFadden, and Adam A Wheeler. Diffuse-interface methods in fluid mechanics. *Annual Review of Fluid Mechanics*, 30(1):139–165, 1998.

[165] John W Cahn and John E Hilliard. Free energy of a nonuniform system. i. interfacial free energy. *The Journal of Chemical Physics*, 28(2):258–267, 1958.

[166] Katrin Talkenberger, Elisabetta Ada Cavalcanti-Adam, Anja Voss-Böhme, and Andreas Deutsch. Amoeboid-mesenchymal migration plasticity promotes invasion only in complex heterogeneous microenvironments. *Scientific Reports*, 7(1):1–12, 2017.

[167] Inbal Hecht, Yasmin Bar-El, Frederic Balmer, Sari Natan, Ilan Tsarfaty, Frank Schweitzer, and Eshel Ben-Jacob. Tumor invasion optimization by mesenchymal-amoeboid heterogeneity. *Scientific Reports*, 5(1):1–12, 2015.

[168] Ali Vaziri-Gohar, Joel Cassel, Farheen S Mohammed, Mehrdad Zarei, Jonathan J Hue, Omid Hajihassani, Hallie J Graor, Yellamelli VV Srikanth, Saadia A Karim, Ata Abbas, et al. Limited nutrient availability in the tumor microenvironment renders pancreatic tumors sensitive to allosteric idh1 inhibitors. *Nature Cancer*, 3:1–14, 2022.

[169] Swati Nagar, Upendra A Argikar, and Donald J Tweedie. Enzyme kinetics in drug metabolism: fundamentals and applications. In *Enzyme Kinetics in Drug Metabolism*, pages 1–6. Springer, 2014.

[170] Shih-Han Kao, Wei-Chung Cheng, Yi-Ting Wang, Han-Tsang Wu, Han-Yu Yeh, Yu-Ju Chen, Ming-Hsui Tsai, and Kou-Juey Wu. Regulation of mirna biogenesis and histone modification by k63-polyubiquitinated ddx17 controls cancer stem-like features. *Cancer research*, 79(10):2549–2563, 2019.

[171] Verena Amberger-Murphy. Hypoxia helps glioma to fight therapy. *Current cancer drug targets*, 9(3):381–390, 2009.

[172] Masoud Najafi, Bagher Farhood, Keywan Mortezaee, Ebrahim Kharazinejad, Jamal Majidpoor, and Reza Ahadi. Hypoxia in solid tumors: a key promoter of cancer stem cell (csc) resistance. *Journal of cancer research and clinical oncology*, 146:19–31, 2020.

[173] Hermann B Frieboes, John S Lowengrub, S Wise, X Zheng, Paul Macklin, Elaine L Bearer, and Vittorio Cristini. Computer simulation of glioma growth and morphology. *Neuroimage*, 37:S59–S70, 2007.

[174] Daniel J Brat, Amilcar A Castellano-Sanchez, Stephen B Hunter, Marcia Pecot, Cynthia Cohen, Elizabeth H Hammond, Sarojini N Devi, Balveen Kaur, and Erwin G Van Meir. Pseudopalisades in glioblastoma are hypoxic, express extracellular matrix proteases, and are formed by an actively migrating cell population. *Cancer research*, 64(3):920–927, 2004.

[175] Alicia Martínez-González, Gabriel F Calvo, Luis A Pérez Romasanta, and Víctor M Pérez-García. Hypoxic cell waves around necrotic cores in glioblastoma: a biomathematical model and its therapeutic implications. *Bulletin of mathematical biology*, 74(12):2875–2896, 2012.

[176] Philipp M Altrock, Lin L Liu, and Franziska Michor. The mathematics of cancer: integrating quantitative models. *Nature Reviews Cancer*, 15(12):730–745, 2015.

[177] Vittorio Cristini, Hermann B Frieboes, Xiaongrong Li, John S Lowengrub, Paul Macklin, Sandeep Sanga, Steven M Wise, and Xiaoming Zheng. Nonlinear modeling and simulation of tumor growth. *Selected topics in cancer modeling: genesis, evolution, immune competition, and therapy*, pages 1–69, 2008.

[178] Leonard M Sander and Thomas S Deisboeck. Growth patterns of microscopic brain tumors. *Physical Review E*, 66(5):051901, 2002.

[179] Jasti S Rao. Molecular mechanisms of glioma invasiveness: the role of proteases. *Nature Reviews Cancer*, 3(7):489–501, 2003.

[180] Pavlo G. Gritsenko, Olga Ilina, and Peter Friedl. Interstitial guidance of cancer invasion. *The Journal of pathology*, 226(2):185–199, 2012.

[181] Aarash Bordbar, Jonathan M Monk, Zachary A King, and Bernhard O Palsson. Constraint-based models predict metabolic and associated cellular functions. *Nature Reviews Genetics*, 15(2):107–120, 2014.

[182] Osbaldo Resendis-Antonio, Alberto Checa, and Sergio Encarnación. Modeling core metabolism in cancer cells: surveying the topology underlying the warburg effect. *PloS one*, 5(8):e12383, 2010.

[183] Ali Taghibakhshi, Maryam Barisam, Mohammad Said Saidi, Navid Kashaninejad, and Nam-Trung Nguyen. Three-dimensional modeling of avascular tumor growth in both static and dynamic culture platforms. *Micromachines*, 10(9):580, 2019.

[184] Szabolcs Suveges, Kismet Hossain-Ibrahim, J Douglas Steele, Raluca Eftimie, and Dumitru Trucu. Mathematical modelling of glioblastomas invasion within the brain: a 3d multi-scale moving-boundary approach. *Mathematics*, 9(18):2214, 2021.

[185] Martina Conte, Sergio Casas-Tintò, and Juan Soler. Modeling invasion patterns in the glioblastoma battlefield. *PLoS computational biology*, 17(1):e1008632, 2021.

[186] O Bavi, M Hosseininia, M Hajishamsaei, and MH Heydari. Glioblastoma multiforme growth prediction using a proliferation-invasion model based on nonlinear time-fractional 2d diffusion equation. *Chaos, Solitons & Fractals*, 170:113393, 2023.

[187] Zhihui Wang, Romica Kerketta, Yao-Li Chuang, Prashant Dogra, Joseph D Butner, Terisse A Brocato, Armin Day, Rong Xu, Haifa Shen, Eman Simbawa, et al. Theory and experimental validation of a spatio-temporal model of chemotherapy transport to enhance tumor cell kill. *PLoS computational biology*, 12(6):e1004969, 2016.

[188] DK Button. Biochemical basis for whole-cell uptake kinetics: specific affinity, oligotrophic capacity, and the meaning of the michaelis constant. *Applied and Environmental Microbiology*, 57(7):2033–2038, 1991.

[189] Deanna M Tiek, Janice D Rone, Garrett T Graham, Evan L Pannkuk, Bassem R Haddad, and Rebecca B Riggins. Alterations in cell motility, proliferation, and metabolism in novel models of acquired temozolomide resistant glioblastoma. *Scientific Reports*, 8(1):7222, 2018.

[190] Richard O Hynes. The extracellular matrix: not just pretty fibrils. *Science*, 326(5957):1216–1219, 2009.

[191] BW Simons and C Brayton. Challenges and limitations of mouse xenograft models of cancer. In *Patient Derived Tumor Xenograft Models*, pages 25–36. Elsevier, 2017.

[192] Stuart Currie, Kavi Fatania, Russell Frood, Ruth Whitehead, Joanna Start, Ming-Te Lee, Benjamin McDonald, Kate Rankeillor, Paul Roberts, Aruna Chakrabarty, et al. Imaging spectrum of the developing glioblastoma: A cross-sectional observation study. *Current Oncology*, 30(7):6682–6698, 2023.

[193] TS Deisboeck, ME Berens, AR Kansal, S Torquato, AO Stemmer-Rachamimov, and EA Chiocca. Pattern of self-organization in tumour systems: complex growth dynamics in a novel brain tumour spheroid model. *Cell proliferation*, 34(2):115–134, 2001.

[194] AR Kansal, S Torquato, GR Harsh Iv, EA Chiocca, and TS Deisboeck. Cellular automaton of idealized brain tumor growth dynamics. *Biosystems*, 55(1-3):119–127, 2000.

[195] Adewale Fadaka, Basiru Ajiboye, Oluwafemi Ojo, Olusola Adewale, Israel Olayide, and Rosemary Emuowhochere. Biology of glucose metabolization in cancer cells. *Journal of Oncological Sciences*, 3(2):45–51, 2017.

[196] Otto Warburg. On the origin of cancer cells. *Science*, 123(3191):309–314, 1956.

[197] Aude Carreau, Bouchra El Hafny-Rahbi, Agata Matejuk, Catherine Grillon, and Claudine Kieda. Why is the partial oxygen pressure of human tissues a crucial parameter? small molecules and hypoxia. *Journal of cellular and molecular medicine*, 15(6):1239–1253, 2011.

[198] Barbara Muz, Pilar de la Puente, Feda Azab, and Abdel Kareem Azab. The role of hypoxia in cancer progression, angiogenesis, metastasis, and resistance to therapy. *Hypoxia*, 3:83, 2015.

[199] Conan K. N. Li. The glucose distribution in 9l rat brain multicell tumor spheroids and its effect on cell necrosis. *Cancer*, 50(10):2066–2073, 1982.

[200] Michael Roslin, Roger Henriksson, Per Bergström, Urban Ungerstedt, and A Tommy Bergenheim. Baseline levels of glucose metabolites, glutamate and glycerol in malignant glioma assessed by stereotactic microdialysis. *Journal of neuro-oncology*, 61(2):151–160, 2003.

[201] Evan Noch and Kamel Khalili. Molecular mechanisms of necrosis in glioblastoma: the role of glutamate excitotoxicity. *Cancer biology & therapy*, 8(19):1791–1797, 2009.

[202] Nannette Jelluma, Xiaodong Yang, David Stokoe, Gerard I Evan, Tobias B Dansen, and Daphne A Haas-Kogan. Glucose withdrawal induces oxidative stress followed by apoptosis in glioblastoma cells but not in normal human astrocytes. *Molecular cancer research*, 4(5):319–330, 2006.

[203] Nicholas A Graham, Martik Tahmasian, Bitika Kohli, Evangelia Komisopoulou, Maggie Zhu, Igor Vivanco, Michael A Teitell, Hong Wu, Antoni Ribas, Roger S Lo, et al. Glucose deprivation activates a metabolic and signaling amplification loop leading to cell death. *Molecular systems biology*, 8(1):589, 2012.

[204] Jill A Gallaher, Joel S Brown, and Alexander RA Anderson. The impact of proliferation-migration tradeoffs on phenotypic evolution in cancer. *Scientific reports*, 9(1):1–10, 2019.

[205] OH Minchenko, OO Riabovol, DO Tsymbal, DO Minchenko, and OO Ratushna. Effect of hypoxia on the expression of nuclear genes encoding mitochondrial proteins in u87 glioma cells. *Ukr Biochem J*, 88(3):54–65, 2016.

[206] Meitham Amereh, Henning Struchtrup, and Ben Nadler. Mathematical modeling of spherical shell-type pattern of tumor invasion. *Symmetry*, 15(2):283, 2023.

[207] Ionut Luchian, Ancuta Goriuc, Darius Sandu, and Mihai Covasa. The role of matrix metalloproteinases (mmp-8, mmp-9, mmp-13) in periodontal and peri-implant pathological processes. *International Journal of Molecular Sciences*, 23(3):1806, 2022.

[208] Kazunori Mori, Tetsu Uchida, Toshihiko Yoshie, Yuko Mizote, Fumihiro Ishikawa, Masato Katsuyama, and Motoko Shibanuma. A mitochondrial ros pathway controls matrix metalloproteinase 9 levels and invasive properties in ras-activated cancer cells. *The FEBS journal*, 286(3):459–478, 2019.

[209] Feini Qu, Farshid Guilak, and Robert L Mauck. Cell migration: implications for repair and regeneration in joint disease. *Nature Reviews Rheumatology*, 15(3):167–179, 2019.

[210] Caroline A Schneider, Wayne S Rasband, and Kevin W Eliceiri. Nih image to imagej: 25 years of image analysis. *Nature methods*, 9(7):671–675, 2012.

[211] Arthur W Lambert and Robert A Weinberg. Linking emt programmes to normal and neoplastic epithelial stem cells. *Nature Reviews Cancer*, 21(5):325–338, 2021.

[212] Basil Bakir, Anna M Chiarella, Jason R Pitarresi, and Anil K Rustgi. Emt, met, plasticity, and tumor metastasis. *Trends in cell biology*, 30(10):764–776, 2020.

[213] Umesh Prasad Yadav, Tashvinder Singh, Pramit Kumar, Praveen Sharma, Harsimrat Kaur, Sadhana Sharma, Sandeep Singh, Santosh Kumar, and Kapil Mehta. Metabolic adaptations in cancer stem cells. *Frontiers in oncology*, 10:1010, 2020.

[214] Jian Chen, Yanjiao Li, Tzong-Shiue Yu, Renée M McKay, Dennis K Burns, Steven G Kernie, and Luis F Parada. A restricted cell population propagates glioblastoma growth after chemotherapy. *Nature*, 488(7412):522–526, 2012.

[215] Erina Vlashi, Chann Lagadec, Laurent Vergnes, Tomoo Matsutani, Kenta Masui, Maria Poulou, Ruxandra Popescu, Lorenza Della Donna, Patrick Evers, Carmen Dekmezian, et al. Metabolic state of glioma stem cells and nontumorigenic cells. *Proceedings of the National Academy of Sciences*, 108(38):16062–16067, 2011.

[216] Rebecca L Klank, Steven S Rosenfeld, and David J Odde. A brownian dynamics tumor progression simulator with application to glioblastoma. *Convergent science physical oncology*, 4(1):015001, 2018.

[217] Yvonne Yang, Marc C Schubert, Thomas Kuner, Wolfgang Wick, Frank Winkler, and Varun Venkataramani. Brain tumor networks in diffuse glioma. *Neurotherapeutics*, 19(6):1832–1843, 2022.

[218] Anoop P Patel, Itay Tirosh, John J Trombetta, Alex K Shalek, Shawn M Gillespie, Hiroaki Wakimoto, Daniel P Cahill, Brian V Nahed, William T Curry, Robert L Martuza, et al. Single-cell rna-seq highlights intratumoral heterogeneity in primary glioblastoma. *Science*, 344(6190):1396–1401, 2014.

[219] Anna M Bielecka-Wajdman, Tomasz Ludyga, Daria Smyk, Wojciech Smyk, Magdalena Mularska, Patrycja Świderek, Wojciech Majewski, Christina Susanne Mullins, Michael Linnebacher, and Ewa Obuchowicz. Glucose influences the response of glioblastoma cells to temozolomide and dexamethasone. *Cancer Control*, 29:10732748221075468, 2022.

[220] Alexander RA Anderson, Mark AJ Chaplain, E Luke Newman, Robert JC Steele, and Alastair M Thompson. Mathematical modelling of tumour invasion and metastasis. *Computational and mathematical methods in medicine*, 2(2):129–154, 2000.

[221] Mark AJ Chaplain, MIROSŁAW LACHOWICZ, ZUZANNA SZYMAŃSKA, and Dariusz Wrzosek. Mathematical modelling of cancer invasion: the importance of cell–cell adhesion and cell–matrix adhesion. *Mathematical Models and Methods in Applied Sciences*, 21(04):719–743, 2011.

[222] Alisha M Mendonsa, Tae-Young Na, and Barry M Gumbiner. E-cadherin in contact inhibition and cancer. *Oncogene*, 37(35):4769–4780, 2018.

[223] Martina McDermott, Alex J Eustace, Steven Busschots, Laura Breen, John Crown, Martin Clynes, Norma O'Donovan, and Britta Stordal. In vitro development of chemotherapy and targeted therapy drug-resistant cancer cell lines: a practical guide with case studies. *Frontiers in oncology*, 4:40, 2014.

[224] Ahyeon Koh, Daeshik Kang, Yeguang Xue, Seungmin Lee, Rafal M Pielak, Jeonghyun Kim, Taehwan Hwang, Seunghwan Min, Anthony Banks, Philippe

Bastien, et al. A soft, wearable microfluidic device for the capture, storage, and colorimetric sensing of sweat. *Science translational medicine*, 8(366):366ra165–366ra165, 2016.

[225] Roland H Wenger, Vartan Kurtcuoglu, Carsten C Scholz, Hugo H Marti, and David Hoogewijs. Frequently asked questions in hypoxia research. *Hypoxia*, 3:35, 2015.

[226] A. Vollmann-Zwerenz, V. Leidgens, G. Feliciello, C.A. Klein, and P. Hau. Tumor cell invasion in glioblastoma. *Int. J. Mol. Sci.*, 21:1932, 2020.

[227] D. Hanahan and R.A. Weinberg. Hallmarks of cancer: The next generation. *Cell*, 144:646–674, 2011.

[228] Y. Huang, W. Hong, and X. Wei. The molecular mechanisms and therapeutic strategies of emt in tumor progression and metastasis. *J. Hematol. Oncol.*, 15:129, 2022.

[229] M. Stakheyeva, V. Riabov, I. Mitrofanova, N. Litviakov, E. Choynzonov, N. Cherdyntseva, and J. Kzhyshkowska. Role of the immune component of tumor microenvironment in the efficiency of cancer treatment: Perspectives for personalized therapy. *Curr. Pharm. Des.*, 23:4807–4826, 2017.

[230] L.M. Ellis and D.J. Hicklin. Vegf-targeted therapy: Mechanisms of anti-tumour activity. *Nat. Rev. Cancer*, 8:579–591, 2008.

[231] J.K. Mouw, G. Ou, and V.M. Weaver. Extracellular matrix assembly: A multiscale deconstruction. *Nat. Rev. Mol. Cell Biol.*, 15:771–785, 2014.

[232] K.J. Wolf, J. Chen, J.D. Coombes, M.K. Aghi, and S. Kumar. Dissecting and rebuilding the glioblastoma microenvironment with engineered materials. *Nat. Rev. Mater.*, 4:651–668, 2019.

[233] J.I. Erices, C. Bizama, I. Niechi, D. Uribe, A. Rosales, K. Fabres, G. Navarro-Martínez, Á. Torres, R. San Martín, and J.C. Roa. Glioblastoma microenvironment and invasiveness: New insights and therapeutic targets. *Int. J. Mol. Sci.*, 24:7047, 2023.

[234] C.-B. Crivii, A.B. Bosca, C.S. Melincovici, A.-M. Constantin, M. Mărginean, E. Dronca, R. Sufletel, D. Gonciar, M. Bungărdean, and A. Șovrea. Glioblastoma microenvironment and cellular interactions. *Cancers*, 14:1092, 2022.

[235] B. Dundar, S.M. Markwell, N.V. Sharma, C.L. Olson, S. Mukherjee, and D.J. Brat. Methods for in vitro modeling of glioma invasion: Choosing tools to meet the need. *Glia*, 68:2173–2191, 2020.

[236] L. Orcheston-Findlay, S. Bax, R. Utama, M. Engel, D. Govender, and G. O'Neill. Advanced spheroid, tumouroid and 3d bioprinted in-vitro models of adult and paediatric glioblastoma. *Int. J. Mol. Sci.*, 22:2962, 2021.

[237] D. Grimm, H. Schulz, M. Krüger, J.L. Cortés-Sánchez, M. Egli, A. Kraus, J. Sahana, T.J. Corydon, R. Hemmersbach, P.M. Wise, and et al. The fight against cancer by microgravity: The multicellular spheroid as a metastasis model. *Int. J. Mol. Sci.*, 23:3073, 2022.

[238] N. Di Caprio and J.A. Burdick. Engineered biomaterials to guide spheroid formation, function, and fabrication into 3d tissue constructs. *Acta Biomater.*, 165:4–18, 2022.

[239] M. Amereh, A. Seyfoori, and M. Akbari. In vitro brain organoids and computational models to study cell death in brain diseases. *In Neuronal Cell Death: Methods and Protocols; Springer: New York, NY, USA*, page 281–296, 2022.

[240] D.M. van Pel, K. Harada, D. Song, C.C. Naus, and W.C. Sin. Modelling glioma invasion using 3d bioprinting and scaffold-free 3d culture. *J. Cell Commun. Signal.*, 12:723–730, 2018.

[241] D. Del Duca, T. Werbowetski, and R.F. Del Maestro. Spheroid preparation from hanging drops: Characterization of a model of brain tumor invasion. *J. Neurooncol.*, 67:295–303, 2004.

[242] F. Mirab, Y.J. Kang, and S. Majd. Preparation and characterization of size-controlled glioma spheroids using agarose hydrogel microwells. *PLoS ONE*, 14:e0211078, 2019.

[243] F. Xu, C. Dawson, M. Lamb, E. Mueller, E. Stefanek, M. Akbari, and T. Hoare. Hydrogels for tissue engineering: Addressing key design needs toward clinical translation. *Front. Bioeng. Biotechnol.*, 10:849831, 2022.

[244] H. Goodarzi Hosseinabadi, E. Dogan, A.K. Miri, and L. Ionov. Digital light processing bioprinting advances for microtissue models. *ACS Biomater. Sci. Eng.*, 8:1381–1395, 2022.

[245] Jr. Pliego, J.R. and J.M. Riveros. Hybrid discrete-continuum solvation methods. *Wiley Interdiscip. Rev. Comput. Mol. Sci.*, 10:e1440, 2020.

[246] E. Gacek, R.R. Mahutga, and V.H. Barocas. Hybrid discrete-continuum multiscale model of tissue growth and remodeling. *Acta Biomater.*, 163:7–24, 2023.

[247] M. Amereh, M. Akbari, and B. Nadler. In-silico study of asymmetric remodeling of tumors in response to external biochemical stimuli. *Sci. Rep.*, 13:941, 2023.

[248] T. Hayami, Y.L. Kapila, and S. Kapila. Mmp-1 (collagenase-1) and mmp-13 (collagenase-3) differentially regulate markers of osteoblastic differentiation in osteogenic cells. *Matrix Biol.*, 27:682, 2008.

[249] M. Amereh, S. Shojaei, T. Walsh, P. Dogra, V. Cristini, B. Nadler, and M. Akbari. Unveiling the role of metabolic rates variation in driving tumor heterogeneity and controlling growth and invasion: Insights from an integrated multiscale in-vitro in-silico framework. *Res. Sq.*, 2023.

[250] N.V. Krakhmal, M.V. Zavyalova, E.V. Denisov, S.V. Vtorushin, and V.M. Perelmuter. Cancer invasion: Patterns and mechanisms. *Acta Naturae*, 7:17, 2015.

[251] P. Friedl and S. Alexander. Cancer invasion and the microenvironment: Plasticity and reciprocity. *Cell*, 147:992–1009, 2011.

[252] D.A. Murphy and S.A. Courtneidge. The 'ins' and 'outs' of podosomes and invadopodia: Characteristics, formation and function. *Nat. Rev. Mol. Cell Biol.*, 12:413–426, 2011.

[253] G. Helmlinger, P.A. Netti, H.C. Lichtenbeld, R.J. Melder, and R.K. Jain. Solid stress inhibits the growth of multicellular tumor spheroids. *Nat. Biotechnol.*, 15:778–783, 1997. [Google Scholar] [CrossRef] [PubMed].

[254] I. Koh, J. Cha, J. Park, J. Choi, S.-G. Kang, and P. Kim. The mode and dynamics of glioblastoma cell invasion into a decellularized tissue-derived extracellular

matrix-based three-dimensional tumor model. *Sci. Rep.*, 8:4608, 2018. [Google Scholar] [CrossRef] [PubMed].

[255] B. Deng, Z. Zhao, W. Kong, C. Han, X. Shen, and C. Zhou. Biological role of matrix stiffness in tumor growth and treatment. *J. Transl. Med.*, 20:540, 2022. [Google Scholar] [CrossRef] [PubMed].

[256] J. Hao and R.A. Weiss. Mechanical behavior of hybrid hydrogels composed of a physical and a chemical network. *Polymer*, 54:2174–2182, 2013. [Google Scholar] [CrossRef].

[257] S. Quintero-Fabián, R. Arreola, E. Becerril-Villanueva, J.C. Torres-Romero, V. Arana-Argáez, J. Lara-Riegos, M.A. Ramírez-Camacho, and M.E. Alvarez-Sánchez. Role of matrix metalloproteinases in angiogenesis and cancer. *Front. Oncol.*, 9:480558, 2019. [Google Scholar] [CrossRef].

[258] E. Henke, R. Nandigama, and S. Ergün. Extracellular matrix in the tumor microenvironment and its impact on cancer therapy. *Front. Mol. Biosci.*, 6:160, 2020. [Google Scholar] [CrossRef].

[259] Z. Wang and T.S. Deisboeck. Computational modeling of brain tumors: Discrete, continuum or hybrid? In *Scientific Modeling and Simulations*, page 381–393. Springer, Berlin/Heidelberg, Germany, 2009. [Google Scholar].